이학박사학위논문

Development of a Stochastic Convection Parameterization and Its Application to Climate Modeling

확률론적 대류 모수화 개발 및 기후 모델링에의 적용

2023년 2월

서울대학교 대학원

지구환경과학부

신 지 훈

Development of a Stochastic Convection Parameterization and Its Application to Climate Modeling

확률론적 대류 모수화 개발 및 기후 모델링에의 적용

지도교수 백 종 진

이 논문을 이학박사 학위논문으로 제출함

2022년 10월

서울대학교 대학원

지구환경과학부

신 지 훈

의 이학박사 학위논문을 인준함

2023년 1월

위 원 장 손 석 우 (인)

부위원장 백 종 진 (인)

위 원 엄 준 식 (인)

위 원 한 지 영 (인)

위 원 송 환 진 (인)

Development of a Stochastic Convection Parameterization and Its Application to Climate Modeling

by

Jihoon Shin

A Dissertation Submitted to the Faculty of the Graduate School of Seoul National University in Partial Fulfillment of the Requirements for the Degree of Doctor of Philosophy

February 2023

Advisory Committee:

Professor Seok-Woo Son, Chair
Professor Jong-Jin Baik, Advisor
Professor Junshik Um
Doctor Ji-Young Han
Professor Hwan-Jin Song

Abstract

Convection parameterization is about modeling convective turbulence involving scales smaller than the scales resolved by a dynamic model. While there are many challenges associated with developing convection parameterization, one major issue that has recently gained attention is stochastic convection parameterization. As the horizontal grid size of numerical weather prediction (NWP) models and climate models gets smaller, convection activity within the grid becomes highly stochastic, and the quasi-equilibrium assumption is not valid anymore. In this study, we investigate the physical processes that generate convective cloud variabilities and develop a stochastic parameterization that simulates the mean and variance of convective tendencies for different grid sizes based on the unified convection scheme (UNICON).

First of all, the characteristics of the global simulation of original UNICON is evaluated. Using Community Earth System Model version 1 with UNICON implemented (Seoul National University Earth Model version 0, SEM0), we analyzed the impacts of El Niño-Southern oscillation (ENSO) and Madden-Julian oscillation (MJO) on the genesis of tropical cyclones (TG). Overall, SEM0 shows much better performance than CESM1 in terms of reproducing the observed impacts of MJO and combined impacts of ENSO and MJO on TG. Using long-term coupled global simulations of UNICON, we also developed a new methodology for ENSO forecast, model-analog (MA) – linear inverse model (LIM) (MA-LIM). MA-LIM nudges sea surface temperature (SST) and sea surface height anomalies forecasted by the LIM into the MA. At short (long) lead month, the LIM (MA) predicts the Niño3.4 SST anomalies better than the MA (LIM). On the other hand, the MA-LIM shows the best performance at

all lead month. The MA-LIM found to substantially remedies the undesirable aspects of the MA.

By extending UNICON, we develop a stochastic UNICON for shallow convection with convective updraft plumes at the surface randomly sampled from the correlated multivariate Gaussian distribution for updraft vertical velocity ($\hat{w}$) and thermodynamic scalars ($\hat{\phi}$), of which standard deviations and inter-variable correlations are derived from the surface layer similarity theory. The updraft plume radius ($\hat{R}$) at the surface follows a power-law distribution with a specified scale break radius. To enhance computational efficiency, we also develop a hybrid stochastic UNICON consisting of n bin plumes and a single stochastic plume, each of which mainly controls the ensemble mean and variance of grid-mean convective tendency, respectively. We evaluated the stochastic UNICON using the Large-Eddy Simulation (LES) of the Barbados Oceanographic and Meteorological Experiment (BOMEX) shallow convection case in a single-column mode. Consistent with the assumptions in the stochastic UNICON, the LES-simulated $\hat{w}$ and $\hat{\phi}$ at the surface follow approximately the half- and full-Gaussian distributions, respectively. LES showed that a substantial portion of the variability in $\hat{\phi}$ at the cloud base stems from the surface, which also supports the concept of stochastic UNICON that simulates various types of moist convection based on the dry stochastic convection launched from the surface. Overall, stochastic UNICON adequately reproduces the LES-simulated grid-mean thermodynamic states as well as the mean and variance of $\hat{\phi}$, including their dependency on the domain size and $\hat{R}$.

In addition to the stochastic initialization at the near-surface, a stochastic mixing model with a machine learning technique is proposed for mass

flux convection schemes. The model consists of the stochastic differential equations (SDEs) for the fractional entrainment rate, fractional detrainment rate, fractional dilution rate, and vertical acceleration. Unknowns in SDEs are parameterized using a deep neural network with the inputs of cloud and environment properties. The deep neural network is found to predict entrainment and detrainment rates better than previously proposed parameterizations. The new mixing model is implemented in stochastic UNICON and tested in a single-column mode for two marine shallow convection cases. It is shown that the simulations with the new mixing model produce realistic mean and variance of various convective updraft properties and that the appropriate amount of stochasticity is generated. Consistently accurate simulations of updraft mass fluxes and moist conserved variables reduce model errors in the original UNICON.

We extended the stochastic UNICON, which was originally formulated for shallow convection, to deep convection by parameterizing the impact of mesoscale organized flow on updraft properties. The extended stochastic UNICON parameterizes thermodynamic properties of updrafts at the near-surface as a multivariate Gaussian distribution, where the variances of the distribution are the summation of variances from non-organized turbulence and mesoscale organized flow. The scale break radius is parameterized as a linear function of the strength of mesoscale organized flow. The free parameters introduced in the formulation of stochastic UNICON are optimized using ten cases of single-column model (SCM) simulations over the ocean. Stochastic UNICON with the optimized parameters significantly reduces the biases of thermodynamic profiles and precipitation rates simulated in the original UNICON for tropical

convection cases. The simulation of the variation in anomalies of temperature and moisture associated with the Madden-Julian oscillation (MJO) is also improved. An additional simulation of an idealized deep convection case shows that stochastic UNICON produces enhanced cloud variabilities with dependency on updraft radius, indicating its ability to represent the coexistence of shallow and deep convection.

The global climate simulation using stochastic UNICON is evaluated and compared with UNICON, focusing on the simulation of the Madden–Julian oscillation (MJO). The performances of UNICON and stochastic UNICON on simulating observed mean climates are comparable, while stochastic UNICON slightly reduces the mean bias of climate variables. For the simulation of intraseasonal variabilities, stochastic UNICON outperforms UNICON in many aspects. Stochastic UNICON improves the simulation of the intensity and propagation patterns of boreal winter MJO, which is too weakly simulated in UNICON. The coherency between MJO-related convection and large-scale circulation is also enhanced, which many climate models underestimate. The improvement of MJO simulation by stochastic UNICON is related to a better representation of the relationship between moisture and convection in the model. The increased frequency of shallow convection in stochastic UNICON leads to stronger moisture convergence that precedes convection activity peak and results in the more robust development of organized convection and more frequent intense precipitation. A precipitation budget analysis reveals that the moisture tendencies due to horizontal advection and convective process are consistently enhanced during MJO developing periods by stochastic UNICON.

Keywords: PhD, CUMG, dissertation, stochastic, convection, parameterization, climate model

Student ID: 2016-20420

Contents

List of Figures

List of Tables

1 Overview

1.1 Parameterization of sub-grid convection

Atmospheric models numerically solve a set of governing equations discretized in time and space. The physical processes involving scales smaller than the scales resolved by the dynamic model should be parameterized. This is what is called sub-grid scale physical parameterizations. Among many physical processes, the characteristic of unresolved turbulent motion is highly dependent on the scale of the dynamic model resolves. Below the horizontal grid scale order of 100 m, which is in the scope of large-eddy simulation (LES), the unresolved turbulent motion is in inertial sub-range so the sub-grid turbulence fluxes can be estimated based on Kolmogorov theory. For the larger horizontal grid scales, convective turbulent motions and clouds are only partially resolved, and those are the scales where the parameterization of convection is needed. According to recent LES studies, the minimum LES resolution to simulate realistic statistics of deep convective clouds is 200 m (Khairoutdinov et al. 2009).

In global atmospheric models, sub-grid turbulence is parameterized with planetary boundary layer (PBL) schemes and convection schemes. The PBL schemes usually treat vertical transport by symmetric and local turbulence based on the local diffusion approach. Currently, many PBL schemes include the treatment of non-local transport by dry convection. Then the convection

schemes are responsible for the non-local transport above PBL due to moist convection. During the last half century, the convection parameterization community has developed various shallow and deep convection schemes, and now the vast majority of operational convection schemes adopted the mass-flux formulation. These mass-flux schemes have their own closure to close their formulation. More specifically, the closure is some vertically integrated quantities (e.g. convective available potential energy (CAPE), convective inhibition (CIN), moisture convergence), which is needed to determine the strength of sub-grid convection in an assumption that convection activity is in equilibrium with the large-scale processes (the quasi-equilibrium assumption proposed by Arakawa and Schubert (1974)). Traditionally, operational weather and climate models have used separate schemes for shallow convection and deep convection with different closures. This leads to the artificial discontinuity between the transition of shallow-to-deep convection.

The interesting and also challenging issues for convection parameterization appear in the weather and climate numerical models operating in the "gray zone" at horizontal grid spacings in the range of 200 m to 10 km. This is the range where convective turbulence is partially resolved. For instance, in $\mathcal{O}(1\,\mathrm{km})$ resolution, the mesoscale convective system can be resolved, but shallow cumuli are still on a sub-grid scale. Many weather and climate models do switch off their convection parameterizations at an arbitrary resolution within the gray zone. However, previous studies indicate that shallow convection and non-local turbulence in the convective boundary layer (CBL) are still in gray zone (= partially resolved) even in 1 km resolution (Honnert et al. 2011, 2020). Furthermore, sub-grid convection is no longer quasi-equilibrium and becomes highly stochastic in the gray-zone scale. Due to the increase of computational

power, now more operational weather and climate models are operating in the gray zone. Hence, there is an urgent need for the development of scale-aware convection parameterizations with a consistent formulation for various convection regimes.

1.2 A unified convection scheme (UNICON)

A unified convection scheme (UNICON) developed by Park (2014a,b) is one of the rare convection schemes designed to simulate subgrid mesoscale organized flow and its impacts on subgrid convection in an explicit way. UNICON simulates all dry-moist, forced-free, and shallow-deep convection in a seamless, consistent and unified way, without relying on the quasi-equilibrium assumption such as the CAPE or CIN closures. UNICON consists of diagnostic multiple convective updrafts rising from the surface, diagnostic multiple convective downdrafts generated from convective updrafts, and prognostic subgrid cold pool and associated mesoscale organized flow within the planetary boundary layer (PBL).

Parameterizing subgrid mesoscale organized flows driven by various sources (e.g., subgrid cold pool, orography, and land-sea ice contrasts) and their impacts on subgrid convection is one major issue in the convection modeling community. Traditional convection scheme based on quasi-equilibrium assumption inevitably lo ses the memory of the plume properties between the model time steps. This lack of plume memory seems to be one reason that conventional diagnostic convection schemes fail to simulate the diurnal cycle of precipitation and the Madden-Julian oscillation (MJO, Madden and Julian (1971)). In UNICON, a convective downdraft can penetrate down into the PBL across the inversion

barrier at the PBL top if forced by sufficient evaporative cooling of precipitation. This generates cold pools which can be characterized by negatively buoyant density current. UNICON solves prognostic budget equations for fractional area and properties of the cold pool which produces the memory effect of convection. The properties of a convective updraft at the surface and the mixing environmental air within and above the PBL are modulated by the subgrid mesoscale organized flow driven by the cold pool.

As explained in Section 1.1, some atmospheric models treat non-local turbulence with multiple schemes, where dry convection is treated by PBL schemes and moist convection by (shallow and deep) convection schemes. However, cumulus growing above the PBL is typically originated from an underlying dry convective plume. Thus, it appears to be more reasonable to simulate both the dry and moist convection within a single convection scheme rather than simulating in separate PBL and convection schemes. An approach in line with this philosophy is an eddy diffusivity–mass flux (EDMF) model (Siebesma et al. 2007). Figure 1.1 summarizes the framework of UNICON compared to the traditional framework.

It was shown that in addition to mean climate, UNICON also successfully simulates the diurnal cycle of precipitation, MJO, and tropical cyclones, all of which have been difficult to simulate in GCMs (Park et al. 2019, 2017). The global simulation results with UNICON are submitted to Coupled Model Intercomparison Project Phase 6 (CMIP6) (Park et al. 2019) and available online.

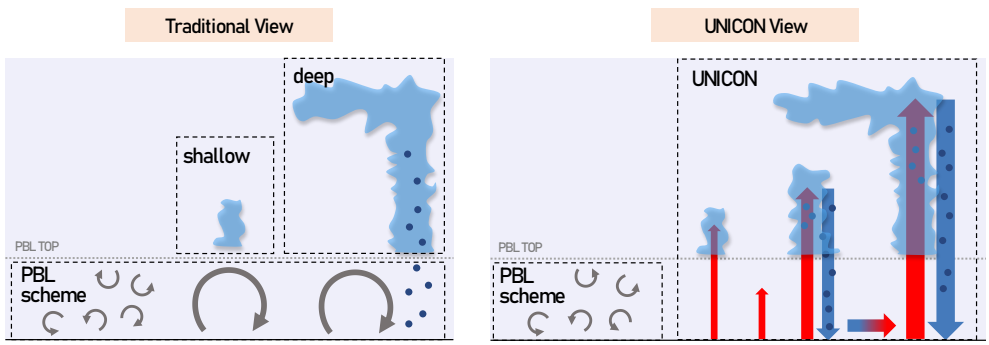

Figure 1.1 Schematic of two different views of subgrid turbulence parameterizations, which are the traditional view and UNICON view. Small gray circular arrows denote local turbulence, and large gray circular arrows denote non-local turbulence within PBL. Vertical red and blue arrows denote convective updrafts and downdrafts, respectively. The horizontal arrow in the right panel indicates cold pools that can affect the properties of newly formed updrafts.

1.3 Stochastic convection parameterization

Convective clouds formed in a similar environment tend to have different thermodynamic properties (Yanai et al. 1973; Esbensen 1978; Arakawa and Schubert 1974). The goal of convection scheme is to reproduce the observed tendency induced by multiple convective plumes. Most convection schemes in general circulation models (GCMs) use an ensemble-mean plume parameterized as a deterministic function of the grid-mean environmental variable (the bulk plume method), which has a fundamental limitation in simulating the spatiotemporal variability generated by multiple convective plumes. Craig and Cohen (2006) noted that the grid-mean convective tendency averaged over the horizontal grid size, $G = \Delta x \Delta y$, where Δx and Δy are the zonal and meridional width of the model grid, respectively, would fluctuate depending on how many plumes exist within the grid.

Figure 1.2 displays the fluctuation of grid-mean convective tendency with different grid sizes. For a grid with $\Delta x = 128\,\mathrm{km}$, there are a number of convective plumes within the grid, thus the grid-mean convective tendency is in a near-equilibrium state. As the grid size gets smaller, the grid-mean convective tendency becomes more fluctuating because a smaller number of convective cells are presented with the grid. Parameterizing the stochastic fluctuation of grid-mean convective tendency is known to influence various aspects of mean climate and variability simulated by GCMs (Lin and Neelin 2000, 2002).

The goal of a stochastic convection scheme is to adequately parameterize the distribution of multiple convective plumes and their impacts on the environment in an equilibrium state. Proper representation of the distribution is important

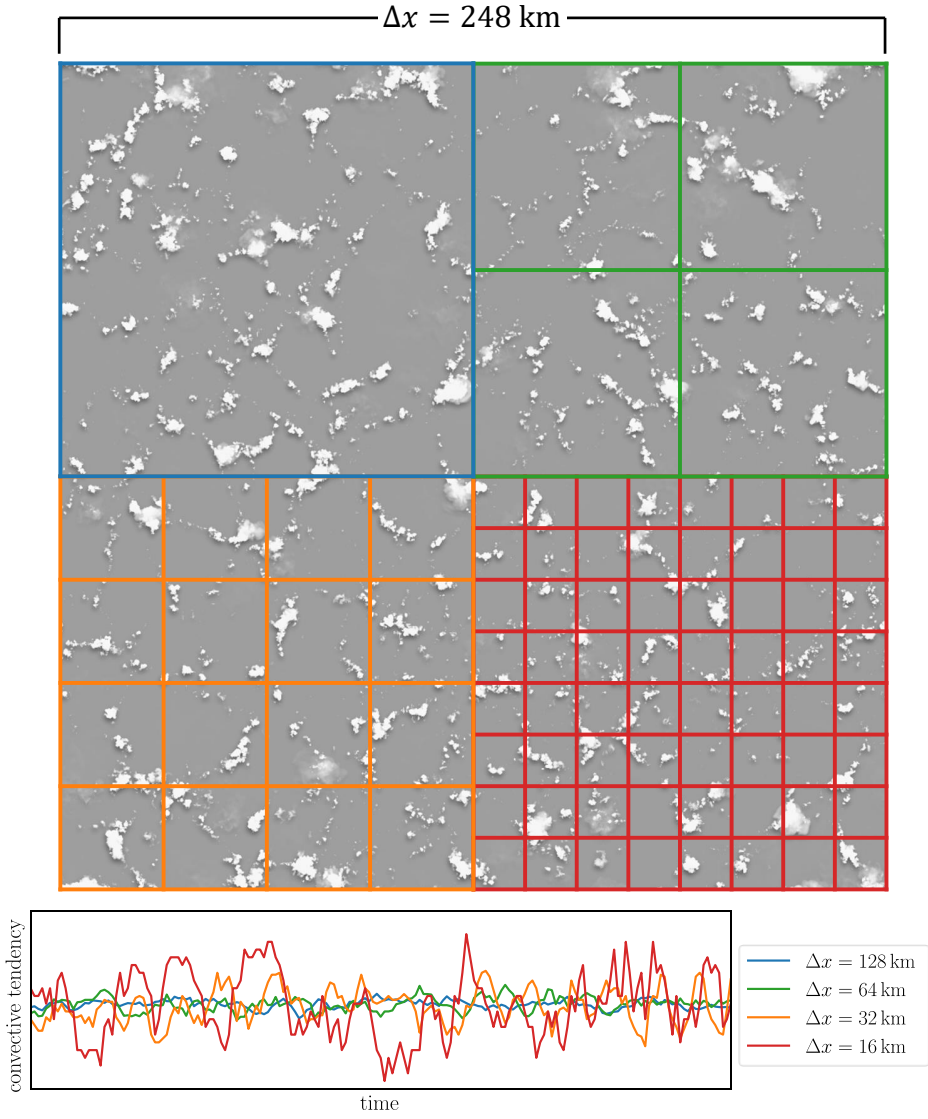

Figure 1.2 Schematic of explaining the stochastic fluctuation of grid-mean convective tendency which depends on horizontal grid size. A domain with size of $G = 248\,\mathrm{km} \times 248\,\mathrm{km}$ is subdivided into smaller grids with $\Delta x = 128\,\mathrm{km},\ 64\,\mathrm{km},\ 32\,\mathrm{km},\ 16\,\mathrm{km}$. The time series of convective tendencies of subdivided grids are shown in the panel below.

for an accurate simulation of the ensemble mean as well as the variance (Arakawa and Schubert 1974). A simple approach is to impose stochastic perturbations directly onto the grid-mean convective tendency generated by a single deterministic ensemble-mean plume (Buizza et al. 1999; Palmer et al. 2009; Teixeira and Reynolds 2008). This method has a weakness since the imposed stochastic perturbations are somewhat arbitrary without an explicit connection with the underlying physical processes.

A more advanced approach is to impose stochastic perturbations on the physical processes controlling the grid-mean convective tendency. One example is the stochastic convection scheme of Plant and Craig (2008) which assumes that the mass flux of the convective updraft plumes follows an exponential distribution, and a grid-mean convective mass flux over a wide range of G was calculated by stochastic sampling from the assumed exponential distribution. The assumed mass-flux distribution method has been a common way to coupling a stochastic convective parameterization with the existing convection schemes (e.g. Keane et al. (2014), Wang et al. (2016), and Sakradzija et al. (2016)). Nevertheless, there is still a lack of understanding of the physical mechanisms that generate the mass-flux distribution. In addition, it is a more challenging issue to model how the mass-flux distribution assumed in a stochastic convection scheme varies depending on the grid size, associated with the gray zone problem.

1.4 Objectives and organization of the dissertation

The objectives of this dissertation can be summarized as follow:

- Assess the physical processes that generate variabilities between convective plumes.

- Formulate a stochastic convection parameterization based on UNICON scheme (stochastic UNICON), which can simulate the development of variabilities of individual convective plumes at the fundamental level.
- Develop a framework to calculate the mean and variance of convective tendency generated by multiple convective plumes presented in a grid.
- Evaluate the various aspects of the simulation results with the proposed stochastic convection scheme, including mean climatology, variabilities, and scale-awareness.

The rest of this dissertation is organized as follows:

- In Chapter 2, the performance of UNICON in global simulations is evaluated regarding the modulation of tropical cyclone activity by ENSO and MJO.
- In Chapter 3, a new methodology for enhancing ENSO predictability is discussed as an application of global simulations of UNICON.
- In Chapter 4, the formulation for stochastic UNICON as stochastic initialization at the near-surface is derived and tested using a single-column model.
- In Chapter 5, a stochastic mixing model for mass-flux convection scheme using a machine learning technique is proposed and tested using a single-column model.
- In Chapter 6, stochastic UNICON is extended to deep convection and tested using a single-column model.
- In Chapter 7, a global climate simulation with stochastic UNICON is evaluated.
- Chapter 8 provides summary and conclusions.

2 Global Simulation of UNICON: Modulation of Tropical Cyclone Activity by ENSO and MJO

2.1 Introduction

Tropical cyclone (TC) activity is influenced by various atmospheric and oceanic variation modes at different time scales. The El Niño-Southern oscillation (ENSO) and Madden-Julian oscillation (MJO; Madden and Julian (1971)), which are the main modes of natural variability in the tropics on the interannual and subseasonal time scales, respectively, are known to exert significant effects on TC activity. Numerous observational studies have documented the impacts of ENSO (Gray 1984; Chan 1985; Lander 1994; Chu and Wang 1997; Wang and Chan 2002; Camargo et al. 2007) and MJO (Liebmann et al. 1994; Maloney and Hartmann 2000b,a; Hall et al. 2001; Camargo et al. 2009) on TC activity in various ocean basins. Chu (2004) reported that El Niño promotes the genesis of TCs (TG, hereafter) in the southeast portions of the western North Pacific (WNP) and central North Pacific, and inhibits TC activity in the northwest portion of the WNP and northern Atlantic Ocean. In the case of MJO, TG during convectively active MJO phases is enhanced by up to four times compared to TG during suppressed MJO phases (Maloney and Hartmann 2000a; Barrett and Leslie 2009; Camargo et al. 2009). Several studies have also

examined the combined effects of ENSO and MJO on TC activity. The results revealed that the effects of ENSO and MJO cannot be added linearly because the modulation of TG by MJO under ENSO conditions is asymmetric (e.g. Li et al. (2012)).

Additionally, there have been efforts to reproduce and understand observed ENSO-TC and MJO-TC relationships using dynamical models. Observed ENSO-TC relationships have been reproduced by various general circulation models (GCMs), which enables the dynamical seasonal forecasting of TC, at least qualitatively (Wu and Lau 1992; Vitart and Anderson 2001; Iizuka and Matsuura 2008; Chen and Lin 2011; Li and Wang 2014; Bell et al. 2014; Chand et al. 2017). However, modeling studies on MJO-TC relationships are very limited because most GCMs have difficulty in reproducing the observed amplitude and phase of MJO (Slingo et al. 1996; Lin et al. 2006) and TC patterns (Vitart 2006), mainly due to the problems in parameterized moist convection processes. Vitart (2009) documented the impact of MJO on the statistics of TCs in the ECMWF forecasting model, and Satoh et al. (2012) and Jiang et al. (2012) conducted similar works based on high-resolution models. These studies adopted hindcast simulations targeting two to four weeks of MJO predictability, such that their results can be sensitive to errors in initial conditions. Kim et al. (2014) examined MJO-TC relationships utilizing a few atmospheric GCMs, but only over the WNP.

Here, we investigate the impacts of ENSO and MJO on TG using a set of long-term coupled GCM simulations produced by the Community Earth System Model version 1 (CESM1; Hurrell et al. (2013)) and Seoul National University Earth System Model Version 0 with a unified convection scheme

(SEM0-UNICON; Park et al. (2019)). The results are then compared to observations. SEM0-UNICON is one of the very few GCMs that simulates observed ENSO, MJO, and their teleconnections reasonably well (Yoo et al. 2015; Ahn et al. 2019), as well as TG and the diurnal cycle of precipitation (Park et al. 2019). To the best of our knowledge, our study is the first attempt to investigate the combined effects of ENSO and MJO on TG utilizing GCMs, which can contribute to improving short-term TC forecasting and understanding changes in TC activity in the future.

2.2 Data and analysis methods

For observational analysis, for the period of January of 1979 to December of 2016 (38 years), TG over the eastern North Pacific and Atlantic oceans was obtained from the TC track data of the National Oceanic and Atmospheric Administration's National Hurricane Center. TG in other regions was obtained from the TC track data of the US Navy's Joint Typhoon Warning Center (Chu et al. 2002). The monthly sea surface temperature (SST) used for defining ENSO came from HadISST/OI.v2 observations (Rayner et al. 2003). Daily outgoing longwave radiation (OLR) and horizontal wind vector at levels of 850 and 200 hPa, which are used for defining MJO, came from observations of the Advanced Very-High-Resolution Radiometer satellite (Liebmann and Smith 1996) and the NCEP-NCAR reanalysis product (Kalnay et al. 1996), respectively. In terms of GCMs, we conducted 400 years of coupled simulations at a 0.95^o latitude x 1.25^o longitude horizontal resolution (nominally, 1 degree) in the pre-industrial period with the CESM1 and SEM0-UNICON (Park et al. 2019) driven by the forcing data obtained from phase six of the Coupled Model

Intercomparison Project (CMIP6; Eyring et al. (2016)). Although not sufficient for reproducing the observed strength of TCs, 1 degree GCM simulations have been used in previous studies to examine the genesis of tropical cyclones (Murakami and Sugi 2010; Strachan et al. 2013). The atmospheric model of SEM0 is the Seoul National University Atmosphere Model Version 0 with a UNICON (SAM0-UNICON) and the other components of SEM0 (e.g., land, ocean, and sea ice models) are identical to those of CESM1. SAM0-UNICON is one of the international GCMs participating in the CMIP6 and is based on the Community Atmosphere Model Version 5 (CAM5; Neale et al. (2010), Park et al. (2014)), but CAM5's shallow (Park and Bretherton 2009) and deep convection schemes (Zhang and McFarlane 1995b) were replaced by UNICON (Park 2014a,b) with a revised treatment of convective detrainment processes (Park et al. 2017). Park et al. (2019) demonstrated that the global mean climate and ENSO simulated by SAM0/SEM0 are similar to those simulated by CAM5/CESM1. However, SAM0/SEM0 substantially improves the simulation of MJO, the diurnal cycle of precipitation, and TG.

The methods we utilized for defining ENSO, MJO, and TG are similar to those presented in Park et al. (2019). El Niño, neutral ENSO, and La Niña events are defined as years in which the standardized detrended monthly SST anomalies averaged over the NINO34 region (170^{o}W-120^{o}W, 5^{o}S-5^{o}N) during the months of November to January are greater than 1, between -1 and 1, and smaller than -1, respectively. To define MJO phases for individual days, we conducted multivariate empirical orthogonal function analysis using 20 to 100 days bandpass filtered, OLR and zonal winds at levels of 850 and 200 hPa averaged over the range of 15^{o}S-15^{o}N. The first two normalized principal components were squared and added to define the daily MJO index. The days

with an MJO index smaller than 1 were defined as "neutral MJO" and the other days were grouped into eight MJO phases (P1, P2, ... , P7, and P8) based on the two principal components. Following the method presented in Park et al. (2019), TG was identified utilizing 6 hourly instantaneous outputs if the relative vorticity at 850 hPa, denoted ξ_{850}, was greater than $12.5 \cdot 10^{-5}$ s^{-1}, the warm-core strength, denoted $\xi_{850} - \xi_{250}$, was greater than $12.5 \cdot 10^{-5}$ s^{-1}, and the two conditions were satisfied at least for two consecutive days. The first time step at which these conditions were simultaneously satisfied was defined as the TC onset time. Due to the short available periods and infrequent occurrence of TCs, the observed TG anomalies associated with the combined variations of ENSO and MJO averaged over the 5^o latitude x 5^o longitude grid boxes were too noisy to be interpreted. To address this issue, following the methods presented in Zhao et al. (2010) and Chand et al. (2017), we computed spatially smoothed TGs by partitioning individual TG events into nearby grid boxes using a two-dimensional Gaussian distribution with a standard deviation of 5^o in both the x and y directions to serve as a normalized probability density function for individual TG events. After defining the ENSO years and MJO days in different phases, the spatially smoothed TGs defined for each 5^o latitude x 5^o longitude grid box were composited onto the phases of ENSO (Fig 2.1) and MJO (Fig 2.2), as well as the combined phases of ENSO and MJO over the globe (Fig 2.3) and in several specific regions (Fig 2.4). We compared the composite results from CESM1 and SEM0 to observed data.

2.3 Results

Figure 2.1 presents the composite TG anomalies during the El Niño and La Niña years obtained from CESM1, SEM0, and observations. During the El

Niño years, the observed TG increases in the central and eastern northern-hemispheric tropical Pacific ocean, where SST (OLR) anomalies are positive (negative), but decreases in the western Pacific and eastern Indian oceans, where SST (OLR) anomalies are negative (positive) (Fig 2.1b). TG also decreases over the far eastern Pacific ocean near the coast of Central America and most of the tropical North Atlantic ocean, although the anomalies in SST and OLR are less pronounced. These results are consistent with previous observational studies (Gray 1984; Chan 1985; Chu and Wang 1997; Ho et al. 2006; Jin et al. 2014). In La Niña years, the aforementioned anomalies are reversed (Fig 2.1e). Qualitatively, both CESM1 and SEM0 reproduced the observed anomalies of SST, OLR, and TG in association with ENSO. However, CESM1 generally underestimates the magnitude of observed anomalies. Both models underestimate the observed TG anomalies over the North Atlantic ocean, where the climatological TGs simulated by CESM1 and SEM0 are lower than the observed values (Park et al. 2019). Compared to the observations, the simulated positive SST and negative OLR anomalies during El Niño years extend too far westward into the western equatorial Pacific and accordingly, the simulated positive TG anomalies also extend too far westward. Similar features can be seen for La Niña years. The pattern correlation (r) between the observed and CESM1-simulated SST anomalies in the tropical region (30^oN-30^oS) is 0.84 (0.86) during the El Niño (La Niña) years. SEM0 produces similar r values of 0.87 (0.88), indicating that both models have similar performance in terms of simulating the observed ENSO. However, both models produce substantially lower pattern correlations for TG anomalies (0.15 (0.25) for CESM1 and 0.23 (0.30) for SEM0), although SEM0 performs slightly better than CESM1.

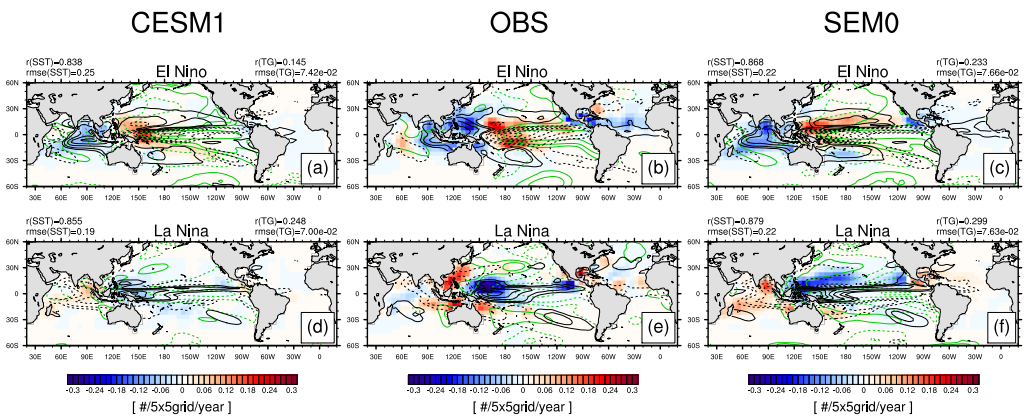

Figure 2.1 (Color) Composite TG anomalies during the (top row) positive and (bottom row) negative phases of ENSO obtained from (left column) CESM1, (center column) observations, and (right column) SEM0. Green lines are the composite anomalies of SST with a contour interval of 0.5 K ($\pm$0.25 K lines are also shown) and black lines are the composite anomalies of OLR with a contour interval of 5 Wm^{-2} ($\pm$2.5 Wm^{-2} lines are also shown). Only statistically significant SST and OLR anomalies above a 95% confidence level based on a two-sided student's t-test are shown. The pattern correlations (r) and rmse values of SST and TG anomalies in the tropical region (30^{o}N-30^{o}S) between the simulations and observation are shown in the upper-left and upper-right corners of the simulation maps, respectively.

Figure 2.2 presents the composite anomalies of TG at different MJO phases. Similar to ENSO, MJO has a significant impact on the variations of regional TG around the world. Similar to the results presented in Camargo et al. (2009), the signs of TG anomalies systematically change depending on MJO phases in all active TC regions. Most TG anomalies are congruent with OLR anomalies, indicating that TCs occur more frequently when latent heat is released by strong mean upward motion (Maloney and Hartmann 2000a). One notable exception is the simultaneous decreases in OLR and TG over the western North Pacific ocean centered at (15^{o}N, 165^{o}E) during MJO phases seven and eight (Fig 2.2k), implying that some factors other than large-scale upward motion also control TG. CESM1 has trouble simulating the observed MJO, as indicated by the very low spatial correlations (r=0.26-0.37) between observed and simulated OLR anomalies compared to SEM0 (r=0.76-0.92). Consequently, the simulated TG anomalies from CESM1 are less realistic (r=0.09$\sim$0.54, root mean squared error (rmse)=8.9$\sim$10.9x10^{-2}) than those from SEM0 (r=0.64$\sim$0.87, rmse=5.0$\sim$7.6x10^{-2}) and weaker than the observations. Similar to the ENSO composite, the simulated TG anomalies associated with MJO over the North Atlantic ocean for both models are weaker than the observations.

Figure 2.3 presents the composite anomalies of TG and OLR in association with the combined variations of ENSO and MJO. The observations reveal that the combined impacts of ENSO and MJO on TG are complicated, which is expected because the ENSO-related anomalies of TG and OLR (Fig 2.1) are comparable in magnitude to the MJO-related anomalies (Fig 2.2), but different in terms of spatial structure. The positive TG anomalies over the South China Sea in the far western North Pacific ocean during La Niña years

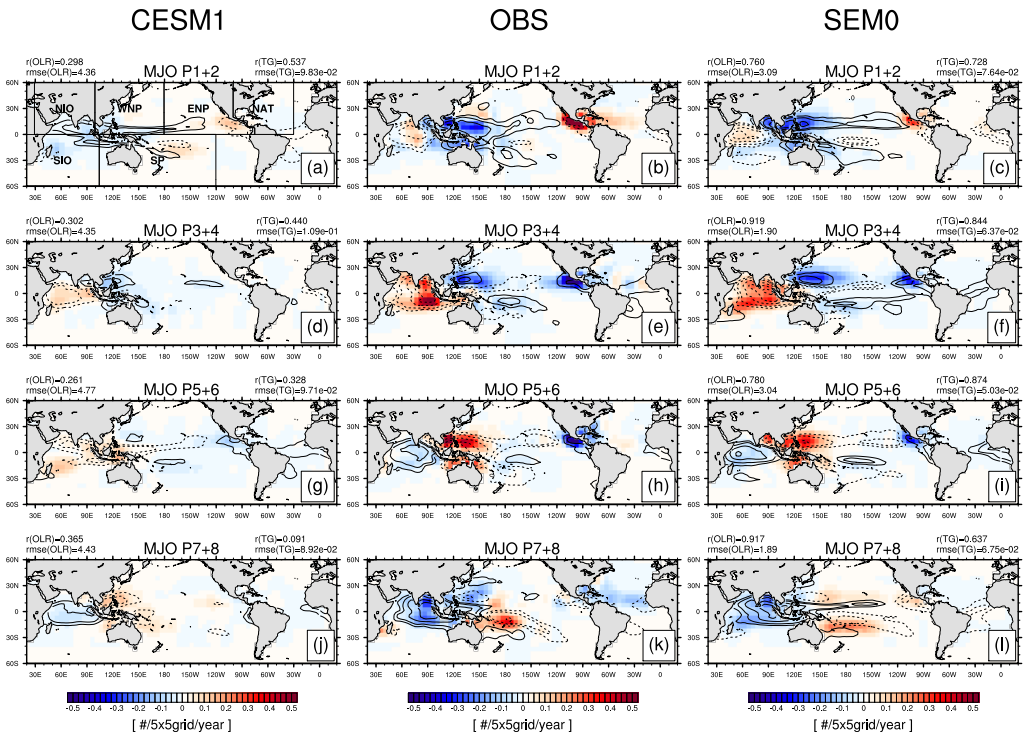

Figure 2.2 (Color) Composite TG anomalies during (first row) MJO phases one and two, (second row) MJO phases three and four, (third row) MJO phases five and six, and (fourth row) MJO phases seven and eight, as obtained from (left column) CESM1, (center column) observations, and (right column) SEM0. Black lines are the composite anomalies of OLR with a contour interval of 5 Wm^{-2} (± 2.5 Wm^{-2} lines are also shown). Only statistically significant OLR anomalies above a 95% confidence level based on a two-sided student's t-test are shown. The pattern correlations (r) and rmse values of OLR and TG anomalies in the tropical region (30^oN-30^oS) between the simulations and observation are shown in the upper-left and upper-right corners of the simulation maps, respectively. Several regions where TC are generated frequently are shown in Fig 2.2a (NIO: Northern Indian Ocean, WNP: Western North Pacific, ENP: Eastern North Pacific, NAT: North Atlantic Ocean, SIO: Southern Indian Ocean, SP: South Pacific).

(Fig 2.1e) are further strengthened during MJO phases five and six (Fig 2.3k), but are reversed during MJO phases one and two (Fig 2.3h). The well-defined positive TG anomalies over the eastern North Pacific and western Atlantic oceans during MJO phases one and two, which are presented in Fig 2.2b, are modulated by ENSO (Figs 2.3b and 2.3h). Regardless, most TG anomalies continue to be congruent with OLR anomalies. In general, as indicated by the higher r values and lower rmse values, SEM0 reproduces the observed anomalies of TG and OLR in association with the combined variations of ENSO and MJO more accurately than CESM1. We speculate that some of the discrepancies between the observations and simulations are a result of the short available period and associated noise in the observational analysis, particularly in the ENSO composites.

Figure 2.4 presents the composite TG anomalies at different phases of ENSO and MJO averaged over several regions in which TCs are generated frequently (see Fig 2.2a). Similar to the previous figures, one can see that the impacts of ENSO and MJO on TG exhibit strong regional dependencies. Over the NAT/NIO/SIO, the observed TG is the largest during La Niña years and smallest during El Niño years, while the opposite is true over the ENP. TCs over the SP (WNP) occur least (most) frequently during neutral ENSO. SEM0 well reproduces the observed dependencies of regional TG on different ENSO phases, at least qualitatively. However, over the WNP, the maximum and minimum TG values are simulated during the El Niño and La Niña years, respectively, instead of during the neutral ENSO. This is due in part to too westward extension of the simulated SST and OLR anomalies in the western tropical Pacific ocean, as mentioned previously (see Fig 2.1). SEM0 also reproduces

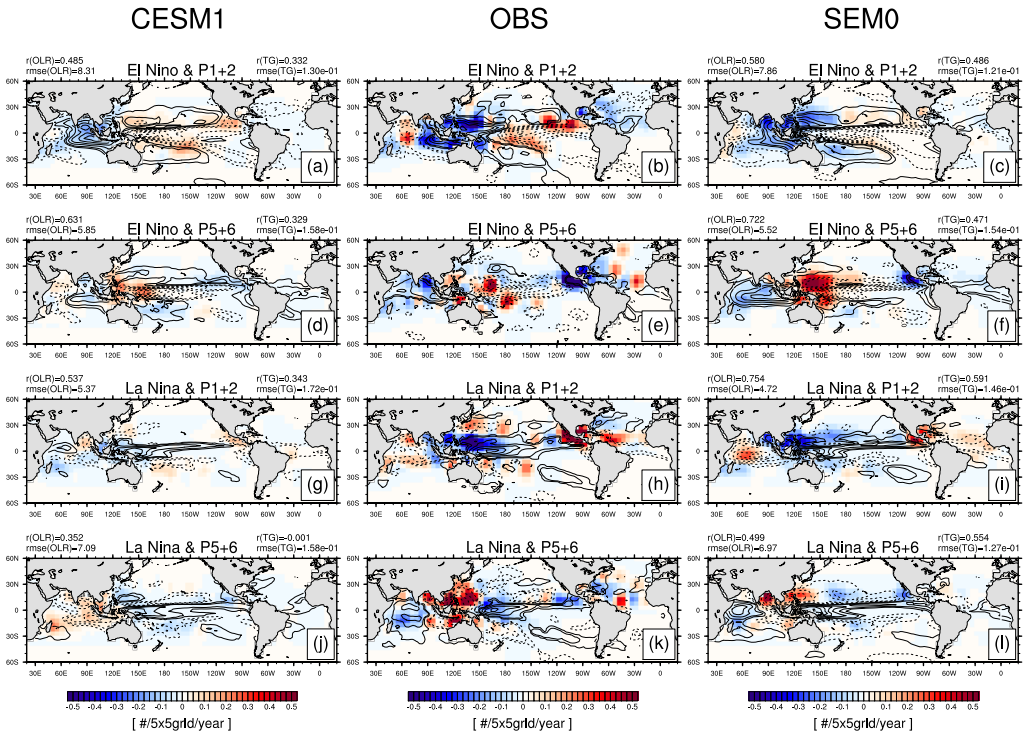

Figure 2.3 (Color) Composite TG anomalies during the (first row) El-Niño and MJO phases one and two, (second row) El-Niño and MJO phases five and six, (third row) La-Niña and MJO phases one and two, and (fourth row) La-Niña and MJO phases five and six obtained from (left column) CESM1, (center column) observations, and (right column) SEM0. Black lines represent the composite anomalies of OLR with a contour interval of 5 Wm^{-2} (± 2.5 Wm^{-2} lines are also shown). Only statistically significant OLR anomalies above a 95% confidence level based on a two-sided students t-test are shown. The pattern correlations and rmse values of OLR and TG anomalies in the tropical region (30^oN-30^oS) between the simulations and observations are shown in the upper-left and upper-right corners of the simulation maps, respectively.

the MJO-related inter-phase variations of the observed TG in each region with reasonable accuracy. Overall, CESM1 performs worse than SEM0.

The impact of ENSO (MJO) on regional TG varies in a complex way depending on the phase of MJO (ENSO). For example, over the ENP and NIO, La Niña enhances TG during the MJO phases five and six, but suppress TG during the MJO phases three and four. Over the NAT, MJO phases one and two enhance TG during La Niña years, but suppress TG during El Niño years. The maximum (minimum) TG values over the WNP are observed during neutral ENSO and MJO phases five and six (La Niña and MJO phases three and four), while the maximum (minimum) TG values over the SIO are observed during La Niña and MJO phases three and four (El Niño and MJO phases seven and eight). To quantify how well the models reproduced the observed dependencies of regional TG on the combined variations of ENSO and MJO, we computed the correlation coefficients and rmse values between the observed and simulated TG values over all of the combined phases of ENSO and MJO in each region (i.e., three ENSO phases multiplied by nine MJO phases, including the neutral MJO phase, results in a total of 27 combined phases). The results are presented in the plots in Figure 2.4. From CESM1 to SEM0, the inter-phase correlation with the observations increases from 0.27 (0.61, 0.25, 0.29, 0.47, and -0.02) to 0.76 (0.76, 0.54, 0.46, 0.77, and 0.68) over the WNP (ENP, NAT, NIO, SIO, and SP). Over the WNP, NAT, and SP, the correlations increase by more than two times. Except over the NIO, the rmse values decrease from CESM1 to SEM0 in all regions. Overall, SEM0 has much better performance than CESM1 in terms of reproducing the observed dependency of TG on the combined variations of ENSO and MJO.

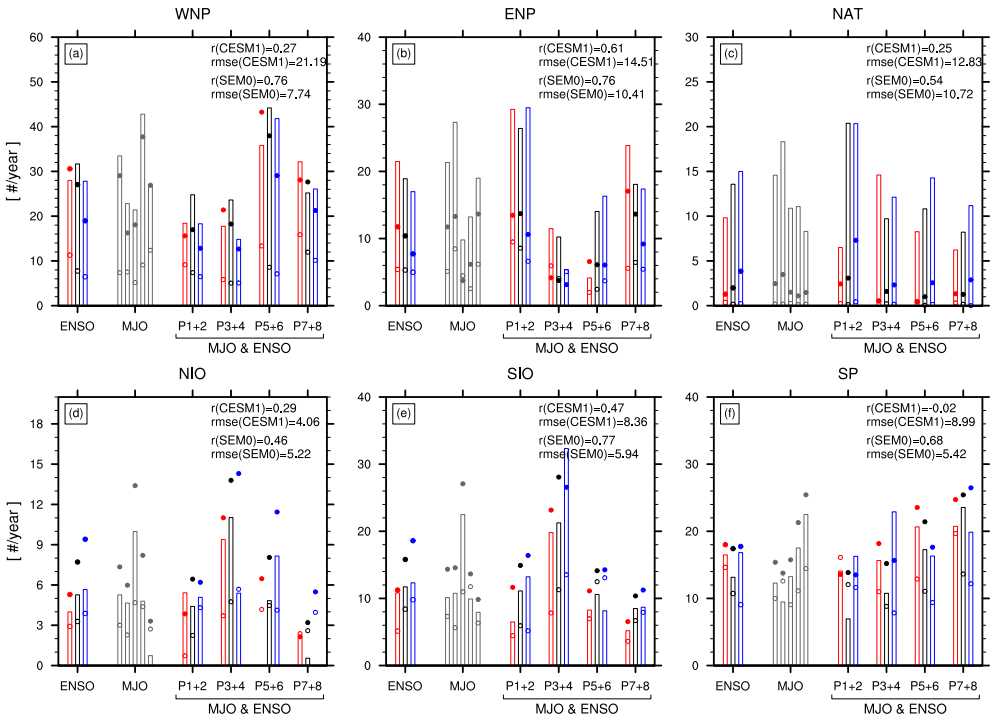

Figure 2.4 Composite TG values averaged over several of the ocean basins presented in Fig 2.2a as functions of the ENSO and MJO phases obtained from the (bars) observations, (closed dots) SEM0, and (open dots) CESM1. The first set of bars and dots (denoted as ENSO) represents the composite TG during the (red) positive, (black) neutral, and (blue) negative phases of ENSO. The second set of bars and dots (denoted as MJO) represents the composite TG during the individual MJO phases (neutral MJO, phases one and two, phases three and four, phases five and six, and phases seven and eight from left to right). The third set of bars and dots (denoted as MJO & ENSO) represents the composite TG for each of the combined phases of ENSO and MJO. The correlations and rmse values between the observed and simulated TG over all combined phases of ENSO and MJO in each region are shown in the upper-right portions of individual plots. To compute these statistics, 27 data points (i.e., three ENSO phases (positive, neutral, negative) $\times$ nine MJO phases (neutral MJO, phases 1–8)) were used for each region.

2.4 Discussion

These improvements from CESM1 to SEM0 are likely a result of the improved simulation of interactions between the TG process and controlling environmental variables, as well as the improved simulations of controlling environmental variables. Additional studies are planned to analyze the sources of these improvements at the process level, which will contribute to understanding the TG processes observed in nature. Finally, SEM0 can serve as a useful tool for studying the interactions between ENSO, MJO, and TCs, as well as their evolutions in a changing climate and methods for improving short-term TC forecasting.

3 Application of Global Simulation of UNICON: Enhancing ENSO Prediction Skill

3.1 Introduction

The El-Niño and Southern Oscillation (ENSO) is the dominant tropical atmosphere-ocean coupled mode. The impact of ENSO is not confined within the tropical Pacific but extends into remote tropical areas, subtropics, and midlatitudes via anomalous Walker and Hadley circulations, equatorial Rossby or Kelvin waves, and quasi-stationary Rossby wave throughout the year (Rasmusson and Carpenter 1982; Ropelewski and Halpert 1987; Lau and Nath 1996; Rowell 2001; Trenberth et al. 1998; Alexander et al. 2002; Park 2004; Park and Leovy 2004; Alexander et al. 2004). An accurate forecast of ENSO is necessary for a reliable weather and climate prediction over the globe. Many general circulation models (GCMs), however, have problems in simulating the basic statistical properties of ENSO (e.g., Bellenger et al. (2014)) and the ENSO-related tropical SST anomalies simulated by most GCMs extend too far west (e.g., Zheng et al. (2012), Li and Xie (2014), Heureux et al. (2019)).

Many statistical methods have been developed to forecast ENSO. Here, we will focus on two Markovian techniques that predict anomalous sea surface temperatures (SSTs) and sea surface heights (SSHs) throughout the tropical Indo-Pacific, linear inverse models (LIMs, Penland and Sardeshmukh (1995))

and model-analogs (MA, Ding et al. (2018, 2019)). The LIM is an empirical dynamic model, which assumes that the temporal evolution of the predictand is described by a multivariate linear Markov process plus some noise that represents rapidly evolving (and hence unpredictable) nonlinearities. MA forecast ensembles are extracted from preexisting long GCM simulations, by finding those states that best match each initial observed anomaly and tracking their subsequent evolution. Newman and Sardeshmukh (2017) showed that the hindcast skill of the multi-model GCM ensemble-mean (MME, hereafter) is comparable to the LIM in the central-western Pacific, but is higher in the eastern Pacific at long lead; generally, however, the LIM had skill that met or exceeded single model ensemble-means. Ding et al. (2018) showed that MA not only effectively reproduces the forecast skill of MME throughout the tropics, but is significantly better in the eastern Pacific despite being based on the same models used for the MME. These studies suggest that potential forecast skill is roughly linear in the central Pacific where the LIM works well, but also has a predictably nonlinear component in the eastern Pacific where the MA works better. Both techniques are anomaly models that, unlike the MME, are identically bias-corrected and do not suffer from initialization shock. However, both also have practical limits due to the need for lengthy observational or GCM simulation datasets and the choice of the state vector, which may or may not represent all of the predictive information in the initial climate state. In our study, we investigate combining them in an model-analog – linear inverse model (MA-LIM), by nudging the monthly SST and SSH anomalies forecasted by the LIM to those forecasted by the MA.

3.2 The Model-Analog-LIM (MA-LIM)

In this section, we briefly summarize the LIM and MA, and explain how we construct the MA-LIM. As described in Penland and Sardeshmukh (1995), the LIM approximates the temporal evolution of a state vector $\mathbf{x}$ with the stochastically-forced linear dynamical system,

$$d\mathbf{x}/dt = \mathbf{L}\mathbf{x} + \xi, \tag{3.1}$$

where $\mathbf{L}$ is the linear system matrix and ξ is a Gaussian white noise forcing vector. From (3.1), the ensemble mean forecast (and most probable state vector) $\mathbf{x}(t+\Delta t)$ at forecast lead Δt is $\mathbf{x}(t+\Delta t) = \exp(\mathbf{L}\Delta t)\mathbf{x}(t)$. The matrix $\mathbf{L}$ is determined by an error variance minimization procedure as $\mathbf{L} = \ln[\mathbf{C}(\tau_0)\mathbf{C}(0)^{-1}]/\tau_0$, where $\mathbf{C}(\tau_0) = \langle \mathbf{x}(t+\tau_0) \cdot \mathbf{x}(t)^T \rangle$ is the covariance matrix at lag τ_0 (=1 month in this study) and the angle bracket denotes the expected mean. Following Newman and Sardeshmukh (2017), our LIM computes temporal evolution of a state vector in the EOF space, so $\mathbf{x}$ represents the leading 16 and 9 principal components (PCs) of monthly SST and SSH anomalies, which explain 76% (80) and 61% (64) of the total variance, respectively, for the GCM simulations (observations). The number of EOF modes retained was chosen by trial-and-error to maximize the cross-validated forecast skill, but the skill is relatively insensitive to this choice.

The MA computes the temporal evolution of SST/SSH anomalies at model grid points by averaging the cases from a long GCM simulation where the SST/SSH fields are similar to the target one (Ding et al. 2018, 2019). More specifically, if the forecast starts from calendar month, t=0, the MA selects the 20 cases with small normalized root-mean-squared error in the tropics, $E(i) \equiv$

$0.5 \cdot [rmse(SST'(0), SST'_p(0,i))/\sigma(SST'_p) + rmse(SSH'(0), SSH'_p(0,i))/\sigma(SSH'_p)]$ at the same calendar month in different years. Here, $SST'(0)/SSH'(0)$ are the monthly anomalies of SST/SSH at the current time step, $SST'_p(0,i)/SSH'_p(0,i)$ are the monthly anomalies of SST/SSH at the calendar month 0 in the ith year obtained from a certain population (from now on, the long-term GCM simulation from which the MA cases are drawn will be referred to as a population), rmse is the spatial root-mean-squared-error in the tropics, and $\sigma(SST'_p)$ and $\sigma(SSH'_p)$ are the spatiotemporal standard deviations of monthly SST/SSH anomalies averaged over the tropical oceans in the population. Again, although the ensemble size was chosen by trial-and-error to optimize the forecast skill, the results are not too sensitive to this choice (see Ding et al. (2018) for further analysis). In this paper, we focus only on combining the single LIM forecast with the ensemble mean MA forecast, although the approach could be employed for individual ensemble members.

The strategy of the MA-LIM is to combine the state vector $\mathbf{x}$ predicted by the LIM with that predicted by the MA (Fig 3.1). To combine the LIM in EOF space and MA in model-grid space, the monthly SST/SSH anomalies obtained by the MA are first projected onto the 16-SST/9-SSH EOFs, and then combined with the LIM with an appropriate weighting factor, w, defined so that $w = 0$ ($w = 1$) returns the LIM (MA) forecast. We have tested sensitivity to w and results are shown below. It was found that $w \approx 0.15$ produced the best forecast skill for the SST anomalies in the Tropics between 25^oS and 25^oN. Because of the EOF truncation used, the reconstructed initial monthly anomalies of SST/SSH for the LIM (i.e., $SST'_L(0)$ in Fig 3.1) are slightly different from the raw monthly anomalies of SST/SSH (i.e., $SST'(0)$ in

Fig 3.1). Moreover, the initial monthly anomalies of SST/SSH obtained from the ensemble mean of the 20 cases for the MA (i.e., $SST'_a(0)$ in Fig 3.1) are also different from $SST'(0)/SSH'(0)$ due in part to sampling uncertainty. In general, $SST'(0)$ is much closer to $SST'_L(0)$ than $SST'_a(0)$, so that our MA-LIM uses $SST'_L(0)/SSH'_L(0)$ as initial conditions.

We perform two analyses: one is a "perfect" model analysis, where the initial target states are drawn from the control run, and the other is an observation analysis, where the initial target states are obtained from observed conditions during Jan 1961 - Dec 2010. We performed the analyses using monthly SST/SSH fields at 1^o latitude x 1^o longitude horizontal resolution in the tropics (25^oS-25^oN). For the perfect model analysis, we use 450 years from the pre-industrial period simulated by the Seoul National University Atmosphere Model Version 0 with a Unified Convection Scheme (SAM0-UNICON, Park et al. (2019)). All model analyses are ten-fold cross validation of the 10 subsets of the simulation data: each subset consists of a 45 year evaluation period (10% of the entire data) and the remaining 405 year population. The EOFs of SST and SSH are obtained from the entire 450 year simulation, while the linear system matrix $\mathbf{L}$ and monthly climatologies of SST/SSH are obtained from the 405 year population. For the hindcast observational analysis, we use 50 years of observed monthly SST (HadISST, Rayner et al. (2003)) and SSH (ECMWF ocean reanalysis, Balmaseda et al. (2013)). Prior to performing the analysis, we detrended the observed monthly SST/SSH in each grid box. Similar to the perfect model analysis, all observational analyses are from the cross-validation of the 10 subsets of the observation data with a 5 year evaluation period in each subset. The EOFs of SST/SSH are obtained from the entire observational record while the linear system matrix $\mathbf{L}$ and monthly climatologies of SST/SSH

at the grid boxes are obtained from the 45 years data excluding the evaluation period. The LIM approach relies on the assumption that $\mathbf{L}$ is independent of the lag τ_0. To test the validity of this assumption, we performed the so-called τ test using the method suggested by Winkler et al. (2001) and verified that both the observation and GCM simulation data used in our study passed the τ test.

SAM0-UNICON (or simply, SAM0), one of the international coupled GCMs participating in phase 6 of the Coupled Model Intercomparison Project (CMIP6; Eyring et al. (2016)), is based on the Community Atmosphere Model version 5 (CAM5; Neale et al. (2010), Park et al. (2014)), but CAM5's shallow (Park and Bretherton 2009) and deep convection schemes (Zhang and McFarlane 1995b) have been replaced by the unified convection scheme described by Park (2014a,b), with a revised treatment of the convective detrainment processes (Park et al. 2017). Park et al. (2019) showed that the global mean climate and ENSO simulated by SAM0 were roughly similar to those of CAM5/Community Earth System Model version 1 (CESM1, Hurrell et al. (2013)); however, SAM0 substantially improved the simulations of the Madden-Julian Oscillation, diurnal cycle of precipitation, and tropical cyclones.

To quantify forecast skill, we transformed the EOF forecasts back into geographic space and computed the anomaly correlation coefficient, $ACC = Cov(SST'_f, SST')/\{\sigma(SST'_f)\cdot\sigma(SST')\}$ and the root-mean-squared error based skill score, RMSSS=1-$rmse(SST'_f, SST')/\sigma(SST')$ as a function of the lead month. Here, $Cov(SST'_f, SST')$ and $rmse(SST'_f, SST')$ are the covariance and root-mean-squared error between the forecasted (SST'_f) and observed (or simulated by SAM0) monthly SST anomalies (SST'), respectively, and σ is the standard deviation.

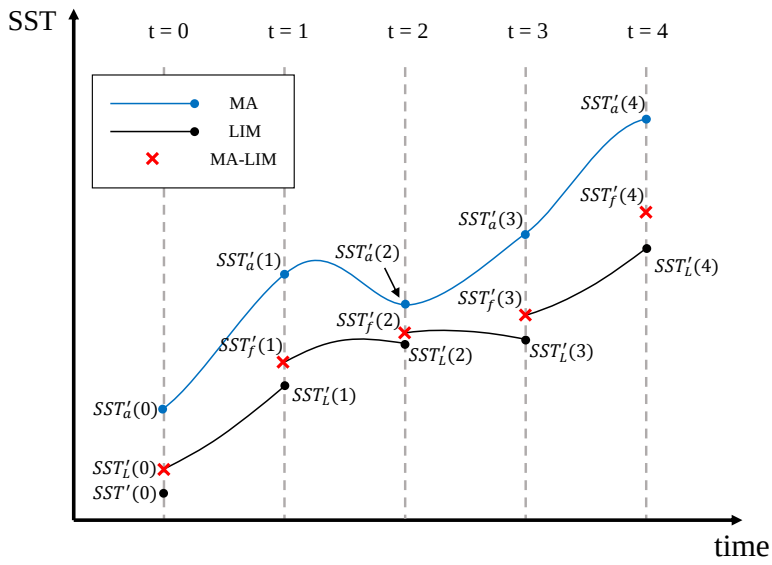

Figure 3.1 Diagram illustrating the MA-LIM for the tropical oceans. The initial monthly SST anomaly used by LIM, $SST'_L(0)$, is constructed from the 16/9 EOFs and then a one month LIM forecast is made to $SST'_L(1)$. Due to the EOF truncation, $SST'_L(0)$ is slightly different from the raw initial monthly SST anomaly, $SST'(0)$. Then, the MA selects 20 cases from the population with anomalous SST/SSH fields similar to $SST'(0)/SSH'(0)$, and computes $SST'_a(0)$, ... $SST'_a(t)$, which is the ensemble average of the EOS-reconstructed 20 selected cases at the forecast time, t. Note that $SST'_a(0)$ is different from $SST'(0)$ and $SST'_L(0)$. The initial conditions of the MA-LIM are set to be identical to those of the LIM. The final forecasted monthly SST anomaly at t=1 is obtained by $SST'_f(1) = (1-w)\cdot SST'_L(1)+w\cdot SST'_a(1)$, where $0 \leq w \leq 1$ is a weighting factor, and these procedures are repeated. In summary, by choosing w=0.15, the MA-LIM can be understood as a LIM slightly nudged by the MA. The same method is used for predicting SSH as well as SST.

3.3 Results

Figure 3.2 shows the Niño3.4 SST prediction skill of the LIM (w=0), MA (w=1), and MA-LIM (w=0.15), as measured by ACC and RMSSS as a function of the lead month, τ. In the perfect model analysis, the LIM has higher skill than the MA for $\tau < 4$ but the MA is more skillful at longer leads (Fig 3.2a). The lower skill of the MA than the LIM at short leads could be due to the errors in the initial condition of the MA: if more accurate initial conditions were used (possible with a longer control run), the MA would likely have a better skill at short leads, too. In contrast to the MA, the MA-LIM ($0 < w < 1$) starts from the same initial condition as the LIM. The performance of the MA-LIM with $w > 0.5$ is roughly between those of the LIM and MA at small τ but becomes similar to that of the MA at large τ because the effect of nudging to the MA is accumulated with time. Surprisingly, the MA-LIM with w=0.15 has a better ACC than the LIM and MA at all τ. The analysis with the RMSSS statistics shows similar results, except that the overall relative performance of the MA to that of the LIM is slightly worse than the one measured by ACC and the crossover τ at which the performance of the MA is identical to that of the LIM has shifted from 4 to 5 months (Fig 3.2b).

In the observational hindcast, however, the crossover τ occurs at ~ 7 months, indicating that the relative performance of the MA with respect to the LIM is degraded from the perfect model to the observation analysis. This is an anticipated result, since the observationally-based LIM also has higher Niño3.4 skill than the MME at short leads (Newman and Sardeshmukh 2017). Also, apart from effects of initalization shock, which appear small in this region (Ding et al. 2018), the MA should not have higher skill than a corresponding

forecast model initialized with the complete climate state. In fact, the SST/SSH anomaly fields in the model simulation are generally different from observations, due to model error, so at $\tau = 0$, the MA in the observational analysis has a lower ACC and RMSSS than does the perfect model analysis. The MA-LIM with a small value of w (w=0.15) performs better than either the LIM and MA for all τ. Since the effect of nugding to the MA is accumulated with time, a small value of w=0.15 does not imply that the non-linearity captured by the MA is insignificant.

Figure 3.3 shows the spatial pattern of ACC in monthly SST anomalies obtained from the LIM at τ=6 and the differences between the MA or MA-LIM and the LIM. Results are shown for the perfect model and observation analyses. The forecast skill of tropical SST anomalies has complex spatial variations. In the perfect model analysis, the overall spatial pattern of ACC from the LIM is similar to the well-known SST anomaly pattern associated with the positive phase of ENSO (Fig 3.3a) with a maximum ACC>0.8 in the southern portion of the central equatorial Pacific Ocean. This is an anticipated result because ENSO is the dominant mode of tropical SST/SSH anomalies. In this region, both the LIM and MA have similar skill, demonstrating that ENSO evolution in the central Pacific in this GCM is well represented by linear dynamics (Penland and Sardeshmukh 1995; Newman and Sardeshmukh 2017). In the eastern equatorial Pacific, western Pacific, and Indian Oceans, the LIM skill is notably worse than the MA skill, suggesting that in these tropical regions, seasonality and/or predictable nonlinearity is important to state evolution. MA performance in other regions, such as the subtropics and Atlantic, is degraded relative to the LIM (Fig 3.3b). The MA-LIM with w=0.15 retains the positive aspects of the MA and substantially remedies the undesirable aspects of the

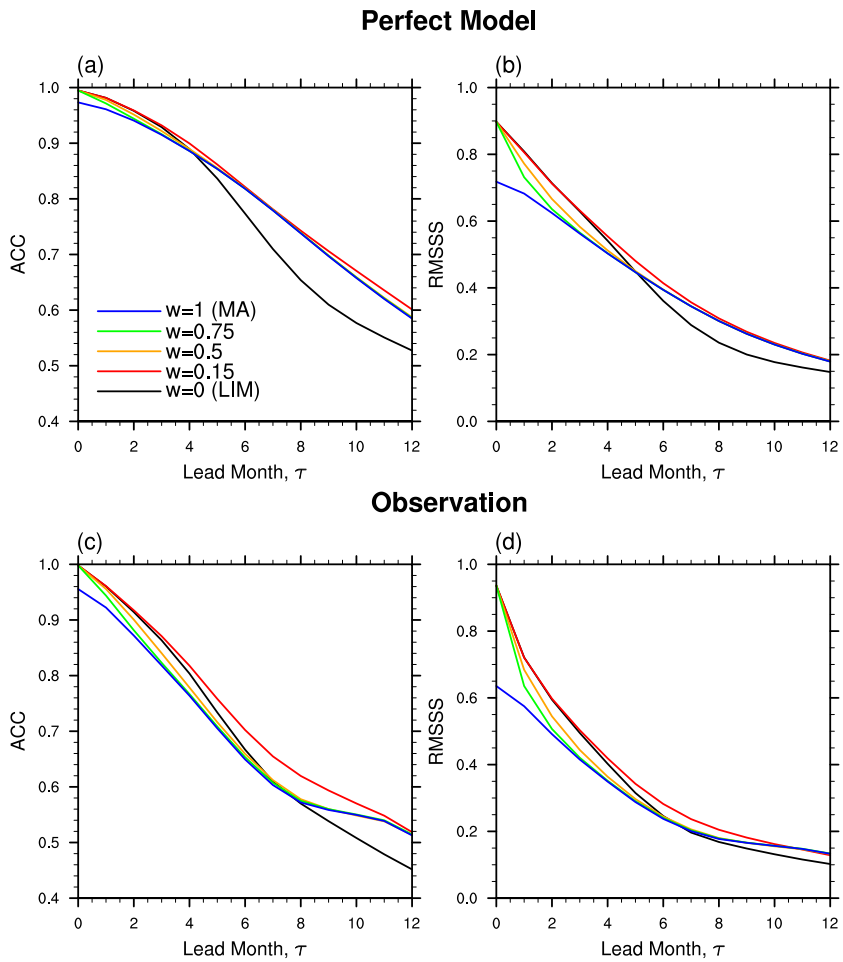

Figure 3.2 The [(a),(c)] anomaly correlation coefficient (ACC) and [(b),(d)] root-mean-squared error based skill score (RMSSS) of the Niño3.4 SST anomalies (170^{o}W-120^{o}W, 5^{o}S-5^{o}N) as a function of the lead month, τ, predicted by the LIM, MA, and MA-LIM with various weighting factor w, obtained from the [(a),(b)] perfect model analysis and [(c),(d)] observational analysis. At τ=0, both ACC and RMSSS are not exactly 1, since the initial monthly SST anomaly of the MA is computed by averaging 20 cases obtained from the GCM simulation while the initial SST anomaly for the LIM and MA-LIM are obtained from the EOF reconstruction of 16/9 EOF modes of tropical SST/SSH anomalies, respectively.

MA, resulting in domain averaged ACC=0.544 that is slightly larger than those of the MA (0.53) and LIM (0.51), with similar improvement seen for RMSSS.

Hindcast skill of the LIM, MA, and MA-LIM in the observational analysis is generally worse than for the perfect model analysis. While this could reflect the fewer samples in the shorter observational record and/or errors in the GCM's simulation of the tropical Pacific, it could also be that tropical Pacific variations in nature are inherently less predictable than within the GCM simulation. Still, the overall spatial patterns of ACC and RMSSS obtained from the LIM in the observational analysis (Figs 3.3d) are similar to those in the perfect model analysis (Figs 3.3a). Note the similarity of the standard deviation of monthly SST anomalies from the SAM0 simulation and observations (compare solid lines in Fig 3.3a and 3.3d). In contrast to the perfect model analysis, except for the eastern Pacific, the MA are generally less skillful than the LIM; the domain averaged ACC (0.307) and RMSSS (0.058) from the MA are substantially lower than those from the LIM (ACC=0.379, RMSSS=0.076). This may be due in part to model error: ENSO-related tropical SST anomalies simulated by most GCMs, including SAM0, typically extend too far westward (Park et al. 2019), and likewise SST skill in the western equatorial Pacific is significantly worse for both the MME and the GCMs that comprise it than for the LIM (Newman and Sardeshmukh 2017). Because the analog evolution is drawn from the GCM simulation, the MA also performs considerably worse than the LIM in the western equatorial Pacific (Fig 3.3e), where SAM0 overestimates the observed standard deviation of monthly SST anomalies (solid lines in Fig 3.3d). Similar to the perfect model analysis, the MA-LIM shows a better performance than the LIM over the eastern equatorial Pacific and Indian Oceans. In addition,

the overall MA-LIM hindcast skill for τ=6 is better than that of the MA and LIM almost everywhere throughout the tropical Indo-Pacific.

Figure 3.4 shows ACC hindcast skill of the Niño3.4 anomalies as a function of the target month and τ for the three methods, presented by comparing LIM skill with the MA minus LIM and MA-LIM minus LIM difference plots. In all cases, the basic features are similar, with relatively lower prediction skill for target months in late spring and early summer. Similar to Fig 3.2, perfect model skill of the MA at short τ is again poorer than for the LIM, while the MA performing better than the LIM at longer leads, primarily for seasons where the performance of the LIM is relatively low. The MA-LIM with w=0.15 retains the advantages of both the LIM at short τ and the MA at long τ, resulting in a better performance than the MA and LIM. The difference is more dramatic comparing the MA-LIM to the LIM in the Niño1.2 region (90^{o}W-80^{o}W, 0^o-10^{o}S; not shown), primarily because the MA itself is relatively more skillful at longer lead there.

The results from the observational analysis are somewhat noisier than those from the perfect model, but show the same basic picture, with the MA-LIM improving LIM skill for predictions of boreal spring Niño3.4 values, where the LIM had lowest skill. For summer, LIM skill is near its minimum, but the MA had no better skill than the LIM and likewise the MA-LIM yielded minimal improvement. On the other hand, for Niño1.2 (not shown), while year-round skill for the MA-LIM exceeds both the MA and LIM (e.g. Figs 3.3d-f), for wintertime verifications the MA-LIM is greatly improved relative to the LIM but is less skillful than the MA itself. The improvements of the SSH forecast skill by the MA-LIM are similar to those of SST both in terms of the spatial distribution and the dependency on τ and target month (not shown). However,

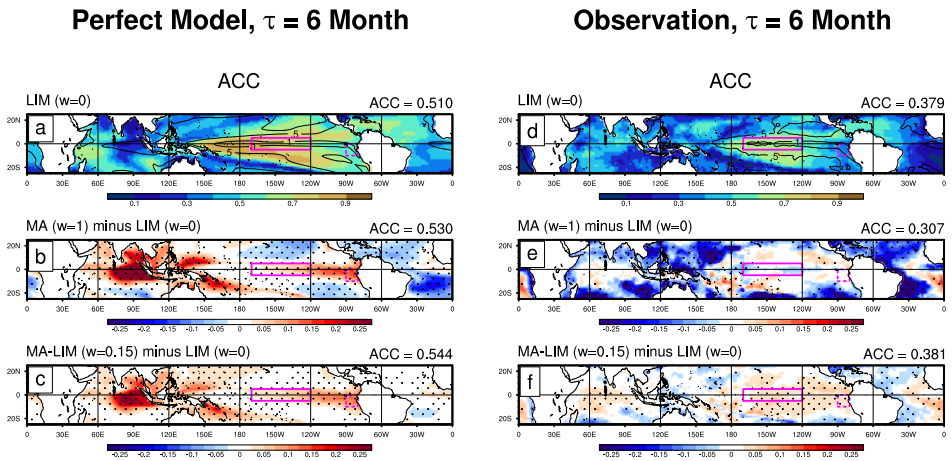

Figure 3.3 Spatial distributions of [(a),(d)] ACC of the SST anomalies at the 6 month lead obtained from the (a) perfect model analysis and (d) observational analysis from LIM. The other figures show the differences between the MA or MA-LIM with w=0.15 and LIM. The grid boxes with statistically significant ΔACC at the 95% confidence level from the bootstrapping (or Monte Carlo) method are denoted by the dot. A domain averaged ACC in the tropical region (25^oS-25^oN) for the LIM, MA, and MA-LIM is shown at the top-right of an individual plot. The solid lines in (a) and (d) are the standard deviations of monthly SST anomaly obtained from the GCM simulation and observation, respectively, with a contour interval of 0.5^oC. The solid and dashed pink boxes denote the Niño3.4 and Niño1.2 regions, respectively.

in the observational analysis, the prediction skill of the MA-LIM in the Atlantic Ocean was in between those of the LIM and MA, where the MA showed a relatively poor prediction skill.

3.4 Discussion

Why does the MA-LIM perform better than either the MA or LIM? A major problem in the MA method is the uncertainty in the initial conditions, which is due in part to insufficient sampling. Because the MA-LIM is designed to start from the LIM's initial condition that is more accurate than that of the MA, the MA-LIM performs better than the MA. On the other hand, the LIM used in our study is a stationary model, that is, the linear system matrix $\mathbf{L}$ or the multivariate covariance matrix $\mathbf{C}$ does not vary with time. The MA-LIM brings the implicit seasonal cycle and nonlinear dynamics in the MA into the LIM in an ad-hoc manner, such that the MA-LIM performs better than the LIM. Another factor is that ENSO also has nonlinear dynamics (An and Jin 2004), which are especially important in the eastern tropical Pacific and can be represented by MA but not LIM.

To further improve the performance of the MA-LIM, it may be necessary to sample more cases from more accurate populations (e.g., more models, improved models, longer runs); refine the sampling and prediction methods of the MA (e.g., use SST/SSH tendencies instead of SST/SSH themselves); and incorporate seasonal cycle directly into $\mathbf{C}$ and $\mathbf{L}$ (e.g., LIM can have variability in the evolution of SST and SSH by constructive interference of the normal modes). We plan to investigate these ways to improve the MA-LIM methodology in the near future.

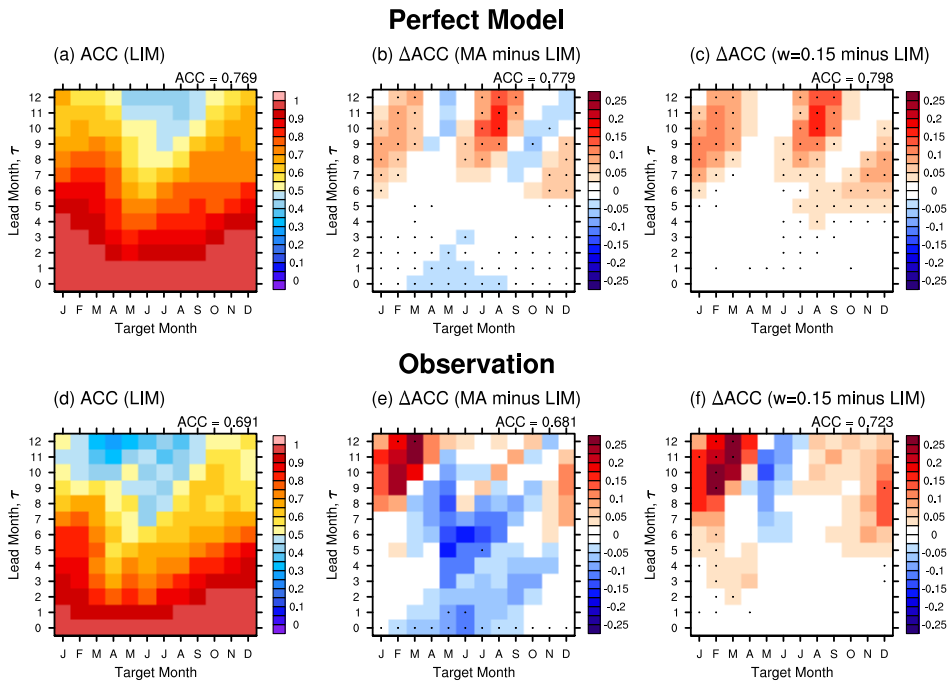

Figure 3.4 (Left) ACC of the Niño3.4 SST anomalies as a function of the target month and lead month τ obtained from the (upper row) perfect model analysis and (lower row) observational analysis with the LIM. The differences between (center) the MA and LIM and (right) the MA-LIM with w=0.15 and LIM are also shown. The domain averaged ACC from the LIM, MA, and MA-LIM with w=0.15 is shown at the top-right of an individual plot. Statistically significant ΔACC at the 95% confidence level from the bootstrapping (or Monte Carlo) method are denoted by the dot.

4 A Stochastic UNICON with Stochastic Initialization at the Near-Surface

4.1 Introduction

As explained in Section 1.3, existing stochastic convection schemes are based on the assumed distribution of a single quantity, usually the grid-mean tendency or the convective mass flux. A more fundamental approach representing the impact of multiple stochastic plumes is to impose stochastic perturbations on the multiple plume properties: number density ($\hat{N}$), radius ($\hat{R}$), vertical velocity ($\hat{w}$), and other thermodynamic scalars ($\hat{\phi}$) of convective updraft plumes. Particularly, the plume size statistics seems to be one of the key ingredients necessary for a scale-adaptive convection scheme (e.g. Park (2014a), Neggers (2015), and Sakradzija et al. (2016)). The radius of a convective updraft plume, $\hat{R}$, is a traditional proxy used for classifying plume types. Many LES studies have shown that thermodynamic profiles of convective plumes are highly dependent on $\hat{R}$, with stronger updrafts being associated with a larger $\hat{R}$ (Böing et al. 2012; Neggers 2015; Khairoutdinov et al. 2009). The plume radius $\hat{R}$ is closely associated with the mass flux ($\hat{M}$) and fractional entrainment rate ($\hat{\epsilon}$), two main sources of convective variability suggested by previous studies. The mass flux is $\hat{M} = \rho \cdot \hat{a} \cdot \hat{w}$ where ρ is air density, $\hat{a}$ is updraft fractional area, and $\hat{w}$ is the relative vertical velocity of convective updraft plume with respect

to the grid-mean vertical velocity. The updraft fractional area is $\hat{a} = \hat{N} \cdot \pi \hat{R}^2$ where $\hat{N}$ $[\# \cdot m^{-2}]$ is the number density of convective updraft plumes.

In this study, we develop a stochastic UNICON by sampling convective updraft plumes at the surface in a random way from the correlated multivariate Gaussian distribution of $\hat{w}$ and $\hat{\phi}$ constructed on the Monin-Obukhov surface layer similarity theory (Monin and Obukhov 1954) and a power-law distribution of $\hat{R}$ with a specified scale break radius. In contrast to the previous studies, we compute stochastic variance from various sources influencing convective activity, rather than from a single source, such that our stochastic UNICON may better represent the observed stochastic variability. Our approach can be understood as an implementation of a dispatcher function introduced by Ooyama (1971) in his theoretical cumulus ensemble model.

4.2 Conceptual framework

4.2.1 Multivariate Gaussian distribution for convective updraft plumes at the surface

The stochastic UNICON inherits the basic concept of the original UNICON, which launches multiple convective updraft plumes from the surface. In the original UNICON, the inter-variable correlations among various thermodynamic scalars of the convective updraft plumes at the surface (i.e., radius $\hat{R}$, where the caret denotes updraft plume properties; relative vertical velocity $\hat{w}$ with respect to the grid-mean vertical velocity; condensate potential temperature $\hat{\theta}_c \equiv \hat{\theta} - (L_v/C_p/\pi) \cdot \hat{q}_l - (L_s/C_p/\pi) \cdot \hat{q}_i$, where L_v and L_s are the latent heats of vaporization and sublimation, respectively, C_p is specific heat at constant pressure, π is an Exner function; total specific humidity $\hat{q}_t \equiv \hat{q}_v + \hat{q}_l + \hat{q}_i$; zonal

and meridional velocity, $\hat{u}$ and $\hat{v}$, respectively; mass and number concentration of aerosols and chemical species $\hat{\xi}$) were assumed to be exactly 1.

Our strategy for a stochastic UNICON is to construct a multivariate Gaussian area PDF $P_a(\alpha)$ for a set of six normalized thermodynamic variables of convective updraft plumes at the surface ($\alpha_{\hat{w}}$, $\alpha_{\hat{\theta}_c}$, $\alpha_{\hat{q}_t}$, $\alpha_{\hat{u}}$, $\alpha_{\hat{v}}$, and $\alpha_{\hat{R}}$, assuming that $\alpha_{\hat{\xi}} = \alpha_{\hat{q}_t}$) using the inter-variable correlations $r_{ij} < 1$ derived from the Monin-Obukhov similarity theory (where $i, j = 1, ..., 6$ denotes $\hat{w}, \hat{\theta}_c, \hat{q}_t, \hat{u}, \hat{v}$, and $\hat{R}$, respectively). The normalized thermodynamic variables are defined as $\alpha_{\hat{w}} = (\hat{w}(\alpha_{\hat{w}}) - \Delta w_\Omega)/\sigma_w$, $\alpha_{\hat{\phi}} = (\hat{\phi}(\alpha_{\hat{\phi}}) - \Delta\phi_\Omega - \bar{\phi}_s)/\sigma_\phi$, and $\alpha_{\hat{R}} = (\hat{R}(\alpha_{\hat{R}}) - R_o)/\sigma_R$. Here, $\phi = \theta_c, q_t, u, v$; σ_w, σ_ϕ, and σ_R are the standard deviations of $\hat{w}$, $\hat{\phi}$, and $\hat{R}$, respectively; $\bar{\phi}_s$ is the grid-mean value at the surface; R_o is the intercept plume radius at $\alpha_{\hat{R}} = 0$; Δw_Ω and $\Delta\phi_\Omega$ are the perturbations associated with the subgrid mesoscale organized flow within the planetary boundary layer (PBL).

The Monin-Obukhov (M-O) similarity theory hypothesizes that any dimensionless characteristic of the turbulence in the surface layer can be described by the parameter, $\zeta = z/L$, where z is the geometric height and L is the Monin-Obukhov length scale (Monin and Obukhov 1954). Several mass-flux parameterization schemes have used the M-O similarity theory to initialize the properties of convective updraft plumes (Cheinet 2003; Siebesma et al. 2007). The M-O similarity theory has been extended to estimate the standard deviations of various thermodynamic scalars within the surface layer (Wyngaard et al. 1971; Panofsky et al. 1977; Liu et al. 1998; Andreas et al. 1998; Wilson 2008). Although there are ongoing debates on which formulation is universally applicable (e.g., see Wilson (2008)), we use the following similarity functions

suggested by Liu et al. (1998), which were shown to produce similar results to the recent surface-layer-resolving LES studies (Maronga and Reuder 2017):

$$\sigma_w/u_* = \phi_{\sigma_w}\Big(\frac{z}{L}\Big) = 1.25\Big(1.0 - 3\frac{z}{L}\Big)^{1/3}, \tag{4.1}$$

$$\sigma_\theta/\theta^* = \phi_{\sigma_\theta}\Big(\frac{z}{L}\Big) = -2.0\Big(1.0 - 8\frac{z}{L}\Big)^{-1/3}, \tag{4.2}$$

$$\sigma_q/q^* = \phi_{\sigma_q}\Big(\frac{z}{L}\Big) = -2.4\Big(1.0 - 8\frac{z}{L}\Big)^{-1/3}, \tag{4.3}$$

where z is the geometric height; $u_* = [(\overline{w'u'})_s^2 + (\overline{w'v'})_s^2]^{1/4}$ is the frictional velocity; $\theta^* = -(\overline{w'\theta'})_s/u_*$; $q^* = -(\overline{w'q'})_s/u_*$; and $(\overline{w'\theta'})_s$, $(\overline{w'q'})_s$, $(\overline{w'u'})_s$, and $(\overline{w'v'})_s$ are the kinemetic surface fluxes of sensible heat, water vapor, zonal and meridional momentum, respectively, by non-organized symmetric turbulent eddies; and $L = -u_*^3\bar{\theta}_v/[gk(\overline{w'\theta'_v})_s]$ is the Monin-Obukhov length scale with a von Karman constant k, a reference virtual potential temperature $\bar{\theta}_v$ and the buoyancy flux at the surface $(\overline{w'\theta'_v})_s$. The correlation $r_{w\theta}$ between w and θ and the correlation r_{wq} between w and q within the surface layer can then be calculated as

$$r_{w\theta} = (\overline{w'\theta'})_s/(\sigma_w\sigma_\theta) = -1/(\phi_{\sigma_w}\phi_{\sigma_\theta}), \tag{4.4}$$

$$r_{wq} = (\overline{w'q'})_s/(\sigma_w\sigma_q) = -1/(\phi_{\sigma_w}\phi_{\sigma_q}), \tag{4.5}$$

where $|r_{w\theta}|$ and $|r_{wq}|$ are in the range of 0.40-0.56 and 0.33-0.46, respectively, depending on the stability $(-z/L)$. Based on the analysis of observation data, Liu et al. (1998) derived the correlation $r_{\theta q}$ as

$$|r_{\theta q}| = |r_{wq}|/|r_{w\theta}| = |\phi_{\sigma_\theta}/\phi_{\sigma_q}| = 0.83. \tag{4.6}$$

In contrast to w, θ, and q, there is no generally accepted similarity function for the standard deviation of horizontal velocity, $\sigma_{uv} \equiv (\overline{u'^2} + \overline{v'^2})^{1/2}$ that can

be expressed as a function of $-z/L$ within the surface layer (Wilson 2008). We use the following empirical formulation suggested by Wilson (2008):

$$\sigma_{uv}^2/u_*^2 = \left[4 + 0.73\left(\frac{\delta}{-L}\right)\right]\cdot\left[1 - \left(\frac{z}{\delta}\right)^{0.25}\right], \tag{4.7}$$

where δ is the PBL height. Assuming that the perturbation of horizontal velocity is aligned along the streamwise wind direction, σ_{uv} can be partitioned into σ_u and σ_v using the wind vector in the lowest model layer, $\boldsymbol{v}$, as $\sigma_u = \sigma_{uv}u/|\boldsymbol{v}|$ and $\sigma_v = \sigma_{uv}v/|\boldsymbol{v}|$. Several surface flux parameterizations have used this assumption (e.g. Siebesma et al. (2003)), which strictly speaking is valid only when the non-streamwise component of turbulence momentum is small (see Wilson (2008)). Under this assumption, the correlation between w and horizontal wind becomes

$$r_{wu} = r_{wv} = u_*^2/(\sigma_{uv}\sigma_w). \tag{4.8}$$

The correlation between horizontal wind and other scalars cannot be determined because neither the surface similarity theory nor the PBL scheme we use provide covariance information among these variables. By simply extending the method of Liu et al. (1998) used for computing $r_{\theta q}$ in (4.6), we compute the inter-variable correlations between horizontal velocity and $\phi = \theta, q$ as

$$r_{u\phi} = min(|r_{wu}|/|r_{w\phi}|,\ |r_{w\phi}|/|r_{wu}|), \tag{4.9}$$

$$r_{v\phi} = min(|r_{wv}|/|r_{w\phi}|,\ |r_{w\phi}|/|r_{wv}|), \tag{4.10}$$

which admittedly have a large uncertainty. However, our sensitivity tests showed that the simulation results are not sensitive to $r_{u\phi}$ and $r_{v\phi}$. Because of this, we could complete the calculation of the inter-variable correlations between w, θ, q, u and v. Because UNICON is formulated in terms of θ_c and q_t which are

conserved during the phase change, we simply assume that the inter-variable correlations and standard deviations of θ and q within the surface layer are identical to those of θ_c and q_t, respectively.

Another important variable we use as a source of convective variability is the radius of the convective updraft plume, $\hat{R}$. As explained in the introduction, $\hat{R}$ affects both the updraft mass flux at the surface and the fractional entrainment rate, two of the most important factors that control convective activity, such that stochastic initialization of $\hat{R}$ at the surface naturally imposes stochastic properties on the nature and nurture of convective updraft plumes. Unfortunately, it turns out that estimating $\hat{R}$ at the near surface from observations or LES is very difficult, because it is hard to define convective updraft plumes in the initial stage of development at the near surface, and small embryo updraft plumes merge with each other during the ascent from the surface to the PBL top and above (see Section 4.4.1). Given that, we simply set r_{Rw}, $r_{R\theta}$, r_{Rq}, r_{Ru}, and r_{Rv} as tunable parameters.

The resulting symmetric cross-correlation matrix for six variables at the top of the surface layer ($\hat{w}, \hat{\theta}_c, \hat{q}_t, \hat{u}, \hat{v}$, and $\hat{R}$), that sets convective variability in our stochastic UNICON is

$$
\begin{array}{c}
\\
\hat{w} \\
\hat{\theta}_c \\
\hat{q}_t \\
\hat{u} \\
\hat{v} \\
\hat{R}
\end{array}
\begin{array}{c}
\begin{array}{cccccc}
\hat{w} & \hat{\theta}_c & \hat{q}_t & \hat{u} & \hat{v} & \hat{R}
\end{array} \\
\begin{pmatrix}
1 & & & & & \\
-1/(\phi_{\sigma_w}\phi_{\sigma_\theta}) & 1 & & & & \\
-1/(\phi_{\sigma_w}\phi_{\sigma_q}) & 0.83 & 1 & & & \\
u_*^2/(\sigma_{uv}\sigma_w) & r_{u\theta} & r_{uq} & 1 & & \\
u_*^2/(\sigma_{uv}\sigma_w) & r_{v\theta} & r_{vq} & 1 & 1 & \\
r_{Rw} & r_{R\theta} & r_{Rq} & r_{Ru} & r_{Rv} & 1
\end{pmatrix}
\end{array}, \tag{4.11}
$$

where ϕ_{σ_w}, ϕ_{σ_θ}, and ϕ_{σ_q} are from (4.1)-(4.3); σ_w and σ_{uv} are from (4.1) and (4.7), respectively; $r_{u\theta}$, r_{uq}, $r_{v\theta}$, and r_{vq} are from (4.9) and (4.10), respectively; and r_{Rw}, $r_{R\theta}$, r_{Rq}, r_{Ru}, and r_{Rv} are specified as tuning parameters. Since the mid-point of the lowest model layer z_o is assumed to be top of the surface layer, all of σ, ϕ, and r_{ij} are computed at $z = z_o$. The cross-correlations of any aerosol species $\hat{\xi}$ are assumed to be identical to those of $\hat{q}_t$. The above matrix can be understood as a dispatcher function suggested by Ooyama (1971).

To initialize (or dispatch) a specific convective updraft plume, we obtained a set of standardized variables for a convective updraft plume ($\alpha_{\hat{w}}$, $\alpha_{\hat{\theta}_c}$, $\alpha_{\hat{q}_t}$, $\alpha_{\hat{u}}$, $\alpha_{\hat{v}}$, and $\alpha_{\hat{R}}$) by stochastically sampling one point from the assumed multivariate Guassian area PDF in the regime of $\alpha_{\hat{w}} > 0$ (it should be noted that $\alpha_{\hat{\theta}_c}$, $\alpha_{\hat{q}_t}$, $\alpha_{\hat{u}}$, $\alpha_{\hat{v}}$, and $\alpha_{\hat{R}}$ can be either positive or negative). The final thermodynamic properties of convective updraft plumes at the surface are calculated as

$$\hat{w}(\alpha_{\hat{w}}) = \sigma_w \cdot \alpha_{\hat{w}} + \Delta w_\Omega, \tag{4.12}$$

$$\hat{\phi}(\alpha_{\hat{\phi}}) = \sigma_\phi \cdot \alpha_{\hat{\phi}} + \bar{\phi}_s + \Delta\phi_\Omega, \quad \phi = q_t, \theta_c, u, v, \xi, \tag{4.13}$$

and to calculate $\hat{R}(\alpha_{\hat{R}})$ at the surface, $\alpha_{\hat{R}}$ is transformed to a power-law distribution, as explained in the next section.

4.2.2 Transformation from the Gaussian to power-law distribution for the updraft plume radius

Consistent with Neggers et al. (2003), our LES analysis for the BOMEX case showed that the updraft plume radius at the cloud base follows a power-law distribution with a power of -2.0 and a certain scale break radius (see Fig 4.7). The power-law and scale break characteristics of the cloud size distribution have been reported for various cloud types (Wood and Field 2011; O'Brien

et al. 2013; Heus and Seifert 2013), implying that when normalized by an appropriate scale break radius, the cloud size distributions for various cloud types can be described by a single distribution. As will be discussed later, our SCM simulation shows that there is a well-defined linear relationship between $\hat{R}$ at the cloud base and $\hat{R}$ at the surface. Based on this, we parameterize the number density PDF of $\hat{R}$ at the surface, P_n, as

$$P_n(\hat{x})/\hat{N} = a_1 \hat{x}^{-b-\hat{x}^c}, \quad \int_0^\infty (P_n(\hat{x})/\hat{N}) d\hat{x} = 1, \tag{4.14}$$

where $\hat{x} = \hat{R}/R_b$ is a dimensionless updraft plume radius normalized by the scale break radius R_b which sets an approximate upper limit for the possible plume size in a given environment; $\hat{N}$ is total updraft number density in units of [# m^{-2}]; $b, c > 0$ are the distribution factors; and a_1 is a normalization constant. In contrast to previous studies, we included an additional power term $-\hat{x}^c$ to better depict the distribution of large plumes above R_b. If $\hat{R} < R_b$, $\hat{x}^c$ becomes small and the plume radius approximately follows the previously suggested power-law distribution with a constant power of $-b$. We estimated b, c, and R_b at the surface by analyzing the LES-simulated $\hat{R}$ at the cloud base for the BOMEX case and then extrapolating to the surface in an ad-hoc manner using the SCM simulations with UNICON. After b and c are estimated, a_1 is obtained using the normalization condition of $\int_0^\infty (P_n(\hat{x})/\hat{N}) d\hat{x} = 1$. The area distribution of the updraft plume radius, $P_a(\hat{x})$, is

$$P_a(\hat{x})/\hat{a} = a_2 \hat{x}^{2-b-\hat{x}^c}, \quad \int_0^\infty (P_a(\hat{x})/\hat{a}) d\hat{x} = 1, \tag{4.15}$$

where $\hat{a} = \hat{N}\pi\hat{R}_e^2$ is the net updraft area fraction, $a_2 = a_1 R_b^2/R_e^2$ is a normalization constant, and $\hat{R}_e$ is the number-weighted, effective mean radius of

convective updraft plumes defined as

$$\hat{R}_e = R_b \cdot \left(\frac{\int_0^\infty \hat{x}^{2-b-\hat{x}^c} d\hat{x}}{\int_0^\infty \hat{x}^{-b-\hat{x}^c} d\hat{x}} \right)^{1/2}, \tag{4.16}$$

which becomes $\hat{R}_e = 0.47 \cdot R_b$ when $b = 2$ and $c = 1.7$.

To calculate $\hat{x} = \hat{R}/R_b$ from $\alpha_{\hat{R}}$ that is stochastically sampled from its multivariate Gaussian area distribution, $P_a(\alpha_{\hat{R}})$, we use the following inverse transformation:

$$\hat{x} = \hat{R}/R_b = F^{-1}(H(\alpha_{\hat{R}})), \quad \hat{x} > 0, \tag{4.17}$$

where F^{-1} is an inverse of the cumulative density function (CDF) of $P_a(\hat{x})$ for $\hat{x} > 0$ and H is the CDF of $P_a(\alpha_{\hat{R}})$ for $-\infty < \alpha_{\hat{R}} < \infty$. Strictly speaking, if $r_{wR} \neq 0$, $P_a(\alpha_{\hat{R}})$ does not follow a full Gaussian because only updrafts ($\alpha_{\hat{w}} > 0$) are sampled at the surface. However, regardless of the values of r_{wR}, $P_a(\alpha_{\hat{R}})$ can be fully transformed into $P_a(\hat{x})$. The method used to calculate the CDF of $\alpha_{\hat{R}}$ for any r_{wR} is explained in Appendix B. In our stochastic UNICON, the distribution of $\alpha_{\hat{R}}$ has no physical meaning, since $\hat{R}$ is assumed to follow a power-law distribution, not a Gaussian distribution: $\alpha_{\hat{R}}$ is merely used to carry the inter-variable correlations between the updraft plume radius and the other thermodynamic variables into the power-law distribution for $\hat{R}$. Because (4.17) is a nonlinear transformation, the cross-correlations between $\alpha_{\hat{R}}$ and $\alpha_{\hat{\phi}}$ (or $\alpha_{\hat{w}}$) in (4.11) differ from those between the transformed $\hat{R}$ and $\hat{\phi}$ (or $\hat{w}$) but the difference is small.

4.2.3 Closure for plume number density and updraft fractional area

To complete the formulation of the radius distribution at the surface, $\hat{N}$ should be determined. Based on the assumption that individual convective events are

independent of each other, Craig and Cohen (2006) hypothesized that in an equilibrium state, the number of convective updraft plumes varies across the grids and also within the grid box over time, and its PDF can be described with the following Poisson distribution:

$$p(G\hat{N}) = e^{-G\hat{N}_e} \cdot \left[\frac{(G\hat{N}_e)^{G\hat{N}}}{G\hat{N}} \right], \quad \int_0^\infty p(G\hat{N}) d(G\hat{N}) = 1, \tag{4.18}$$

where $\hat{N}_e$ is the ensemble-mean number density of convective updraft plumes at the surface, calculated as

$$\hat{N}_e = \hat{A}_s(\Omega)/\pi\hat{R}_e^2, \tag{4.19}$$

where $\hat{A}_s$ is the ensemble-mean net updraft fractional area at the surface and $\hat{R}_e$ is the effective plume radius defined in (4.16). $\hat{A}_s(\Omega)$ is calculated as a function of the mesoscale convective organization (Ω, Eqs.(72) and (75) in Park (2014a)) with an externally specified value for the non-organized state, $\hat{A}_s|_{\Omega=0}$ (our SCM uses a fixed $\hat{A}_s|_{\Omega=0} = 0.033$ for the BOMEX case which is in a non-organized state. See Table 4.3); $\hat{R}_e$ is computed from (4.16) using b, c, and R_b; $\hat{N}_e$ is obtained from (4.19); $\hat{N}$ is stochastically sampled from (4.18) at each time step; then the net updraft area fraction $\hat{a} = \hat{N}\pi\hat{R}_e^2$ is calculated. The net area fraction $\hat{a}$ can be determined only after integrating the area fraction of sampled updraft plumes, so $\hat{a}$ in (4.15) is unknown before sampling. Thus, the plume radius is set to the expected value, $\hat{R}_e$, to determine $\hat{a}$. This completes the computation of (4.14) and (4.15). Because stochastic sampling is performed at each time step in a fully independent way, temporal coherency of stochastic fluctuations is not taken into account in our stochastic UNICON.

4.2.4 Sampling of convective updraft plumes: full and hybrid stochastic methods

In this section, we compare several methods for sampling convective updraft plumes from the assumed multivariate distribution and discuss how the individual sampling method influences the computation of the ensemble-mean and variance of the grid-mean convective tendency. For this, we simply assume that the individual launching events of convective updraft plumes are independent of each other (i.e., Poisson process), and that the entire spatiotemporal variations of grid-mean convective tendency can be explained by stochastically-sampled convective updraft plumes within the grid box. We defined three plume types based on the way how to compute the normalized thermodynamic variable α from an area PDF $P_a(\alpha)$. A stochastic plume has α stochastically sampled from $P_a(\alpha)$, a single bulk plume has $\bar{\alpha} = \int_{-\infty}^{\infty} \alpha P_a(\alpha) d\alpha$, and a bin plume has α averaged over a certain interval (see Eq.(B4)). With these three plumes, we define the following sampling methods: • a full stochastic plume method (FULL), • a single stochastic plume method, • a bulk plume method (BULK), and • a hybrid method consisting of n bin plumes and a single stochastic plume (HYBn).

Consider a grid box with the horizontal grid size, G in which $G\hat{N}$ updraft plumes exist in an equilibrium state and $\hat{N}$ is the number of plumes per unit area in units of [#/m^2]. If η_s is the convective tendency generated by a single stochastic plume (see Appendix A), the ensemble-mean and variance of the grid-mean convective tendency generated by different $G\hat{N}$ stochastic plumes are $G\hat{N}\mu(\eta_s)$ and $G\hat{N}\sigma^2(\eta_s)$, respectively, where $\mu(\eta_s)$ and $\sigma^2(\eta_s)$ denote the ensemble-mean and variance of grid-mean convective tendency generated by a

single stochastic plume. Although this full stochastic plume method is the most ideal approach, it is computationally expensive because we need to compute the convective tendencies of all of the different $G\hat{N}$ plumes. Our goal is to find an efficient way to reproduce the ensemble-mean and variance of the grid-mean convective tendency as generated by the full stochastic method.

The ensemble-mean and variance of grid-mean convective tendency generated by a single stochastic plume (i.e., identical $G\hat{N}$ stochastic plumes exist in the grid column) are $\mu(G\hat{N}\eta_s)=G\hat{N}\mu(\eta_s)$ and $\sigma^2(G\hat{N}\eta_s)=(G\hat{N})^2\sigma^2(\eta_s)$, respectively, which overestimates the true variance (hereafter, "true" refers to the results from the full stochastic method). On the other hand, the variance generated by a single bin plume is 0, underestimating the true variance.

Let's consider a hybrid method consisting of n bin plumes and a single stochastic plume. If the ensemble-mean of the grid-mean convective tendency generated by the n bin plumes, η_b is the same as that of a single stochastic plume, η_s [i.e., $\mu(\eta_b) = \mu(\eta_s)$] and the grid-mean convective tendency from this hybrid method is computed as the following weighted average,

$$\eta_H = (G\hat{N} - \sqrt{G\hat{N}}) \cdot \eta_b + \sqrt{G\hat{N}} \cdot \eta_s, \tag{4.20}$$

then the ensemble-mean and variance of the grid-mean convective tendency from this hybrid method are $\mu(\eta_H) = G\hat{N}\mu(\eta_s)$ and $\sigma^2(\eta_H) = G\hat{N}\sigma^2(\eta_s)$, respectively, which are identical to those from the full stochastic method. If n bin plumes are carefully constructed to reproduce the true ensemble-mean convective tendency, the hybrid method consisting of n bin plumes and a single stochastic plume can reproduce both the true ensemble-mean and the variance of grid-mean convective tendency generated by the full stochastic method. The means of constructing the bin plumes in stochastic UNICON are explained in

Appendix B. We will test two hybrid methods: one with 3-bin plumes of different $\hat{R}$ and the other updraft thermodynamic scalars set to be identical (HYB3), and the other with 12-bin plumes generated by the combination of three bins of $\hat{R}$, two bins of $\hat{\theta}_c$, and two bins of $\hat{q}_t$ at the surface (HYB12). Table 4.1 summarizes the different possible configurations of stochastic UNICON used in our study. Table 4.2 shows the pseudo-code of stochastic UNICON.

4.3 Simulation setting

4.3.1 Large eddy simulation (LES)

Using the University of California Los Angeles (UCLA) LES model (Stevens et al. 1999, 2005), we simulated the Barbados Oceanographic and Meteorological Experiment (BOMEX) (Holland and Rasmusson 1973) shallow convection case over the ocean following the settings of Siebesma et al. (2003). The UCLA LES solves a set of anelastic equations with a Smagorinsky subgrid scheme and has been used to study boundary layer turbulence, and both shallow and deep convection (Hohenegger and Stevens 2013). In our simulation, radiation and the production of precipitation are turned-off. The domain size is 6.4 km $\times$ 6.4 km $\times$ 3.0 km and the grid size is 25 m $\times$ 25 m $\times$ 25 m. The model was run for 6 hours and various outputs from time intervals of one minute during the last hour (a total of 60 instantaneous snapshots) are analyzed. Cloud statistics at the cloud base are obtained at $z_{base} = 612.5$ m.

We use the cloud detection algorithm of Dawe and Austin (2012), which detects clouds by considering the spatiotemporal connectivity of cloudy grid cells. The core is defined as the grid boxes with positive condensate, vertical velocity, and buoyancy, while cloud is defined as the grid boxes with condensate.

Table 4.1 Several possible configurations of stochastic UNICON. The relative variance is the theoretical spatiotemporal variability of grid-mean convective tendency in an equilibrium state with respect to that of the FULL method. Here, $G\hat{N}$ is obtained from (4.18).

Method	Number of Bin Plume	Number of Stochastic Plume	Relative Variance	Abbreviation
Single Bulk Plume	1	0	0	BULK
Spectral Bin Plume	n	0	0	BINn
Single Stochastic Plume	0	1	$G\hat{N}$	STO1
Full Stochastic Plume	0	$G\hat{N}$	1	FULL
Hybrid Stochastic Plume	n	1	1	HYBn

Table 4.2 A pseudocode for stochastic UNICON. For a given thermodynamic scalar ϕ, $\bar{\phi}(z)$ is the grid-mean value; $(\overline{w'\phi'})_s$ is the surface flux; $\Delta\phi_\Omega$ is the mesoscale perturbation induced by subgrid cold pools (Eq.(73),(74) in Park (2014a)); $\hat{\phi}$ is the plume properties at the surface; $\alpha_{\hat{\phi}}$ is the normalized plume properties; and σ_ϕ is the standard deviation of ϕ at the surface. $G = \Delta x \Delta y$ is the area of the grid box; Ω is the mesoscale convective organization (Eq.(72) in Park (2014a)); $\hat{A}_s$ is the expected net updraft area fraction at the surface; R_b is the scale break radius; and $\eta(z)$ is the final grid mean convective tendency.

Procedure STOCHASTIC UNICON

Input : $\bar{\phi}(z), (\overline{w'\phi'})_s, G, \Omega, \Delta\phi_\Omega$

1. Construction of a multivariate Gaussian area PDF for updraft plumes at the surface

$P_a(\alpha_{\hat{\phi}}) \leftarrow r_{ij} \leftarrow (\overline{w'\phi'})_s$ Construct a multivariate Gaussian area PDF for $\alpha_{\hat{\phi}}$ where $\hat{\phi} = [\hat{w}, \hat{\theta}_c, \hat{q}_t, \hat{u}, \hat{v}, \hat{R}]$ [(4.11)].

$\hat{A}_s, R_b \leftarrow G, \Omega$ Compute $\hat{A}_s$ (Eq.(75) in Park (2014a)) and R_b as a function of Ω and G.

$P_a(\hat{R}), \hat{R}_e \leftarrow R_b$ Compute an area PDF for $\hat{R}$ at the surface [(4.15),(4.16)].

$\hat{N}_e = \hat{A}_s / \pi \hat{R}_e^2$ Calculate the expected number density of updraft plumes at the surface [(4.19)].

$\hat{N} \leftarrow G, \hat{N}_e$ Stochastically sample the plume number density at the surface from the Poisson distribution [(4.18)].

2. Computation of the grid mean convective tendency $\eta(z)$

case "FULL":	**case** "HYBn":
$n_s = G\hat{N}$; $n_b = 0$	$n_s = 1$; $n_b = n$

for $i = 1$ **to** n_s **(Loop for the stochastic plumes)** :

$\alpha_{\hat{\phi}} \leftarrow P_a(\alpha_{\hat{\phi}})$ Stochastically sample $\alpha_{\hat{\phi}}$ from $P_a(\alpha_{\hat{\phi}})$

$\hat{\phi} \leftarrow \alpha_{\hat{\phi}}, \sigma_\phi, \Delta\phi_\Omega; R_b$ Compute updraft thermodynamic scalars at the surface [(4.12),(4.13),(4.17)].

$\eta_s^i(z) \leftarrow \hat{\phi}, \bar{\phi}(z)$ Compute convective tendency induced by a single stochastic plume

for $i = 1$ **to** n_b **(Loop for the bin plumes)** :

$\alpha_{\hat{\phi}} \leftarrow P_a(\alpha_{\hat{\phi}})$ Compute $\alpha_{\hat{\phi}}$ for the i^{th} bin plume from $P_a(\alpha_{\hat{\phi}})$

$\hat{\phi} \leftarrow \alpha_{\hat{\phi}}, \sigma_\phi, \Delta\phi_\Omega; R_b$ Compute updraft thermodynamic scalars at the surface [(4.12),(4.13),(4.17)].

$\eta_b^i(z) \leftarrow \hat{\phi}, \bar{\phi}(z)$ Compute convective tendency induced by the bin plumes

case "FULL":	**case** "HYBn":
$\eta(z) = \sum_{i=1}^{G\hat{N}} \eta_s^i(z)$	$\eta_b(z) = \sum_{i=1}^{n_b} \eta_b^i(z) / G\hat{N}$
	$\eta(z) = (G\hat{N} - \sqrt{G\hat{N}}) \cdot \eta_b(z) + \sqrt{G\hat{N}} \cdot \eta_s^1(z)$

3. Update the mesoscale organization variables, Ω and $\Delta\phi_\Omega$

Output : $\eta(z), \Omega, \Delta\phi_\Omega$

The algorithm also detects dry updraft plumes as the grid boxes containing the Couvreux tracer (Couvreux et al. 2010) with a concentration higher than the horizontal mean value above a certain threshold (i.e., one spatial standard deviation at each height). The Couvreux tracer is a radioactively decaying passive tracer emitted from the surface with a decaying time scale $\tau_0 = 5min.$ Because the detection of dry plumes is made layer by layer without considering vertical coherency, this method is deficient in detecting the Lagrangian evolution of individual dry updraft plumes. To address this problem, we imposed additional Lagrangian tracers using the online Lagrangian Particle Tracking Module (LPTM; Heus et al. (2008a)). A total number of 308500 particles are imposed at the midpoint of the lowest model layer, $z = 12.5$ m at $t = 5$ hour and the locations of the individual Lagrangian particles are recorded every minute. For each core, we identified its embryo dry convective plume by tracing the Lagrangian particles from the core down to the surface. These Lagrangian particles will be referred to as conditionally-sampled particles. In this way, we can track the evolution of individual dry convective updraft plumes from the surface to its lifting condensation level (LCL) and above.

4.3.2 Single-column model (SCM)

The single-column model (SCM) used in our study is identical to the one used by Park (2014b) and Park and Bretherton (2009). It uses a leap-frog time stepping method with a model integration time step $\Delta t = 300$ $[sec]$ and a downstream Eulerian space differencing (semi-Lagrangian) method for computing the vertical advection of temperature and horizontal wind (water substances and the other tracers) from the specified grid-mean subsidence rate at the vertical resolution of 80 vertical layers. As for LES, the SCM is

forced by constant $LHF = 153$ [W m^{-2}] and $SHF = 9.5$ [W m^{-2}] at $SST = 300.4$ [K] and $P_s = 1015$ [hPa] for six hours with a specified grid-mean cold and dry horizontal advection, subsidence and geostrophic wind. Following LES, radiation and the production of precipitation are turned-off, such that our SCM does not generate subgrid mesoscale organized flow within the PBL in association with subgrid cold pools (i.e. $\Delta w_\Omega = \Delta \phi_\Omega = 0$ in (4.12),(4.13)). The results from the last hour of the simulation are analyzed.

4.4 Results

4.4.1 Evaluation of the conceptual framework of stochastic UNICON using LES

A multivariate Gaussian distribution of stochastic updraft plumes at the surface

Stochastic UNICON assumes a multivariate Gaussian distribution for various thermodynamic scalars of convective updraft plumes at the surface ($\hat{w}$, $\hat{\theta}_c$, $\hat{q}_t$, $\hat{u}$, $\hat{v}$, $\hat{\xi}$, and $\hat{R}$) with inter-variable correlations estimated from the surface layer similarity theory and intuition. In this section, we evaluate these assumptions using the BOMEX LES simulation. Figure 4.1 shows a joint area PDF among $\{\alpha_w, \alpha_{\theta_c}, \alpha_{q_t}, \alpha_u, \alpha_v\}$ at the top of the lowest model layer obtained from the LES simulation. We assumed that subgrid turbulence is isotropic, and standard deviations of the subgrid velocities were diagnosed by $\sigma_{w,sub} = \sigma_{u,sub} = \sigma_{v,sub} = \sqrt{(2/3) \cdot TKE_{sub}}$, where $TKE_{sub} = 0.09$ [m^2 s^{-2}] is the mean subgrid TKE at the surface obtained from the Smagorinsky subgrid scheme. Because the grid size of the LES is not small enough to resolve entire turbulences in the surface layer, we included the variance from subgrid turbulences in our analysis.

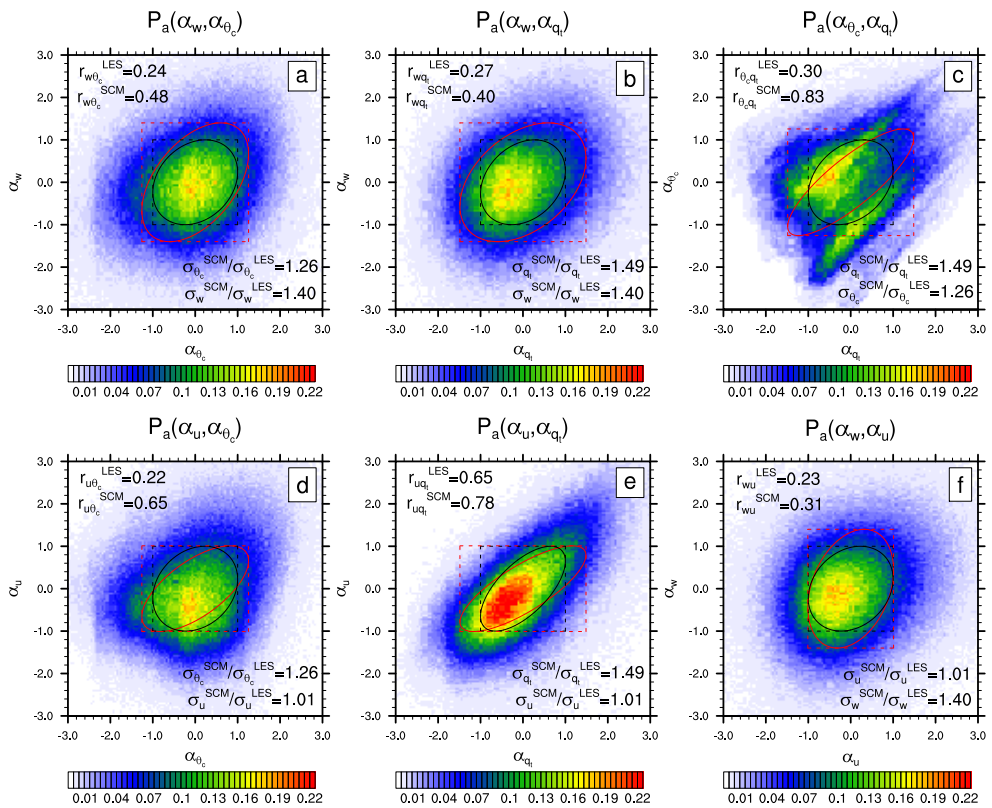

Figure 4.1 The joint area PDF between (a) α_w and α_{θ_c}, (b) α_w and α_{q_t}, (c) α_{θ_c} and α_{q_t}, (d) α_u and α_{θ_c}, (e) α_u and α_{q_t}, and (f) α_w and α_u at the top of the lowest model layer ($z = 25\,\mathrm{m}$) obtained from the BOMEX LES simulation. The black and red ellipses show one σ range of the joint area PDF derived from the LES and similarity theory, respectively. Here, σ is the standard deviation and r is the correlation coefficient between two variables.

Using $\sigma_{w,sub}$ ($\sigma_{u,sub}$, $\sigma_{v,sub}$), we constructed a normalized Gaussian velocity distribution from which subgrid w (u, v) is sampled in a random way and added to the grid mean w (u and v), resulting in the total w (u, v) shown in Fig 4.1. A rough visual comparison of the joint PDF from the LES and stochastic UNICON indicates that overall, a correlated multivariate Gaussian distribution is an acceptable assumption, although the joint PDF between α_{θ_c} and α_{q_t} simulated by the LES has two separated maxima that cannot be reproduced by the multivariate Gaussian distribution. Compared with LES, stochastic UNICON tends to overestimate both the standard deviation and inter-variable correlation. These discrepancies reflect in part the uncertainty in the assumed similarity functions of (4.1)-(4.3), which were derived from the analysis of various LES simulations over land.

Only a portion of the near surface air shown in Fig 4.1 can develop into convective updraft plumes. Stochastic UNICON assumes that these embryo updraft plumes at the surface (i.e., a portion of symmetric turbulent eddies within the surface layer parameterized by UNICON) are uniformly distributed over a range of $0 \leq \alpha_{\hat{w}} < \infty$ and their area PDF follows a half Gaussian distribution with a specified net updraft fractional area at the surface, $0 \leq \hat{A}_s(\Omega) \leq 0.5$ (e.g., $\hat{A}_s|_{\Omega=0} = 0.033$ for the BOMEX case). This assumption is different from those used in other studies in that only surface air with strong positive w (i.e., the air on the right tail of the Gaussian distribution) can develop into convective updraft plumes (e.g., D'Andrea et al. (2014)). To evaluate which assumption is more reasonable, we determined that only the Lagrangian tracers at $z = 25$ m will eventually grow into the core updraft plumes (i.e., conditionally-sampled particles), and the number PDF of these was plotted in Fig 4.2. Because the Lagrangian tracers were uniformly seeded near the surface,

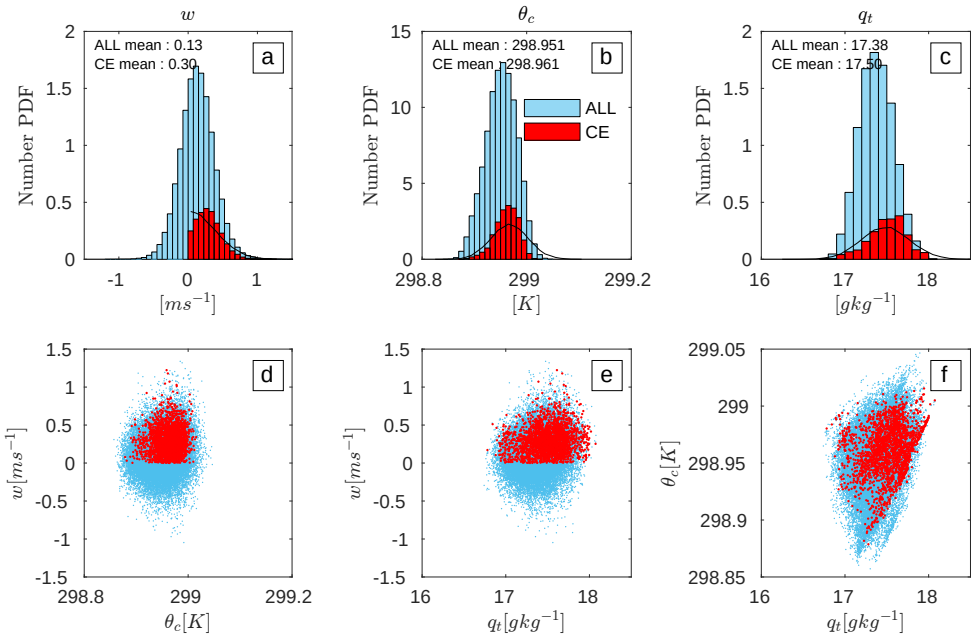

Figure 4.2 The LES-simulated [(a),(b),(c)] number PDF of (a) w, (b) θ_c, (c) q_t and [(d),(e),(f)] joint scatter plots between (d) w and θ_c, (e) w and q_t, and (f) θ_c and q_t of the all Lagrangian particles at $z = 25\,\mathrm{m}$ (blue) and the core-embryo (CE) Lagrangian particles that eventually grow into the core updraft plumes (red). The area PDFs of convective updraft plumes at the surface parameterized by stochastic UNICON are also shown as black curves. The scales of the red bar and black curves are arbitrary. The Lagrangian particles are released at $t = 5hr$ and these plots are from the data at $t = 5 \sim 6hr$.

the number PDF of the Lagrangian tracers shown in Fig 4.2 can be understood as an area PDF of the embryo updraft plumes. The fraction of the number of conditionally-sampled Lagrangian particles to that of total Lagrangian particles is approximately 0.025, which is smaller than $\hat{A}_s|_{\Omega=0} = 0.033$. Considering that stochastic UNICON is designed to simulate forced convection as well as free convection, this discrepancy is not unreasonable. For comparison, the PDFs of the entire Lagrangian tracers and convective updraft plumes parameterized by stochastic UNICON are also plotted. Consistent with Fig 4.1, the number PDFs of the entire Lagrangian tracers roughly follow a Gaussian distribution. However, the vertical velocity of the conditionally-sampled embryo updraft plumes at the surface seems to follow the half-Gaussian distribution more closely than the truncated-Gaussian distribution, supporting the assumption used in UNICON. In contrast to $\hat{w}$, the distributions of $\hat{\theta}_c$ and $\hat{q}_t$ follow a Gaussian distribution with a weak negative skewness, which are also similar to the PDFs assumed in the stochastic UNICON. It should be noted that even though $\hat{w}$ follows a half-Gaussian distribution, $\hat{\theta}_c$ and $\hat{q}_t$ can follow a Gaussian distribution, because the assumed inter-variable correlations between $\hat{w}$ and $\hat{\theta}_c$ (also $\hat{q}_t$) are smaller than 1 in stochastic UNICON (see (4.11) and Fig 4.1). The joint PDFs of $\hat{w}$, $\hat{\theta}_c$, and $\hat{q}_t$ indicate that the covariance characteristics between the various thermodynamic scalars of the embryo updraft plumes are similar to those of the entire symmetric turbulent eddies within the surface layer. Consistent with the upward sensible and latent heat fluxes at the surface, the mean values of $\hat{\theta}_c$ and $\hat{q}_t$ of the embryo updraft plumes are slightly larger than those of the layer-mean values with a weak positive slope in their joint PDFs with $\hat{w}$.

Vertical evolution of stochastic updraft plumes from the surface to the cumulus base

Figure 4.3 shows several snapshots of vertically-projected Lagrangian tracers after being released from the surface. As mentioned, the Lagrangian tracers are segregated (or conditionally-sampled) by individual cores (i.e., the core index in Fig 4.3) identified with the cloud detection algorithm, which will be referred to as core-embryo (CE for simplicity) tracers. At $t = 0$ when all Lagrangian tracers are at the surface, the CE tracers are spread widely in the form of scattered air parcels or separated sub-plumes (Fig 4.3a). As a result, it is somewhat ambiguous to define the radius and area fraction of convective updraft plumes at the surface. As the positively buoyant air parcels ascend from the surface, the spread of CE tracers is greatly reduced (Figs 4.3b, c), indicating the merging of nearby air parcels that is not parameterized in the current stochastic UNICON. At $t = 13$ min, the projected air parcels are in the form of well-organized, nearly circular plumes and the spread of the air parcels at each height is further reduced (Figs 4.3d, e). Although the merging of air parcels during the ascent contributes to the vertical profile of the size distribution of convective updraft plumes, a visual inspection of Fig 4.3 also indicates that a large portion of the size distribution comes from the surface. This supports the stochastic UNICON that is constructed with the assumed size distribution of convective updraft plumes at the surface.

Figure 4.4 shows the vertical profiles of dry and saturated updraft plumes detected by various methods. The shapes of the vertical profiles of the CE tracers are roughly similar to those of the Couvreux tracers but the CE tracers have a stronger $\hat{w}$, cooler $\hat{\theta}_c$, and moister $\hat{q}_t$ than the Couvreux tracers. Above

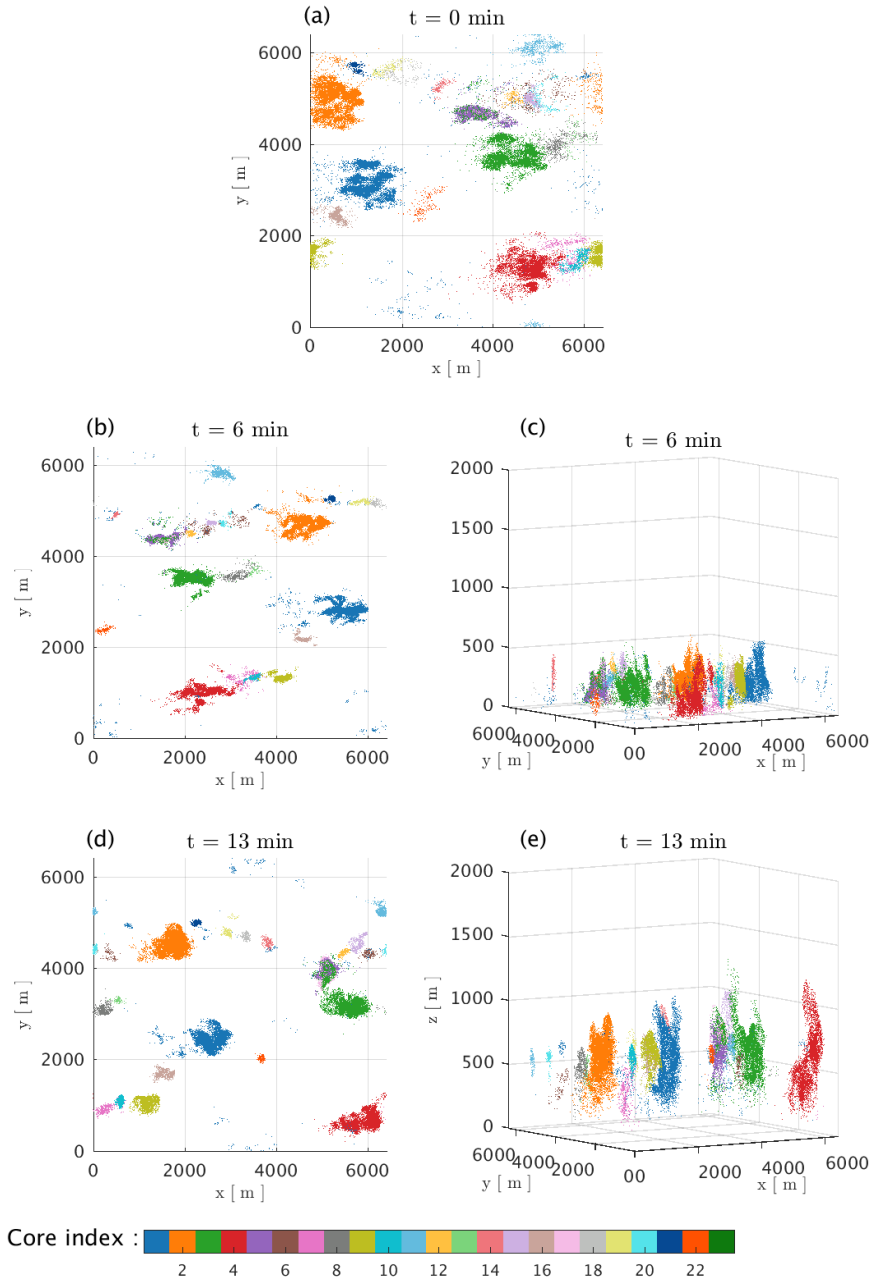

Figure 4.3 Snapshots of the conditionally-sampled Lagrangian tracers that eventually grow into the cores (i.e., core-embryo Lagrangian tracers) at several different time steps after being released from the surface. The colors denote the core indices identified by the cloud detection algorithm.

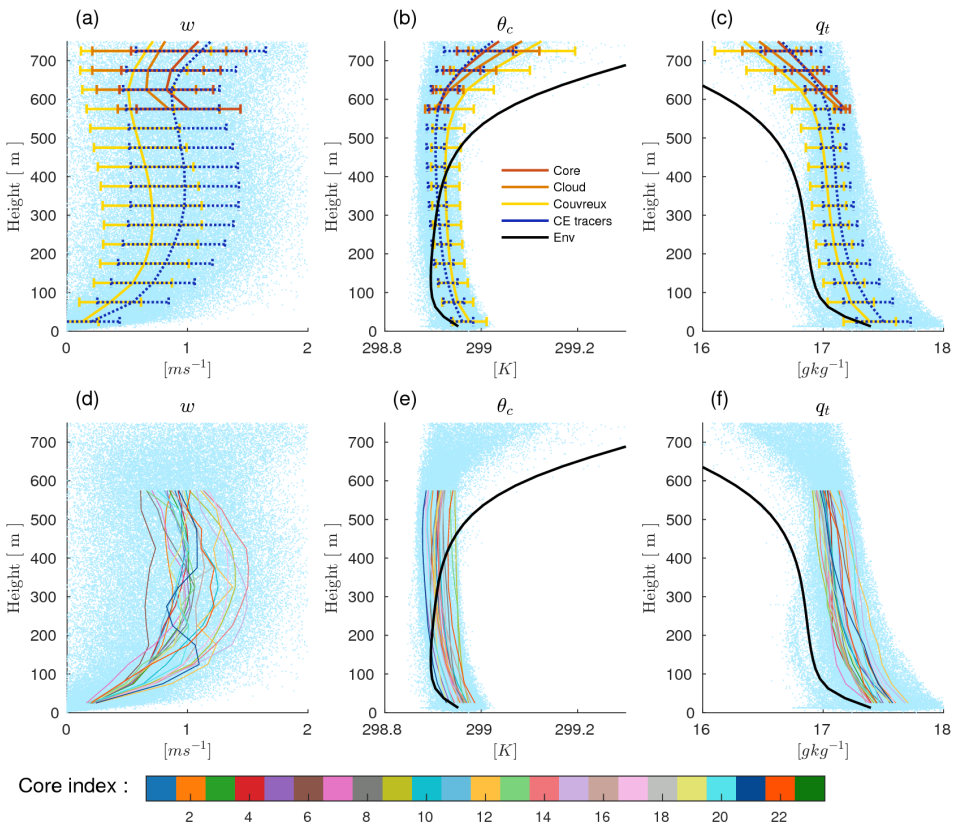

Figure 4.4 The mean vertical profiles and their spreads (one standard deviation) of w, θ_c, q_t for the [(a),(b),(c)] 'Core', 'Cloud', 'Couvreux tracers', 'Core-Embryo (CE) tracers' and 'Enviromnent (Env)' and [(d),(e),(f)] CE tracers segregated by the individual core indices. The light blue dots in the background denote individual CE tracers.

the LCL, the mean values of $\hat{\theta}_c$ and $\hat{q}_t$ of the CE tracers are between those of the cloud and the core, while those of the Couvreux tracers are between those of the cloud and the environment, indicating that our CE tracer works better than the Couvreux tracer in detecting dry updraft plumes that are growing into saturated updraft plumes. Consistent with the similarity theory (Sorbjan 1986), the maximum $\hat{w}$ tends to exist in the middle of the PBL at around $z = 300 \sim 400$ m, across which the updraft buoyancy changes from positive to negative, since the environment in the upper PBL is influenced by the warm free air entrained from above the PBL (Fig 4.4b). Also shown are the mean thermodynamic profiles of the CE tracers that are segregated by individual cores below the cloud base. At the near surface, the inter-CE spread of $\hat{w}$ is small but becomes large as the plumes rise. On the other hand, the spreads of $\hat{\theta}_c$ and $\hat{q}_t$ do not change much with height (in fact, the spread slightly decreases with height for $\hat{q}_t$) and the high (low) values of $\hat{\theta}_c$ and $\hat{q}_t$ at the lower PBL tend to be maintained all the way up to the cloud base. This implies that in contrast to $\hat{w}$, a substantial portion of the variability in $\hat{\theta}_c$ and $\hat{q}_t$ of convective updraft plumes at the cloud base stems from the variability at the surface.

Updraft plumes statistics in the cloud layer

We showed that a large proportion of the variability in convective updraft plumes at the cloud base originates from the variability at the surface layer. In this section, we examine the variability of saturated updraft plumes in the cloud layer. The plume statistics in the cloud layer for the BOMEX case has been documented in many studies (e.g., Siebesma et al. (2003), Romps and Kuang (2010), Dawe and Austin (2012, 2013)).

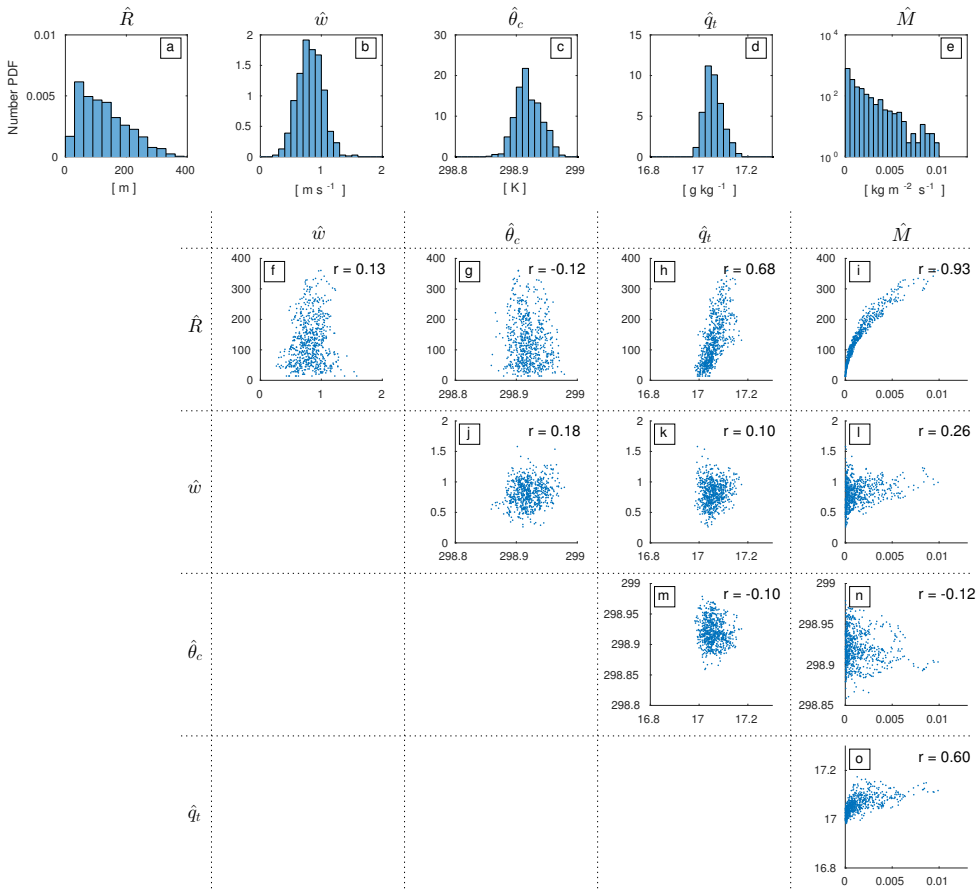

Figure 4.5 [(a)-(e)] Number PDF and [(f)-(o)] joint scatter plots of various updraft core properties at the cloud base obtained from the analysis of 60 snapshots of the BOMEX LES during $t = 5 \sim 6hr$. In (f)-(o), r is the correlation coefficient between two variables and an individual dot denotes the mean value of the grid boxes with the same core index in each snapshot.

Figure 4.5 shows the number PDFs and joint scatter plots for various updraft core properties at the cloud base, $z_{base} = 612.5\,\mathrm{m}$. Except for the left end of the PDF, the number PDF of the updraft plume radius decreases with $\hat{R}$, with a maximum of $\hat{R} \approx 400\,\mathrm{m}$.

Approximately all $\hat{w}$, $\hat{\theta}_c$, and $\hat{q}_t$ follow a Gaussian distribution with a weak skewness. It is interesting to note that the PDF of $\hat{w}$ changes from the near half-Gaussian at the surface to the full Gaussian at the cloud base due to the vertical acceleration of convective updraft plumes during ascent, while the PDFs of $\hat{\theta}_c$ and $\hat{q}_t$ do not significantly change from the surface to the cloud base. Consistent with the hypothesis suggested by Craig and Cohen (2006), the sub-domain distribution of updraft mass flux $\hat{M}$ at the cloud base follows an exponential distribution. The magnitudes of the inter-variable correlations, r, are slightly different from those of Dawe and Austin (2012), although the signs are similar. A couple of notable aspects are a very strong positive correlation between $\hat{R}$ and $\hat{M}$ ($r = 0.93$); a strong positive correlation between $\hat{R}$ and $\hat{q}_t$ ($r = 0.68$), which reflects a weaker entrainment dilution of larger plumes during ascent; and a strong positive correlation between $\hat{q}_t$ and $\hat{M}$, which is due in part to the strong $r(\hat{R},\hat{M})$ and $r(\hat{R},\hat{q}_t)$. On the other hand, $\hat{\theta}_c$ is very weakly or even negatively correlated with $\hat{R}$ and $\hat{q}_t$, probably due to the buoyancy reversal across the mid-PBL at around $z = 400\,\mathrm{m}$ (see Fig 4.4e), above which entrainment mixing increases $\hat{\theta}_c$ but decreases $\hat{q}_c$ in proportion to the inverse $\hat{R}$. At the surface, $r(\hat{\theta}_c,\hat{q}_t) = 0.3$, which decreases down to $r(\hat{\theta}_c,\hat{q}_t) = -0.1$ at the cloud base and gradually approaches $r = -1$ as the updraft rises in the cloud layer (not shown).

Figure 4.6 shows the composited vertical profiles of updraft core properties classified by the plume radius at the cloud base, $\hat{R}_{base}$. Our analysis is slightly

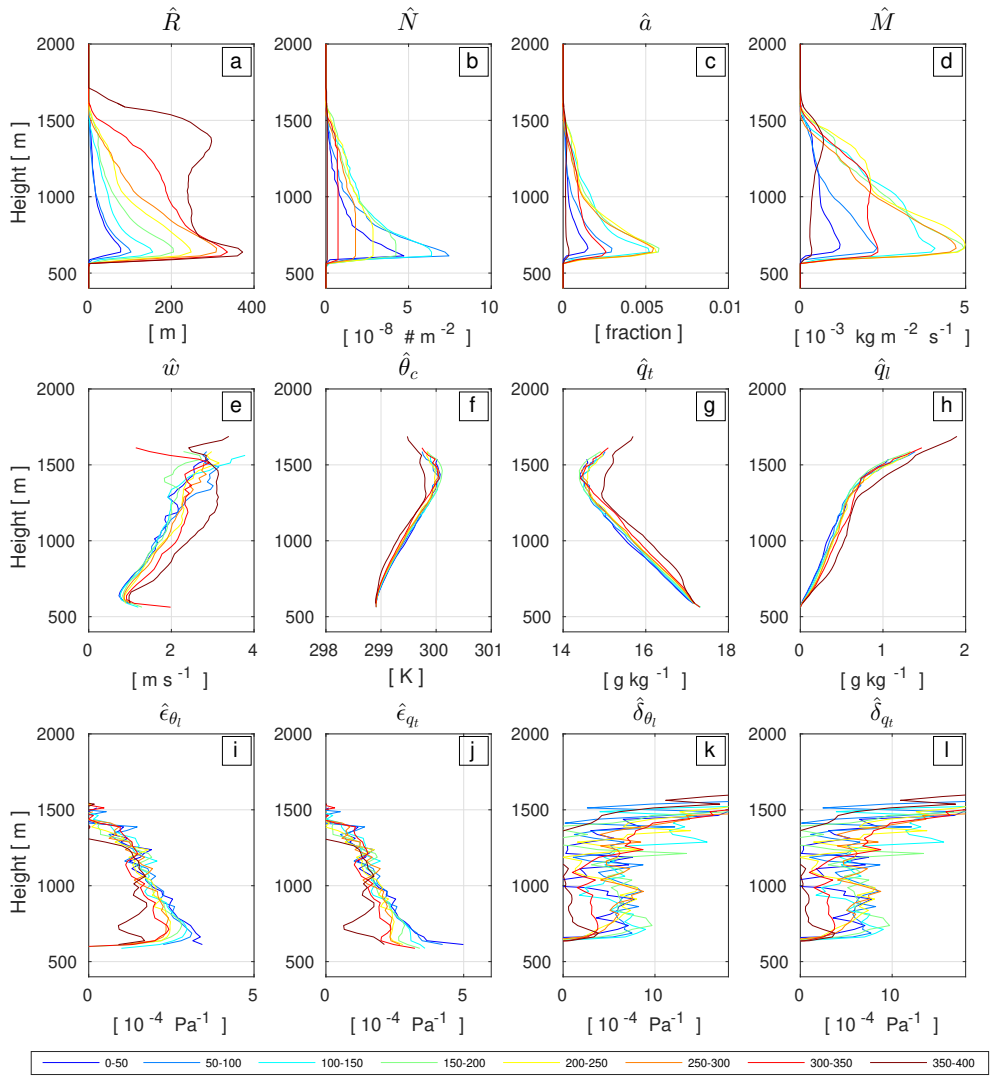

Figure 4.6 Composite vertical profiles of the updraft core properties as a function of the updraft plume radius $\hat{R}$ at z_{base} (shown at the bottom in unit of [m]) obtained from the analysis of 60 snapshots of the BOMEX LES simulations during $t = 5 \sim 6hr$. In the bottom row, $\hat{\epsilon}$ and $\hat{\delta}$ are the fractional entrainment and detrainment rates, respectively, estimated by assuming a steady-state plume for the conservative scalars, θ_c and q_t.

different from Neggers (2015), which used the radius of vertically-projected plumes instead of the radius at each level as a compositing basis. As shown, the thermodynamic properties of the core plumes in the cloud layer are well classified by $\hat{R}_{base}$. Similar composite analysis using $\hat{w}_{base}$, $\hat{\theta}_{c,base}$, or $\hat{q}_{t,base}$ instead of $\hat{R}_{base}$ showed weaker distinction among the composited thermodynamic profiles than those shown in Fig 4.6 (not shown). This indicates that consistent with previous studies (Dawe and Austin 2012; Romps and Kuang 2010), the variability of convective plumes in the cloud layer is controlled more effectively by $\hat{R}_{base}$ than by other thermodynamic variables, supporting the validity of spectral-binning convection schemes based on plume radius such as Neggers (2015) and stochastic UNICON. Larger $\hat{R}_{base}$ tends to be associated with larger (smaller) $\hat{w}$, $\hat{q}_t$, and $\hat{q}_l$ ($\hat{N}$ and $\hat{\theta}_c$) but $\hat{a}$ and $\hat{M}$ seem to show non-monotonic dependency on $\hat{R}_{base}$. The plume radius decreases with height but the biggest plumes ($\hat{R}_{base} > 300\,\mathrm{m}$) maintain their sizes at up to $z = 1300$ m where a strong inversion exists. In the lower cloud layer, small plumes have a larger number density ($\hat{N}$) than large plumes but their $\hat{N}$ decreases rapidly with height, implying a more efficient entrainment dilution and buoyancy loss of smaller plumes. The fractional entrainment ($\hat{\epsilon}$) and detrainment rates ($\hat{\delta}$) estimated by assuming a steady-state plume (Betts 1975) are much noisier than other thermodynamic variables with a tendency of larger plumes to be associated with a smaller $\hat{\epsilon}$ and $\hat{\delta}$. Dawe and Austin (2013) noted that $\hat{\epsilon}$ and $\hat{\delta}$ estimated from the direct measurement method instead of the bulk plume method have a functional dependency on $\hat{\epsilon}(\hat{B}, d\bar{\theta}_v/dz)$ and $\hat{\delta}(\hat{w}, \hat{\chi}_c)$, where $\hat{B}$ is the updraft buoyancy and $\hat{\chi}_c$ is the critical mixing fraction. Given that $\hat{B}$ and $\hat{w}$ are strongly dependent on $\hat{R}$, our results do not contradict these findings.

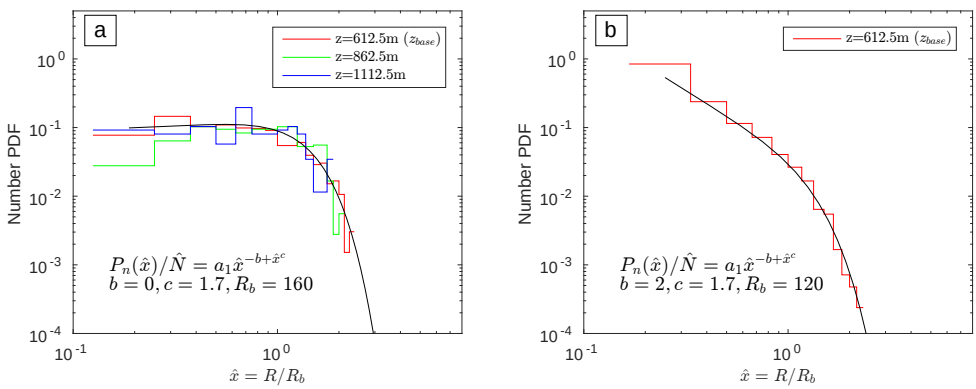

Figure 4.7 Number PDF of normalized updraft plume radius ($\hat{x} = \hat{R}/R_b$) and the best fitting line with (4.14) at various heights obtained from the analysis of 60 snapshots of the BOMEX LES during $t = 5 \sim 6hr$. In (a), the updraft plume is defined as the core grids (i.e., $w > 0$, $q_l > 0$, and $B > 0$) identified by the cloud detection algorithm by considering spatiotemporal connectivity. In (b), the updraft plume is defined as the horizontally consecutive grids with $w > 0.1\,\mathrm{m\,s^{-1}}$.

Figure 4.7 shows the number PDFs of the normalized plume radius, $\hat{x} = \hat{R}/R_b$, at three different heights and with the best fitting lines for (4.14). The fitting parameters of $b = 0$, $c = 1.7$, and $R_b = 160\,\mathrm{m}$ well capture the size distribution of core plumes at all heights (Fig 4.7a) but $b = 0$ is smaller than the value suggested by previous studies (e.g., Neggers et al. (2019)). This is due in part to the cloud detection algorithm we use, which is known to underestimate (overestimate) the number of small (large) plumes, since it does not detect clouds that exist for only one time step and treats small plumes detached from their larger parent plumes as parts of the parent plumes for a certain amount of time (Dawe and Austin 2012). Stochastic UNICON is designed to simulate dry and forced convection as well as free and moist convection. To be more consistent with the plumes parameterized by stochastic UNICON, we re-defined the plumes as horizontally consecutive grid cells with $w > 0.1\,\mathrm{m\,s^{-1}}$ and plotted their number PDF at the cloud base in Fig 4.7b. The resulting number PDF follows a well-defined power-law distribution with $b = 2$ and a smaller scale break radius of $R_b = 120\,\mathrm{m}$. Previous studies derived the power-law distribution using the vertically-projected (i.e., a two-dimensional projection of cloud fields taken from high altitudes) cloud size (Neggers et al. 2003), which, as shown in Fig 4.7b, seems to also be applicable for the size distribution at a specific height. We also examined a deep convection case in a radiative-convective equilibrium over the ocean and found that the same power-law distribution with $b = 2$ and $c = 1.7$ reasonably represents the size distribution of deep convective clouds with a larger R_b. To simulate both shallow and deep convection in a seamless way, R_b needs to be parameterized as a function of appropriate variables (e.g., self-aggregation or mesoscale convective organization in our UNICON, Eq.(72) in Park (2014a)). Although it is not clear whether the scale break radius is the

result of real physical processes or an artificial quantity depending on the size of the sampling domain (e.g., Yuan (2011)), it seems to be a useful parameter for any subgrid convection scheme that is designed to simulate subgrid plumes. The detailed parameterization of R_b that is applicable to both shallow and deep convection will be reported in a separate paper.

4.4.2 Single-column model (SCM) simulation of the BOMEX case

Vertical profiles of grid-mean and updraft thermodynamic properties

Figure 4.8 shows the vertical profiles of various thermodynamic scalars obtained from the LES and various configurations of SCM simulations of the BOMEX case described in Section 4.2.4 (i.e., a full stochastic plume method, a single bulk plume method, and a hybrid method with three bin-plumes and one stochastic plume). The model parameters used in our simulations are identical to the ones used in Park et al. (2017, 2019) but we adjusted two tuning parameters, a_2 (a moist mixing coefficient, Eq.(31) of Park (2014a)) from 1 to 4 and $\hat{A}_s|_{\Omega=0}$ (updraft fractional area at the surface for a non-organized state, Eq.(19) of Park (2014a)) from 0.04 to 0.033. The model parameters used for SCM simulations are summarized in Table 4.3. Theoretically, if combined with a perfect plume model, a full stochastic plume method with $G\hat{N}$ different stochastic plumes can reproduce both the observed ensemble-mean and variance of grid-mean convective tendency in an equilibrium state, such that it can serve as a reference configuration to evaluate the performance of the bulk plume method employed in most convection schemes and the hybrid method developed in our study.

All three SCM configurations adequately reproduce the LES-simulated vertical profiles of grid-mean $\tilde{\theta}_c$ and $\tilde{q}_t$. The full stochastic method shows the

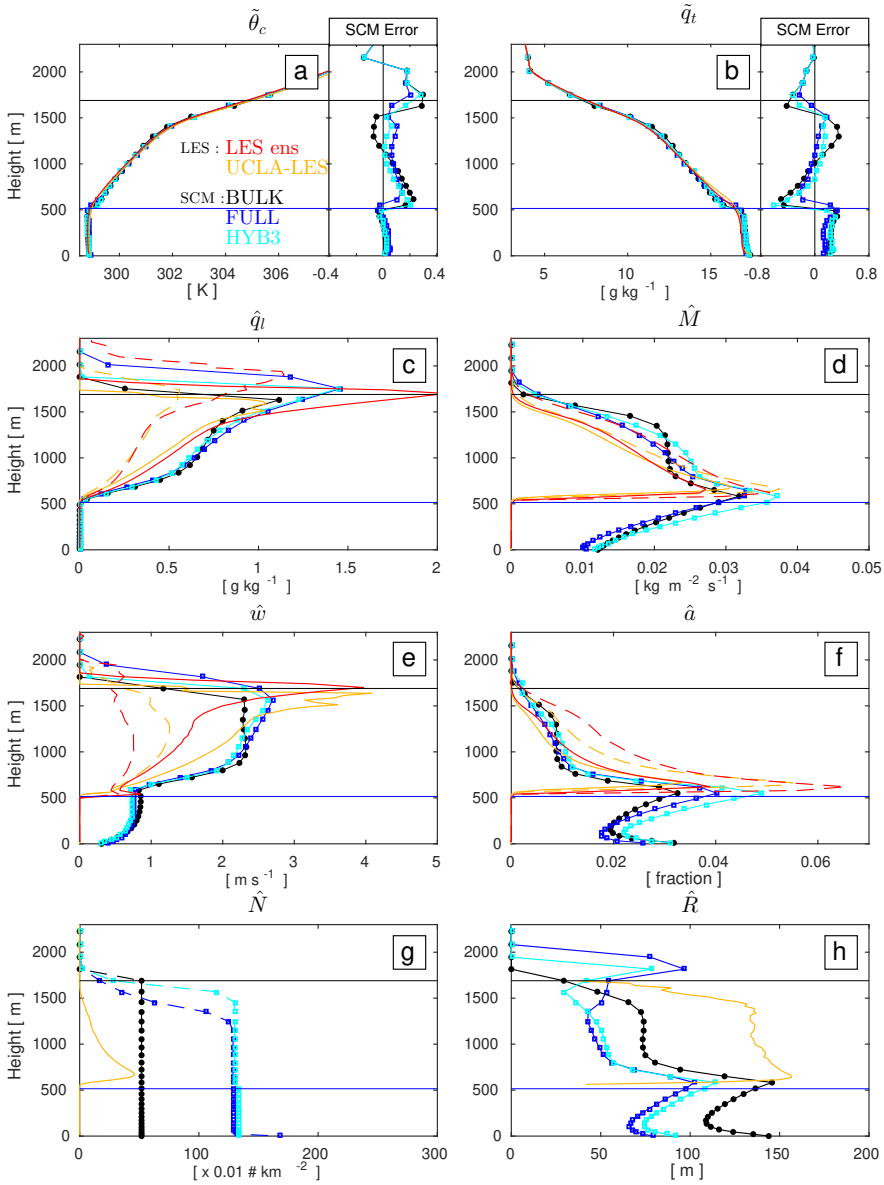

Figure 4.8 Vertical profiles of [(a),(b)] grid-mean θ_c and q_t and [(c)-(h)] various updraft plume properties averaged over $t = 3 \sim 6hr$ simulated by stochastic UNICON in various configurations (BULK, FULL, and HYB3) compared with those from the multimodel LES ensemble and UCLA-LES for the BOMEX case. Both LES and SCM have a domain size of $G = 6.4 \times 6.4\,\mathrm{km}^2$. In (a)-(b), SCM errors with respect to the LES ensemble are also shown on the right side. In (c)-(h), the red and orange solid (dotted) lines denote the core updraft (cloudy updraft). In each panel, the blue horizontal line is the PBL height and the black line is the level of neutral buoyancy (LNB) of a single bulk plume.

Table 4.3 The model parameters used for the SCM simulations of the BOMEX case with stochastic UNICON. The specified power-law distribution for the radius of convective updraft plumes corresponds to the effective updraft radius, $\hat{R}_e = 79.9\,\mathrm{m}$ ((4.16)) and the ensemble-mean plume number density of $\hat{N}_e = \hat{A}_s|_{\Omega=0}/\pi\hat{R}_e^2 = 1.64 \times 10^{-6}\,\#\,\mathrm{m}^{-2}$ ((4.19)).

Parameter	Description	Original Value	New Value	Possible Range
a_2	Moist mixing coefficient	1.0	4.0	$0 \leq a_2$
$\hat{A}_s\|_{\Omega=0}$	Updraft fractional area at the surface when $\Omega = 0$ (no mesoscale organization)	0.040	0.033	$0 \leq \hat{A}_s\|_{\Omega=0} \leq A_s\|_{max}$
R_b	Scale break radius	-	170 m	$0 < R_b$
b	Power-law exponent of the updraft radius distribution	-	2.0	$0 \leq b$
r_{Rw}	Correlation between $\alpha_{\hat{R}}$ and $\alpha_{\hat{w}}$	-	0.0	$-1.0 \leq r_{Rw} \leq 1.0$
$r_{R\theta_c}$	Correlation between $\alpha_{\hat{R}}$ and $\alpha_{\hat{\theta}_c}$	-	0.0	$-1.0 \leq r_{R\theta_c} \leq 1.0$
r_{Rq_t}	Correlation between $\alpha_{\hat{R}}$ and $\alpha_{\hat{q}_t}$	-	0.0	$-1.0 \leq r_{Rq_t} \leq 1.0$

best performance, the bulk method suffers from warm and dry biases in the lower and uppermost cloud layer just below the level of neutral buoyancy (LNB, located at around $z \sim 1700$ m), and the hybrid method has warm and dry biases in the lower cloud layer. Ideally, the mean thermodynamic states simulated by the three SCM configurations should be identical. Imperfect selection of the bulk and n-bin plumes as well as insufficient sampling in a non-equilibrium state are responsible for the discrepancies in the simulated mean thermodynamic state by the three SCM methods. A successful simulation of the mean state by the full stochastic method implies that stochastic UNICON is appropriately tuned and the assumed multivariate Gaussian distribution of stochastic updraft plumes at the surface is working well.

The properties of convective updraft plumes simulated by UNICON are roughly similar to those of LES. In-cloud liquid water content (LWC, $\hat{q}_l$, Fig 4.8c) simulated by SCM is similar to that of the LES cores with a maximum in-cloud LWC of higher than 1 [g kg^{-1}] near the LNB. The updraft mass flux simulated by the SCM ($\hat{M}$, Fig 4.8d) is slightly larger than that of the LES cores which are known to represent only 80 ∼90 % of turbulent fluxes in the cloud layer (Siebesma et al. 2003). The updraft mass flux simulated by the full stochastic method is very similar to that of cloudy updrafts in the LES ensemble. Our SCM slightly overestimates the LES-simulated updraft vertical velocity ($\hat{w}$, Fig 4.8e) and underestimates the updraft fractional area ($\hat{a}$, Fig 4.8f) in the lower and mid cloud layer but the overall vertical patterns are similar. The number density of convective updraft plumes simulated by the full stochastic method ($\hat{N}$, Fig 4.8g) decreases rapidly in the upper cloud layer where a trade inversion layer exists, and also near the surface where stochastic sampling from the multivariate Gaussian distribution occasionally produces negatively

buoyant updraft plumes of a very small size, which are immediately detrained into the environment. The hybrid method shows a qualitatively similar feature as the full stochastic method but the layer with a constant $\hat{N}$ extends upward above because only one stochastic plume is used in the hybrid simulation. The radius of convective updraft plumes simulated by the SCM ($\hat{R}$, Fig 4.8h) has a peak just above the PBL top and another peak slightly above LNB, indicating that the largest plume survived up to this level. Compared to the SCM, the UCLA-LES simulates smaller $\hat{N}$ and larger $\hat{R}$, which is due in part to the LES cloud detection algorithm treating small plumes detached from their larger parent plumes as parts of the parent plumes for a certain amount of times, as previously mentioned. We note that compared to LES, our stochastic SCM simulates $\hat{N}$ to be too persistent with height. Consequently, the vertical variation of SCM-simulated $\hat{a}$ is mainly controlled by $\hat{R}$, although the vertical variation of LES-simulated $\hat{a}$ is largely controlled by $\hat{N}$. This feature might be addressed by implementing a stochastic entrainment parameterization for the convective updraft plume, which is a future research subject.

We also tested the hybrid method with 12 bin plumes generated by the combination of three bins of $\hat{R}$, two bins of $\hat{\theta}_c$, and two bins of $\hat{q}_t$ at the surface (HYB12), which produced more realistic grid-mean profiles of θ_c and q_t than HYB3, more similar to those of the full stochastic method (not shown). Overall, both the full stochastic and hybrid methods reproduce the LES results reasonably well.

PDFs of updraft properties at the cloud base

Figure 4.9 shows the number PDFs and joint scatter plots of the updraft plume properties at the cloud base obtained from the full stochastic SCM.

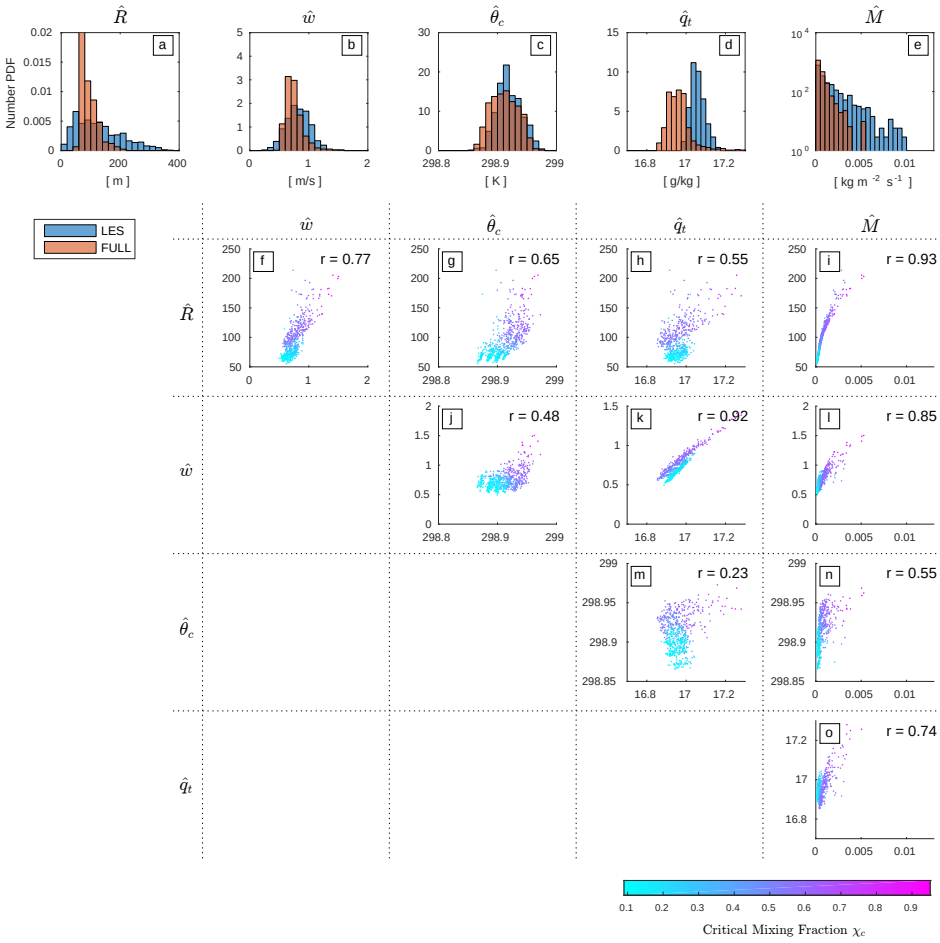

Figure 4.9 [(a)-(e)] Number PDF and [(f)-(o)] joint scatter plots of various updraft plume properties at the cloud base simulated by stochastic UNICON using a FULL method. Individual snapshots at every 10 minutes during $t = 5 \sim 6hr$ from 10 ensemble simulations are used for these plots (total 120 snapshots). In (a)-(e), the results from LES (i.e., Fig 5) are also shown for comparison. In (f)-(o), r is the correlation coefficient between two variables with different colors denoting different critical mixing fraction, $\hat{\chi}_c$.

Compared to LES, the full stochastic SCM simulates more small plumes and less large plumes (Fig 4.9a), which are speculated to be associated with the aforementioned problem in the LES cloud detection algorithm and entrainment merging of the updraft plumes in LES that is not parameterized in current stochastic UNICON. We found that there is a strong linear relationship between the SCM-simulated plume radii at the cloud base and surface, $\hat{R}_{base} = 0.57 \cdot \hat{R}_{sfc} + 50$ [m], implying that the distribution of $\hat{R}$ at the surface is well maintained up to the cloud base. Because it is hard to compute $\hat{R}_{sfc}$ from the LES simulation, it is uncertain whether the LES portrays a similar strong relationship between $\hat{R}_{sfc}$ and $\hat{R}_{base}$. Due to the entrainment merging of air parcels during ascent (see Fig 4.3), the strength of the LES-simulated linear relationship, if any, is likely to be weaker than that of SCM. The distribution patterns of individual $\hat{w}$, $\hat{\theta}_c$, and $\hat{q}_t$ from the full stochastic SCM are roughly similar to those of LES, although SCM simulates slightly drier mean q_t than SCM at the cloud base. Both the full stochastic SCM and LES have an approximate exponential distribution of subgrid $\hat{M}$ but SCM has a steeper slope than LES because SCM has more small plumes with a weak vertical velocity than LES (see Fig 4.9a and Figs 4.10a,b). Stochastic UNICON reproduces the theoretical exponential distribution of subgrid $\hat{M}$ hypothesized by Craig and Cohen (2006).

The joint scatter plots simulated by stochastic UNICON have common and contrasting aspects with those of LES as shown in Fig 4.5. Both the full stochastic SCM and LES simulate strong positive $r(\hat{M}, \hat{R})$, $r(\hat{R}, \hat{q}_t)$, and $r(\hat{M}, \hat{q}_t)$, which can be easily understood from the definition of $\hat{M} \equiv \hat{\rho} \cdot (\pi \hat{R}^2 / G) \cdot \hat{w}$ for a single plume and the property that a large (small) plume can maintain a high (small) $\hat{q}_t$ with weak (strong) entrainment dilution during ascent in the

sub-cloud layer (see Fig 4.5 and Fig 4.10). However, $\hat{w}$ in the SCM has stronger positive correlations with other variables than in LES. In addition, the positive correlations between $\hat{\theta}_c$ and other variables are stronger than those in LES, which produces a negative $r(\hat{\theta}_c, \hat{q}_t)$ and $r(\hat{\theta}_c, \hat{R})$. We speculate that the latter is in part associated with too strong positive $r_{\theta q} = 0.83$ at the surface assumed for the multivariate Gaussian distribution [(4.6)]: LES indicates a smaller $r_{\theta q}$ at the near surface (compare Fig 4.4e and 4.4f) and a sensitivity simulation with $r_{\theta q} = 0.1$ reduced $r(\hat{w}, \hat{\theta}_c)$ from 0.48 to 0.25 and $r(\hat{q}_t, \hat{\theta}_c)$ from 0.23 to 0.02, approaching that of LES (not shown). The former is speculated to be associated with various stochastic processes in LES, which are not fully parameterized in current stochastic UNICON. As shown in Fig 4.4, $\hat{w}$ shows more complex vertical variations than $\hat{\theta}_c$ and $\hat{q}_t$. The merging of small plumes during ascent and the associated fluctuations of entrainment drag, detrainment thrust, or other stochastic processes (e.g., fluctuations of environmental properties) may contribute to this complex variation of $\hat{w}$.

Stochastic UNICON parameterizes $\hat{\epsilon}$ as a function of $\hat{B}$, $\hat{w}$, $\hat{q}_l$, and environmental relative humidity using a buoyancy sorting, which adds more variation to $\hat{\epsilon}$ parameterized as an inverse function of $\hat{R}$. Some inter-variable correlations (e.g., $r(\hat{w}, \hat{\theta}_c)$, $r(\hat{w}, \hat{R})$, $r(\hat{q}_t, \hat{R})$, and $r(\hat{q}_t, \hat{\theta}_c)$) tend to be suppressed by variability in the critical mixing fraction χ_c (we note that the mixture with the mixing fraction χ between 0 (updraft air) and χ_c is entrained). Future parameterizations of additional stochastic processes (e.g., plume merging and the stochastic mixing of updraft plumes, and the stochastic fluctuation of environmental air) with a more realistic specification of $r_{\theta q}$ in the multivariate Gaussian distribution at the surface may improve the characteristics of the inter-variable correlations.

Updraft profiles composited by the plume radius at the cloud base

Figure 4.10 shows the composite vertical profiles of the updraft properties as a function of the plume radius at the cloud base, simulated by the full stochastic SCM. Stochastic UNICON simulates $\hat{R}$ smaller than the LES. However, similar to the LES, the plumes with larger $\hat{R}$ ascend to a higher level and have larger $\hat{w}$, $\hat{q}_t$, and $\hat{q}_l$ and smaller $\hat{N}$ and $\hat{\theta}_c$ in the cloud layer. The updraft fractional area $\hat{a} = \pi \hat{R}^2 \hat{N}$ and mass flux $\hat{M} = \rho \hat{a} \hat{w}$ do not show monotonic variations with $\hat{R}$ due to the decrease of $\hat{N}$ with $\hat{R}$, which are also similar to LES. In UNICON, the fractional mixing rate $\hat{\epsilon}_0$ (also the fractional entrainment rate, $\hat{\epsilon}$, and the fractional detrainment rate, $\hat{\delta}$) is parameterized as an inverse function of $\hat{R}$, such that larger plumes have small $\hat{\epsilon}_0$ ($\hat{\epsilon}$ and $\hat{\delta}$). Due to higher $\hat{B}$ and $\hat{w}$, large plumes in the cloud layer have higher $\hat{\chi}_c$ than small plumes, which increases (decreases) $\hat{\epsilon}$ ($\hat{\delta}$). This buoyancy sorting competes with the effect of $\hat{R}$ on $\hat{\epsilon}$, resulting in an unexpected stronger $\hat{\epsilon}$ for larger plumes in the lower cloud layer (Fig 4.10j). From the cloud base to $z = 750 \sim 800$ m, the accumulated entrainment in large plumes is roughly similar to that of small plumes. Further above, large plumes experience much weaker entrainment dilution, resulting in more rapid increases of $\hat{w}$ and $\hat{q}_l$ with height than small plumes. These features, however, are not evident in LES, implying a need to refine the buoyancy sorting in stochastic UNICON. In contrast to LES (Fig 4.6b), the number concentration of small plumes in the lower and mid cloud layer does not decrease with height, presumably due in part to the absence of the parameterization of merging plumes in the current stochastic UNICON. Due to stochastic sampling of the negatively buoyant updrafts at the surface, $\hat{\chi}_c$ is smaller than 1 and $\hat{\delta}$ is positive near the surface. Overall, stochastic UNICON adequately reproduces

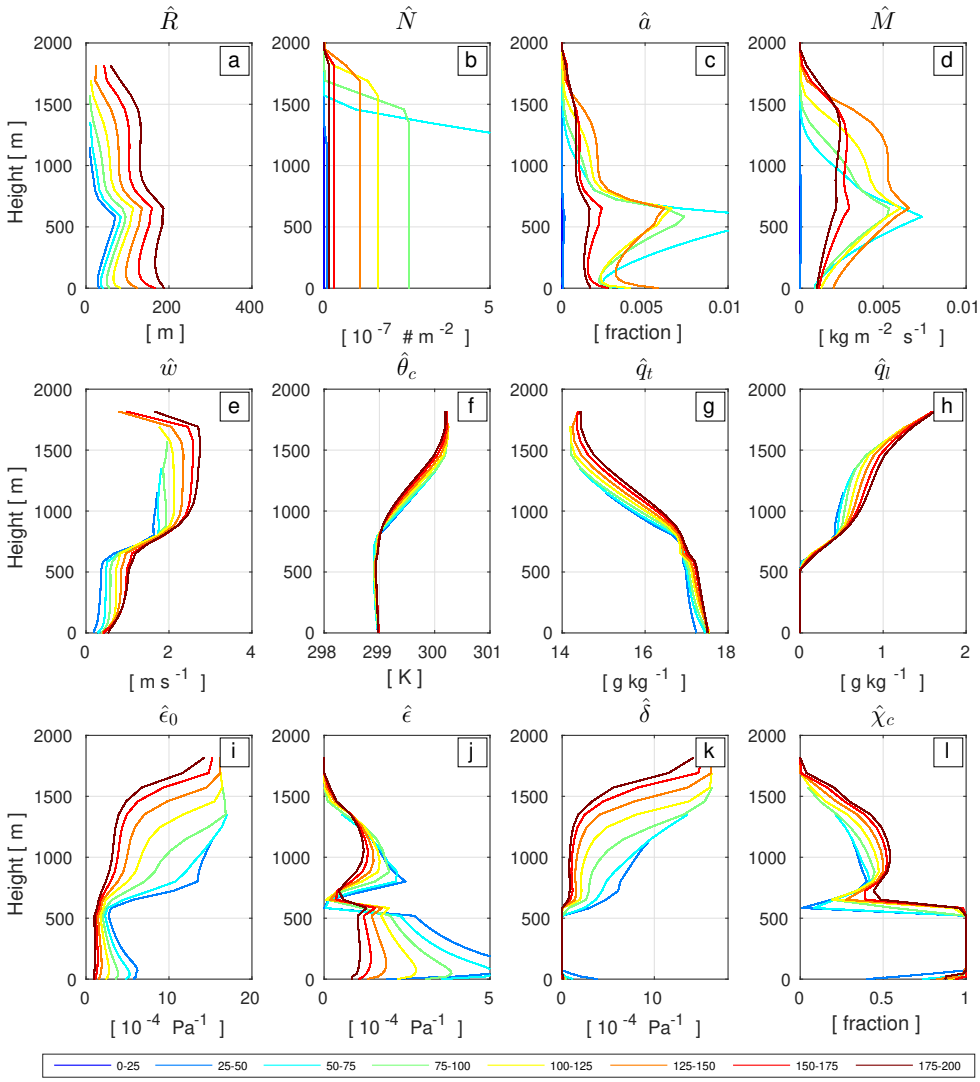

Figure 4.10 Composite vertical profiles of updraft plume properties as a function of the updraft plume radius at the cloud base, $\hat{R}_{base}$ (shown at the bottom in unit of [m]) during $t = 5 \sim 6hr$ obtained from the 10 ensemble simulations of the full stochastic UNICON.

the dependency of updraft properties on the plume radius simulated by LES, at least on a qualitative basis.

Variance statistics simulated by the full and hybrid stochastic UNICON

Figure 4.11 shows the time evolution of grid-mean $\hat{M}$ (which controls grid-mean convective tendency) simulated by the full and hybrid stochastic methods at various horizontal resolutions. As explained in Section 4.2, the hybrid method is designed to reproduce the mean and variance of grid-mean convective tendency simulated by the full stochastic method in a computationally efficient way. In an equilibrium state, temporal fluctuations of grid-mean $\hat{M}$ in stochastic UNICON can be generated by three processes: a stochastic sampling of the plume number ($G\hat{N}$) from the Poisson distribution, $p(G\hat{N})$ [(4.18)]; a stochastic sampling of $\hat{R}$ from the correlated multivariate Gaussian distribution of $\alpha_{\hat{R}}$. which is transformed into the power-law distribution of $\hat{R}$ [(4.15)]; and a stochastic sampling of $\hat{w}$ and $\hat{\phi}$ from the half- and full-Gaussian distributions of $\alpha_{\hat{w}}$ and $\alpha_{\hat{\phi}}$, respectively. The variability shown in Fig 4.11 is a combined result of these processes. As expected, the decrease with G of expected temporal variance (e.g., $\sigma(\hat{M})/\mu(\hat{M})$ on the top-right of the individual plot) is simulated by the full stochastic method and successfully reproduced by the hybrid method. The grid-mean $\hat{M}$ simulated by the hybrid method is slightly higher than that of the full stochastic method, reflecting the deficiency of using three bin plumes in simulating the true grid-mean tendency. When 12 bin plumes were used (HYB12), the simulated temporal variability became more similar to that of the full stochastic method (not shown). At $G = 1.6 \times 1.6\,\mathrm{km}^2$, the expected plume number is $G\hat{N}_e = G\hat{A}_s/(\pi\hat{R}_e^2) = 4.46$ and the plume number $G\hat{N}$ as

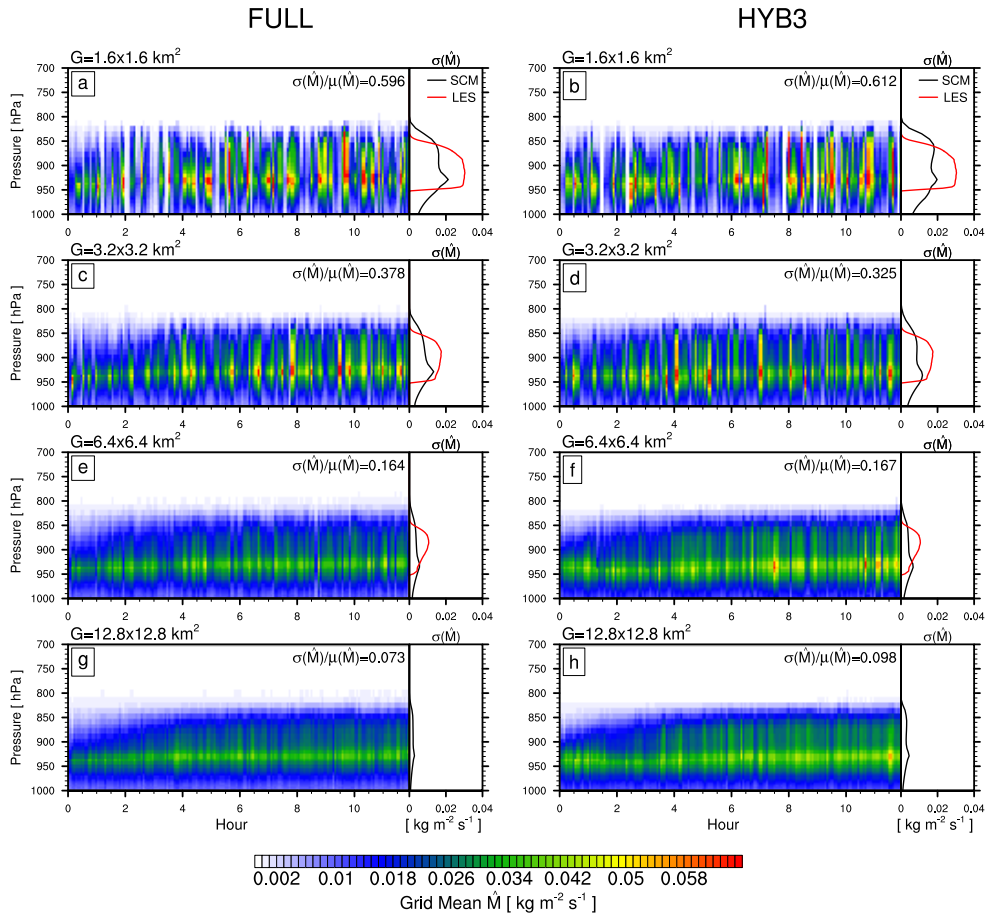

Figure 4.11 Time series of the grid mean updraft mass flux ($\hat{M}$) for the BOMEX case simulated by stochastic UNICON with the FULL (left) and HYB3 (right) methods at various G shown on the top left of individual plot. A normalized temporal standard deviation of grid mean $\hat{M}$ at z_{base} during $t = 3 \sim 6hr$ ($\sigma(\hat{M})/\mu(\hat{M})$) is denoted on the top right of the individual plot. The line plots on the right side are the vertical profiles of the temporal standard deviation of grid mean $\hat{M}$ during $t = 3 \sim 6hr$ [$\sigma(\hat{M})$] obtained from the SCM and LES.

sampled from the Poisson distribution and the associated $\hat{M}$ can be zero at some time steps. The PBL top height simulated by the SCM changes in a discontinuous way, which adds additional variance to Fig 4.11. In the cloud layer, both methods simulate smaller variance than the LES (see the line plots on the right side), which is presumably because SCM simulates too persistent $\hat{N}$ with height as mentioned before (Fig 4.8g).

Figure 4.12 shows the PDF of the grid-mean $\hat{M}$ at the cloud base simulated by the hybrid SCM and LES at various G along with the theoretically-predicted PDFs. This figure shows the distribution of grid-mean $\hat{M}$, while Fig 4.9e shows the distribution of $\hat{M}$ for individual updraft plumes within the grid box. At various values of G, the distribution of grid-mean $\hat{M}$ simulated by the hybrid stochastic UNICON is similar to that from theory (solid vs. dash on Fig 4.12a). To sample the grid-mean $\hat{M}$ at various values of G, we divided the default LES simulation results at $G = 6.4 \times 6.4\,\mathrm{km}^2$ into 2×2 (4×4) sub-domains for computing the LES-simulated PDF in the grid size of $G = 3.2 \times 3.2\,\mathrm{km}^2$ ($G = 1.6 \times 1.6\,\mathrm{km}^2$). Due to the small number of samples, the LES results are somewhat noisy but the overall distributions are similar to those of SCM. The hybrid method with 12 bin plumes (HYB12) and full stochastic method produced results very similar to HYB3 (not shown). In summary, our stochastic UNICON successfully reproduces the expected distribution of grid-mean $\hat{M}$ at various G, enhancing the scale-adaptive characteristics of the original UNICON.

Sensitivity simulations

Figure 4.13 shows the sensitivities of stochastic UNICON to the grid size G, number of bin plumes n, and stochastic perturbations imposed on the updraft plumes at the surface. The full stochastic method launches (or dispatches) more

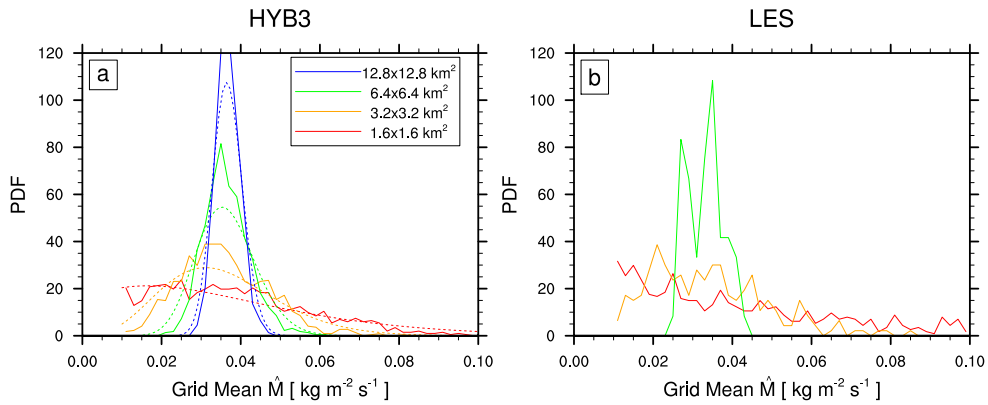

Figure 4.12 Histogram of grid mean $\hat{M}$ at z_{base} sampled at each time step during $t = 5 \sim 6hr$ in various G obtained from the (a) 100 ensemble HYB3 simulations and (b) LES in the cloud pixels. In the case of LES, the simulation was run in the domain size of $G = 6.4$ x 6.4 km^2 and then divided into various sub-domains to obtain the statistics shown in (b). The dashed lines in (a) are the theoretical distribution of grid mean $\hat{M}$ from Craig and Cohen (2006) for $\hat{M} = 0.036\,\mathrm{kg\,m^{-2}\,s^{-1}}$ and $\hat{N} = 1.17 \times 10^{-6}\,\#\,\mathrm{m^{-2}}$. These values of $\hat{M}$ and $\hat{N}$ are the ensemble-mean values of the SCM simulations.

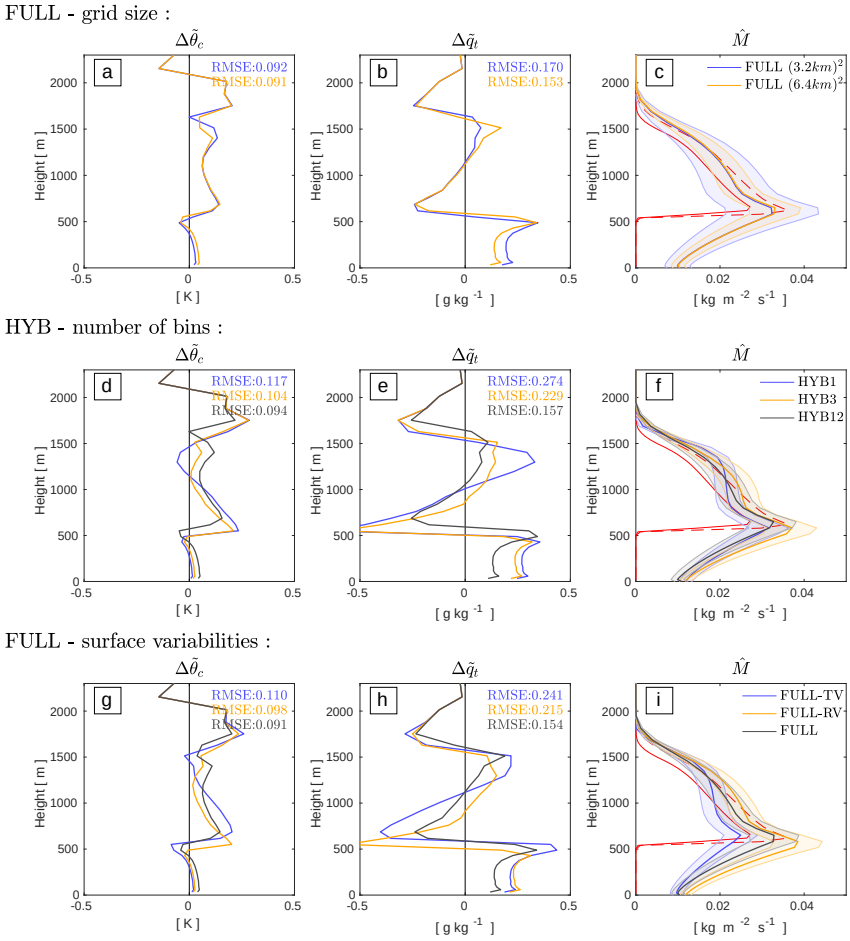

Figure 4.13 Sensitivity of stochastic UNICON to [(a),(b),(c)] G with the FULL method, [(d),(e),(f)] the number of bin plumes with the HYB method, and [(g),(h),(i)] the source of variability of convective updraft plumes at the surface with the FULL method. The first two columns show the biases of grid-mean θ_c and q_t against the multimodel LES ensemble mean (with a root-mean-squared error) and the third column shows grid-mean $\hat{M}$ and its spread (one standard deviation) during the period of $t = 3 \sim 6hr$. In the bottom row, FULL incorporates all sources of variability of convective updraft plumes at the surface during stochastic sampling (both $\hat{R}$ and other thermodynamic scalars, $\hat{\phi}$, including $\hat{w}$), FULL-RV only contains the variability in $\hat{R}$ at the surface, and FULL-TV only contains the variability in $\hat{\phi}$ and $\hat{w}$ at the surface. In the right column, the red solid (dotted) line denotes mean $\hat{M}$ of core updraft (cloudy updraft) obtained from the multimodel LES ensemble.

updraft plumes ($G\hat{N}$) as G increases. At $G = 6.4 \times 6.4\,\mathrm{km}^2$ and $G = 3.2 \times 3.2\,\mathrm{km}^2$, the expected number of updraft plumes are $G\hat{N}_e = G\hat{A}_s/(\pi\hat{R}_e^2) = 67.4$ and 16.8, respectively. If averaged over a long time, the ensemble mean of the grid-mean convective tendency will be insensitive to G, but the variance of grid-mean convective tendency is likely to increase as G decreases. As shown in Figs 4.13a-c, this anticipated behavior is reproduced by stochastic UNICON: the ensemble means of $\bar{\theta}_c$, $\bar{q}_t$, and grid-mean $\hat{M}$ simulated by the full stochastic SCM at $G = 6.4 \times 6.4\,\mathrm{km}^2$ are very similar to those at $G = 3.2 \times 3.2\,\mathrm{km}^2$, while the variance of the grid-mean $\hat{M}$ increases from $G = 6.4 \times 6.4\,\mathrm{km}^2$ to $G = 3.2 \times 3.2\,\mathrm{km}^2$.

The hybrid method (HYBn) consists of n bin plumes mainly controlling the ensemble mean and a single stochastic plume controlling the variance of the grid-mean convective tendency. The relative contributions of the n bin plumes and one stochastic plume to the grid-mean convective tendency at $G = 6.4 \times 6.4\,\mathrm{km}^2$ are $\gamma_b \equiv (G\hat{N}_e - \sqrt{G\hat{N}_e})/G\hat{N}_e = 88\,\%$ and $\gamma_s \equiv \sqrt{G\hat{N}_e}/G\hat{N}_e = 12\,\%$, respectively [(4.19),(4.20)], and γ_b (γ_s) decreases (increases) as G decreases. As a result, the hybrid method becomes more similar to the full stochastic method as G decreases. At the default $G = 6.4 \times 6.4\,\mathrm{km}^2$, the grid-mean convective tendency is thus mainly determined by the bin plumes and the mean profiles simulated by the hybrid methods shown in Figs 4.13d-f are very similar to those from the spectral bin method with the same number of bin plumes (BINn, not shown). The mass flux profile from HYB1 does not change much with height in the layers between $z = 850$ and $z = 1250$ [m] but decreases rapidly at greater heights, resulting in a positive bias of $\bar{q}_t$ at approximately $z = 1300$ [m] due to the excessive moisture convergence at this height (Fig 4.13f). Compared to HYB1, HYB3 simulates more realistic and

smooth vertical profiles for $\hat{M}$, $\bar{\theta}_c$, and $\bar{q}_t$, which are further improved in HYB12, which produces very similar results to the full stochastic method. Note that the spread of the grid-mean $\hat{M}$ simulated by HYB3 and HYB12 is very similar to that of HYB1, because all hybrid methods use a single stochastic plume that controls the variance of the grid-mean convective tendency. In summary, if the bins are chosen appropriately, the HYBn method can reproduce the ensemble-mean and variance of convective tendency simulated by the FULL method.

The fluctuation of the plume radius is an important source of variability but other thermodynamic variables may also contribute substantially. We ran two additional full stochastic SCMs by with only the stochastic perturbations of the updraft thermodynamic properties activated ($\hat{w}$ and $\hat{\phi} = \hat{\theta}_c, \hat{q}_t, \hat{u}, \hat{v}$) (FULL-TV) and only the stochastic perturbations of $\hat{R}$ activated (FULL-RV) at the surface, respectively. The default full stochastic method (FULL) includes all types of stochastic perturbations. As shown in Figs 4.13g-i, the stochastic perturbations of $\hat{w}$ and $\hat{\phi}$ are as important as those of $\hat{R}$ in correctly simulating the mean thermodynamic state, although $\hat{R}$ has a slightly larger impact than $\hat{w}$ and $\hat{\phi}$, as indicated by the smaller rmse errors in FULL-RV than FULL-TV. When all stochastic perturbations are included, the rmse errors are minimized, implying that a successful stochastic convection scheme needs to parameterize various sources of variability.

4.5 Discussion

There are several important aspects that have not been examined in our study. Since the updraft fractional area at the surface for a non-organized

state is fixed as a constant, our model does not simulate the feedback between stochastic fluctuations and the closure (Plant and Craig 2008; Keane and Plant 2012). Because we performed stochastic sampling at each time step in a fully independent way, temporal coherency of stochastic fluctuations is not taken into account. Although our HYBn method is carefully designed to reproduce both the ensemble mean and variance of the full stochastic method, the reproduction of higher-order statistics (e.g., skewness) is not guaranteed, particularly, when only a few plumes exist in the grid box. In the near future, we have a plan to explore these aspects. To further improve stochastic UNICON, we are also planning to revise the similarity function to build a more realistic multivariate Gaussian distribution at the surface; refine buoyancy sorting; parameterize other stochastic processes, such as the stochastic entrainment and merging of updraft plumes; and generalize stochastic UNICON to handle deep convection as well as shallow convection, which will presumably involve appropriate parameterizations of the scale break radius R_b as a function of the mesoscale convective organization and the size of the grid box.

5 Parameterization of Stochastically Entraining Convection using Machine Learning Technique

5.1 Introduction

The mass flux schemes compute changes in the mass flux and properties of convection, where the key process is the mixing between cumulus and nearby environment by entrainment and detrainment. The convective entrainment and detrainment are complex turbulent mixing processes involving the phase change of hydrometeors, so constitute one of the largest sources of uncertainty in GCMs (Murphy et al. 2004; Klocke et al. 2011).

Entrainment and detrainment are also important in that they are the main sources of variabilities among convective clouds. The main challenge in modern convection parameterizations is to represent a realistic distribution of clouds in a given environment. Many stochastic convection schemes are based on assumed mass flux distribution. However, there were also attempts to understand underlying physical processes responsible for developing the cloud variabilities. The variabilities among convective clouds can be generated from the variabilities from the near-surface or cloud base, or by the stochastic mixing process (Romps and Kuang 2010).

Entrainment and detrainment of mass are defined as the mass flux crosses into (entrainment) or out of (detrainment) cloud volume. The entrainment and detrainment rates of a cloud at a given height can be formally defined as (Siebesma 1998)

$$E = - \oint_{\hat{\boldsymbol{n}}\cdot(\boldsymbol{u}-\boldsymbol{u}_i)<0} \rho \hat{\boldsymbol{n}} \cdot (\boldsymbol{u} - \boldsymbol{u}_i) dl, \tag{5.1}$$

$$D = - \oint_{\hat{\boldsymbol{n}}\cdot(\boldsymbol{u}-\boldsymbol{u}_i)>0} \rho \hat{\boldsymbol{n}} \cdot (\boldsymbol{u} - \boldsymbol{u}_i) dl, \tag{5.2}$$

where E and D are the entrainment and detrainment rates [$\mathrm{kg\,m^{-1}\,s^{-1}}$], respectively, ρ is the density of air, $\hat{\boldsymbol{n}}$ is an outward unit vector perpendicular to the interface, $\boldsymbol{u}$ is the velocity of air at the cloud interface, and $\boldsymbol{u}_i$ is the velocity of the cloud interface. Entrainment and detrainment are often represented as the fractional entrainment and detrainment rates $\epsilon = E/M$ and $\delta = D/M$ [$\mathrm{m^{-1}}$], where $M = \rho w a$ is the convective mass flux, w is the vertical velocity, and a is the cross-sectional area of the cloud.

Due to their importance on weather and climate models, many studies have been conducted to parameterize the entrainment and detrainment in the last several decades. Many of them are in a form of deterministic formulas as a function of cloud and environment properties. Neggers et al. (2002) proposed $\epsilon \propto 1/w$ assuming a constant mixing timescale. Gregory (2001) proposed $\epsilon \propto B/w^2$ and Salzen and McFarlane (2002) proposed $\epsilon \propto dB/dz$, where B is the buoyancy of the cloud. Lu et al. (2016) suggested a parameterization based on fitting a power-law equation of w, B, and turbulent dissipation rate on ϵ. Dawe and Austin (2013) suggested power law fits of $B\partial\overline{\theta_v}/\partial z$ on ϵ and $w\chi_c$ on δ, where $\overline{\theta_v}$ is the environmental virtual potential temperature and χ_c is the critical mixing fraction. Another notable way of parameterizing ϵ and δ is the

buoyancy sorting scheme (Raymond and Blyth 1986; Kain and Fritsch 1990). Buoyancy sorting schemes assume a spectrum of mixed air between clouds and the environment, and then the mixtures with positive (negative) buoyancy are entrained (detrained). However, some deficiencies are reported for the original Kain-Fritsch buoyancy sorting scheme, so improvements to the Kain-Fritsch scheme were developed for practical use (Bretherton et al. 2004a; Rooy and Siebesma 2008; Park 2014a).

Another view of mixing of convection is as a purely stochastic process (Romps and Kuang 2010). Romps and Kuang (2010) modeled entrainment as discrete events which may be described as a stochastic Poisson process. The model is motivated by the observation that cloud-base properties are uncorrelated with upper-level cloud properties (i.e. cloud variabilities are generated by the mixing process). However, subsequent studies suggest that the stochastic mixing model also needs to include some kind of dependency on cloud properties to simulate various regimes of convection (Romps 2016; Suselj et al. 2019). In summary, the modern view of entrainment and detrainment processes is that they are strongly dependent on cloud properties and also exhibit a considerable randomness (Dawe and Austin 2013).

Another important issue about the mixing process is the role of the moist cloud shell which is a subsiding or negatively buoyant region around the cloud core. Traditionally entrainment and detrainment rates are diagnosed using the budget equations of conservative scalars between updrafts and environment, without considering the cloud shell. After Romps (2010), several methods have been developed to calculate entrainment and detrainment rates directly from large-eddy simulations (LESs) (Dawe and Austin 2011a; Yeo and Romps 2013; Wang 2020). These studies revealed that the presence of a cloud shell biases

the budget calculations. In addition, Hannah (2017) showed that entrainment and dilution of scalars are not well correlated, suggesting a need for the explicit consideration of cloud heterogeneity.

In this study, we will introduce neural stochastic differential equations (SDEs) for the mixing process of convective clouds. The stochastic differential equations have been extensively used in dynamic systems with random processes and are a very useful tool to describe the Lagrangian motion of turbulent flows. The neural SDEs, also called the latent SDEs, are the SDEs that their drift and diffusion are modeled by neural network (Tzen and Raginsky 2019; Li et al. 2020). Use of the machine learning (ML) model helps to explain the complex non-linear system that is hard to be physically modeled. Four uncertain parameters in the governing equations of mass flux schemes are modeled using neural SDEs: ϵ, δ, fractional dilution rate of scalars, and vertical acceleration. In this framework, the dependence of the mixing process on cloud properties and also the stochasticity in the mixing process can be modeled realistically. Also, the effect of cloud shells in the mixing process is considered.

5.2 Conceptual framework

5.2.1 Stochastic equations for vertical evolution

Following Siebesma (1998), the governing equations for individual updrafts can be formulated using the conservation law of mass and a scalar variable $\hat{\phi}$ (superscript hat denotes updraft and overline denotes grid mean) with a steady-state plume approximation ($\partial\psi/\partial t = 0$, where ψ is any convection properties):

$$\frac{\partial \hat{M}}{\partial z} = \hat{M}(\epsilon - \delta), \tag{5.3}$$

$$\frac{\partial(\hat{M}\hat{\phi})}{\partial z} = \hat{M}(\hat{\phi}_\epsilon \epsilon - \hat{\phi}_\delta \delta) + \hat{M}\hat{S}_\phi, \tag{5.4}$$

where $\hat{S}_\phi$ is the source of ϕ within an updraft and $\hat{\phi}_\epsilon$ ($\hat{\phi}_\delta$) is average ϕ of entraining (detraining) air. Combining (5.3) and (5.4),

$$\frac{\partial \hat{\phi}}{\partial z} = -\epsilon(\hat{\phi} - \hat{\phi}_\epsilon) + \delta(\hat{\phi} - \hat{\phi}_\delta) + \hat{S}_\phi. \tag{5.5}$$

In most bulk plume schemes, the entraining air is assumed to have same properties as the environmental air ($\hat{\phi}_\epsilon = \overline{\phi}$) and the detraining air is assumed to have same properties as the mean updraft air ($\hat{\phi}_\delta = \hat{\phi}$), which reduce (5.5) to $\partial\hat{\phi}/\partial z = -\epsilon(\hat{\phi} - \overline{\phi}) + \hat{S}_\phi$. However, previous studies found that the entraining air does not have properties of the environment because of the existence of subsiding cloud shell that includes the recently detrained air from the cloud core (Dawe and Austin 2011b; Hannah 2017).

Directly modeling $\hat{\phi}_\epsilon$ and $\hat{\phi}_\delta$ is hard since it might need additional prognostic equations for the cloud shell. As an alternative, we define the fractional dilution rate ϵ_ϕ as the tendency of $\hat{\phi}$ by the mixing process divided by the anomaly of $\hat{\phi}$. In a steady state, ϵ_ϕ can be formulated as

$$\epsilon_\phi = -\frac{\partial\hat{\phi}/\partial z - \hat{S}_\phi}{\hat{\phi} - \overline{\phi}} = \frac{\epsilon(\hat{\phi} - \hat{\phi}_\epsilon) - \delta(\hat{\phi} - \hat{\phi}_\delta)}{\hat{\phi} - \overline{\phi}}. \tag{5.6}$$

The fractional dilution rate can be understood as a diagnosed fractional entrainment rate obtained using the scalar budget equation. As explained in the introduction, the use of wrong diagnoses for the entrainment rate (not considering the effect of cloud shells) might prevent the accurate calculation of mass fluxes and scalars simultaneously. As so, we will use different mixing rates for mass flux (ϵ and δ) and scalars (ϵ_ϕ), while the identical ϵ_ϕ is used for all scalars.

The vertical velocity of updraft also can be described by (5.5) with the source term of buoyancy, vertical pressure gradient force , and the Coriolis force (which is typically neglected). Since the vertical pressure gradient force term is hard to be parameterized, most parameterizations of vertical velocity equation partition the vertical pressure gradient force term into buoyancy and entrainment terms and use the form of

$$\hat{w}\frac{\partial \hat{w}}{\partial z} = a\hat{B} - b\epsilon\hat{w}^2, \tag{5.7}$$

where a and b are constants. a and b are found to be highly case-dependent (Roode et al. 2012) and sensitive to how the convective updrafts are defined (Wang and Zhang 2014). This is due to the fact that the pressure gradient force term, which is hard to be physically parameterized, is the dominant sink term in the vertical velocity budget (Roode et al. 2012). This motivates the use of machine learning for the total vertical acceleration $d\hat{w}/dt = \dot{w}$, rather than modeling each term.

The strategy of our stochastic mixing model is to set stochastic differential equations (SDEs) using a neural network for the most uncertain parameters: ϵ, δ, ϵ_ϕ, and $\dot{w}$. Since SDE is usually used to explain the time evolution, the fractional mixing rates are expressed as mixing time scales in the unit of $[s^{-1}]$. They can be converted from the fractional mixing rates in unit height, as

$$\epsilon^t = \hat{w}\epsilon, \tag{5.8}$$

$$\delta^t = \hat{w}\delta, \tag{5.9}$$

$$\epsilon_\phi^t = \hat{w}\epsilon_\phi. \tag{5.10}$$

The final governing equations for the vertical evolution of the mass flux and scalars of individual convective updrafts are expressed as total derivatives,

following the convention of Lagrangian models of turbulent flows:

$$\begin{cases} \dfrac{1}{\hat{M}}\dfrac{d\hat{M}}{dt} = \epsilon^t - \delta^t \\ \dfrac{d\hat{\phi}}{dt} = -\epsilon_\phi^t(\hat{\phi} - \overline{\phi}) + \hat{S}_\phi^t \\ \dfrac{d\hat{w}}{dt} = \dot{w} \end{cases} \tag{5.11}$$

where $\hat{S}_\phi^t$ is the source of $\hat{\phi}$ in unit time. Note that the equations are written in total derivative, but $\hat{M}$, $\hat{\phi}$, and $\hat{w}$ are time-invariant in a given environment due to the steady-state assumption. Here, ϵ^t, δ^t, ϵ_ϕ^t, and $\dot{w}$ are determined by the following stochastic differential equations:

$$d\log(\epsilon^t) \;=\; \mu_1 \left[\log(\epsilon^t)_{\exp} - \log(\epsilon^t)\right] dt \;+\; \sigma_1 dW_1, \tag{5.12}$$

$$d\log(\delta^t) \;=\; \mu_2 \left[\log(\delta^t)_{\exp} - \log(\delta^t)\right] dt \;+\; \sigma_2 dW_2, \tag{5.13}$$

$$d\log(\epsilon_\phi^t) \;=\; \mu_3 \left[\log(\epsilon_\phi^t)_{\exp} - \log(\epsilon_\phi^t)\right] dt \;+\; \sigma_3 dW_3, \tag{5.14}$$

$$d\dot{w} \;=\; \mu_4 \left[\dot{w}_{\exp} - \dot{w}\right] dt \;+\; \sigma_4 dW_4. \tag{5.15}$$

For the variables of $\chi_i = \{\log(\epsilon^t),\ \log(\delta^t),\ \log(\epsilon_\phi^t),\ \dot{w}\}$, the four equations can be summarized as

$$d\chi_i = \mu_i \left[\chi_{i,\exp} - \chi_i\right] dt + \sigma_i dW_i, \tag{5.16}$$

where σ_i is the diffusion coefficient, dW_i is the increment of Wiener process, $\chi_{i,\exp}$ is the expected value at a given state. μ_i, $\chi_{i,\exp}$, and σ_i in (5.16) are machine learned as described in Section 5.2.2. From those, the stochastic differential equations are solved to get χ_i, and χ_i is then inserted into the final governing equations ((5.11)). The equations can be understood as the continuous time limit of the first-order autoregressive model (AR(1)) (Brockwell et al. 1991; Stramer et al. 1996). The drift terms of the equations indicate that

χ_i approach to $\chi_{i,\mathrm{exp}}$, where the speed of the drift is determined by μ_i. The use of log for the mixing rates of ϵ^t, δ^t, and ϵ^t_ϕ guarantees that those mixing rates are always positive. Also, LES (Dawe and Austin 2013) and aircraft observation (Cheng et al. 2015) studies show that the fractional entrainment and detrainment rates are well modeled by log-normal distributions.

The proposed framework allows us to account for the time coherency of the mixing rates, in contrast to the model of Romps (2010) that assumes independent discrete entrainment events. This is a more realistic approach since turbulent eddies of various spatiotemporal scales experience non-linear interactions. The time series of $\log_{10}(\epsilon^t)$ derived from the BOMEX LES (Figure 5.1) clearly show that the entrainment is an autocorrelated process. The lag-1 autocorrelations of $\log(\epsilon^t)$, $\log(\delta^t)$, $\log(\epsilon^t_\phi)$, and $\dot{w}$ with $\Delta t = 60\,\mathrm{s}$ calculated using our dataset are found to be 0.529, 0.582, 0.376, and 0.555, respectively.

In numerical implementations, the SDEs are used as discretized form:

$$\chi_i^t - \chi_i^{t-1} \;=\; \mu_i \left[\chi_{i,\mathrm{exp}} - \chi_i^{t-1}\right] \Delta t \;+\; \sigma_i \sqrt{\Delta t}\,\xi_i, \tag{5.17}$$

where ξ_i is the white Gaussian noise $N(0,1)$, Δt is the time step size, and χ_i^t and χ_i^{t-1} are χ_i at times of t and $t - \Delta t$, respectively.

5.2.2 Machine learning model configuration

The unknown parameters in SDEs, μ_i, $\chi_{i,\mathrm{exp}}$, and σ_i, are modeled using a deterministic feed-forward neural network. The network accepts properties of a convective updraft and environment at a given height as inputs. The selection of the input variables will be discussed in Section 5.4. The feed-forward neural network has three hidden layers with 16 neurons in each layer. Scaled exponential linear unit (SELU) activation functions (Klambauer et al.

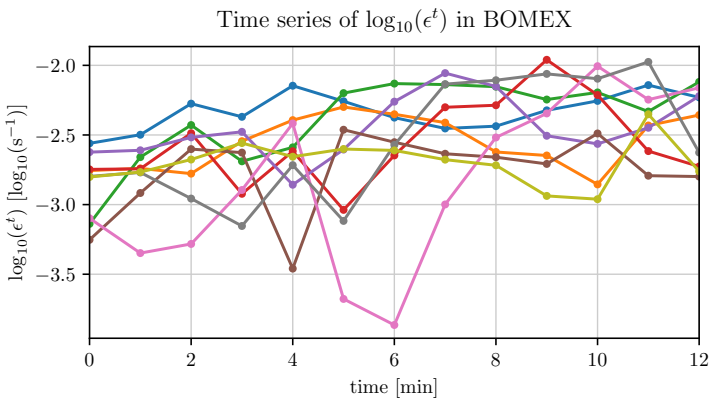

Figure 5.1 Time series of $\log_{10}(\epsilon^t)$ measured in the BOMEX LES. 9 time series are derived from randomly selected updrafts starting from the height of 600 m and lasting more than 12 minutes. The updrafts are tracked in a Lagrangian way as described in Appendix C. The simulation setup for the BOMEX LES is described in Section 5.3.1.

2017) follow each hidden layer. SELU helps the output distribution to retain a mean of 0 and a standard deviation of 1 which in turn avoids exploding and vanishing gradients. Before the final output layer, a dropout layer with a rate of 0.2 is added to reduce the risk of overfitting. The structure of the feed-forward network is optimized to give the best performance.

The unknown parameters in SDEs, μ_i, $\chi_{i,\mathrm{exp}}$, and σ_i, cannot be directly measured from the LES dataset. Then how is the neural network trained for μ_i, σ_i, and $\chi_{i,\mathrm{exp}}$ which can not be directly obtained from the LES dataset? From (5.17), it can be derived that the distribution of χ_i^t, $P(\chi_i^t)$, is a normal distribution with mean of $\chi_i^{t-1} + \mu_i \left[\chi_{i,\mathrm{exp}} - \chi_i^{t-1}\right] \Delta t$ and standard deviation of $\sigma_i\sqrt{\Delta t}$. Δt corresponds to the LES output frequency of 60 s. While training the network, a probabilistic layer is embedded as a final layer so that the outputs are probability distributions of $P(\chi_i^t)$. The training network is trained such that the modeled $P(\chi_i^t)$ is the best fit to LES data samples by minimizing the loss function l which is defined as

$$l = -\frac{1}{n}\sum_{i=1}^{n} \log f(x_i|\theta), \tag{5.18}$$

where n is the number of training samples, f is the probability density function (pdf), x_i is training samples, and θ is parameters of the pdf. The data samples are trained altogether regardless of height and time of sampling. The configuration of the deep learning network is depicted in Figure 5.2.

5.2.3 Stochastic initialization of convective updrafts at the near-surface

To fully represent the variabilities between convective updrafts, near-surface variabilities should also be realistic. For the stochastic initialization of convec-

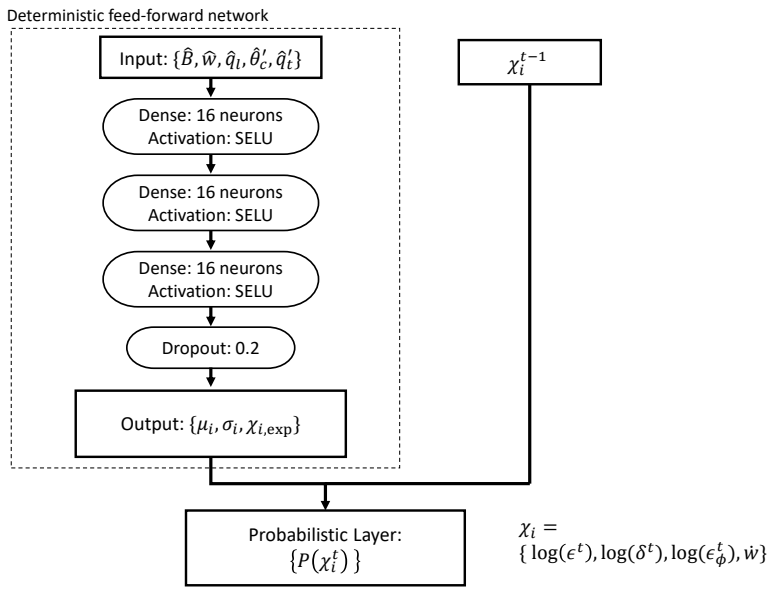

Figure 5.2 A diagram of how the probabilistic deep learning network is connected for training. The network is trained to minimize negative log-likelihood. After the training, the deterministic feed-forward network part is used to determine the parameters of the stochastic differential equations.

tive updrafts at the near-surface, we follow the method specified in Section 4.2. Vertical velocity and thermodynamic scalars of convective updrafts at the near-surface are randomly sampled from the multivariate Gaussian distribution with a constraint of $w > 0$, where standard deviations and inter-variable correlations are derived from the surface-layer similarity theory. The number density PDF of updraft radius R at the surface is parameterized as (4.15). In this study, R_b is set to 170 m, which represents the typical size of shallow convection. We assume that correlations between updraft radius and other updraft variables are zero at the surface.

5.3 Experimental setting

5.3.1 Large-eddy simulations

The University of California, Los Angeles large-eddy simulation (UCLA-LES) model (Stevens et al. 1999, 2005) is used to simulate two shallow convection cases. The UCLA-LES solves a set of anelastic equations with the turbulence model of Smagorinsky-Lilly. Cloud microphysical processes are parameterized based on the two-moment warm rain scheme of Seifert and Beheng (2001) with modifications detailed in Stevens and Seifert (2008).

The first case is the Barbados Oceanographic and Meteorological Experiment (BOMEX) (Holland and Rasmusson 1973) following the settings of Siebesma et al. (2003). In this simulation, radiation and the production of precipitation are turned off. The domain size is 6.4 km $\times$ 6.4 km $\times$ 3.0 km, and the grid size is 25 m $\times$ 25 m $\times$ 25 m. The model is run for 6 h, and outputs from time intervals of one minute during the last 2 hours (a total of 120 instantaneous snapshots) are analyzed.

The second case is the Rain in Cumulus over the Ocean (RICO) field campaign following the settings of vanZanten et al. (2011). The domain size is 12.8 km × 12.8 km × 4.0 km, and the grid size is 40 m × 40 m × 40 m. The model is run for 24 h, and outputs from time intervals of one minute during the last 4 hours (a total of 240 instantaneous snapshots) are analyzed. For the RICO case, the production of precipitation is allowed and the number density of cloud droplets is set to a fixed value of $70\,\mathrm{cm}^{-3}$.

Individual clouds are detected using the cloud tracking algorithm of Dawe and Austin (2012) which tracks clouds by considering the spatiotemporal connectivity of cloudy grid cells. The algorithm categorizes cloudy grid cells into three types. The "core" region is defined as the grid boxes with positive condensate, vertical velocity, and buoyancy, and the "condensed" region is defined as the grid boxes with condensate. The "plume" region is defined as the grid boxes having positive vertical velocity and containing radioactively decaying passive tracer emitted continuously from the surface with a concentration higher than one spatial standard deviation at each height (Couvreux et al. 2010). Additionally, all condensed points are also flagged as plume points, so that the condensed region is always a subset of the plume. The decaying time scale of the passive tracer is set to 15 minutes in the BOMEX case and 30 minutes in the RICO case.

It is important to determine the cloud type that corresponds to convective updrafts in a convection scheme when developing the convection scheme using LES data. Typically, convection schemes are designed to represent the properties of the cloud core region. In our study, we focus on the analysis of plume regions with positive vertical velocity (hereinafter referred to as convective updrafts). This is for two reasons, first to include dry convection in

the sub-cloud layer, and second to allow forced convection (negatively buoyant but have positive vertical velocity). We add a constraint that vertical velocity should be greater than zero, to exclude cloud shell or convective downdraft.

The entrainment and detrainment rates of convective updrafts are measured using the method of Yeo and Romps (2013). The entrainment and detrainment rates are calculated by counting the number of Lagrangian particles that go into or out of the cloud interface in finite time and height intervals. In our LES simulations, Lagrangian particles are imposed using the online Lagrangian Particle Tracking Module (LPTM; Heus et al. (2008a)). A total number of 2031297 particles for the BOMEX case and 1605133 particles for the RICO case are imposed, and the properties of individual Lagrangian particles are recorded every 30 seconds. The entrainment and detrainment rates are calculated for each convective updraft using a time interval of 30 s and a height interval of 50 m.

Finally, the fractional dilution rate ϵ_ϕ^t and vertical acceleration $\dot{w}$ of individual convective updrafts are calculated. Also, our framework needs mixing rates at current time step (χ_i^t) and previous time step (χ_i^{t-1}). The method of calculating these variables is explained in Appendix C. For every model layer and sampling time, input and output variables for training the neural network are obtained. We exclude the samples at the time steps when a convective updraft merges with other updrafts or is split into multiple updrafts. We also exclude the samples at the lowest model layer. This results in a total of 48845 samples for the BOMEX case and 238606 samples for the RICO case.

5.3.2 Single-column model

The single-column model (SCM) used in our study is the single-column version of Community Atmospheric Model version 5 (CAM5) with the unified convection scheme (UNICON; Park (2014a)) implemented, identical to the one used by (Park et al. 2019). The model has 80 vertical layers and uses the leap-frog time stepping method with a time step of 300 s. SCM is driven by same forcing specified in LES simulations, each for the BOMEX and RICO cases. UNICON computes the vertical evolution of conservative scalars $\phi = \{\theta_c, q_t, u, v, \zeta\}$ within convective updrafts and downdrafts.

Our mixing model is implemented in the UNICON scheme and substitutes the existing mixing model which is a modified version of the buoyancy sorting algorithm. The vertical velocity equation is also replaced. The trained neural network is converted to a Fortran code using the Fortran-Keras Bridge (FKB) library (Ott et al. 2020). Original UNICON simulates convective downdrafts, associated mesoscale organized flow, and its effect on convection. In our SCM experiments, we disable convective downdrafts and associated mesoscale organization flow since the distribution of near-surface thermodynamic variables in the presence of mesoscale organization has not yet been studied. The standard RICO case simulated by UCLA-LES does not show notable mesoscale organization for the first 24 hours (Seifert and Heus 2013; Seifert et al. 2015). However, we note that transport due to convective downdrafts in the RICO case is relatively small compared to updrafts but not negligible (Heus et al. 2008b; Suselj et al. 2019).

The conversion rate of cloud water to rain, the autoconversion rate, in the original UNICON is based on Kessler (1969), where it is linearly proportional

to cloud water content when the cloud water content is larger than a threshold value. The threshold value and the autoconversion efficiency are specifically tuned to produce a reasonable amount of precipitation in global simulations. However, we found that the original autoconversion scheme produces an excessive amount of precipitation and severely distorts the distribution of cloud properties for the RICO case. Thus we utilize the autoconversion scheme of Khairoutdinov and Kogan (2000) in the form of

$$\left(\frac{\partial q_r}{\partial t}\right)_{\text{auto}} = c\hat{q}_c^a \hat{N}_c^b, \tag{5.19}$$

where q_r is the rain water specific humidity, $\hat{q}_c = \hat{q}_l + \hat{q}_i$ is the specific humidity of in-cumulus condensate, $\hat{N}_c = \hat{N}_l + \hat{N}_i$ is the number density of cloud droplets ($\hat{N}_l$: the number density of liquid cloud droplets, $\hat{N}_i$: the number density of ice cloud droplets), and a, b, and c are the fitting parameters. The values of the fitting parameters are set equal to Kogan (2013), which are specifically fitted to the RICO case. The values are $a = 4.22$, $b = -3.01$, and $c = 7.98 \times 10^{10}$ when $\hat{q}_c$ is in unit of $\mathrm{kg\,kg^{-1}}$ and $\hat{N}_c$ is in unit of $\mathrm{cm^{-3}}$. The autoconversion scheme cannot be implemented in UNICON in general cases, since the microphysics in UNICON is a simple single-moment scheme. Thankfully, since the RICO case assumes a constant cloud droplet number density of $70\,\mathrm{cm^{-3}}$, the parameterized autoconversion rate becomes a function only of $\hat{q}_c$. We do not change the other rain processes like accretion and evaporation since the simulated rain rate of the RICO case is found to be sensitive only to the autoconversion process.

Finally, a free parameter in UNICON is tuned to simulate reasonable mass flux. The only parameter changed is the convective updraft fractional area at the surface $\hat{A}_s$, changed from the original value of 0.040 to 0.025. The value of the parameter was determined by selecting the one with the lowest RMSE

of $\overline{\theta_c}$ and $\overline{q_t}$ among several SCM simulations with different $\hat{A}_s$. The SCM simulation with the new mixing model takes $\sim 15\%$ more time compared to the original UNICON, mainly due to the computation of the neural network. The computation time can be reduced by using computationally cheaper activation function or by reducing the size of the network. Accommodating the neural network adds about 220 KB of memory footprint per process (including loading related libraries), which is negligible compared to the total memory consumption of the model code.

5.4 Training and testing of the machine learning model

5.4.1 Training of the machine learning model

The neural network described in Section 5.2.2 is trained and tested with the combined samples from the BOMEX and RICO cases. The total 287451 samples are randomly partitioned into the training set, validation set, and test set, with ratios of 64%, 16%, and 20%, respectively. The validation set is used to estimate the model skill during the training of the model, and the test set is used to evaluate the performance of the model after the training. The neural network of three hidden layers with 16 neurons per layer is iteratively updated through the stochastic gradient descent with a batch size (number of samples used in a single update of model weights) of 32 and a learning rate of 0.001 with the Adam optimizer (Kingma and Ba 2015).

As the training progresses, the loss function evaluated from the training set (training loss) keeps decreasing, while the loss function evaluated from the validation set (validation loss) stops decreasing and starts to increase at some point due to overfitting. In order to prevent overfitting, the neural network is

trained until the validation loss does not decrease for the following 50 epochs. The training takes 250∼500 epochs depending on the random state of the stochastic gradient descent. The neural network is trained and tested using TensorFlow library (Abadi et al. 2015) and TensorFlow Probability library (Dillon et al. 2017). The hyperparameters that affect the model performance, which are batch size, learning rate, number of hidden layers, and number of neurons per layer, are tuned with Keras Tuner library (O'Malley et al. 2019) to get the optimal performance. We also tested the single-hidden-layer version of the neural network using the same number of trainable parameters as our multi-layer neural network (a total of 673 parameters; 84 neurons for the single hidden layer). The single-hidden-layer neural network showed 89 % of R^2 compared to the multi-layer version while predicting the fractional entrainment rate.

5.4.2 Selecting input variables for the machine learning model

We selected input variables for the ML model that are physically meaningful for predicting mixing rates. This is also an important procedure to reduce the size of the network and the computation time. First, the candidates of input variables are chosen from previous studies. The candidates are buoyancy $\hat{B} = (\hat{\theta}_v - \overline{\theta_v})/\overline{\theta_v}$, vertical velocity $\hat{w}$, specific humidity of liquid water $\hat{q}_l$, anomaly of condensate potential temperature $\hat{\theta}'_c = \hat{\theta}_c - \overline{\theta_c}$, anomaly of the total water specific humidity $\hat{q}'_t = \hat{q}_t - \overline{q_t}$, vertical gradient of environmental virtual potential temperature $\partial\overline{\theta_v}/\partial z$, updraft radius $\hat{R} = \sqrt{\hat{a}/\pi}$, and environmental vertical wind shear $V_{\text{shear}} = \sqrt{(\partial\overline{u}/\partial z)^2 + (\partial\overline{v}/\partial z)^2}$.

The thermodynamic variables are all in the form of the anomaly with respect to the mean environment (if $\overline{q_l} = 0$). In fact, the most fundamental variables describing the thermodynamic states of updrafts and environment are

$\hat{\theta}_c$, $\overline{\theta_c}$, $\hat{q}_t$, and $\overline{q_t}$. However, if the ML model is trained with these variables, it cannot be used in a climate different from the one in which it was trained (e.g. warm climate). This is a well-known issue of machine learning based physics parameterization (Rasp et al. 2018). Therefore, we select anomalous variables to limit the sample space. It is also a physically rational choice since turbulent mixing is proportional to the difference in properties of the two fluids. Previous studies indicate that relative humidity in environment is an important factor affecting entrainment and detrainment rates (Bechtold et al. 2008; Lu et al. 2018; Stirling and Stratton 2012; Zhao et al. 2018; Zhu et al. 2021). However, relative humidity is not considered as a potential input variable here since the anomaly of the total water specific humidity $\hat{q}_t'$ which has a similar physical meaning as relative humidity was found to be a better proxy.

In order to select the input variables, we calculate permutation importance (PI; Altmann et al. (2010)) to quantify the relative importance of the variables. The permutation importance is defined as the decrease in a model score when the values of a single variable are randomly shuffled. We calculate the increase in mean squared error (MSE) when input variables are permuted, for the neural networks predicting $\log(\epsilon)$, $\log(\delta)$, $\log(\epsilon^t)$, $\log(\delta^t)$, $\log(\epsilon^t_\phi)$, and $\dot{w}$. To increase statistical significance, 20 random permutations for each input variable are done. For this analysis, the training of the neural network is only done for the data samples with $\hat{q}_l > 0$ since the cloud tracking in the sub-cloud layer is inaccurate (Dawe and Austin 2012).

Table 5.1 shows the results of the permutation importance analysis. Dawe and Austin (2013) found that the fractional entrainment rate is best predicted by $\hat{B}$ and $\partial\overline{\theta_v}/\partial z$. In our analysis, $\partial\overline{\theta_v}/\partial z$ shows the largest PI values for predicting $\log(\epsilon)$ and $\log(\epsilon^t)$. However, the buoyancy $\hat{B}$ has relatively low PI

Table 5.1 Permutation importance of the candidates of input variables and base mean squared error (MSE) when predicting $\log(\epsilon)$, $\log(\delta)$, $\log(\epsilon^t)$, $\log(\delta^t)$, $\log(\epsilon^t_\phi)$, and $\dot{w}$. Permutation importance is written as percentage [%] of increased MSE when the variable is permuted with respect to base MSE. Note that all the variables are normalized before training. Mean and standard deviation for 20 permutations are shown. The finally selected variables are denoted in bold.

	$\hat{\boldsymbol{B}}$	$\hat{\boldsymbol{w}}$	$\hat{\boldsymbol{q}}_{\boldsymbol{l}}$	$\hat{\boldsymbol{\theta}}'_{\boldsymbol{c}}$	$\hat{\boldsymbol{q}}'_{\boldsymbol{t}}$	$\boldsymbol{\partial\overline{\theta_v}/\partial z}$	$\hat{R}$	V_{shear}	MSE
$\log(\epsilon)$	28.2 ± 0.7	18.0 ± 0.3	45.4 ± 1.0	44.1 ± 0.9	54.6 ± 1.0	175.7 ± 2.1	21.5 ± 0.5	8.6 ± 0.3	0.633
$\log(\delta)$	21.6 ± 0.8	854.9 ± 5.2	114.7 ± 1.6	12.8 ± 0.6	39.4 ± 0.7	87.4 ± 0.9	5.5 ± 0.2	15.4 ± 0.4	0.324
$\log(\epsilon^t)$	27.8 ± 0.6	39.9 ± 1.0	14.0 ± 0.3	22.7 ± 0.8	67.5 ± 1.3	140.7 ± 1.7	19.2 ± 0.5	7.9 ± 0.3	0.619
$\log(\delta^t)$	21.4 ± 0.8	301.4 ± 2.3	108.5 ± 1.1	11.5 ± 0.4	19.8 ± 0.7	78.7 ± 1.0	6.0 ± 0.2	13.8 ± 0.3	0.582
$\log(\epsilon^t_\phi)$	10.5 ± 0.3	46.0 ± 0.5	5.2 ± 0.2	2.8 ± 0.1	14.5 ± 0.4	26.8 ± 0.5	15.2 ± 0.3	3.3 ± 0.2	0.804
$\dot{w}$	24.3 ± 0.5	103.2 ± 1.7	26.1 ± 0.6	60.1 ± 1.1	90.6 ± 1.4	127.8 ± 1.6	15.8 ± 0.7	7.6 ± 0.4	0.463

values for predicting $\log(\epsilon)$ and $\log(\epsilon^t)$. This is thought to be because our definition of convective updraft includes regions with positive and negative buoyancy, while Dawe and Austin (2013) used the core region for the analysis. For $\log(\delta)$ and $\log(\delta^t)$, the vertical velocity $\hat{w}$ shows the largest PI values, which is one of the best predictors pointed out by Dawe and Austin (2013) as well.

The log of the fractional dilution rate $\log(\epsilon_\phi^t)$ does not have predictors with significantly high PI values. This indicates that the fractional dilution rate cannot be predicted well by a single variable. For the vertical acceleration $\dot{w}$, $\partial\overline{\theta_v}/\partial z$ shows the largest PI, followed by $\hat{w}$ and $\hat{q}_t'$. In contrast, $\hat{B}$ shows a relatively low PI value, which seems to be an unexpected result because buoyancy is a main source of the vertical velocity budget. Wang and Zhang (2014) reported that the buoyancy term becomes small in the vertical momentum budget when convective updraft is defined to include negative buoyancy region.

Among the candidates of input variables, the vertical wind shear V_{shear} has the lowest PI values and the updraft radius $\hat{R}$ has the second lowest. Moreover, there is a possibility that PIs of other variables excluding these two variables are underestimated. As displayed in Figure 5.3, the variables other than $\hat{R}$ and V_{shear} are highly correlated. When variables are correlated, their permutation importances tend to be underestimated. This is because the permutation of one variable has little effect on model performance since the same information can be obtained from the correlated variables. The low correlations of V_{shear} and $\hat{R}$ with other variables confirm that the low PI values of these variables actually represent the low importance of these variables. The vertical wind shear is one of the main factors controlling the cloud-top entrainment of stratocumulus (Mellado 2017), but it seems to have a low impact on cumulus-type convection. The low dependency of ϵ and δ on shallow cumulus radius is also pointed out

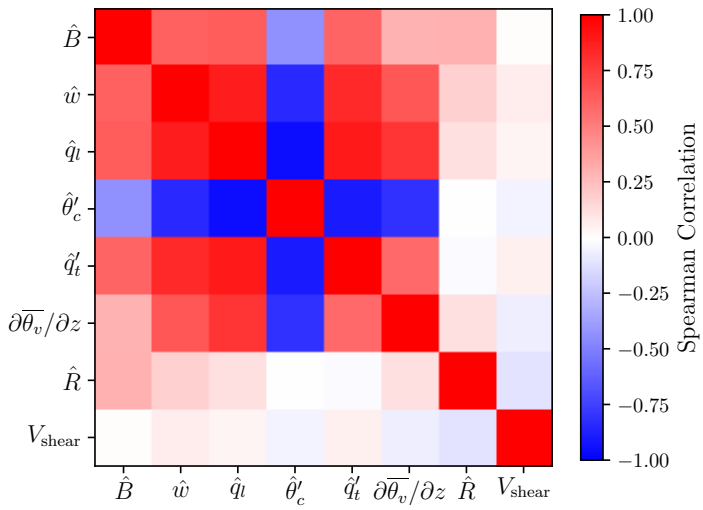

Figure 5.3 A plot of cross-correlation matrix for the candidates of input variables. Spearman correlation is used to see a monotonic relationship between variables.

by Dawe and Austin (2013). For this reason, we choose the final input variables excluding these two: $\hat{B}$, $\hat{w}$, $\hat{q}_l$, $\hat{\theta}'_c$, $\hat{q}'_t$, and $\partial\overline{\theta_v}/\partial z$.

5.4.3 Performance of the machine learning model

In this subsection, the performance of the ML model for predicting the mixing rates is tested. We compare our model with various parameterizations of entrainment and detrainment rates proposed by previous studies. In addition, the multiple linear regression model with same inputs as the ML model for predicting dependent variables of $\log(\epsilon)$ and $\log(\delta)$ is examined (log is used to ensure that ϵ and δ are positive). The list of tested parameterizations is given in Table 5.2. The fitting and evaluation of the parameterizations are done with separate subsets of the dataset, where the fitting is done with the training set plus validation set, and the evaluation is done with the test set (see Section 5.4.1 for how the dataset is partitioned). The fitting parameters in the parameterizations are newly fitted to our dataset without using the default values. The entrainment model of Lu et al. (2016) was suggested in two versions, with and without turbulent dissipation rate ($\epsilon = a\hat{B}^b\hat{w}^c\hat{\varepsilon}^d$ or $\epsilon = a\hat{B}^b\hat{w}^c$ where ε is the turbulent dissipation rate). Here, we use the version without turbulent dissipation rate since the turbulent dissipation rate is hard to be calculated in one-dimensional convection parameterization. The buoyancy sorting is original version of Kain and Fritsch (1990), where $\epsilon = \epsilon_0\hat{\chi}_c^2$ and $\delta = \epsilon_0(1-\hat{\chi}_c)^2$ with $\epsilon_0 = 0.02\,\mathrm{m}^{-1}$ which is a typical value for shallow convection. Except for the ML model, other parameterizations are fitted only on data samples with $\hat{q}_l > 0$ and $\hat{B} > 0$ since some parameterizations require a positive buoyancy condition. We note that this analysis is not a fair comparison for the performance of the parameterizations since each parameterization has its own method of

Table 5.2 A list of tested entrainment and detrainment parameterizations. a, b, and c are fitting parameters. The linear regression model for the entrainment or detrainment is $Y = a_0 + a_1\hat{B} + a_2\hat{w} + a_3\hat{q}_l + a_4\hat{\theta}'_c + a_5\hat{q}'_t + a_6\partial\overline{\theta_v}/\partial z$, where $Y = \{\log(\epsilon), \log(\delta)\}$, and a_i $(i = 0, ..., 6)$ are fitting parameters.

Entrainment Model	Figure	Detrainment Model	Figure	Reference
$\epsilon = a/\hat{R}$	Fig. 5.4a	-	-	Turner (1963)
$\epsilon = a/\hat{w}$	Fig. 5.4b	-	-	Neggers et al. (2002)
$\epsilon = a\hat{B}/\hat{w}^2$	Fig. 5.4c	-	-	Gregory (2001)
$\epsilon = a\hat{B}^b\hat{w}^c$	Fig. 5.4d	-	-	Lu et al. (2016)
$\epsilon = a\hat{B}^b(\partial\overline{\theta_v}/\partial z)^c$	Fig. 5.4e	$\delta = a\hat{w}^b\hat{\chi}_c^c$	Fig. 5.5a	Dawe and Austin (2013)
Buoyancy Sorting	Fig. 5.4f	Buoyancy Sorting	Fig. 5.5b	Kain and Fritsch (1990)
Linear Regression	Fig. 5.4g	Linear Regression	Fig. 5.5c	This study
Machine Learning	Fig. 5.4h	Machine Learning	Fig. 5.5d	This study

computing entrainment/detrainment rate and defining cloud region. Although many of these parameterizations are designed to predict bulk entrainment and detrainment rates, this analysis tests the performance of predicting directly measured entrainment and detrainment rates. The purpose of this analysis is to examine how well the ML model can explain the dependency of the mixing rates on cloud and environment properties.

Figure 5.4 shows the joint PDF of LES measured ϵ versus predicted ϵ by various parameterizations. As discussed in the previous section, $\hat{R}$ is not a good predictor for ϵ ($R^2 = 0.055$; Figure 5.4a). A simple $\hat{w}^{-1}$ relation shows $R^2 = 0.287$, which is found to perform reasonably well as a single variable parameterization (Figure 5.4b). The parameterization of Dawe and Austin (2013) does not show good performance in our analysis (Figure 5.4e), implying that the parameterization is only applicable for the core region. The buoyancy sorting scheme shows almost no skill for predicting ϵ (Figure 5.4f). The original Kain and Fritsch (1990) scheme is found to have some deficiency, for example, produces too small ϵ in low relative humidity environment (Kain 2004). Rooy et al. (2013) demonstrated that the simple function with height performs better than the original Kain-Fritsch scheme when predicting ϵ in the BOMEX case. The best parameterization except the ML model is the parameterization of Lu et al. (2016) (Figure 5.4d) which is slightly better than the multiple linear regression model. The ML model shows $R^2 = 0.655$ and outperforms the second-best parameterization of Lu et al. (2016) nearly by double the variance explained.

For the fractional detrainment rate δ (Figure 5.5), the ML model outperforms other parameterizations with $R^2 = 0.665$. Here, the parameterization of Dawe and Austin (2013) exhibits reasonable predictive performance ($R^2 =$

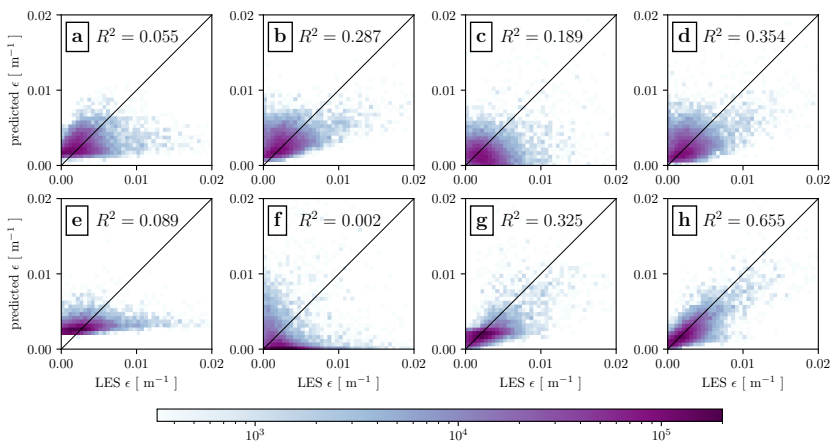

Figure 5.4 Joint probability density functions of LES measured ϵ versus predicted ϵ by various parameterizations for individual clouds. (a) $\epsilon = a/\hat{R}$, (b) $\epsilon = a/\hat{w}$, (c) $\epsilon = a\hat{B}/\hat{w}^2$, (d) $\epsilon = a\hat{B}^b\hat{w}^c$, (e) $\epsilon = a\hat{B}^b(\partial\overline{\theta_v}/\partial z)^c$, (f) buoyancy sorting scheme, (g) multiple linear regression model ($\log(\epsilon) = a_0 + a_1\hat{B} + a_2\hat{w} + a_3\hat{q}_l + a_4\hat{\theta}'_c + a_5\hat{q}'_t + a_6\partial\overline{\theta_v}/\partial z$), and (h) machine learning model. a, b, c, and a_i ($i = 0, ..., 6$) are fitting parameters.

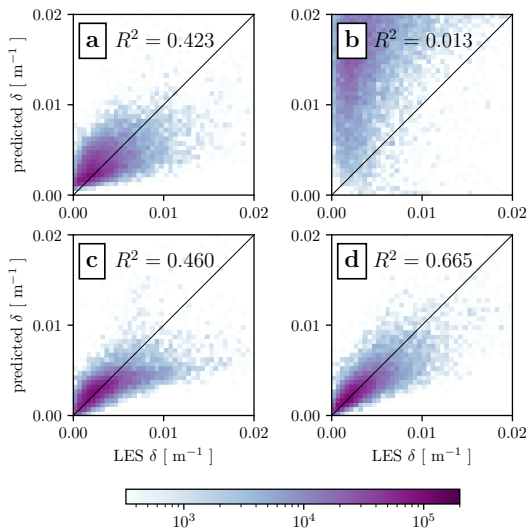

Figure 5.5 Joint probability density functions of LES measured δ versus predicted δ by various parameterizations for individual clouds. (a) $\delta = a\hat{w}^b\hat{\chi}_c^c$, (b) buoyancy sorting scheme, (c) multiple linear regression model ($\log(\delta) = a_0 + a_1\hat{B} + a_2\hat{w} + a_3\hat{q}_l + a_4\hat{\theta}_c' + a_5\hat{q}_t' + a_6\partial\overline{\theta_v}/\partial z$), and (d) machine learning model. a, b, c, and a_i ($i = 0, ..., 6$) are fitting parameters.

0.423; Figure 5.5a), unlike the entrainment parameterization. This predictive performance is largely due to the dependence of δ on the vertical velocity, where simple $\hat{w}^{-1}$ parameterization shows $R^2 = 0.404$ (not shown). The buoyancy sorting scheme shows low prediction skill and produces too large δ value (Figure 5.5b). Bretherton et al. (2004a) reported that the original Kain-Fritsch scheme can produce excessive detrainment since all the negative buoyant mixtures are detrained from the updraft. A more realistic approach is not to detrain the negative buoyant mixture with a positive vertical velocity that can travel a certain length scale (Bretherton et al. 2004a; Park 2014a). It seems that the fractional detrainment rate can be explained well by simple regression formula with a small number of variables compared to the fractional entrainment rate.

In addition to ϵ and δ, the skill for predicting $\dot{w} = dw/dt$ is tested (Figure 5.6). The most commonly used parameterization, (5.7), surprisingly exhibits almost the same performance as the ML model. However, the parameterization can produce expected performance only when the entrainment rate is accurately predicted. One interesting fact we found is that the entrainment drag term of the vertical velocity equation should utilize the fractional dilution rate ϵ_ϕ, rather than the fractional mass entertainment rate ϵ. If ϵ is used, the prediction skill decreases as $R^2 = 0.014$ (not shown). The vertical momentum is affected by the presence of cloud shell like other scalar variables, so the use of the fractional dilution rate is more appropriate. The ML model predicts $\dot{w}$ with lower prediction skill compared to ϵ and δ. This result may indicate that large stochasticity acts on vertical acceleration due to the uncertainty caused by the vertical pressure gradient, or the ML model does not work well for predicting $\dot{w}$.

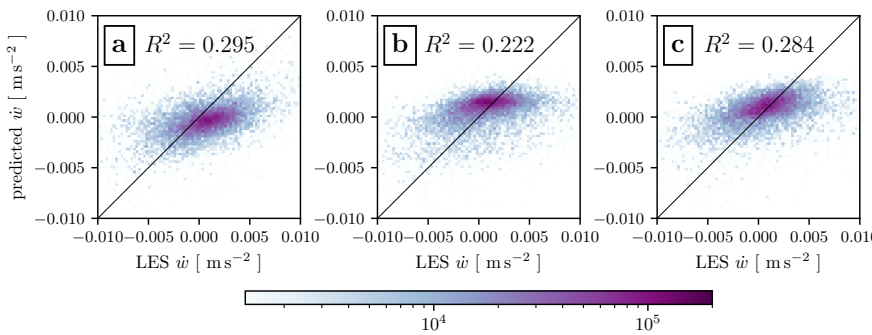

Figure 5.6 Joint probability density functions of LES measured $\dot{w}$ versus predicted $\dot{w}$ by various parameterizations for individual clouds. (a) $\dot{w} = a\hat{B} - b\epsilon_\phi \hat{w}^2$, (b) multiple linear regression model, and (c) machine learning model. a and b are fitting parameters.

The superior performance of neural network is due to its ability to approximate the arbitrary continuous function from multiple inputs (Cybenko 1989). Figure 5.7 shows the relationship between ϵ and six selected input variables for the ML model. $\hat{B}$, $\hat{w}$, $\hat{q}_l$, and $\hat{q}_t'$ are negatively correlated with ϵ, while $\hat{\theta}_c'$ is positively correlated with ϵ. $\partial\overline{\theta_v}/\partial z$ does not show a noticeable relationship with ϵ, which displays the largest permutation importance value (Table 5.1). This suggests that other variables obscure the true strength of the dependence of ϵ on $\partial\overline{\theta_v}/\partial z$. The relationship between input variables and δ is a little more complex than that between input variables and ϵ (Figure 5.8). δ shows non-monotonic responses to $\hat{q}_l$, $\hat{\theta}_c'$, and $\hat{q}_t'$. Here, a strong inverse relationship between $\hat{w}$ and δ is apparent, where $\hat{w}$ explains largest variabilities on δ among other variables. The ML model successfully reproduce the dependency of ϵ and δ on the six input variables throughout the sample space (red lines in Figure 5.7 and Figure 5.8). However, the ML model tends to slightly underestimates ϵ.

5.5 Single-column model simulation results

The new mixing model is tested using the SCM simulations of the BOMEX and RICO cases. We simulate different configurations of SCM listed in Table 5.3 in order to figure out the source of cloud variabilities. ML-FullVar is the default configuration with the machine learning based mixing model, where both the stochastic mixing and stochastic initialization are enabled. ML-MixVar is the same configuration as ML-FullVar, but the stochastic initialization is disabled by setting the initial condition of updrafts as the mean values of the surface PDF. ML-InitVar is the same configuration as ML-FullVar but with the stochastic mixing disabled. The stochastic mixing can be disabled

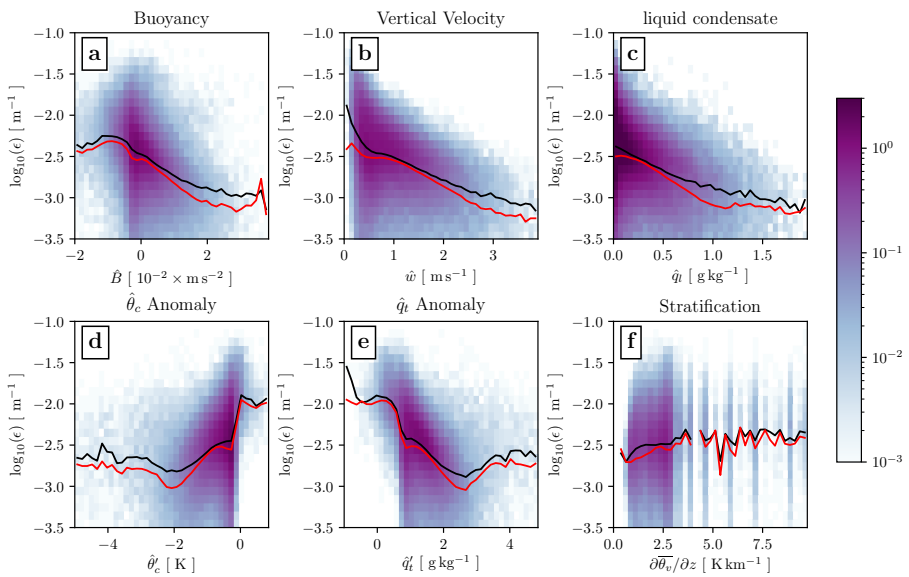

Figure 5.7 Joint probability density functions of LES measured $\log_{10}(\epsilon)$ versus selected six input variables for the ML model for individual clouds. (a) buoyancy, (b) vertical velocity, (c) liquid condensate, (d) $\hat{\theta}_c$ anomaly, (e) $\hat{q}_t$ anomaly, and (f) vertical gradient of environmental virtual potential temperature. Black lines indicate the mean of LES measured $\log_{10}(\epsilon)$ as a function of the x-axis variable, and red lines indicate the mean $\log_{10}(\epsilon)$ predicted by the ML model as a function of the x-axis variable.

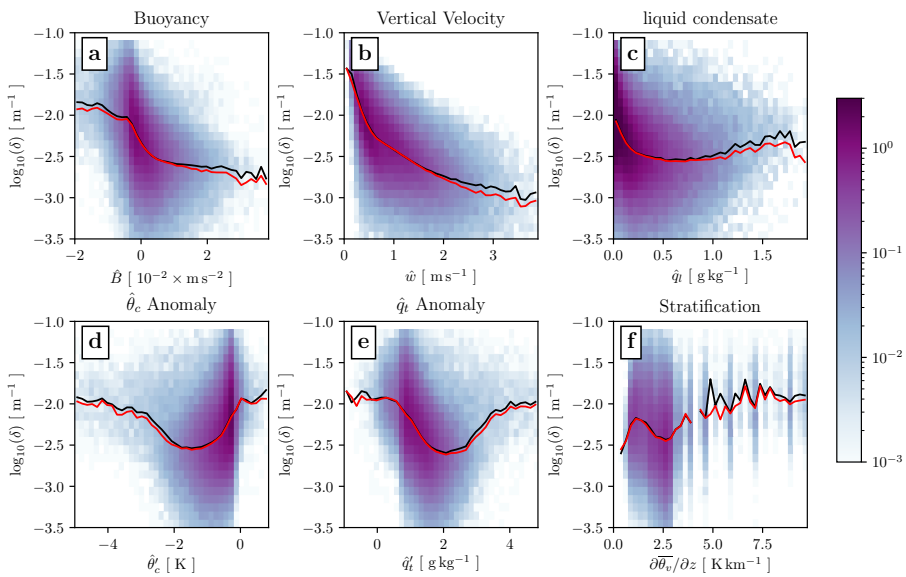

Figure 5.8 Joint probability density functions of LES measured $\log_{10}(\delta)$ versus selected six input variables for the ML model for individual clouds. (a) buoyancy, (b) vertical velocity, (c) liquid condensate, (d) $\hat{\theta}_c$ anomaly, (e) $\hat{q}_t$ anomaly, and (f) vertical gradient of environmental virtual potential temperature. Black lines indicate the mean of LES measured $\log_{10}(\delta)$ as a function of the x-axis variable, and red lines indicate the mean $\log_{10}(\delta)$ predicted by the ML model as a function of the x-axis variable.

Table 5.3 A list of SCM simulation configurations. P14-NoVar is slightly different from the original UNICON, where the fractional updraft area at the surface $\hat{A}_s$ is changed from 0.040 to 0.025, convective downdrafts by mixing are not allowed, and the auto-conversion scheme is replaced by Kogan (2013).

Configuration Name	Mixing Model	Stochastic Mixing	Stochastic Initialization
ML-FullVar	Machine Learninig	On	On
ML-MixVar	Machine Learninig	On	Off
ML-InitVar	Machine Learninig	Off	On
P14-InitVar	Park (2014a)	Off	On
P14-NoVar	Park (2014a)	Off	Off
UNICON	Park (2014a)	Off	Off

by setting the mixing rates as its expected value, $\chi_{i,\mathrm{exp}}$. In addition, we test the mixing model of Park (2014a) with the stochastic initialization on and off. Note that P14-NoVar is slightly different from the original UNICON, where the fractional updraft area at the surface $\hat{A}_s$ is changed from 0.040 to 0.025, convective downdrafts by mixing are not allowed, and the auto-conversion scheme is replaced by Kogan (2013).

5.5.1 Mean vertical profiles

Figure 5.9 shows the simulated vertical profiles of various updraft properties for the BOMEX case. Here, we compare ML-FullVar with the original UNICON to examine the performance of the new mixing model with respect to the existing scheme. UNICON exhibits cold and moist biases in the sub-cloud layer, and warm and dry biases in the cloud layer below 1300 m (Figures 5.9a and 5.9e). ML-FullVar reduces these biases, especially for $\overline{q_t}$. The root-mean-square error (RMSE) of $\overline{\theta_c}$ and $\overline{q_t}$ are reduced by 3% and 34% in ML-FullVar, respectively, compared to UNICON. Based on the fact that the physical tendency of the mean conservative scalar $\overline{\phi}$ due to the multiple updrafts can be expressed as $(\partial\overline{\phi}/\partial t)_{\mathrm{conv}} = -\partial\left[\sum_i \hat{M}^i(\hat{\phi}^i - \overline{\phi})\right]/\partial z$ (i denotes individual updrafts), the reduction of the error can be contributed by more realistic simulation of updraft mass flux and moist conservative scalars within updrafts. ML-FullVar simulates a smooth mass flux profile similar to LES, while UNICON simulates mass flux with a rapid slope change near the height of 1500 m (Figure 5.9h). The rapid decrease of mass flux near the inversion height in UNICON occurs since the bulk plume scheme lacks variation in convection top heights and terminates at a certain height (see Section 4.4). ML-FullVar also simulates realistic $\hat{\theta}_c$ and $\hat{q}_t$ in the cloud layer below 1500 m, where simulated profiles are not much

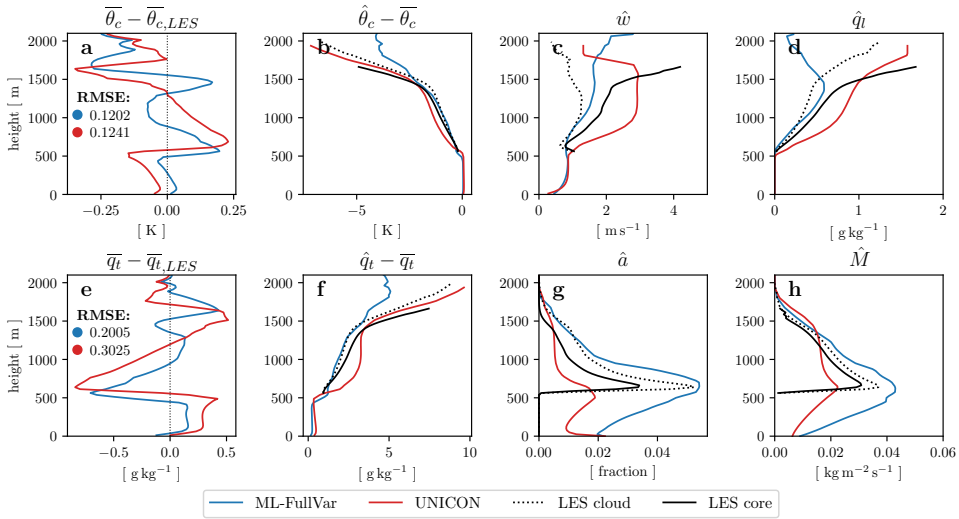

Figure 5.9 Vertical profiles of (a)(e) error of environmental mean moist conserved variables with respect to LES, (b)(f) difference of the moist conserved variables from updrafts with respect to the environmental mean moist conserved variables, (c) updraft vertical velocity, (d) updraft liquid water, (g) updraft fractional area, and (h) updraft fractional mass flux averaged over $t = 4 \sim 6$ h simulated by ML-FullVar and the original UNICON for the BOMEX case. In (a) and (e), root-mean-square errors of $\overline{\theta_c}$ and $\overline{q_t}$ within LES vertical domain are shown.

deviated from LES cloud and core profiles (Figures 5.9b and 5.9f). In contrast, UNICON shows a rapid increase of $\hat{q}_t - \overline{q_t}$ (decrease of $\hat{\theta}_c - \overline{\theta_c}$) in the lower cloud layer, which results in relative θ_c flux divergence (q_t flux convergence) in the lower cloud layer and the excessive dry biases (warm biases). UNICON also suffers from rapid increases of $\hat{w}$ and $\hat{q}_l$ in the lower cloud layer and shows too large values throughout the cloud layer compared to LES. The reason for the rapid increases will be discussed later. For the BOMEX case, the updraft fractional area and the mass flux in ML-FullVar are likely to represent the LES cloud rather than the LES core. However, they can be easily controlled by the surface updraft fractional area $\hat{A}_s$ which is apparently the most important tuning parameter.

The simulated vertical profiles for the RICO case lead to similar discussions as for the BOMEX case (Figure 5.10). For the RICO case, UNICON exhibits excessive warm and dry biases in the cloud layer above 1700 m up to $> 2\,\mathrm{K}$ and $< -2\,\mathrm{g\,kg^{-1}}$, respectively. ML-FullVar greatly reduces the biases, where 59% of RMSE in $\overline{\theta_c}$ and 47% of RMSE in $\overline{q_t}$ are reduced. The large biases in the upper cloud layer in the UNICON simulation are mainly due to the fact that UNICON simulates too small updraft mass flux (Figure 5.10h). The lack of mass flux convergence in the upper cloud layer leads to excessive warm and dry biases. Here again, UNICON exhibits the rapid increases of $\hat{w}$, $\hat{q}_l$, and $\hat{q}_t - \overline{q_t}$ (decrease of $\hat{\theta}_c - \overline{\theta_c}$) in the lower cloud layer, while ML-FullVar shows the smoother and realistic profiles. Notably, the simulated profiles in ML-FullVar are more likely to follow LES core profiles, although the ML model is trained for the non-core region. However, simulated profiles of $\hat{\theta}_c - \overline{\theta_c}$, $\hat{q}_t - \overline{q_t}$ above the inversion height of $\sim$2000 m are largely deviated from the LES core or cloud profiles. For LES, the constraints of $q_l > 0$ and $B > 0$ lead to sampling

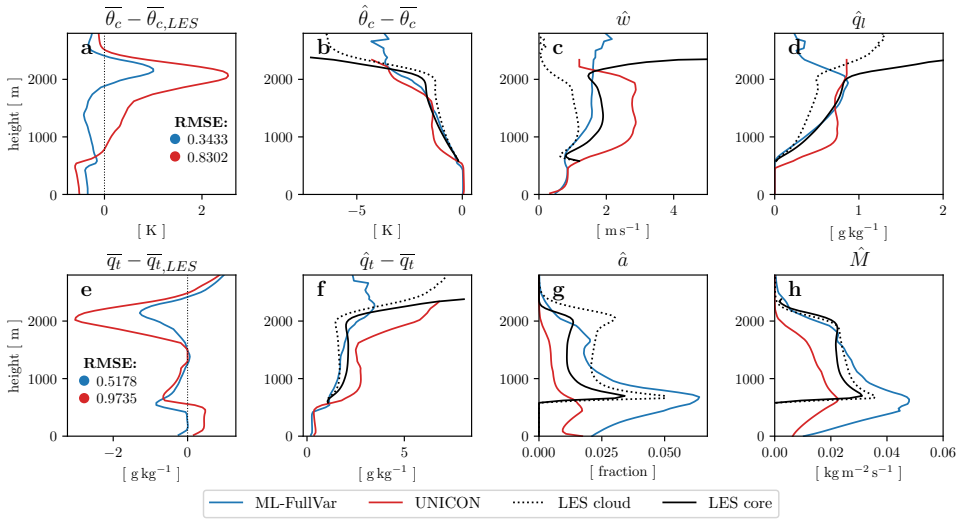

Figure 5.10 Vertical profiles of (a)(e) error of environmental mean moist conserved variables with respect to LES, (b)(f) difference of the moist conserved variables from updrafts with respect to the environmental mean moist conserved variables, (c) updraft vertical velocity, (d) updraft liquid water, (g) updraft fractional area, and (h) updraft fractional mass flux averaged over $t = 20 \sim 24\,\mathrm{h}$ simulated by ML-FullVar and the original UNICON for the RICO case. In (a) and (e), root-mean-square errors of $\overline{\theta_c}$ and $\overline{q_t}$ within LES vertical domain are shown.

of highly undiluted air parcels above the inversion height, characterized as a large magnitude of anomalies. In contrast, negatively buoyant and unsaturated updrafts are included in ML-FullVar, so the magnitude of anomalies is much smaller.

5.5.2 Cloud variabilities

To see how cloud variabilities in the stochastic mixing model are evolved vertically, we draw the normalized mass flux distribution of various variables (Figure 5.11 and Figure 5.12). The normalized mass flux is defined as $\hat{M}\Delta\phi/\sum\hat{M}\Delta\phi$ at each height, where $\Delta\phi$ is a bin of variable ϕ, slightly modifying the method of Romps (2016). Starting with the BOMEX case, Figure 5.11 demonstrates that ML-FullVar and ML-MixVar well reproduce the cloud variance in LES overall. The results of the two simulations are remarkably similar, which implies that the stochastic mixing process is the main source of cloud variabilities. ML-InitVar produces some variance but much smaller compared to LES. The deterministic parameterizations of the entrainment process have proposed a theory that cloud variabilities can be generated by the amplification of cloud-base variabilities (e.g. Neggers et al. (2002)). However, as shown in this analysis, cloud variabilities can be represented correctly only when the randomness in the mixing process is considered.

The variances of two moist conserved variables (first and second rows of Figure 5.11) remain small in the sub-cloud layer. After updrafts penetrated the planetary boundary layer (PBL), the variances start to increase with respect to height. Compared to LES, ML-FullVar and ML-MixVar tend to simulate less diluted updrafts, resulting in means of the moist conserved variables biased away from the environment profiles. The mean and variance of the vertical

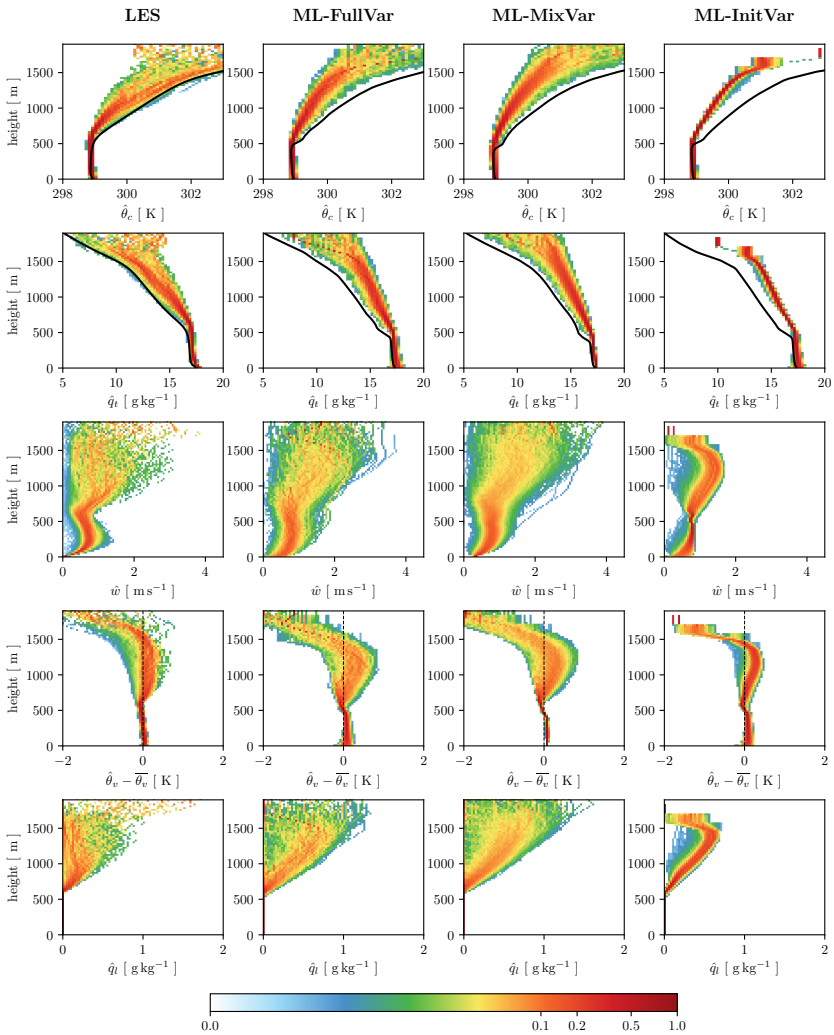

Figure 5.11 Normalized mass flux distributions as functions of various variables simulated by LES, ML-FullVar, ML-MixVar, and ML-InitVar for the BOMEX case. Each row represents $\hat{\theta}_c$, $\hat{q}_t$, $\hat{w}$, $\hat{\theta}_v - \overline{\theta_v}$, and $\hat{q}_l$, respectively. Solid lines denote mean environmental profiles.

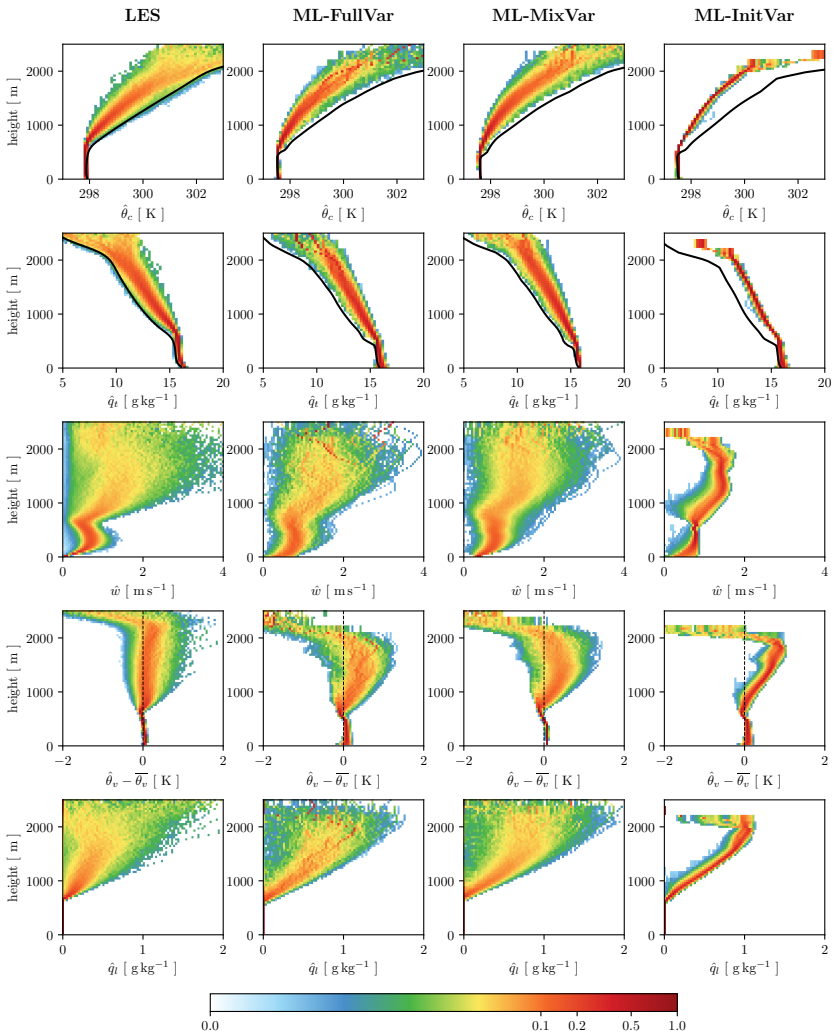

Figure 5.12 Normalized mass flux distributions as functions of various variables simulated by LES, ML-FullVar, ML-MixVar, and ML-InitVar for the RICO case. Each row represents $\hat{\theta}_c$, $\hat{q}_t$, $\hat{w}$, $\hat{\theta}_v - \overline{\theta_v}$, and $\hat{q}_l$, respectively. Solid lines denote mean environmental profiles.

velocity $\hat{w}$ increase in the lower sub-cloud layer, and the mean $\hat{w}$ decreases in the upper sub-cloud layer (third row). The mean and variance of $\hat{w}$ increase above the PBL and are distributed for a wide range of 0–3 $\mathrm{m\,s^{-1}}$, due to the large stochasticity within vertical acceleration (Figure 5.6). A sensitivity simulation with the standard vertical velocity equation ((5.7)) displays a much smaller variance of $\hat{w}$ (not shown). The buoyancy of the updrafts is mostly positive near the surface but becomes negative near the PBL top height (fourth row), which is related to convective inhibition. After the inhibition layer, most of the updraft mass flux become positively buoyant, while some are negatively buoyant. Above 1500 m, almost every updraft becomes negatively buoyant. ML-FullVar and ML-MixVar overestimate the variance of buoyancy in the cloud layer compared to LES. Finally, the variance of liquid water content $\hat{q}_l$ increases within the cloud layer and ranges from 0 to 1.5 $\mathrm{g\,kg^{-1}}$. ML-FullVar and ML-MixVar produce larger $\hat{q}_l$ than LES, but as shown in Figure 5.9d , they tend to represent the core properties rather than the non-core region.

The normalized mass flux distributions in the RICO case show similar results (Figure 5.12). The RICO case shows wider spectra of updraft properties than the BOMEX case, with vertical velocity up to $4\,\mathrm{m\,s^{-1}}$ and liquid water content up to $2\,\mathrm{g\,kg^{-1}}$. ML-FullVar and ML-MixVar simulate these variabilities quite well.

Figure 5.13 shows the Paluch diagrams (scatter plots of two moist conserved variables) at 1000 m simulated by LES and the five SCM configurations in the BOMEX case. The scatters located upper-left are the updrafts that are less diluted and have properties of near surface, and the scatters located lower-right are the updrafts that are highly diluted and have properties of the environment at 1000 m. The LES simulates updrafts with various thermodynamic states,

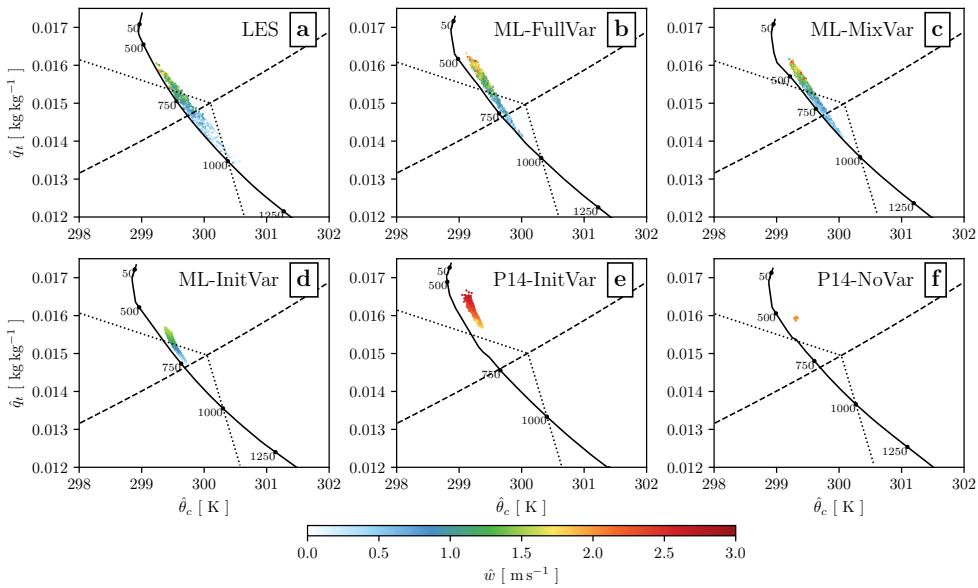

Figure 5.13 The Paluch diagrams of LES and SCM simulations at 1000 m for the BOMEX case. Each point corresponds to a single convective updraft colored by vertical velocity. The solid line corresponds to the mean environmental profile, the dashed line denotes the saturation, and the dotted line denotes the neutral buoyancy. The circles on the mean environmental profile are labeled with the corresponding heights in meters.

where many convective updrafts are negatively buoyant and even unsaturated (Figure 5.13a). However, these negatively buoyant updrafts account for a lower fraction of the total mass flux compared to the positively buoyant updrafts as seen from Figure 5.11, due to their low vertical velocity. The positively buoyant updrafts have vertical velocity up to $2\,\mathrm{m\,s^{-1}}$. ML-FullVar and ML-MixVar produce the spectrum of updrafts similar to LES. They also simulate the negatively buoyant and unsaturated updrafts, but with a much smaller number of unsaturated updrafts. ML-InitVar simulates a narrower spectrum of updrafts compared to LES and does not produce any unsaturated updrafts at this level. P14-InitVar produces a narrow spectrum of less diluted updrafts, with excessively high vertical velocities. While ML-InitVar and P14-InitVar use different mixing models, they produce a similar amount of variabilities by the stochastic initialization of updrafts. The configuration with zero stochasticity, P14-NoVar, shows virtually no variabilities as expected. It appears that the mixing model of Park (2014a) underestimates the dilution of updrafts in the lower cloud layer, which results in the steep increases of vertical velocity and liquid water content.

The Paluch diagrams of the RICO case at 1500 m show wider spectra of updrafts compared to the BOMEX case (Figure 5.14). Here again, ML-FullVar and ML-MixVar well reproduce the updraft spectrum of LES, but the number of unsaturated updrafts is greatly reduced. Our definition of the convective updrafts in LES allows negatively buoyant or unsaturated convection that is decoupled from the mixing layer. Using the classification of Stull (1985), these are passive clouds that are remnants of the old decaying clouds or are formed due to gravity waves. It seems that our mixing model only simulates the active and forced convection which penetrate the convective inhibition layer, even

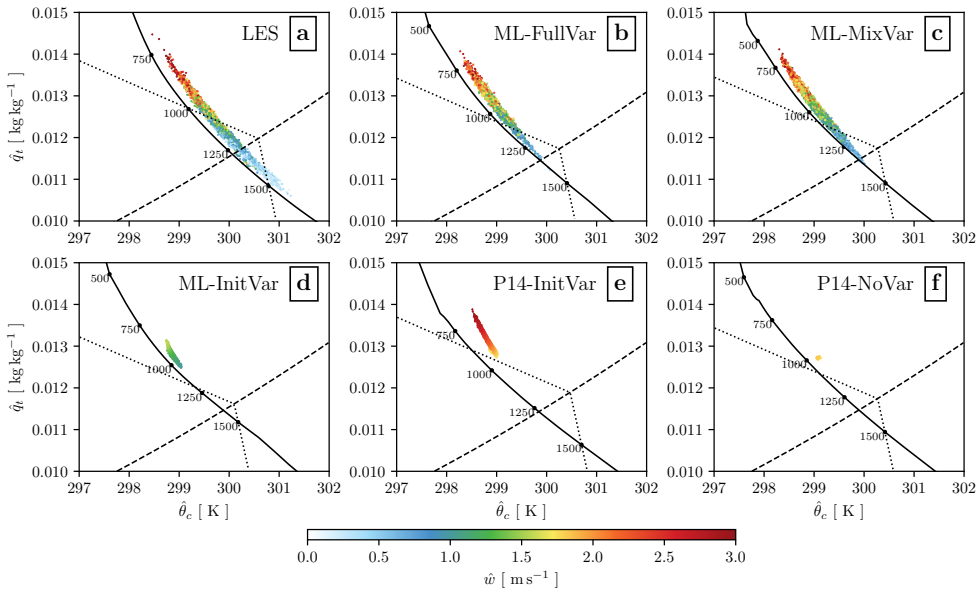

Figure 5.14 The Paluch diagrams of LES and SCM simulations at 1500 m for the RICO case. Each point corresponds to a single convective updraft colored by vertical velocity. The solid line corresponds to the mean environmental profile, the dashed line denotes the saturation, and the dotted line denotes the neutral buoyancy. The circles on the mean environmental profile are labeled with the corresponding heights in meters.

though we trained the ML model for all types of convection. While the impact of passive clouds is small compared to active clouds, passive clouds can be handled explicitly like the stochastic convection scheme of Sakradzija et al. (2015). At least for the active and forced convection, the new mixing model well represents the development of variabilities of various variables from the surface. Not shown in this paper, ML-FullVar and ML-MixVar are capable of realistically simulating the joint PDFs and correlations of other updraft properties as well (e.g. $\hat{w}$ vs $\hat{q}_t$).

Finally, as a measure of the stochasticity in the mixing process, we calculate the correlation profiles between updraft properties at cloud base and any height (Figure 5.15 and Figure 5.16). Here the cloud base is defined as the minimum height at which the total cloud fraction has a local maximum. If the mixing process is a purely deterministic function of cloud properties, then cloud properties will be highly correlated with cloud-base properties. In contrast, if the mixing process is a purely stochastic process, then the upper-level cloud properties will lose correlation with cloud-base properties rapidly. The correlation profiles of the BOMEX LES show exponential decreases of the correlations in the cloud layer for $\hat{\theta}_c$, $\hat{q}_t$, and $\hat{w}$ (Figure 5.15). The correlations of $\hat{\theta}_c$ and $\hat{q}_t$ are smaller than 0.5 at 800 m and approach 0 above 1200 m. In the sub-cloud layer, the correlations are uniform with the values around 0.7 and 0.3 for $\hat{\theta}_c$ and $\hat{q}_t$, respectively. The correlation of $\hat{w}$ shows a relatively slow decrease and saturates at the value around 0.3 in the cloud layer. In the sub-cloud layer, $\hat{w}$ loses correlation exponentially as getting farther from the cloud base and approaches correlation of 0 near the surface. The results of the BOMEX LES are consistent with those of Dawe and Austin (2012).

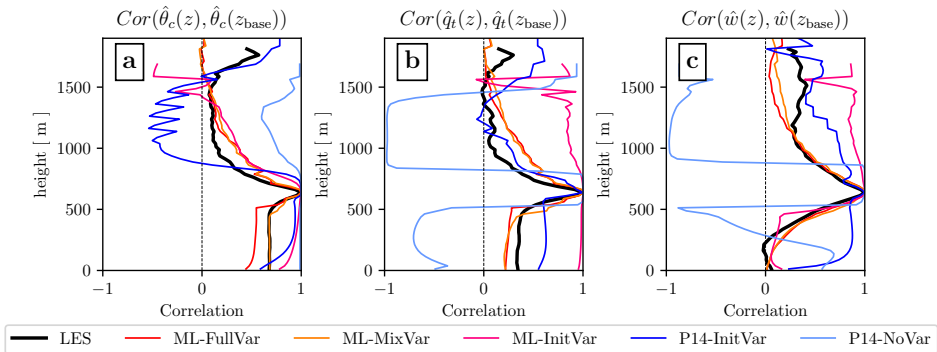

Figure 5.15 Correlation profiles between simulated updraft properties at cloud-base height z_{base} and at any height z for (a) $\hat{\theta}$, (b) $\hat{q}_t$, and (c) $\hat{w}$ in the BOMEX case.

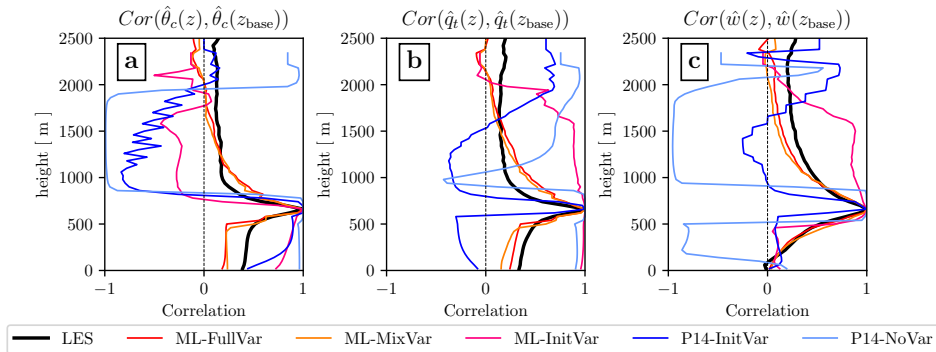

Figure 5.16 Correlation profiles between simulated updraft properties at cloud-base height z_{base} and at any height z for (a) $\hat{\theta}$, (b) $\hat{q}_t$, and (c) $\hat{w}$ in the RICO case.

The correlation profiles of ML-FullVar and ML-MixVar are remarkably similar to LES, with exponential decreases of correlation in the cloud layer. ML-FullVar and ML-MixVar also produce realistic correlation profiles in the sub-cloud layer. One notable deficiency of ML-FullVar and ML-MixVar is that they simulate relatively slow decreases of correlations in the cloud layer for $\hat{\theta}_c$ and $\hat{q}_t$. The correlation profiles of the other SCM configurations are deviated largely from LES profiles and do not display a systematic trend. The largest correlation values are from P14-NoVar, which shows correlations around 1 or -1. The correlations can be changed from 1 to -1 or vice-versa when the ordering of the variable is reversed while updrafts are ascending. The high correlation values represent the lack of stochasticity in P14-NoVar. ML-InitVar and P14-InitVar show smaller correlations compared to P14-NoVar, but the profiles do not resemble the LES profiles.

The results of the RICO case are similar to those of the BOMEX case (Figure 5.16). In the RICO case, correlations of $\hat{\theta}_c$ and $\hat{q}_t$ decrease rapidly below 1000 m and are saturated to the values of 0.1–0.2 in LES. ML-FullVar and ML-MixVar show much slower decreases of the correlations compared to LES.

5.6 Machine learning model dependency on dataset

In order for the proposed method to be used in full GCM simulations, the machine learning model should simulate realistic convection properties under diverse conditions. It is ideal to train the ML model with the convection statistics from various large-scale conditions, ranging from shallow to deep convection regimes. In this study, however, the ML model is trained on only

two marine shallow convection cases. Since the training and the validation is done with the same BOMEX and RICO cases, there is a possibility that the ML model is overfitted to the BOMEX and RICO cases and may not be applicable for other cases. To determine the impact of this issue, we train the ML model on one of the BOMEX/RICO cases and see if the performance degrades when tested on the other case. Here, we consider three datasets for the training and testing: BOMEX+RICO, BOMEX, and RICO.

Table 5.4 summarizes the offline test performance of the ML model when different combinations of the datasets are used for training and testing. In general, the ML model works best when the same dataset is used for training and testing. The ML model trained on the BOMEX+RICO dataset can predict ϵ and δ of all three datasets reasonably well, with R^2 slightly lower than when the same dataset is used for training and testing. The noticeable decreases of R^2 are found when predicting the RICO or BOMEX+RICO dataset with the ML model trained on the BOMEX dataset. This is because the RICO dataset has samples from stronger updrafts compared to the BOMEX dataset. The RICO dataset includes samples with $\hat{B} > 2 \times 10^{-2}\,\mathrm{m\,s^{-2}}$, $\hat{w} > 3\,\mathrm{m\,s^{-1}}$, and $\hat{q}_l > 1\,\mathrm{g\,kg^{-1}}$, which rarely exist in the BOMEX dataset (Figure 5.17).

The SCM experiments with the ML models trained on the different datasets are also tested. Here, ML-FullVar configurations with the ML model trained on BOMEX+RICO, BOMEX, and RICO datasets are referred to as ML[BOMEX+RICO], ML[BOMEX], and ML[RICO], respectively. RMSEs of $\overline{\theta_c}$ and $\overline{q_t}$ from the SCM experiments are summarized in Table 5.5. Among the tested configurations, ML[BOMEX+RICO] has the smallest RMSEs for the BOMEX and RICO cases. It is notable that ML[BOMEX+RICO] shows slightly better performance compared to the case when the training and testing case is the same. In

summary, the offline and SCM tests above suggest that the performance of the ML model is guaranteed when the data range of testing is a subset of the data range of training (data denote the inputs and outputs of the ML model). Considering using the ML model for cases other than BOMEX and RICO, the ML model can be used if updraft statistics for that case are within the ranges of BOMEX and RICO.

5.7 Discussion

Our framework can be extended to deep convection, but there are several aspects to be considered. First, specific humidity of cloud ice is needed to be included as model input. The updraft radius is currently excluded from the model input, but there is some evidence that the updraft radius plays an important role in the development of deep convection (Khairoutdinov et al. 2009). In addition, the production of convective downdraft during the mixing process should be considered.

In recent years, there have been several attempts to replace whole subgrid physics with machine learning based parameterization (Rasp et al. 2018; Yuval and O'Gorman 2020). The method promises great performance, but since machine learning works as a black box, underlying physics is inexplicable. Also, the method is not well generalized in unseen climates when appropriate physical constraints are not applied (Rasp et al. 2018; Beucler et al. 2021). This study can be regarded as an attempt to applying machine learning only for the process that physically based formulation is difficult, which is the mixing of convection. The proposed method can be more resilient to unseen climates since training space is much smaller compared to full ML physics parameterizations.

Table 5.4 Table of R-squared (R^2) between ϵ (δ in parentheses) predicted by the machine learning model and LES measured ϵ (δ) when different combinations of the datasets are used for training and testing.

Training \ Testing	BOMEX+RICO	BOMEX	RICO
BOMEX+RICO	0.655 (0.665)	0.679 (0.637)	0.637 (0.661)
BOMEX	0.583 (0.418)	0.699 (0.706)	0.588 (0.442)
RICO	0.629 (0.648)	0.662 (0.568)	0.655 (0.653)

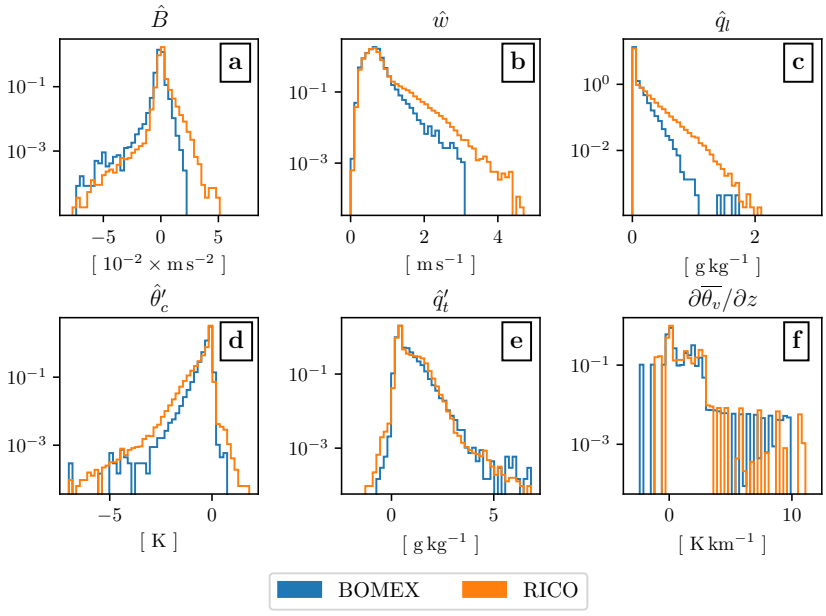

Figure 5.17 Histograms of (a) buoyancy, (b) vertical velocity, (c) liquid condensate, (d) $\hat{\theta}_c$ anomaly, (e) $\hat{q}_t$ anomaly, and (f) vertical gradient of environmental virtual potential temperature for the BOMEX and RICO datasets.

Table 5.5 Root-mean-square errors (RMSEs) of $\overline{\theta_c}$ [K] and $\overline{q_t}$ [$\mathrm{g\,kg^{-1}}$] simulated by ML[BOMEX+RICO], ML[BOMEX], ML[RICO], and the original UNICON for the BOMEX and RICO cases. RMSEs are calculated within the LES vertical domain.

Metrics / Model	BOMEX		RICO	
	$\overline{\theta_c}$ RMSE	$\overline{q_t}$ RMSE	$\overline{\theta_c}$ RMSE	$\overline{q_t}$ RMSE
ML[BOMEX+RICO]	0.1202	0.2005	0.3433	0.5178
ML[BOMEX]	0.1206	0.2283	0.3805	0.5702
ML[RICO]	0.1737	0.3855	0.3961	0.5398
UNICON	0.1241	0.3025	0.8302	0.9735

In addition, mass and energy are conserved since adiabatic processes are still calculated in analytical ways (e.g. phase change of water and radiative heating). It is expected that the neural stochastic differential equation framework used in this study can be applied to other stochastic physics parameterizations.

6 Extending Stochastic UNICON to Deep Convection and Single-Column Model Results

6.1 Introduction

A main issue in convection parameterization is to represent the impact of ensembles of convective clouds within a model grid. A widely used simplification to this problem is the bulk plume approach which considers a single entraining plume. The bulk plume based mass flux schemes have been extensively used in operational atmospheric models due to their computational efficiency (Bechtold et al. 2008; Kain and Fritsch 1990; Tiedtke 1989). However, the bulk plume based mass flux schemes have a limitation on expressing different types of convective clouds since a single plume is used to represent the ensemble mean of multiple convective clouds. Another type of scheme, such as the Arakawa-Schubert scheme (Arakawa and Schubert 1974), considers multiple convective updrafts with different cloud-top heights (Pan and Randall 1998; Zhang and McFarlane 1995a). However, their quasi-equilibrium closures are known to be unsuitable for simulating shallow convection (Yano and Plant 2020). For these reasons, many modelers use separate shallow and deep convection schemes to express the coexistence of shallow and deep convection.

Recently, there have been attempts to develop convection parameterizations that are capable of representing a spectrum of convective clouds without using

separate schemes for different cloud types (Baba 2019; Neggers 2015; Suselj et al. 2019; Yang et al. 2021; Yoshimura et al. 2015). Global simulations with these schemes have shown improvements in both the mean state and variability of the simulated global atmospheric circulation, particularly in the intensity and frequency of the simulated Madden-Julian oscillation (MJO). The spectral representation of convection has been found to contribute to reproducing the moisture supply from shallow convection to sustain organized convection (Baba and Giorgetta 2020; Baba 2021). This supports the importance of shallow convection in preconditioning the lower troposphere for developing the MJO, as investigated in many studies (Cai et al. 2013; Janiga and Zhang 2016). Furthermore, Lawrence and Rasch (2005) showed that spectral representation of convection parameterization can enhance the efficiency of vertical transport of tropospheric tracers.

While several spectral convective parameterizations have been successfully implemented in general circulation models (GCMs), there is still a lack of understanding of how variability between convective clouds is formed. In addition, proper convective closure is required to simulate realistic transitions between different cloud types. Traditional convective closures based on a quasi-equilibrium assumption inevitably lose the memory of the cloud properties between the model time steps. This lack of memory seems to be one reason that conventional diagnostic convection schemes fail to simulate a realistic diurnal cycle of precipitation. This motivates the parameterization of mesoscale organized flow and its impact on convection. Mesoscale organized flow is also important in that it enhances the variabilities of convective clouds. A large-eddy simulation (LES) study of Kurowski et al. (2018) demonstrated that mesoscale organized flow greatly increases cloud variabilities by increasing the

standard deviation of near-surface thermodynamic variables and reducing the entrainment rate of clouds. This implies that the enhanced cloud variabilities in the deep convection regime are generated by multiple physical processes and manifested as a joint distribution of multiple cloud properties.

In this study, we extend stochastic UNICON to deep convection by parameterizing the increased variabilities of convective updraft properties by mesoscale organized flow. The multivariate distribution of thermodynamic variables and updraft radius at the near-surface is parameterized as a function of the strength of mesoscale organized flow. Four free parameters are introduced in the formulation of stochastic UNICON, and they are optimized using single-column model (SCM) simulations at multiple observation sites. It is best practice to optimize unknown model parameters using a number of global model simulations. However, the optimization problems regarding global simulations are complicated because a single evaluation of an objective function is expensive and it is usually hard to calculate the gradient of the objective function, so a number of evaluations are unavoidable (Neelin et al. 2010). Therefore, this study proposes an optimization method using SCM simulations, which are much cheaper to compute, of diverse cloud types, including stratus, stratocumulus, shallow convection, and deep convection. This procedure will provide provisional parameter values for global model simulations. Recently, an increasing number of studies have utilized a single-column model to calibrate the parameters in their parameterizations (Couvreux et al. 2021; De La Chevrotiere et al. 2014; Hourdin et al. 2021; Langhans et al. 2019; Pathak et al. 2021). Hourdin et al. (2021) showed that the optimization of a 3D GCM can be accelerated by reducing parameter space with SCM tuning procedure, and Pathak et al. (2021) demonstrated that the performance of a host GCM

is considerably improved with the model parameters calibrated using an SCM. The performance of stochastic UNICON will be evaluated over the SCM cases, focusing on how the stochastic closure changes the characteristics of simulated convection. Particularly, MJO simulated in the Dynamics of the Madden-Julian Oscillation (DYNAMO) case is analyzed in detail. In addition, the cloud variabilities simulated by stochastic UNICON in a near-equilibrium are evaluated with an idealized tropical convection case.

6.2 Stochastic Unified Convection Scheme for Deep Convection

6.2.1 Thermodynamic Variables

UNICON parameterizes cold pools by solving prognostic equations for the net fractional area (a_{cp}) and the mean conservative scalars of cold pools. The prognostic treatment of cold pools generates convective memory between the model time steps. The cold pools in UNICON are defined as a portion in the planetary boundary layer (PBL) where buoyancy is less than a certain threshold. The inflows and outflows on cold pools are the source and sink of a_{cp}, and the fluxes at cold pool boundaries control the mean properties of cold pools. The main inflow to cold pools is convective downdrafts driven by the evaporation of precipitation (see Section 2d in Park (2014a) for a detailed derivation of the prognostic equations). From the prognosed cold pool properties, perturbations of thermodynamic scalars of a convective updraft driven by the cold pools at the near-surface, $\Delta\phi_{\Omega}$, are calculated at each time step (see Appendix D). The strength of mesoscale organized flow is represented by the mesoscale organization parameter Ω, which is defined as

$$\Omega = \frac{a_{\rm cp}}{1 - \hat{A}_{\rm max}}, \quad 0 \leq \Omega \leq 1 \tag{6.1}$$

where $\hat{A}_{\rm max}$ is the maximum updraft fractional area and specified as 0.1. Ω plays a similar role to *org* parameter from Mapes and Neale (2011) in that it represents the strength of mesoscale organization with a prognosed variable. However, there is a difference in that UNICON also prognoses other thermodynamic properties of mesoscale organized flow and their impact on convective updrafts.

Section 4.2.1 describes a method of constructing a joint PDF of properties of updrafts by non-organized turbulence at the near-surface from the surface-layer similarity theory. The vertical velocity and thermodynamic scalars of convective updrafts at the near-surface are randomly sampled from the multivariate Gaussian distribution, where standard deviations and inter-variable correlations are derived from the surface-layer similarity theory. The standard deviations and correlations are defined in (4.1)-(4.11) (σ_i and r_{ij}, respectively, where $i, j = w, \theta_c, q_t, u, v, \xi$).

As mentioned in the introduction, mesoscale organized flow increases the variances of near-surface thermodynamic variables and greatly enhances cloud variabilities. The increased variances of near-surface thermodynamic variables due to mesoscale organized flow are parameterized by exploiting the cold pool computation in UNICON. We assume that the final joint PDF is multivariate Gaussian where the variance of each thermodynamic variable is summation of variances from non-organized turbulence and mesoscale organized flow. In addition, the variance from mesoscale organized flow is assumed to be proportional to $(\Delta\phi_\Omega)^2$. The total standard deviation of thermodynamic scalar

σ_ϕ^* is parameterized as

$$\sigma_\phi^* = \sqrt{c_1 {\sigma_\phi}^2 + c_2 (\Delta\phi_\Omega)^2}, \tag{6.2}$$

where c_1 and c_2 are tunable parameters. c_1 $(0 < c_1 \leq 1)$ is introduced to describe the effect of reduced variance when small eddies in the lower boundary layer coalesce to form convective updrafts. The final thermodynamic properties of convective updrafts at the near-surface are derived as

$$\hat{\phi} = \sigma_\phi^* \alpha_{\hat{\phi}} + \overline{\phi}_s, \tag{6.3}$$

where $\alpha_{\hat{\phi}}$ is a random sample from a standard multivariate Gaussian with the correlation matrix of r_{ij}, assuming that the correlation matrix is the same as that derived from the similarity theory.

6.2.2 Updraft Radius

The scale break radius R_b sets an approximate upper limit for the possible plume size in a given environment. Although the factors controlling the scale break of convective clouds have not been well studied, it has been reported that cold pools play an important role in increasing the horizontal size of convective clouds. At the boundaries of cold pools, strong convergence due to gust front promotes forced uplifts that are significantly larger than shallow cumulus (Böing et al. 2012). The biggest clouds are formed where multiple cold pools collide (Feng et al. 2015). These updrafts with larger radii are less affected by entrainment and eventually become deeper.

In that sense, we parameterize the scale break radius as a linear function of the mesoscale organization parameter Ω:

$$R_b = R_b|_{\Omega=0} + (R_b|_{\Omega=1} - R_b|_{\Omega=0})\Omega, \tag{6.4}$$

where $R_b|_{\Omega=0}$ and $R_b|_{\Omega=1}$ are R_b at $\Omega = 0$ and $\Omega = 1$, respectively. For simplicity, we assume that correlations between updraft radius and other updraft variables are zero at the near-surface.

6.2.3 Updraft Sampling Method and a Discussion on Updraft Variabilities

In Section 4.2.4, several methods to sample convective updrafts from the joint PDF at the near-surface are proposed. In the proposed methods, an ensemble of updrafts is generated by dividing the joint PDF into a specified number of bins and updrafts are launched with the average values of bins. However, a large number of bins are needed to approximate the true ensemble from the multivariate distribution. Here, "true ensemble" refers to the updraft ensemble in which an infinite number of updrafts are randomly sampled from the joint PDF.

In this study, we use a Monte-Carlo method to sample convective updrafts from the joint PDF. A specified number of updrafts are sampled stochastically from the joint PDF, where the updrafts have equal fractional area. Each sampled updraft has a fractional area of $\hat{a} = \hat{A}_s/n_s$, where $\hat{A}_s$ is the total updraft fractional area at the near-surface and n_s is the number of updrafts to be sampled ($\hat{A}_s = 0.04$ and $n_s = 5$ is used in this study). This method is similar to the sampling strategy used in Sušelj et al. (2013). The sampling method can simulate the ensemble mean of convective tendencies from the true ensemble when averaged for a long time but inevitably generates large stochastic fluctuation with small n_s. The value of $n_s = 5$ is chosen from the SCM simulations of a tropical convection case with varying n_s. The result of the sensitivity test shows that using a larger number of updrafts (more continuous

updraft distribution) reduces the simulated biases and that the simulation results converge at about $n_s > 10$. However, the computational time of the convection scheme increases twofold or more at $n_s = 10$. The value of $n_s = 5$ is chosen as a trade-off between the model performance and computational cost.

Physically speaking, cloud variabilities are formed by two stochastic processes, stochastic initialization (at the near-surface or cloud-base height) and stochastic mixing with the environment (Romps and Kuang 2010). The parameterization of Suselj et al. (2019) is one of the modern stochastic parameterizations built on this physical basis. The scheme uses the near-surface distribution of updrafts and the Poisson distribution of the entrainment rate by assuming that entrainment is a discrete random process. However, previous LES studies have demonstrated that entrainment is highly dependent on cloud and environment properties while it exhibits a considerable amount of stochasticity (Dawe and Austin 2013). The variabilities of updrafts in stochastic UNICON are formed by the evolution of updrafts which are initialized from the near-surface distribution, where the entrainment and detrainment rates are parameterized as complex functions of updraft properties. More specifically, the mixing between an updraft and the environment is inversely proportional to updraft radius $\hat{R}$ and a buoyancy sorting algorithm determines the entrainment and detrainment rates from the mixed air. The mesoscale organized flow increases the variabilities of updrafts and produces deeper convective clouds by initializing larger updrafts which have reduced entrainment rates.

6.3 Validation of the Framework Using LES Datasets

In order to validate the assumptions used in the formulation of stochastic UNICON, a series of radiative-convective equilibrium simulations with different

radiative cooling rates and vertical shear strengths are conducted with the University of California, Los Angeles large-eddy simulation (UCLA-LES) model (Stevens et al. 1999, 2005). Following Cohen and Craig (2006), the radiative forcing is provided as a cooling rate profile, where the cooling rate is constant up to the height of 400 hPa and decreases linearly to 0 between 400 and 200 hPa. A fixed sea surface temperature of 300 K is imposed as a lower boundary condition. For the sheared cases, the mean wind specified in Tompkins (2000) is nudged in a time scale of $\tau = 1$ hr. Four LES configurations with a cooling rate of $-2\,\mathrm{K\,day^{-1}}$ or $-4\,\mathrm{K\,day^{-1}}$ and with or without wind shear are simulated, denoted as DEEP2K-S, DEEP4K-S, DEEP2K, and DEEP4K.

Two-moment mixed-phase microphysics (Seifert and Beheng 2006) is used, and surface fluxes are calculated by a similarity theory, where aerodynamic roughness length is obtained from Charnock's relation. The domain size used is $204.8 \times 204.8 \times 26.4\,\mathrm{km^3}$, with a horizontal resolution of 200 m and a stretched grid system in the vertical (vertical grid size is 50 m below the height of 1200 m and increases with a ratio of 0.6 % above). To achieve an equilibrium state faster, long-term (3 weeks) simulations with quadrupled grid size are preceded, and then three days of high-resolution simulations are initiated with the horizontally averaged profiles at the last time step of the coarser resolution simulations. The model outputs from time intervals of 2 hr during the last 20 hr (10 instantaneous snapshots) are analyzed. An updraft core grid is defined as a grid point that has positive buoyancy, nonzero cloud condensate, and positive vertical velocity, and all consecutive core grids are regarded as the same core. The cold pool air is defined where buoyancy is less then $-0.005\,\mathrm{m\,s^{-2}}$ following Tompkins (2001). The net fractional area of cold pools (a_{cp}) is measured as a fraction of the volume occupied by cold pool air below the PBL height, and the mean

perturbation of ϕ of cold pools ($\Delta\phi_{\rm cp}$) is calculated by averaging the anomalies (deviation from grid-mean value) of cold pool air. The PBL height is determined as a height where vertical buoyancy flux is minimum. In addition to the deep convection cases, the LES of the BOMEX case is included in this analysis, where the setting of the simulation is explained in Section 6.4. The model outputs from time intervals of 1 minute during the last 1 hr (60 instantaneous snapshots) are analyzed for the BOMEX LES.

First, the parameterization of the distribution of thermodynamic variables is evaluated on how well (6.2) explains the standard deviations of updraft properties measured in the LES cases. It is hard to directly measure the statistics of convective updrafts at the near-surface since there is no objective method to define convective updrafts in the subcloud layer. Therefore, we measure the standard deviations of updraft core properties at the cloud-base height ($z_{\rm base}$) as a proxy of updraft variabilities in the subcloud layer. This is based on the LES experiment in Chapter 4. We showed that the variabilities of updrafts do not change much in the subcloud layer, especially for θ_c and q_t, using a Lagrangian particle tracking method. The variance of updraft vertical velocity can increase several times during ascent, but we presume that the increase of the variance at the near-surface will increase the variance at the cloud-base height. While evaluating σ_ϕ^* in (6.2), $\Delta\phi_\Omega$ is computed as a method explained in Appendix D with the cold pool properties measured in the LES cases. The tunable parameters are set to $c_1 = 0.908$ and $c_2 = 0.482$ as optimized in Section 6.5.

Figure 6.1 shows scatter plots of predicted σ_ϕ^* versus measured σ_ϕ of updraft cores at the cloud-base height for $\phi = \theta_c$, q_t, and w. For θ_c and w (Figures 6.1a and 6.1c), five LES cases show linear relationships between the two quantities,

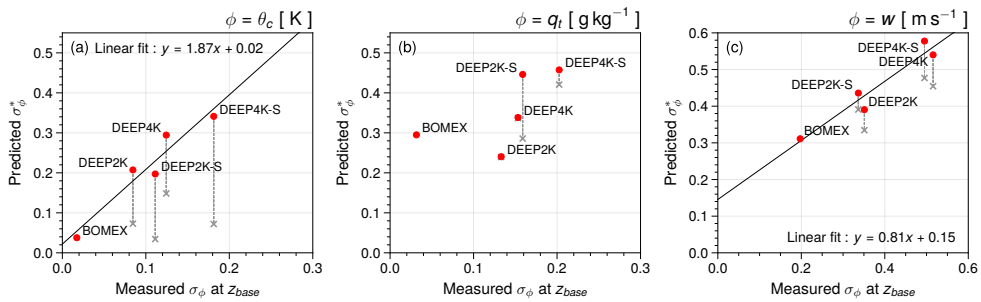

Figure 6.1 Scatter plots of predicted σ^*_ϕ from (6.2) versus measured σ_ϕ of updraft cores at the cloud-base height ($z_{\rm base}$) for (a) $\phi = \theta_c$, (b) $\phi = q_t$, and (c) $\phi = w$ in the five LES cases. The gray cross underneath each red point indicates σ^*_ϕ computed ignoring the effect of mesoscale organization (i.e., $\Delta\phi_\Omega = 0$). In (a) and (c), linear regression lines and formulas are displayed.

justifying the parameterization. The updraft variabilities in the DEEP cases are significantly larger than those of the BOMEX case, and the DEEP cases with higher cooling rates show larger variabilities. Particularly, variabilities of $\phi = \theta_c$ are largely increased by mesoscale organized flow, comparing σ^*_ϕ computed with and without the mesoscale organization effect. This is also confirmed in the distribution of θ_c at the near-surface, where the standard deviations of θ_c are much larger than those predicted by the similarity theory. In contrast to θ_c and w, the data points for $\phi = q_t$ do not show a clear linear relationship (Figure 6.1b). We suspect that this unexpected result is due to the underestimation of the mesoscale organization effect for q_t. Particularly, $\Delta q_{t,\mathrm{cp}}$ in DEEP2K and DEEP4K are measured values close to zero. The difference between the mean q_t of cold pools and the environment is small since q_t at cold pool center regions is lower than the environment and q_t at cold pool boundaries is higher than the environment (not shown). This is closely related to "water vapor rings" in tropical oceanic cold pools (Langhans and Romps 2015). Over the ocean, latent heat flux is enhanced in cold pools due to the high near-surface wind speed by density currents, and then the water vapor is transported to the leading edges of cold pools. New convective clouds are triggered by the lifting of relatively moist air at the cold pool boundaries (Feng et al. 2015; Torri et al. 2015). This complex mechanism is not implemented in the current formulation of UNICON, so the moistening of updrafts by the mesoscale organization might be underestimated.

Next, the parameterization of the distribution of the updraft radius is evaluated. Similar to thermodynamic variables, the radii of updraft cores are measured at the cloud-base height. In Chapter 4, we demonstrated that

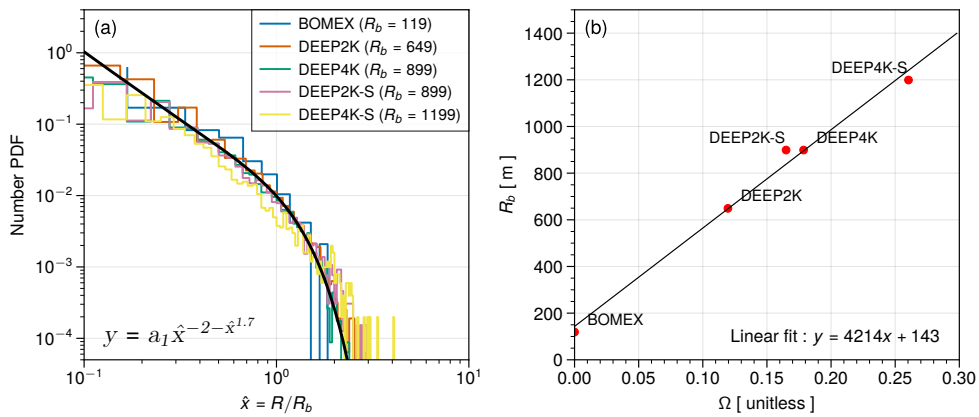

Figure 6.2 (a) Number PDFs of normalized updraft core radius ($\hat{x} = R/R_b$) measured at the cloud-base height in the five LES cases. The black line denotes the parameterization of (4.14). The value of R_b for each case is computed as a non-linear fit to the parameterization in log-log space. (b) Scatter plot of scale break radius R_b versus mesoscale organization parameter Ω measured in the five LES cases and a linear regression line.

the distribution of the updraft core radius in the BOMEX case is well explained by the proposed parameterization of (4.14). Figure 6.2a shows that the distributions of updraft core radius in the DEEP cases also well follow the parameterization with different R_b. Furthermore, a strong linear relationship between R_b and Ω is found (Figure 6.2b), justifying the parameterization of (6.4). A similar discussion can be found in Neggers et al. (2019). They showed that the maximum size of convective clouds is controlled by spatial organization using the LES of a precipitating trade wind cumuli case.

6.4 Single-Column Model Experiment Setup

The single-column model (SCM) used in this study is the single-column version of Community Atmospheric Model version 5 (CAM5). Original UNICON that is identical to the one used by Park et al. (2019) and stochastic UNICON with extension to deep convection are implemented in the model. A series of single-column model simulations are performed for eleven different cases over the ocean listed in Table 6.1 for the optimization of tunable parameters and the evaluation of stochastic UNICON. The listed cases are selected to simulate various cloud types over the ocean. While the development in this study targets deep convection, the cases of shallow convection and stratiform clouds are also included so that the optimization is not biased toward deep convection cases. Land cases are not considered in this study because one of the parameters to be optimized ($R_b|_{\Omega=1}$) is found to be highly dependent on whether the simulation location is land or ocean. Therefore, we focus on the simulation of oceanic convection, which has a greater impact on global circulation. The cases can be categorized into two types: time-varying forcing experiments and idealized experiments.

Table 6.1 A list of single-column model simulation cases. The case length in parenthesis denotes the length of LES experiments. GATE = Global Atmospheric Research Program's Atlantic Tropical Experiment, ARM = Atmospheric Radiation Measurement, CFMIP = Cloud Feedback Model Intercomparison Project, GASS = Global Atmospheric System Studies. The DARWIN case is not included in the optimization cases but is used for independent testing.

Name	Long Name	Lat	Lon	Start Date	Length	Regime	Reference
GATEIII	GATE Phase III	9	336	Aug 1974	20d	Tropical convection	Houze and Betts (1981)
TOGAII	Tropical Ocean Global Atmosphere	-2	154	Dec 1992	21d	Tropical convection	Webster and Lukas (1992)
DYNAMO-AMIE	Dynamics of the Madden-Julian Oscillation	-1	73	Oct 2011	90d	Tropical convection	Yoneyama et al. (2013)
DYNAMO-North	Dynamics of the Madden-Julian Oscillation	3	76	Oct 2011	90d	Tropical convection	Yoneyama et al. (2013)
DARWIN	Darwin ARM Site	-12	131	Nov 2004	120d	Tropical convection	May et al. (2008)
BOMEX	Barbados Ocean and Meteorological Experiment	15	300	Jun 1969	5d (6h)	Shallow convection	Siebesma et al. (2003)
RICO	Rain and Cumulus over Oceans	18	299	Dec 2004	3d (1d)	Shallow convection	Rauber et al. (2007)
CGILSS6	CFMIP-GASS SCM/LES Intercomparison	17	211	Jul 1997	30d (10d)	Shallow cumulus	Zhang et al. (2013)
CGILSS11	CFMIP-GASS SCM/LES Intercomparison	32	231	Jul 1997	30d (10d)	Stratocumulus	Zhang et al. (2013)
CGILSS12	CFMIP-GASS SCM/LES Intercomparison	35	235	Jul 1997	30d (10d)	Stratus	Zhang et al. (2013)
DYCOMSRF01	Dynamics and Chemistry of Marine StratoCu	32	239	Jul 2001	2d (4h)	Stratocumulus	Stevens et al. (2005)

Table 6.2 Settings of idealized SCM simulation cases. N_c is the specified cloud droplet concentration. RICO and CGILS use simple bulk flux schemes for surface flux calculation. The radiation calculation of DYCOMSRF01 (denoted as *) uses the simplified radiation flux model described in Stevens et al. (2005).

Name	Surface flux	Radiation	Geostrophic forcing	Precipitation	N_c [cm^{-3}]
BOMEX	Prescribed	Off	On	Off	-
RICO	Bulk	Off	On	On	70
CGILSS12	Bulk	On	Off	On	100
CGILSS11	Bulk	On	Off	On	100
CGILSS6	Bulk	On	Off	On	100
DYCOMSRF01	Prescribed	On*	On	Off	-

The GATEIII, TOGAII, DYNAMO-AMIE, DYNAMO-North, and DARWIN cases are time-varying forcing experiments that are simulated with time-varying forcing data collected during intensified observation periods (IOP). The simulated profiles and surface precipitation rates of these cases can be directly compared with observations. The total tendencies of temperature T and moisture q in SCM are calculated by adding large-scale advective tendencies and tendencies from physical processes:

$$\frac{\partial T}{\partial t} = \left(\frac{\partial T}{\partial t}\right)_{\text{xyadv}} + \left(\frac{\partial T}{\partial t}\right)_{\text{zadv}} + \left(\frac{\partial T}{\partial t}\right)_{\text{phys}}, \tag{6.5}$$

$$\frac{\partial q}{\partial t} = \left(\frac{\partial q}{\partial t}\right)_{\text{xyadv}} + \left(\frac{\partial q}{\partial t}\right)_{\text{zadv}} + \left(\frac{\partial q}{\partial t}\right)_{\text{phys}}. \tag{6.6}$$

Here, the large-scale advective tendencies are given as

$$\left(\frac{\partial T}{\partial t}\right)_{\text{xyadv}} = -\mathbf{V}\cdot\nabla T, \quad \left(\frac{\partial T}{\partial t}\right)_{\text{zadv}} = -\omega\frac{\partial T}{\partial p} + \frac{\omega}{c_p}\alpha, \tag{6.7}$$

$$\left(\frac{\partial q}{\partial t}\right)_{\text{xyadv}} = -\mathbf{V}\cdot\nabla q, \quad \left(\frac{\partial q}{\partial t}\right)_{\text{zadv}} = -\omega\frac{\partial q}{\partial p}, \tag{6.8}$$

where $\mathbf{V}$ is the horizontal wind vector, ω is the vertical pressure velocity, and $\alpha = 1/\rho_{air}$ is the specific volume of air. The horizontal advective tendencies ($-\mathbf{V}\cdot\nabla T$, $-\mathbf{V}\cdot\nabla q$) are prescribed, while the vertical advective tendencies are calculated from prescribed ω and model simulated vertical gradients. To compute the vertical advection from ω, we use a downstream Eulerian difference for temperature and a semi-Lagrangian method for water substances and the other tracers. Sea surface temperature is prescribed so that the surface scheme in CAM5 calculates the surface fluxes. In addition, the observed profiles of horizontal winds are prescribed. The time-varying forcing experiments are conducted with 30 vertical levels and a model time step of $\Delta t = 1200\,\text{s}$. The DARWIN case originally spans more than five months, from November 3, 2004

to April 29, 2005. However, the forcing for this site is not continuous and broken into 11 segments, so we choose the longest continuous segment.

The BOMEX, RICO, CGILSS12, CGILSS11, CGILSS6, and DYCOMSRF01 cases are idealized experiments that produce near-equilibrium states with idealized (or time-averaged) forcings. These cases are designed to conduct LES intercomparison experiments in controlled environments. For these cases, we simulate the SCM with the same settings and forcings as the LES to compare with the LES results. The settings of the cases are summarized in Table 6.2, and detailed settings are available in their companion LES intercomparison studies (BOMEX : Siebesma et al. (2003); RICO : vanZanten et al. (2011); CGILS : Blossey et al. (2013), DYCOMSRF01 : Stevens et al. (2005)). In BOMEX and RICO, radiation schemes are disabled; instead, radiative cooling tendencies are specified. The cloud droplet concentration is specified for RICO, but it does not affect the SCM simulation because UNICON uses simple single moment microphysics. The idealized experiments are conducted with 80 vertical levels and a model time step of $\Delta t = 300\,\mathrm{s}$. More vertical levels (80 levels) are used compared to time-varying forcing experiments (30 levels) since turbulence and clouds are concentrated in the lower troposphere.

For the idealized experiments, LES model outputs are considered observations. We use publicly available LES model outputs of LES intercomparison studies for the DYCOMSRF01 (12 models) and CGILS (6 models) cases. For the BOMEX and RICO cases, we simulate those with UCLA-LES with the settings of Siebesma et al. (2003) and vanZanten et al. (2011), respectively. The only difference with these intercomparison studies is that we use smaller grid sizes of $25 \times 25 \times 25\,\mathrm{m}^3$ and $40 \times 40 \times 40\,\mathrm{m}^3$ for the BOMEX and RICO

cases, respectively (domain sizes are $6.4 \times 6.4 \times 3.0\,\mathrm{km}^3$ and $12.8 \times 12.8 \times 4.0\,\mathrm{km}^3$, respectively).

6.5 Optimization

6.5.1 Optimization Strategy

Undetermined parameters in stochastic UNICON are optimized using multiple SCM cases to increase the accuracy of simulations under various large-scale environments. Ten SCM cases, except the DARWIN case, are used for the optimization, while the DARWIN case is used for an independent test. The relatively long observation period of the DARWIN case (120 days) provides sufficient time length for the independent test. The following four parameters of stochastic UNICON are subject to optimization: $R_b|_{\Omega=0}$, $R_b|_{\Omega=1}$, c_1, and c_2. We choose moist static energy (MSE $= c_pT + gz + L_vq_v$, where g is the gravitational acceleration and q_v is the water vapor specific humidity) and surface precipitation rate to measure model performance. The moist static energy is chosen because it contains information about both temperature and moisture and is a good diagnostic variable for convective transport. The standard approach to dealing with optimization problems that involve multiple cases or variables is multiobjective optimization (Deb 2014; Neelin et al. 2010). In multiobjective optimization, objective functions of different variables are lumped into a single weighted cost function. Typically, the weighted cost function is defined as $J = \sum_k w_k f_k$, where w_k is the weight and f_k is the objective function such as the square error or root-mean-squared error (RMSE). The selection of w_k is arbitrary because it depends on how a particular user evaluates accuracy in certain cases or certain variables.

Using the multiobjective approach, we define the cost function for our optimization problem as

$$J = \frac{1}{N_{case}} \sum_{k=1}^{N_{case}} \left[\frac{1}{2} \cdot \mathrm{RMSE}^*(\mathrm{MSE}_k) + \frac{1}{2} \cdot \mathrm{RMSE}^*(\mathrm{PREC}_k) \right], \tag{6.9}$$

$$\mathrm{RMSE}^*(\phi_k) = \frac{\mathrm{RMSE}(\phi_{k,\mathrm{UNICON-STO}})}{\mathrm{RMSE}(\phi_{k,\mathrm{UNICON}})}, \tag{6.10}$$

where $N_{case} = 10$ is the number of SCM cases, MSE_k and PREC_k are the moist static energy and surface precipitation rate of each case, respectively, and RMSE^* is the relative RMSE where the RMSE of stochastic UNICON is divided by the RMSE of original UNICON.

Before calculating the RMSE of moist static energy, simulated moist static energy is interpolated into the vertical levels of observations (IOP observations for the time-varying forcing cases and LES for the idealized cases). Precipitation rates are 12-hour running averaged to remove high-frequency noise due to the Monte-Carlo sampling method of stochastic UNICON. Finally, RMSEs are calculated using all time steps and entire vertical levels during the case period. We calculate the RMSEs of precipitation rates only for the time-varying forcing cases. The idealized cases are boundary-layer cloud cases which produce significantly lower precipitation rates than deep convection cases. Also, the LES intercomparison results of RICO and CGILS (only CGILSS6 produces non-negligible precipitation) show very different precipitation rates among LES models (Blossey et al. 2013; vanZanten et al. 2011). For these reasons, $\mathrm{RMSE}^*(\mathrm{PREC}_k)$ is set to 1 for the idealized SCM cases.

We use Bayesian optimization method to search a global minimum of cost function J. Bayesian optimization is suitable when the objective function $f(x)$ (where x is a vector of parameters) is expensive to evaluate and the gradient of

$f(x)$ is unavailable, so an optimization based on gradient descent is not feasible. The Bayesian optimization also tolerates stochastic noise in $f(x)$ and quantifies the uncertainty. The Bayesian optimization consists of a surrogate model and an acquisition function. The surrogate model estimates the distribution of the function $f(x)$ based on the previously evaluated points ((x_1, $f(x_1)$), (x_2, $f(x_2)$), ..., (x_n, $f(x_n)$)) using Gaussian process regression (Rasmussen 2003). The acquisition function suggests next evaluation point that minimizes the function $f(x)$ based on the results of the surrogate model. The process is repeated for a fixed number of iterations, and evaluation points consequently approach to global minimum of $f(x)$.

The search space for the parameters is set as $R_b|_{\Omega=0}$=[50, 500], $R_b|_{\Omega=1}$=[1000, 5000], c_1=[0.1, 1.0], and c_2=[0.1, 1.5]. The search space is determined sufficiently broadly in consideration of physically possible range of each parameter. Before optimization, we evaluate 200 initial points selected by Latin hypercube sampling (Mckay et al. 1979) in the search space. Finally, the Bayesian optimization is conducted with 800 iterations, using expected improvement (Jones et al. 1998) as the acquisition function. The optimized value x_{opt} is defined where the posterior mean of the Gaussian process is minimum because our cost function J includes a substantial amount of stochasticity. The optimization is done with a python Bayesian optimization library, GPyOpt (González et al. 2016).

6.5.2 Optimization Results

The optimized values of the parameters x_{opt} are $R_b|_{\Omega=0} = 108\,\mathrm{m}$, $R_b|_{\Omega=1} = 2190\,\mathrm{m}$, $c_1 = 0.908$, and $c_2 = 0.482$ (Table 6.3). After about 400 iterations, the result of the optimization is converged. The first row of Figure 6.3 shows all

Table 6.3 Optimized parameters in stochastic UNICON

Parameter	Search range	Optimized value	Description
$R_b\|_{\Omega=0}$	50-500	108 m	Scale break radius at the near-surface at $\Omega = 0$ [(6.4)]
$R_b\|_{\Omega=1}$	1000-5000	2190 m	Scale break radius at the near-surface at $\Omega = 1$ [(6.4)]
c_1	0.1-1.0	0.908	Scaling factor for variance from non-organized turbulence [(6.2)]
c_2	0.1-1.5	0.482	Scaling factor for variance from mesoscale organized flow [(6.2)]

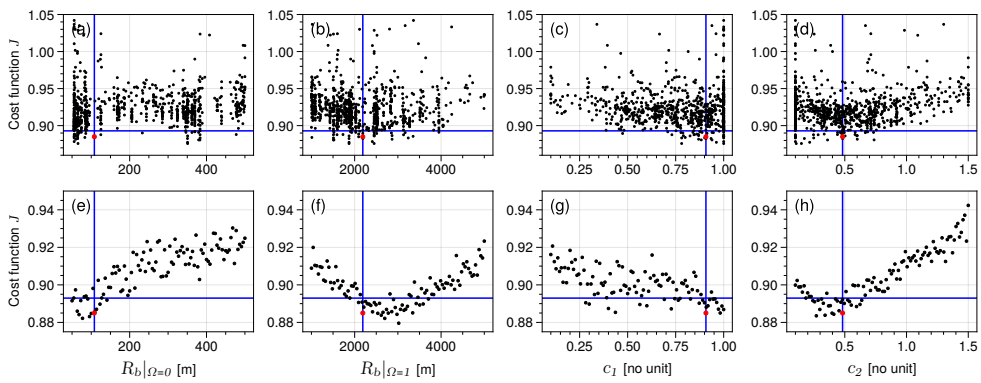

Figure 6.3 (a-d) Scatter plots of the evaluation points during the Bayesian optimization. (e-h) Scatter plots of the evaluation points of the single-parameter sensitivity test, which varies a single parameter while fixing other parameters as the optimized values. Vertical blue lines denote the optimized parameters x_{opt} where the posterior mean of the Gaussian process is minimum. Horizontal blue lines denote the minimum value of the posterior mean at x_{opt} ($J = 0.893$). Red dots denote the cost function evaluated at x_{opt} ($J = 0.885$).

evaluation points during the Bayesian optimization. Some of the evaluation points have cost functions greater than 1, where stochastic UNICON performs worse than original UNICON. Most evaluation points have cost functions smaller than 0.95. The posterior mean of the Gaussian process at x_{opt} is measured as 0.893, and the cost function evaluated at x_{opt} is 0.885.

We can roughly see parameter sensitivity from each of Figure 6.3a-d (i.e., smaller cost functions near the optimized value), but it is not clear since the evaluation points in the 4-dimension parameter space are projected to single parameter space. In order to visualize the parameter sensitivity, a single-parameter sensitivity test is conducted. The test varies a single parameter while fixing other parameters as the optimized values. For each parameter, 100 points equally spaced within the search space of the parameter are evaluated. The sensitivity test shows that all four parameters have considerable impacts on the performance of stochastic UNICON (second row of Figure 6.3). Roughly, the Bayesian optimization seems to approach true optimum. However, in the case of $R_b|_{\Omega=1}$, smallest cost functions are observed near 3000 m. This value is larger than the optimized value (Figure 6.3f). The Bayesian optimization can underperform when the noise level is high in objective functions (Letham et al. 2019). One possible solution is to perform multiple ensemble simulations for each case to reduce variance in the cost function.

Table 6.4 summarizes the relative RMSEs of moist static energy and surface precipitation rate simulated by stochastic UNICON with the optimized parameters. Optimized stochastic UNICON outperforms original UNICON in most cases. The improvement is apparent for the thermodynamic profiles of tropical convection cases, where RMSEs in moist static energy are reduced by 21-45 %. The precipitation rates are also significantly improved in stochastic UNICON

Table 6.4 Relative RMSEs (RMSE(UNICON-STO)/RMSE(UNICON)) of moist static energy and surface precipitation rate simulated by (first row) new stochastic UNICON and (second row) the previous version of stochastic UNICON in Section 4 with the optimized parameters for the SCM cases.

		TOGAII	GATEIII	DYNAMO-AMIE	DYNAMO-North	DARWIN	BOMEX	RICO	CGILSS6	CGILSS11	CGILSS12	DYCOMSRF01
UNICON-STO (new)	MSE	0.780	0.788	0.547	0.588	0.759	0.718	0.971	0.957	0.981	0.959	1.000
	PREC	0.869	1.003	0.789	0.748	0.699	-	-	-	-	-	-
UNICON-STO (old)	MSE	1.008	0.954	0.650	0.773	0.893	0.718	0.976	0.957	0.981	0.959	1.000
	PREC	0.882	0.957	0.746	0.725	0.757	-	-	-	-	-	-

except in the GATEIII case. For the idealized cases, the significant reduction of RMSE is only notable in the BOMEX case. The performances of original UNICON and stochastic UNICON are almost identical for the DYCOMSRF01 case. The detailed single-column simulation results of optimized stochastic UNICON are described in Section 6.6.

In addition to new stochastic UNICON, RMSEs of the previous version of stochastic UNICON in Section 4 (old stochastic UNICON hereinafter) are evaluated (second row of Table 6.4). Old stochastic UNICON is developed for shallow convection, so there is a conceptual inconsistency in simulating deep convection that the impact of non-organized turbulence is treated stochastically, but the impact of the mesoscale organization is treated deterministically (i.e., the same mesoscale perturbations are added to convective updrafts). We applied the scale break radius parameterization of (6.4) for old stochastic UNICON; otherwise, deep convection would not be generated. For consistency, the optimized values in Table 6.3 are also used for old stochastic UNICON, except c_2 which is not available in old stochastic UNICON. Old stochastic UNICON is exactly the same as new stochastic UNICON when the mesoscale organization is absent, so the simulation results of the two schemes are identical for the idealized cases other than RICO. The RMSEs of the RICO case show only a slight difference between the two schemes due to weak mesoscale organization. For the tropical convection cases, old stochastic UNICON shows consistently higher RMSEs of moist static energy compared to new stochastic UNICON, showing performances in between original UNICON and new stochastic UNICON. Interestingly, RMSEs of precipitation rates of old stochastic UNICON are similar to those of new stochastic UNICON. We are not sure about the reason for this, but we anticipate that old and new stochastic UNICONs have a

similar mechanism on vertical moisture transport by shallow convection, which is important for precipitation. The result suggests that both the stochastic impacts of non-organized turbulence and mesoscale organization contribute to the performance improvement in stochastic UNICON.

6.6 Single-Column Model Simulation Results

6.6.1 Time-varying Forcing Experiments

Table 6.5 summarizes the RMSEs of temperature, specific humidity, moist static energy, and precipitation simulated by UNICON and stochastic UNICON for the time-varying forcing SCM cases. Stochastic UNICON displays consistently lower RMSEs than UNICON for all variables except precipitation in the GATE case. The reduction of RMSEs of moist static energy by stochastic UNICON is both contributed by the decrease in RMSEs of temperature and specific humidity. Vertical profiles of the simulated biases in these SCM cases (Figures 6.4-6.6) demonstrate that stochastic UNICON reduces the persistent biases in UNICON, which is characterized by negative temperature bias in the upper troposphere and dry bias in the lower troposphere. The DARWIN case, which is not included in the optimization, also shows considerable performance improvement by stochastic UNICON with optimized parameters (Figure 6.6). The result suggests that the parameters are less likely to be overfitted to the cases subject to optimization. To get more insights into the characteristics of the simulation of stochastic UNICON, we will discuss in detail the simulation results of the TOGAII and DYNAMO-AMIE cases.

The TOGAII case's IOP took place in the western Pacific warm pool region, and the SCM simulation results of 21 days starting from 18 December

Table 6.5 RMSEs (in the form of RMSE(UNICON-STO)/RMSE(UNICON)) of temperature, specific humidity, moist static energy, and surface precipitation rate simulated by stochastic UNICON and original UNICON for the time-varying forcing SCM cases. The rate of change in RMSE is denoted in parenthesis.

	TOGAII	GATEIII	DYNAMO-AMIE	DYNAMO-North	DARWIN
T (K)	2.409 / 2.770 (−13.0 %)	1.645 / 1.794 (−8.3 %)	2.646 / 3.492 (−24.2 %)	3.203 / 4.408 (−27.3 %)	3.191 / 3.659 (−12.8 %)
q ($\mathrm{g\,kg^{-1}}$)	0.574 / 0.785 (−26.9 %)	0.455 / 0.767 (−40.6 %)	0.623 / 1.316 (−52.7 %)	0.928 / 1.726 (−46.2 %)	1.101 / 1.818 (−39.4 %)
MSE (kJ)	3.094 / 3.969 (−22.0 %)	2.131 / 2.706 (−21.2 %)	3.099 / 5.666 (−45.3 %)	4.541 / 7.727 (−41.2 %)	4.076 / 5.366 (−24.1 %)
PREC ($\mathrm{mm\,day^{-1}}$)	3.870 / 4.452 (−13.1 %)	4.768 / 4.754 (0.3 %)	3.378 / 4.281 (−21.1 %)	3.090 / 4.131 (−25.2 %)	4.344 / 6.216 (−30.1 %)

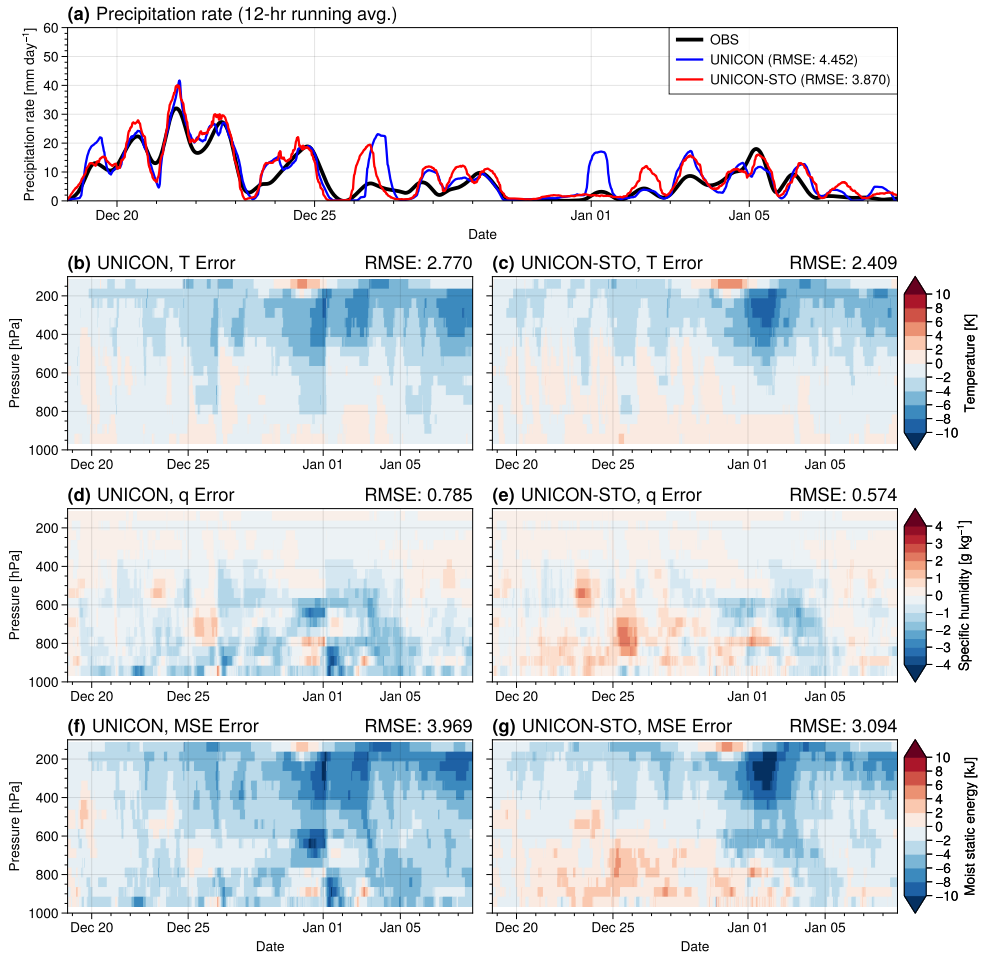

Figure 6.4 (a) Time series of surface precipitation rates from IOP observation and UNICON and UNICON-STO simulations in the TOGAII case. The time series are smoothed with 12-hour running averages. (b)-(g) Errors of temperature, specific humidity, and moist static energy simulated by UNICON and UNICON-STO, with respect to observation, in the TOGAII case. Root mean squared errors are given at the upper right of each plot.

1992 are shown in Figure 6.4. Two groups of rainfall events are observed during 18-29 December and 1-7 January (Figure 6.4a). Most of the rainfall during these periods is from mesoscale convective system (MCS) scale squall lines (Rickenbach and Rutledge 1998). The first group of rainfall events is associated with a prominent MJO event, which started in early December and decayed during the end of December (Lin and Johnson 1996). Both UNICON and stochastic UNICON skillfully predict approximate variations of observed precipitation rates. However, UNICON overestimated the intensities of rainfall peaks on 19 December, 26 December, and 1 January, which increases the RMSE of UNICON. The negative temperature biases above 500 hPa level in UNICON are reduced in stochastic UNICON. However, stochastic UNICON shows a stronger negative temperature bias centered at 300 hPa level on 2 January. The negative temperature bias is due to the lack of heat source during the very end of December. This period is a decaying period of the MJO when the fraction of stratiform precipitation from anvil clouds is high (Johnson et al. 2016). Johnson et al. (2016) showed that the apparent heat source (Q_1) in the upper troposphere is highest when the fraction of stratiform precipitation is high, using radar data during TOGA. The intense heating effect of anvil stratiform precipitation is due to its large cover and association with the freezing of hydrometeors (0 °C level is about 650 hPa level). UNICON produces strong convection on 1 January, which reduces the negative temperature bias in the upper troposphere, but it seems unrealistic, as seen from the overestimated rain peak on 1 January. These results suggest that UNICON and stochastic UNICON do not realistically simulate anvil clouds and their impacts with the current formulation. The negative humidity bias of original UNICON is reduced in stochastic UNICON, but the relatively weak positive humidity bias

is produced in stochastic UNICON during December. The negative moist static energy bias is reduced in stochastic UNICON, with positive biases in the lower troposphere and negative biases in the upper troposphere.

The DYNAMO-AMIE case is part of the Dynamics of the Madden-Julian Oscillation (DYNAMO) field campaign and the ARM Madden-Julian Oscillation Investigation Experiment (AMIE) field campaign, where the forcing data were collected from Gan island on Addu Atoll for 90 days beginning on 1 October 2011 (Figure 6.5). This case shows the lifecycles of the MJO and the associated developing and decaying of convective systems over the Indian Ocean. During DYNAMO-AMIE, three large-scale convective events (LCEs) are observed, which are referred to as LCE1, LCE2, and LCE3 following Powell and Houze Jr. (2013). LCE1 and LCE2 are associated with robust MJO events, and multiple large MCSs were observed by the radar system on Addu Atoll during these periods (Powell and Houze Jr. 2013). LCE3 is associated with a less prominent MJO event, and an isolated MCS and several squall lines were observed during the period. The MJO phase calculated by the method of Wheeler and Hendon (2004) provides a broad-scale view of the phase of convection activity over the tropical Indo-Pacific (Figure 6.5a). At the DYNAMO-AMIE location, phases 8-3 correspond to active convection MJO phases and phases 4-7 are inactive MJO phases. The precipitation enhancements during LCE1 and LCE2 are consistent with active MJO phases. However, the LCE3 period corresponds to phases 4 and 5 which are inactive MJO phases. The detailed analysis of the simulations depending on MJO phases will be discussed in Section 6.6.2.

Stochastic UNICON shows the RMSE of simulated precipitation that is 21 % less than UNICON. UNICON produces a number of rain peaks with erro-

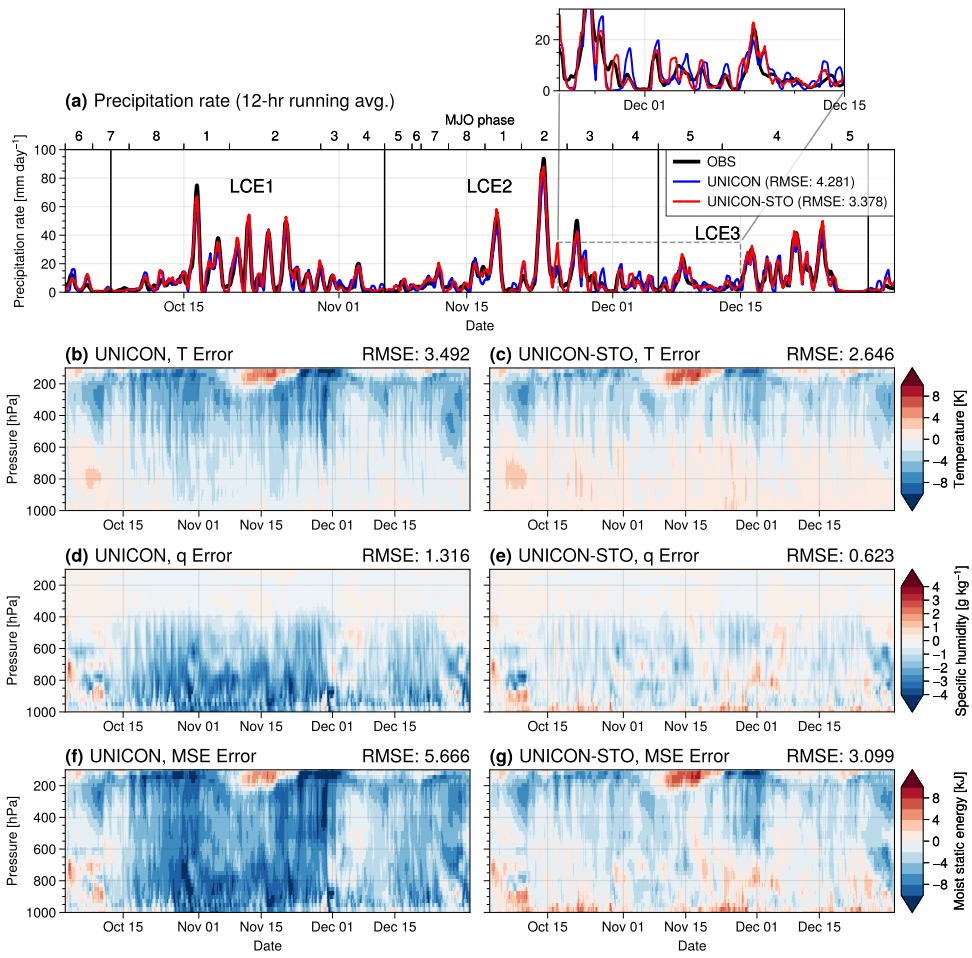

Figure 6.5 (a) Time series of surface precipitation rates from IOP observation and UNICON and UNICON-STO simulations in the DYNAMO-AMIE case. The time series are smoothed with 12-hour running averages. Wheeler and Hendon (2004) MJO phases are denoted along the top axis. Durations of three large-scale convective events (LCEs) are denoted with black vertical lines. (b)-(g) Errors of temperature, specific humidity, and moist static energy simulated by UNICON and UNICON-STO, with respect to observation, in the DYNAMO-AMIE case. Root mean squared errors are given at the upper right of each plot.

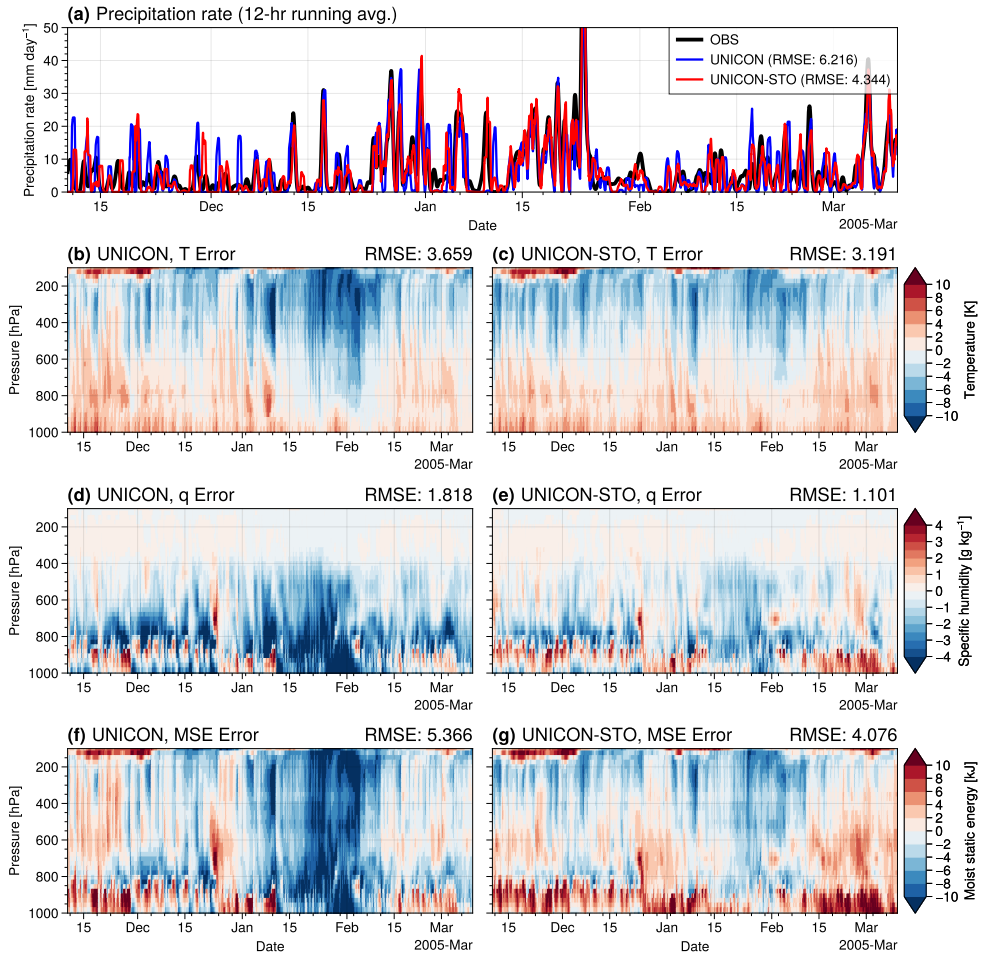

Figure 6.6 (a) Time series of surface precipitation rates from IOP observation and UNICON and UNICON-STO simulations in the DARWIN case. The time series are smoothed with 12-hour running averages. (b)-(g) Errors of temperature, specific humidity, and moist static energy simulated by UNICON and UNICON-STO, with respect to observation, in the DARWIN case. Root mean squared errors are given at the upper right of each plot.

neously estimated intensity, especially during the decaying stage of MJO events (Figure 6.5a). The overestimated rain peaks are produced from late November to early December (the last part of LCE2). UNICON displays continuous strong negative temperature biases in the upper troposphere, and the bias is strongest during this period (Figure 6.5b). Due to the bias, UNICON produces unrealistically strong convection to stabilize the atmosphere, as in the TOGAII case. UNICON also shows negative humidity and moist static energy biases. Stochastic UNICON significantly reduces the temperature, humidity, and moist static energy biases. Still, stochastic UNICON displays a negative upper-level temperature bias, especially during the MJO decaying periods, implying that the diabatic heating from anvil clouds and stratiform precipitation system is underestimated.

To better understand the simulation results, time-averaged vertical profiles of convective mass fluxes and tendencies due to convection and planetary boundary layer (PBL) schemes are drawn (Figure 6.7). The plotted tendencies include tendencies from turbulent mixing and convection microphysics but do not include tendencies from stratiform microphysics and radiation. Among the five cases, stochastic UNICON produces stronger updraft mass fluxes below 500 hPa level and slightly weaker mass fluxes at upper levels, compared to UNICON. This is because stochastic UNICON launches a spectrum of multiple updrafts, so less buoyant updrafts are detrained into the environment at lower levels. The downdraft mass flux in stochastic UNICON is also larger at lower levels since downdrafts are generated from negatively buoyant detrained air.

Stochastic UNICON shows higher heating tendencies by convection compared to UNICON, considering that the tendencies due to the PBL scheme are limited in the boundary layer (second row of Figure 6.7). This enhanced

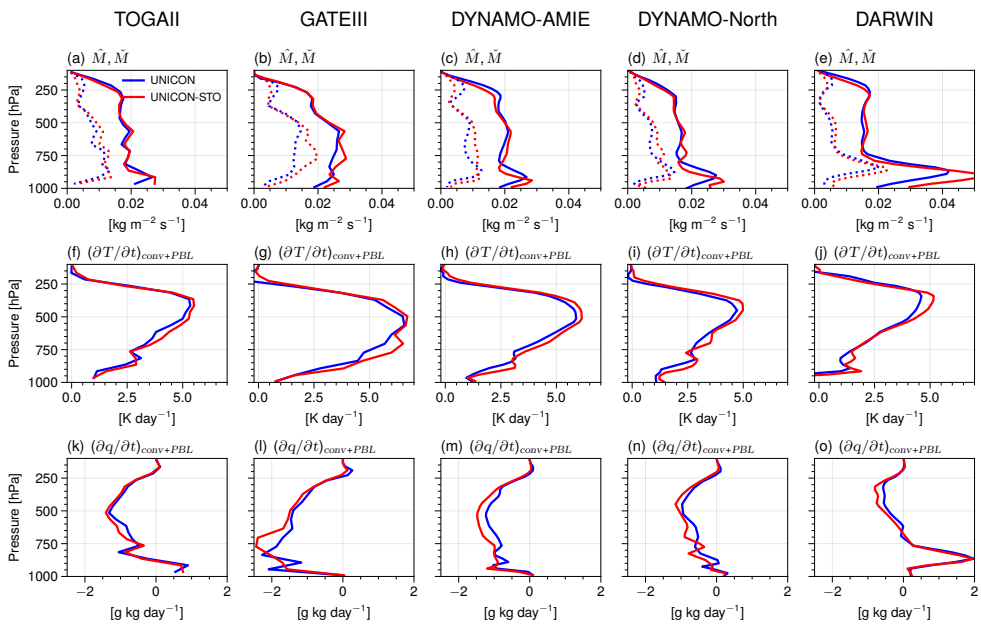

Figure 6.7 Vertical profiles of time-averaged (a)-(d) convective updraft mass flux ($\hat{M}$, solid lines) and downdraft mass flux ($\check{M}$, dashed lines), (e)-(h) temperature tendency by convection and PBL schemes, and (i)-(l) specific humidity tendency by convection and PBL schemes simulated by UNICON and stochastic UNICON in the time-varying forcing SCM cases.

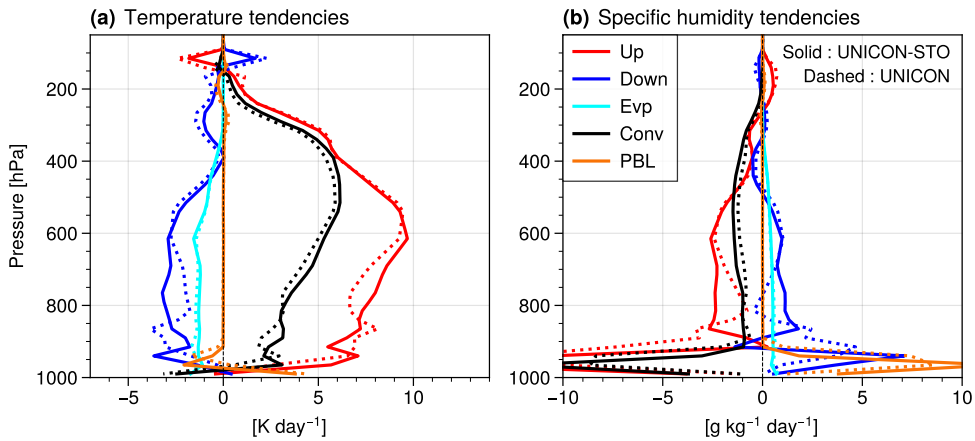

Figure 6.8 Vertical profiles of time-averaged (a) temperature and (b) specific humidity tendencies by convective updrafts (Up), convective downdrafts (Down), evaporation of convective precipitation within the environment (Evp), total convective processes (Conv), and the PBL scheme (PBL) simulated by UNICON and stochastic UNICON in the DYNAMO-AMIE case. Solid lines denote stochastic UNICON, and dashed lines denote UNICON.

convective heating contributes to reducing the negative temperature biases presented by UNICON. In the specific humidity tendencies, stochastic UNICON displays higher drying tendencies by convection in the mid-troposphere. This seems to be contrary to the result that stochastic UNICON reduces dry biases of UNICON. In fact, the higher drying tendency in the mid-troposphere contributes to reducing the dry bias because it increases the vertical gradient of specific humidity, so the specific humidity tendency due to vertical advection ($-\omega \partial q/\partial p$) is increased. This will be discussed in detail in Section 6.6.2.

Figure 6.8 shows temperature and specific humidity tendencies separated by detailed convective processes in the DYNAMO-AMIE case. The convective updrafts generate heating tendency (drying tendency) mostly by the production of convective precipitation, and convective downdrafts generate cooling tendency (moistening tendency) mostly by evaporation of convective precipitation. The increased heating and drying tendencies of stochastic UNICON are contributed both by convective updrafts and downdrafts, where convective updrafts contribute below 500 hPa level and convective downdrafts contribute above 500 hPa level.

6.6.2 Simulated MJO in the DYNAMO-AMIE Case

In this subsection, the characteristics of simulated MJO in the DYNAMO-AMIE case are analyzed in detail. Figure 6.9 shows smoothed anomalies of temperature (T'), specific humidity (q'), and moist static energy (MSE$'$) in the DYNAMO-AMIE case. In observation, slight positive anomalies in temperature in the upper troposphere are concurrent with positive moisture anomalies for each LCE when convection activities are high (Figures 6.9a and 6.9d). It is observed that the heights of positive moisture anomalies increase

as time progresses during each LCE. At the early stages of LCEs, strong moistening begins between 850 and 700 hPa after dry anomalies. The positive moisture anomalies are vertically extended as convection activities increase. Stochastic UNICON successfully captures the positive temperature and moisture anomalies during the active convection periods and the progressively increasing heights of positive moisture anomalies. However, stochastic UNICON overestimates the magnitude of temperature anomalies at the upper levels (Figure 6.9c). Original UNICON does not correctly capture the oscillation of temperature and moisture anomalies, and the simulated positive anomalies during LCE2 are indistinct. In addition, too strong positive temperature anomalies are generated at the beginning of LCE1 and LCE3. The intense heating tendency at the end of LCE2 indicates that unrealistically strong convection is simulated, which produces overestimated rain peaks during this period (Figure 6.5a). The results here suggest that stochastic UNICON can improve the MJO simulation by representing a more realistic interaction between large-scale forcings and convection.

Figure 6.10 shows vertical profiles of relative humidity, updraft mass flux, and normalized probability of convection top composited by the active MJO phases (phases 8-3) and inactive MJO phases (phases 4-7). The observed relative humidity is significantly higher during the active MJO phases than during the inactive MJO phases throughout the troposphere (Figure 6.10a). The environment with higher relative humidity promotes deeper convection by reducing the dilution of convective updrafts by mixing. The simulated relative humidity profiles also display dependency on MJO phases. However, UNICON and stochastic UNICON simulate lower relative humidity below the 450 hPa level and higher relative humidity above compared to observation. Notably, the

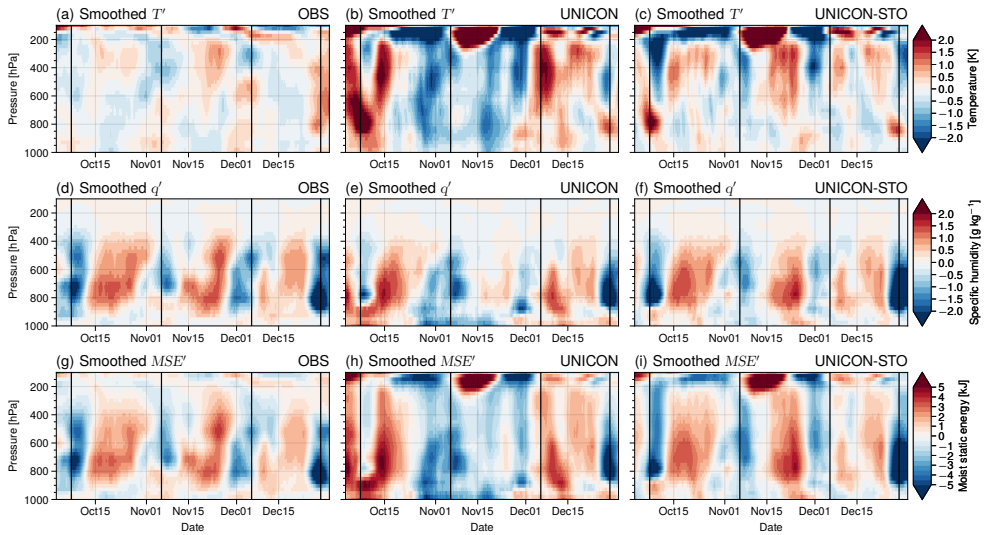

Figure 6.9 Smoothed anomalies of (a)-(c) temperature (T'), (d)-(f) specific humidity (q'), and (g)-(i) moist static energy (MSE$'$) from observation, UNICON, and UNICON-STO in the DYNAMO-AMIE case. All anomalies are calculated relative to the mean value of the entire period and smoothed by 5-day running averages. Durations of three large-scale convective events (LCEs) are denoted with black vertical lines.

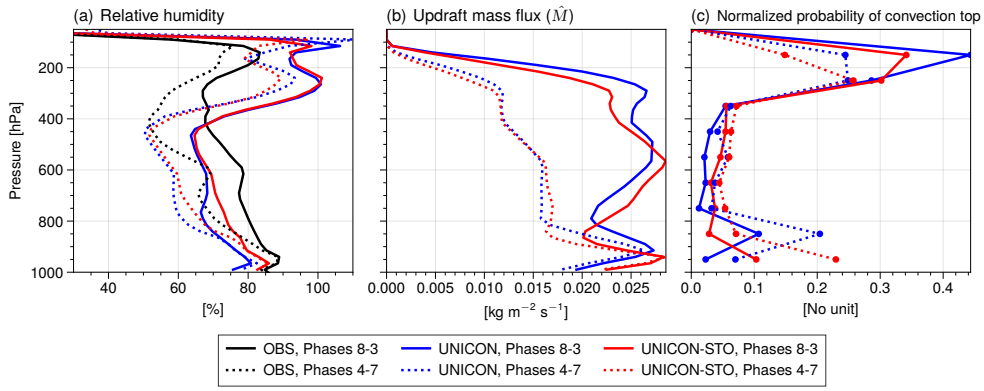

Figure 6.10 Vertical profiles of time-averaged (a) relative humidity, (b) updraft mass flux, (c) normalized probability of convection top during MJO phases 8-3 and phases 4-7 in the DYNAMO-AMIE case, simulated by UNICON and UNICON-STO. For relative humidity, profiles from observation are also shown. The normalized probability of convection top is calculated by accumulating the fractional area of saturated updraft top in each 100 hPa bin and then normalizing by the total sum of the bins.

relative humidity close to 100 % at heights above 300 hPa indicates the excessive amount of high-level clouds in the SCM simulations. Stochastic UNICON reduces the relative humidity bias of UNICON below 600 hPa level. The simulated updraft mass flux above 850 hPa level during the active MJO phases is much higher than that during the inactive MJO phases (Figure 6.10b). It is notable that the updraft mass fluxes at the near-surface do not change much along with MJO phases, implying that the variation of convection activity associated with the MJO is mainly modulated by the moistening above 850 hPa level. During the active MJO phases, convective updrafts with higher top heights are more frequently generated, consistent with the radar observation of Powell and Houze Jr. (2013). Stochastic UNICON produces more frequent shallower convection and stronger mass fluxes in the lower troposphere compared to UNICON (Figures 6.10b and 6.10c).

In order to understand the characteristics of cloud population generated by stochastic UNICON, the distributions of mesoscale organization parameter (Ω) and updraft radius ($\hat{R}$) are drawn (Figure 6.11). During the active MJO phases, the simulated mesoscale organization parameters are increased by 14 % and 7 % on average for UNICON and stochastic UNICON, respectively. The increased organization during the active MJO phases is expected to be due to the increased evaporation of convective precipitation during the active MJO phases. Stochastic UNICON simulates generally higher mesoscale organization than UNICON due to the increased downdraft mass flux (Figures 6.7a and 6.7d). The (mass-flux weighted) mean updraft radius at 1000 hPa level is also increased during the active MJO phases since the near-surface updraft radius is an increasing function of the mesoscale organization parameter. Stochastic

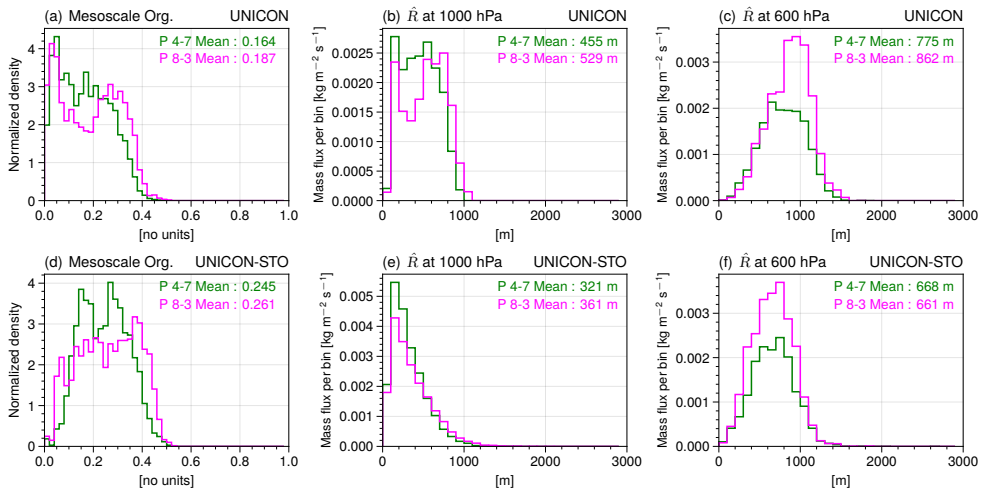

Figure 6.11 (a)(d) Normalized density of mesoscale organization parameter Ω, and histogram of updraft radius showing mass flux per bin (with a bin size of 100 m) at 1000 hPa level ((b), (e)) and 600 hPa level ((c), (f)) simulated by UNICON and stochastic UNICON during MJO phases 4-7 (green) and phases 8-3 (magenta). The mean values of the distributions are denoted at the upper right corner of each plot.

UNICON shows an updraft radius distribution weighted on small radii which is significantly different from UNICON.

The difference between the updrafts simulated in UNICON and stochastic UNICON is evident in the radius distribution at 600 hPa level (Figures 6.11c and 6.11f). UNICON simulates updrafts with larger radii during the active phases, while stochastic UNICON produces similar distributions and mean values of radius between the active and inactive phases. In UNICON, a single bulk plume increases its radius during ascent without being completely detrained, so updrafts with larger radii at the near-surface have larger radii even in upper levels. In contrast, in stochastic UNICON, convective updrafts with small radii are detrained in relatively lower levels, so radius distributions at 600 hPa level become similar. This result reveals the ability of stochastic UNICON to express the coexistence of shallow and deep convection.

Figure 6.12 shows vertical profiles of tendencies by convection and PBL schemes, all physical processes, and vertical advection during the active and inactive MJO phases. The heating and drying tendencies by convection are greatly enhanced during the active MJO phases. As seen in Figure 6.7, stochastic UNICON simulates higher heating and drying tendencies by convection compared to UNICON, both during the active and inactive phases. The simulated tendencies by all physical processes are comparable with tendencies from convection and PBL schemes, with the little amount of cooling (up to $-2\,\mathrm{K\,day^{-1}}$) and moistening (up to $0.5\,\mathrm{g\,kg^{-1}\,day^{-1}}$) being added by stratiform microphysics and radiation schemes. The temperature and specific humidity tendencies by physical processes can be calculated by subtracting advective tendencies from total tendencies and have the same definitions as the apparent

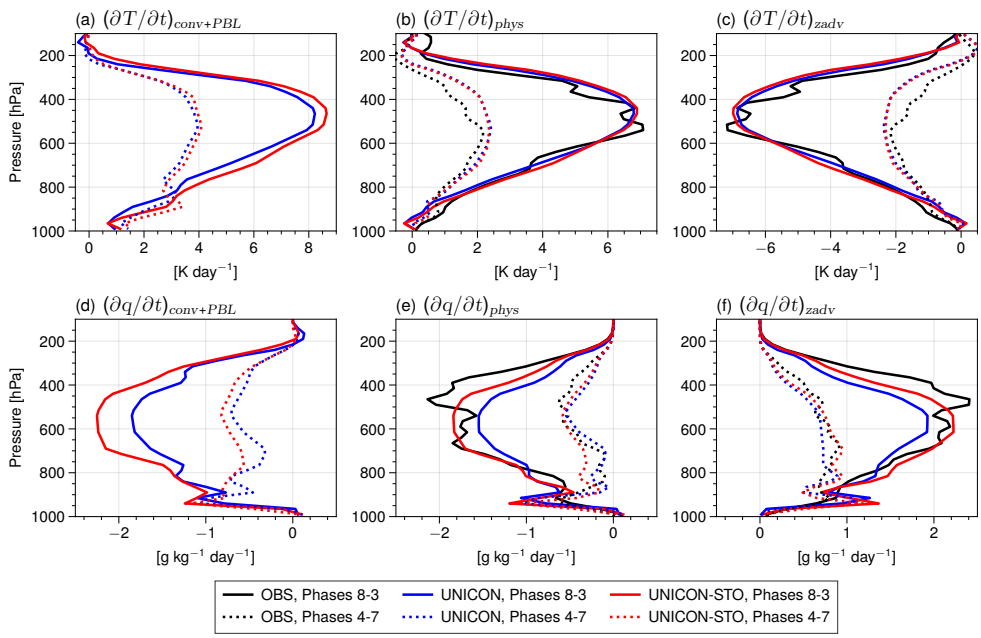

Figure 6.12 Vertical profiles of time-averaged tendencies of temperature and specific humidity by (a)(d) convection and PBL schemes, (b)(e) all physical processes, and (c)(f) vertical advection simulated by UNICON and stochastic UNICON during MJO phases 8-3 and phases 4-7 in the DYNAMO-AMIE case. For (b)(c)(e)(f), profiles from observation are also shown.

heat source (Q_1) and apparent moisture sink (Q_2), respectively. The simulated $(\partial T/\partial t)_{\text{phys}}$ of UNICON and stochastic UNICON closely match with observation during the active phases but are overestimated during the inactive phases. The simulated $(\partial q/\partial t)_{\text{phys}}$ of stochastic UNICON exhibits stronger drying than that of UNICON during the active MJO phases, which is more closely matches with observation. The tendencies by vertical advection are almost inverse of physical tendencies, compensating each other. The increased drying by convection is compensated by the increased moistening by vertical advection in stochastic UNICON, and the net effect of the two is slightly increased moistening, which reduces the dry biases of UNICON.

6.6.3 Idealized Experiments

In this subsection, results from the idealized SCM experiments are presented and discussed. Figure 6.13 shows simulated vertical profiles of various updraft properties averaged over $t = 4 \sim 6$ h in the BOMEX case. UNICON exhibits cold and moist biases in the sub-cloud layer and in the layer 1300-1700 m and warm and dry biases in the cloud layer below 1300 m. Stochastic UNICON reduces these biases, where RMSEs are reduced by 31 % and 39 % in $\overline{\theta_c}$ and $\overline{q_t}$ profiles, respectively. UNICON shows mass flux with a rapid slope change near the inversion height since the bulk plume in UNICON terminates at a certain height (Figure 6.13h). Stochastic UNICON simulates a much smoother mass flux profile similar to LES. Stochastic UNICON also simulates $\hat{\theta}_c$ and $\hat{q}_t$ profiles that closely match with the LES cloud and core profiles, while UNICON produces colder and more humid updrafts in the lower cloud layer. UNICON and stochastic UNICON both suffer from rapid increases of $\hat{w}$ and $\hat{q}_l$ in the

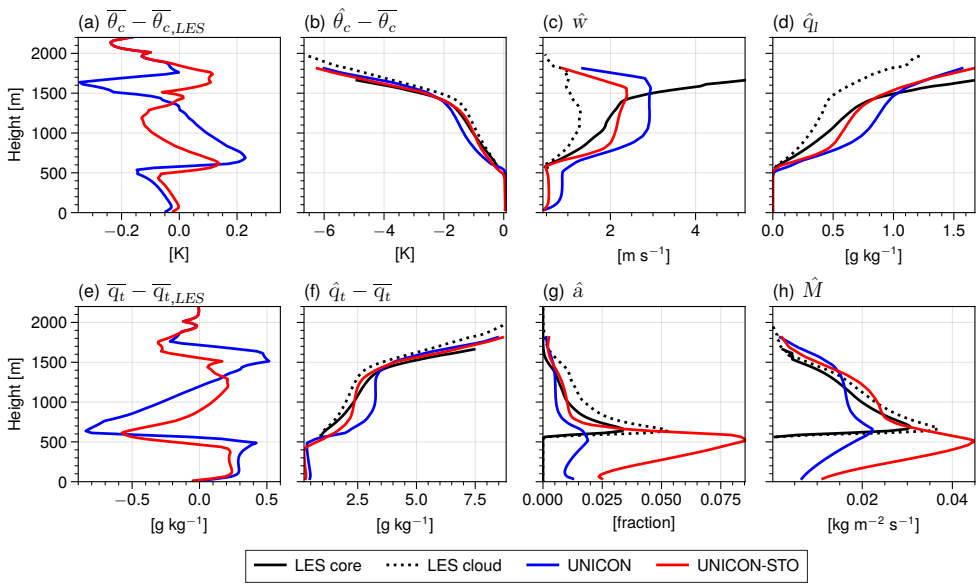

Figure 6.13 Vertical profiles of (a)(e) error of $\overline{\theta_c}$ and $\overline{q_t}$ with respect to LES, (b)(f) difference of the moist conserved variables from updrafts with respect to the environmental mean moist conserved variables, (c) updraft vertical velocity, (d) updraft liquid water, (g) updraft fractional area, and (h) updraft fractional mass flux averaged over $t = 4 \sim 6$ h simulated by UNICON and stochastic UNICON in the BOMEX case.

lower cloud layer, but stochastic UNICON reduces the discrepancy between the profiles from LES and SCM simulations in the cloud layer.

In the RICO case, UNICON displays excessive warm and dry biases near the inversion height of approximately 2000 m up to $> 2\,\mathrm{K}$ and $< -2\,\mathrm{g\,kg^{-1}}$, respectively (Figure 6.14). Stochastic UNICON slightly reduces the biases in the cloud layer below the inversion, but the biases near the inversion height are not alleviated. The biases indicate that the inversion heights are underestimated in UNICON and stochastic UNICON. The rapid decrease of $\hat{\theta}_c - \overline{\theta_c}$ (rapid increase of $\hat{q}_t - \overline{q_t}$) near the inversion height in UNICON and stochastic UNICON appears at about 400 m lower heights compared to LES, indicating that convective updrafts terminate at lower levels in the SCM simulations. Here again, UNICON and stochastic UNICON exhibit the rapid increases of $\hat{w}$ and $\hat{q}_l$ in the lower cloud layer. $\hat{a}$ and $\hat{M}$ are underestimated in UNICON, and stochastic UNICON simulates $\hat{a}$ and $\hat{M}$ profiles that better match with LES. However, $\hat{a}$ and $\hat{M}$ are rapidly decreased at lower levels than the LES profiles in both UNICON and stochastic UNICON. As demonstrated in Chapter 5, the biases presented in the RICO case can be significantly reduced by implementing a stochastic mixing model with a more realistic formula for entrainment and detrainment rates.

Figure 6.15 shows vertical profiles of environmental moist conserved thermodynamic variables and cloud fraction simulated by UNICON and stochastic UNICON in the CGILSS6, CGILSS11, and CGILSS12 cases. UNICON and stochastic UNICON simulate inversion heights only about half that of LES ensembles and have more humid boundary layers. The PBL scheme of CAM5 (Park and Bretherton 2009) explicitly includes cloud-top entrainment, but it

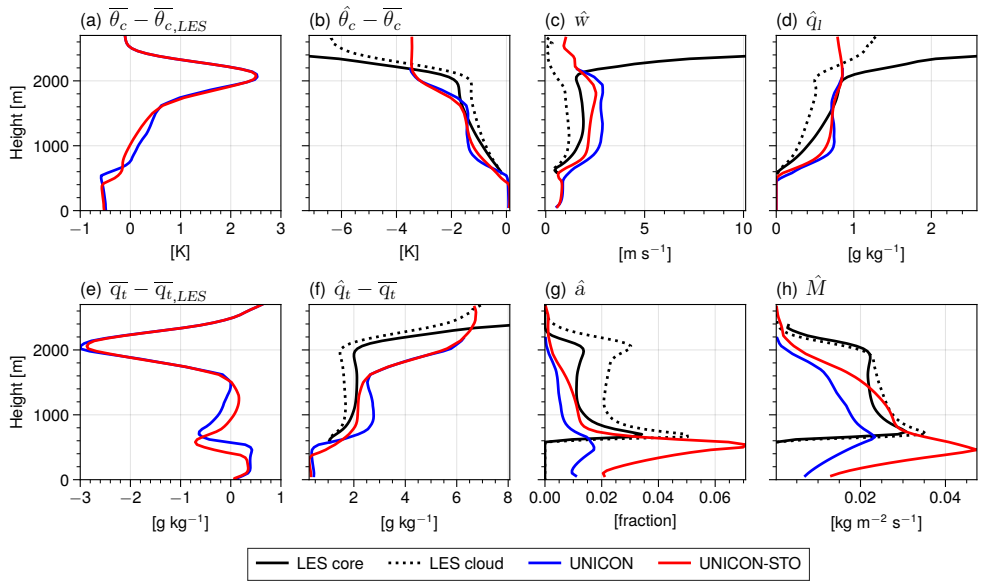

Figure 6.14 Vertical profiles of (a)(e) error of $\overline{\theta_c}$ and $\overline{q_t}$ with respect to LES, (b)(f) difference of the moist conserved variables from updrafts with respect to the environmental mean moist conserved variables, (c) updraft vertical velocity, (d) updraft liquid water, (g) updraft fractional area, and (h) updraft fractional mass flux averaged over $t = 20 \sim 24$ h simulated by UNICON and stochastic UNICON in the RICO case.

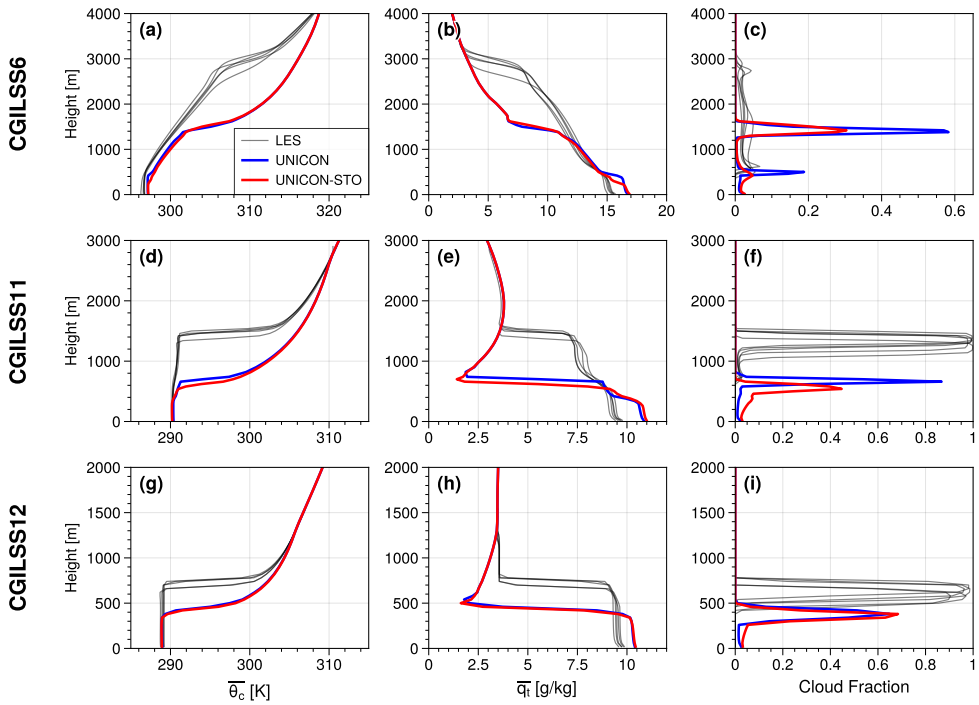

Figure 6.15 Vertical profiles of (a)(d)(g) environmental condensate potential temperature, (b)(e)(h) environmental total water specific humidity, and (c)(f)(i) cloud fraction averaged over the last day of the simulation period ($t = 216 \sim 240$ h) simulated by UNICON and stochastic UNICON in the CGILSS6 (first row), CGILSS11 (second row), and CGILSS12 (third row) cases. The profiles of six LES models from the LES intercomparison study are drawn for reference.

seems that the cloud-top entrainment is considerably underestimated. Particularly, in the CGILSS6 case, a cumulus cloud layer in the LES models is developed when stratocumulus is formed at the inversion height during days 1-5 and becomes a shallow convection regime (Blossey et al. 2013). In contrast, UNICON and stochastic UNICON failed to develop a cloud layer from decoupled stratocumulus to shallow convection in CGILSS6. Many issues might be associated with simulating realistic feedbacks between radiation, cloud, and boundary-layer turbulence. The intercomparison study of CGILS showed that SCMs have large uncertainties in simulating stratocumulus topped boundary layer (Zhang et al. 2013). One possible explanation is that UNICON and stochastic UNICON do not consider downdrafts originated from the inversion. UNICON and stochastic UNICON launch convective updrafts only from the near-surface. However, in the stratocumulus-topped boundary layer, the entrainment of warm and dry tropospheric air, which favors evaporative cooling, contributes to local changes in buoyancy and generates downdrafts at an inversion height. The mass flux of downdrafts is comparable to that of updrafts and has a nonnegligible impact on the heat and moisture fluxes within the boundary layer (Davini et al. 2017). The simulated environmental profiles from UNICON and stochastic UNICON are similar in the CGILS cases, while the RMSEs of UNICON are slightly reduced by stochastic UNICON (Table 6.4). The DYCOMSRF01 case is integrated only for 4 hours, so the environmental thermodynamic profiles simulated from UNICON and stochastic UNICON are almost identical, and not much deviated from the initial profiles (not shown).

6.6.4 Cloud Variabilities in a Near-Equilibrium Environment

In the time-varying forcing cases, it is difficult to isolate the cloud variabilities that are simulated in stochastic UNICON. In order to get the statistics of cloud variabilities in a near-equilibrium environment of a deep convection regime, an additional SCM simulation of the idealized GATE case is conducted, which uses time-averaged large-scale forcing from the GATEIII observed period. This case is documented in Fu et al. (1995), Khairoutdinov et al. (2009), and Xu et al. (1992). We use the same setting as the time-varying forcing cases for running the case, but the radiation tendency specified in Xu et al. (1992) is used instead of the radiation scheme for this case. In addition, the temperature and moisture profiles are relaxed toward prescribed profiles with a relaxation time scale of $\tau = 6\,\mathrm{hr}$ to avoid drifting of the thermodynamic states. The simulation is run for 90 days, and the statistics of updrafts are collected for the period, excluding the first ten days.

Figure 6.16 shows the number PDFs of various updraft properties at the near-surface and the cloud-base height of 580 m. The cloud-base height is defined as the lowest height where the mean updraft liquid water specific humidity ($\hat{q}_l$) is greater than $0.01\,\mathrm{g\,kg^{-1}}$. UNICON parameterizes the impact of mesoscale organized flow by adding deterministic perturbation $\Delta\phi_\Omega$ to updraft properties at the near-surface [(4.13)]. Therefore, the distributions of $\hat{w}$ and $\hat{\theta_c}$ at the near-surface simulated by UNICON show small variances, with the mean values of approximately $0.5\,\mathrm{m\,s^{-1}}$ and 298 K, respectively (Figures 6.16a and 6.16b). The variances are not zero because the cold pool properties simulated by UNICON fluctuates over time and the environment is also not in a perfect equilibrium. The distribution of $\hat{q}_t$ at the near-surface in UNICON shows two

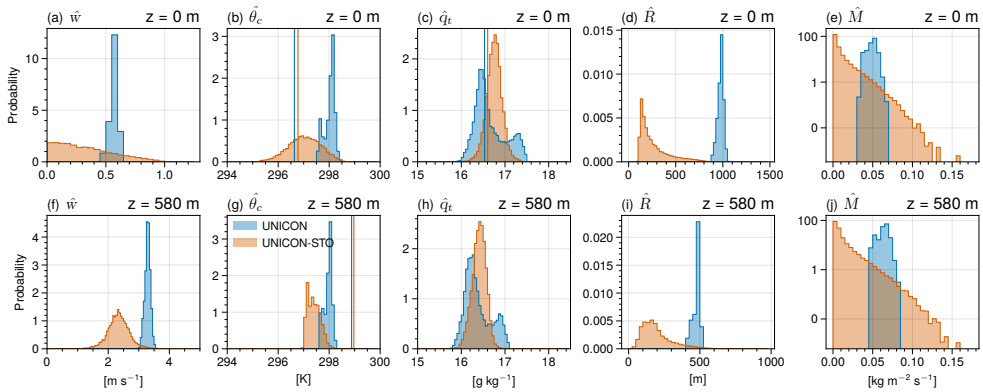

Figure 6.16 Number PDF of various updraft properties at the near-surface (first row) and at the cloud-base height of 580 m (second row) simulated by UNICON and stochastic UNICON in the idealized GATE case. The vertical lines in (b), (c), and (g) denote grid-mean values ($\overline{\theta_c}$ and $\overline{q_t}$) at each height. Note that the y-axis of (e) and (j) is in log scale.

peaks and has a relatively large variance because the simulated q_t perturbation by mesoscale organized flow, $\Delta q_{t,\Omega}$, oscillates with two peaks in the UNICON simulation. The oscillation seems to be a numerical issue, but we are unsure about the exact reason. The mean perturbations by mesoscale organizaged flow simulated by UNICON are $\Delta w_\Omega = 0.47\,\mathrm{m\,s^{-1}}$, $\Delta\theta_{c,\Omega} = 1.34\,\mathrm{K}$, and $\Delta q_{t,\Omega} = -0.057\,\mathrm{g\,kg^{-1}}$ in the idealized GATE case. The distributions of updraft radius and mass flux at the near-surface also show small variances, with the mean values of $1000\,\mathrm{m}$ and $0.05\,\mathrm{kg\,m^{-2}\,s^{-1}}$, respectively.

Compared to UNICON, stochastic UNICON shows larger variances of thermodynamic variables (except $\hat{q}_t$), updraft radius, and mass flux at the near-surface. This is because stochastic UNICON parameterizes the impact of mesoscale organized flow in a stochastic manner by increasing the variances of the joint PDF of updraft properties. The simulated standard deviations of updraft thermodynamic properties are $\sigma_w^* = 0.47\,\mathrm{m\,s^{-1}}$, $\sigma_{\theta_c}^* = 0.80\,\mathrm{K}$, and $\sigma_{q_t}^* = 0.19\,\mathrm{g\,kg^{-1}}$. The distribution of $\hat{w}$ of stochastic UNICON is half Gaussian because the constraint of $w > 0$ is applied to the multivariate Gaussian. The distributions of $\hat{\theta}_c$ and $\hat{q}_t$ of stochastic UNICON are close to Gaussian. As the updraft radius is parameterized as a power-law distribution with a scale break in stochastic UNICON, the distribution of $\hat{R}$ is weighted on a smaller radius (Figure 6.16d). Finally, stochastic UNICON reproduces the theoretical exponential distribution of $\hat{M}$ hypothesized by Craig and Cohen (2006). Stochastic UNICON also exhibits larger variabilities of updrafts at the cloud-base height (second row of Figure 6.16). The shapes of the distributions of $\hat{w}$ and $\hat{\theta}_c$ simulated by stochastic UNICON are deformed at the cloud-base height since the updrafts with relatively smaller $\hat{w}$ and $\hat{\theta}_c$ are detrained in the sub-cloud layer.

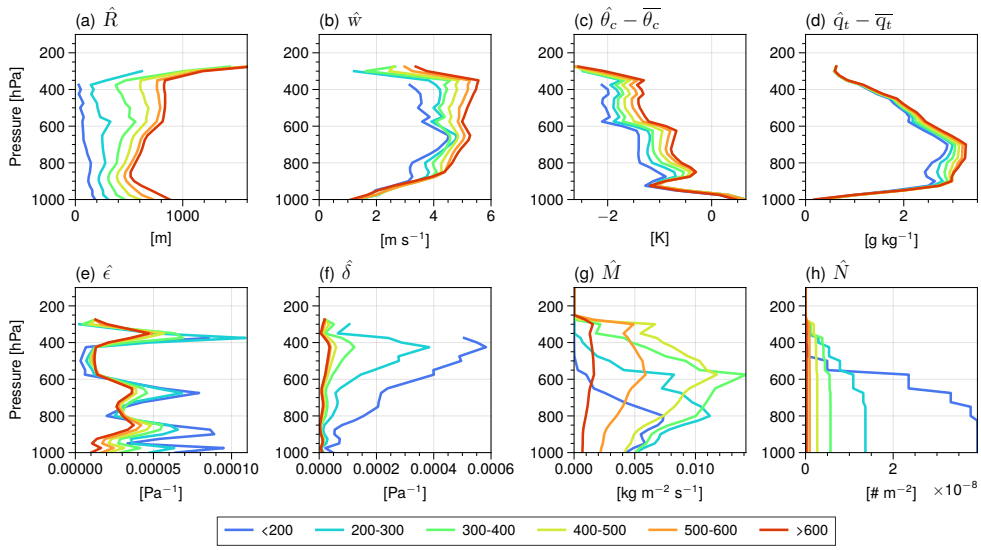

Figure 6.17 Composite vertical profiles of updraft properties according to the updraft radius at the cloud-base height (shown at the bottom in a unit of meters) obtained from the stochastic UNICON simulation of the idealized GATE case. $\hat{\epsilon}$ and $\hat{\delta}$ are the fractional entrainment and detrainment rates, respectively, and $\hat{N}$ is the number density of updrafts.

The increased variabilities of updrafts in the sub-cloud layer also contribute to increasing variabilities in the cloud layer. Particularly, the updraft radius plays a critical role in generating the cloud layer variabilities. Figure 6.17 shows composited vertical profiles of updraft properties according to the updraft radius at the cloud-base height, simulated by stochastic UNICON. The wider updrafts tend to have larger $\hat{w}$, $\hat{\theta}_c$, and $\hat{q}_t$. The degree of mixing between an updraft and the environment is inversely proportional to the updraft radius in stochastic UNICON. Therefore, the fractional entrainment and detrainment rates are lower for larger updrafts (Figures 6.17e and 6.17f). Larger updrafts experience less mixing and have greater buoyancy and vertical velocity. The difference from the shallow convection case is revealed in the relationship between $\hat{R}$ and $\hat{\theta}_c$. In the simulation of the BOMEX case, larger $\hat{R}$ is associated with smaller $\hat{\theta}_c$ due to decreased entrainment (see Chapter 4). However, in the case of deep convection, larger updrafts tend to have larger $\hat{\theta}_c$ since the diabatic heating from the production of precipitation increases in larger updrafts. The updrafts that are small and have low buoyancy have large detrainment rates, so they lose mass flux at lower levels and are consequently detrained at the lower levels (Figures 6.17g and 6.17h). The updrafts with radii smaller than 300 m at the cloud-base height can be considered shallow convection, and they have a considerable contribution to total mass flux in the lower troposphere. The improvements in the simulations of the tropical convection cases by stochastic UNICON appear to be related to the representation of shallow convection.

6.7 Discussion

Our study suggests several important aspects to further improve stochastic UNICON, including a more realistic representation of the life cycle of a

mesoscale convective system and the downdrafts originated from cloud-topped inversion. These issues are also crucial in other convection parameterizations and are subjects that need further study. Finally, although only SCM cases over the ocean were considered in this study, optimization of stochastic UNICON under more general conditions can be expected by adding SCM cases over the continent.

7 Global Climate Simulation with Stochastic UNICON

7.1 Introduction

The Madden-Julian oscillation (MJO; Madden and Julian 1971) is the dominant mode of intraseasonal variability in the tropical atmosphere. It is characterized by eastward-propagating envelopes of convective cloud clusters that are coupled with large-scale atmospheric circulation. The MJO interacts with a variety of weather and climate phenomena, including monsoonal system (Lavender and Matthews 2009; Lorenz and Hartmann 2006; Singh et al. 1992; Taraphdar et al. 2018), El Niño-Southern Oscillation (ENSO) (Hendon et al. 2007; Lee et al. 2019; Moon et al. 2011), and tropical cyclone activity (Camargo et al. 2009; Hall et al. 2001; Liebmann et al. 1994; Maloney and Hartmann 2000a,b). The ability of general circulation models (GCMs) to accurately simulate the intensity, spatial structure, and dispersion relation of the MJO is critical for predicting tropical variabilities and their future projections.

Despite the importance, state-of-art GCMs still have shortcomings in realistically simulating the MJO. Most models participated in Coupled Model Intercomparison Project phase 5 (CMIP5) simulate underestimated MJO amplitude and low coherency between large-scale wind field and convection system (Ahn et al. 2017). With considerable improvement in physics parameterizations,

the general performance on the simulation of the MJO is improved in the CMIP6 models compared to the CMIP5 models (Orbe et al. 2020; Ahn et al. 2020; Chen et al. 2022). However, the CMIP6 models still underestimate MJO amplitude and struggle to simulate realistic eastward propagation patterns (Le et al. 2021; Chen et al. 2022). The realistic representation of the MJO in GCMs is a challenging task in that it involves physical processes with large uncertainties. Particularly, parameterizing subgrid convection is thought to account for a large portion of the uncertainties because of the stochastic nature of atmospheric convection. One important issue related to MJO simulation is the parameterization of organized convection. The MJO is associated with squall lines and mesoscale convective systems (MCS), which have substantially different characteristics from unorganized convection. The mesoscale convective organization significantly modulates the transport of heat, moisture, and momentum by moist convection (Houze Jr 2004). Chen et al. (2021) implemented an organized convection parameterization in a GCM and reported that the organized convection parameterization improves the representation of the MJO and reduces precipitation biases over the tropics.

Another critical issue in MJO simulation is a spectral and/or stochastic representation of convective clouds in convection parameterizations. In a typical grid size of a GCM, a spectrum of convective clouds is formed in a stochastic way. It is important to represent the coexistence of shallow and deep convection since shallow convection supplies moisture to the lower troposphere to sustain organized convection in developing MJO (Cai et al. 2013; Janiga and Zhang 2016). In addition, cloud systems in developing MJO undergo a transition from shallow to deep convection, so there is an emerging demand for developing convection parameterization that represents different types of convection in

a continuous and unified way. Several spectral convection schemes have been proposed to represent different cloud types (Baba 2019; Neggers 2015; Suselj et al. 2019; Yang et al. 2021; Yoshimura et al. 2015). Global simulations with these schemes have shown improvements in the intensity and frequency of the simulated MJO without degrading mean climatology (Baba and Giorgetta 2020; Baba 2021). The results from the aforementioned GCM experiments suggest that spectral convection parameterization and organized convection parameterization can alleviate a problem known as "MJO-mean state trade-off" in GCMs, a problem where modifications in the convection parameterizations that improve MJO simulation tend to degrade the mean state (Chen and Mapes 2018; Hannah and Maloney 2011).

In this study, we evaluate the global simulation of stochastic UNICON, focusing on the intraseasonal variability represented by the MJO. Two climate simulations of SAM0-UNICON atmospheric GCM with UNICON and stochastic UNICON are compared and evaluated against observations. First, we demonstrate the model diagnostics on the simulations of global climatologies and discuss spatial distributions of the model biases. Next, various model diagnostics for the MJO are presented to demonstrate the impacts of the spectral parameterization. To understand the physical processes of simulated MJO, we conduct the precipitation budget analysis from Adames (2017). We deeply discuss the simulated relationship between moisture and precipitation and how the spectral representation of convection helps improve the moisture-precipitation relationship and MJO simulation.

7.2 Methods

7.2.1 Stochastic UNICON

In this study, we will use a Monte-Carlo method to sample convective updrafts from the joint PDF, as in Chapter 6. Each sampled updraft has a fractional area of $\hat{a} = \hat{A}_s/n_s$, where $\hat{A}_s$ is the total updraft fractional area at the near-surface and n_s is the number of updrafts to be sampled ($n_s = 5$ is used in this study). Table 7.1 lists the parameters and their values used in stochastic UNICON. c_1, c_2, $R_b|_{\Omega=0}$, and $R_b|_{\Omega=1}$ are the tunable parameters newly introduced in stochastic UNICON. The values of c_1, c_2, and $R_b|_{\Omega=0}$ are set by rounding the values that were calibrated using a single-column model (SCM) in Chapter 6. The value of $R_b|_{\Omega=1}$ over the ocean is set as 3500 m, which is larger than the SCM-calibrated value of 2190 m. In addition, the values of parameters related to the autoconversion process in cumulus (c_{at} and $\hat{q}_{c,\text{crit}}$) over land are modified, to match the mean precipitation over land.

7.2.2 Model experiments

The atmospheric GCM (AGCM) model used in this study is SAM0-UNICON (Park et al. 2019). SAM0-UNICON uses the same dynamic core and physics parameterizations as CAM5, except for shallow and deep convection and macrophysics schemes. The finite volume dynamic core (Lin and Rood 1996), the double-moment stratiform microphysics scheme of Morrison and Gettelman (2008), the Rapid Radiative Transfer Method for GCMs (RRTMG) radiation scheme (Iacono et al. 2008; Pincus et al. 2003), the planetary boundary layer (PBL) scheme of Bretherton and Park (2009), and the aerosol conversion scheme of Liu et al. (2012) are the identical components with CAM5. The macrophysics

Table 7.1 Parameters and their values used in the global simulation with stochastic UNICON. The parameters that are newly added or have different values from UNICON are listed.

Parameter	Value	Description
c_1	0.9	Scaling factor for the variance from non-organized turbulence
c_2	0.5	Scaling factor for the variance from mesoscale organized flow
$R_b\|_{\Omega=0}$	110 m	Scale break radius at the near-surface at $\Omega = 0$
$R_b\|_{\Omega=1}$	3500 m (ocean), 9000 m (land)	Scale break radius at the near-surface at $\Omega = 1$
c_{at}	$4.0 \times 10^{-3}\,\mathrm{m}^{-1}$ (land)	Autoconversion efficiency over land; Originally $2.0 \times 10^{-3}\,\mathrm{m}^{-1}$ in UNICON
$\hat{q}_{c,\mathrm{crit}}$	$5.0 \times 10^{-4}\,\mathrm{kg\,kg}^{-1}$ (land)	Critical in-cumulus liquid water content for the formation of precipitation over land; Originally $6.0 \times 10^{-4}\,\mathrm{kg\,kg}^{-1}$ in UNICON

of Park et al. (2014) in CAM5 is modified to include detrained cumulus (Park et al. 2017). Finally, UNICON replaces shallow and deep convection schemes in CAM5, which parameterizes all subgrid dry and moist convection.

We ran two global climate simulations, one with UNICON and the other with stochastic UNICON, with a horizontal resolution of $0.9^\circ \times 1.25^\circ$, 30 vertical levels, a model physics time step of $\Delta t = 1800\,\mathrm{s}$, and a dynamics time step of $\Delta t = 225\,\mathrm{s}$. Hereinafter, the two simulations are referred to as UNICON and UNICON-STO, respectively. The simulations are conducted for 36 years, from January 1979 to December 2014, according to the Atmospheric Model Intercomparison Project (AMIP) configuration described in the CMIP6 experiments specification (Eyring et al. 2016). The CMIP6 forcing data are prescribed as described in Park et al. (2019). Following the AMIP configuration, the observed sea surface temperature and sea ice fraction are prescribed, and a land model (Community Land Model version 4; CLM4) is coupled to simulate land surface states. The simulations are initialized from the atmosphere and land states on January 1, 1979 simulated in the historical coupled simulation of SAM0-UNICON.

7.2.3 MJO diagnostics and MJO precipitation budget

We use the CLIVAR MJO Working Group diagnostics package (Waliser et al. 2009) to obtain diverse MJO diagnostics. Daily anomalies are obtained by removing the mean and first three harmonics of the annual cycle over the 1979–2014 period. Then, the anomalies are bandpass-filtered using a 101-point Lanczos filter to extract the intraseasonal anomalies within 20–100 day time scales. The MJO phase composites are computed using the real-time multivariate MJO index (RMM index; Wheeler and Hendon 2004), defined as

the first two principal components of intraseasonal daily anomalies of outgoing longwave radiation (OLR), and 850 and 200 hPa zonal winds averaged over 15 °S-15 °N.

To understand the characteristics of MJO propagation in the global simulations, a precipitation budget analysis of Adames (2017) is conducted. The precipitation budget is a variant of the moisture budget where the inverse of the convective moisture adjustment time scale is weighted in each term to account for the moisture–precipitation relationship. The vertically integrated moisture budget equation can be written as follows:

$$\frac{\partial \langle q \rangle'}{\partial t} = -\left\langle u \frac{\partial q}{\partial x} \right\rangle' - \left\langle v \frac{\partial q}{\partial y} \right\rangle' + E' + C', \tag{7.1}$$

$$C' = -\left\langle \omega \frac{\partial q}{\partial p} \right\rangle' - P', \tag{7.2}$$

where q is the specific humidity, u and v are the zonal and meridional wind speeds, respectively, and ω is the vertical pressure velocity; P and E are the precipitation and evaporation, respectively. The angle brackets indicate the mass-weighted vertical integral from the surface to 100 hPa, and the prime symbol denotes the intraseasonal (20–100 days band-filtered) anomalies. The term C denotes the convectively driven column process, which is the sum of the vertical advection of moisture and the precipitation.

The relationship between moisture and precipitation over the tropical ocean is hypothesized as a nonlinear relationship (Bretherton et al. 2004b), and it can be approximated in the following form:

$$P\left(R_h\right) = P_0 \exp\left(aR_h\right), \tag{7.3}$$

where $R_h = \langle q \rangle / \langle q_s \rangle$ is the column relative humidity (CRH), q_s is the saturation specific humidity, and P_0 and a are constants. The values of P_0 and a are deter-

mined from observational data and the two simulations (see Section 7.3.3). By linearizing (7.3), the anomalous precipitation can be linked with the anomalous moisture:

$$P' \cong \frac{\langle q \rangle'}{\overline{\tau_c}}, \quad \overline{\tau_c} = \frac{\langle \overline{q_s} \rangle}{a\overline{P}}, \tag{7.4}$$

where τ_c is the convective moisture adjustment time scale and the overbar denotes a 100-day low-pass filtered field. τ_c is analogous to the adjustment time scale in the simplified Betts-Miller convective adjustment scheme (Betts and Miller 1986; Frierson 2007), and it determines the strength of the conversion of moisture anomaly to precipitation. Finally, the budget equation for the precipitation anomaly can be written as

$$\frac{\partial P'}{\partial t} = -\frac{1}{\overline{\tau_c}} \left\langle u \frac{\partial q}{\partial x} \right\rangle' - \frac{1}{\overline{\tau_c}} \left\langle v \frac{\partial q}{\partial y} \right\rangle' + \frac{E'}{\overline{\tau_c}} + \frac{C'}{\overline{\tau_c}} \tag{7.5}$$

7.2.4 Observational data

For the evaluation of the model mean climates, the following datasets are used: the Clouds and the Earth's Radiant Energy System Energy Balanced and Filled (CERES-EBAF; Loeb et al. 2009) for shortwave and longwave cloud radiative forcing; the European Centre for Medium-Range Weather Forecasts Interim Reanalysis (ERAI; Simmons et al. 2007) for temperature, relative humidity, sea level pressure, and zonal wind; the European Remote Sensing Satellite Scatterometer (ERS; Bentamy et al. 1999) for ocean surface wind stress; the Willmott–Matsuura (Willmott; Willmott and Matsuura 1995) data for land surface air temperature; the Global Precipitation Climatology Project (GPCP) monthly product version 2.1 (Adler et al. 2003) for global precipitation rate. These datasets are interpolated onto the native model grid to obtain mean climate diagnostics.

For the MJO diagnostics and precipitation budget analysis, the following datasets are used. We use the National Oceanic and Atmospheric Administration (NOAA) daily interpolated OLR product (Liebmann and Smith 1996) and daily averaged precipitation rate from the Tropical Rainfall Measuring Mission 3B42 version 7 (TRMM 3B42v7; Huffman et al. 2007) product. Various atmospheric state variables are obtained from the fifth generation of the European Centre for Medium-Range Weather Forecasts (ECMWF) reanalysis (ERA5) product (Hersbach et al. 2020). The hourly ERA5 data are averaged daily. The atmospheric field variables that are used in the precipitation budget analysis are obtained at 27 pressure levels between 1000 and 100 hPa. OLR and ERA5 data are obtained for the period 1979-2014, and precipitation data are obtained for the period 1998-2014. All observational data and model outputs for the MJO diagnostics and budget analysis are interpolated onto a $2.5^\circ \times 2.5^\circ$ horizontal grid using areal conservative remapping.

7.3 Results

7.3.1 Mean State

Figure 7.1 is a Taylor diagram (Taylor 2001) summarizing the model performance in reproducing the observed global mean climate. The mean RMSEs of the two simulations are similar; however, UNICON-STO exhibits an 18 % smaller mean bias compared to UNICON. More than 10 % of biases are reduced from UNICON to UNICON-STO for shortwave cloud forcing (SWCF), land rainfall, Pacific surface stress, and relative humidity. While UNICON and UNICON-STO both overestimate standardized deviations of the majority of the climate variables, UNICON-STO reduces standardized deviation of SWCF,

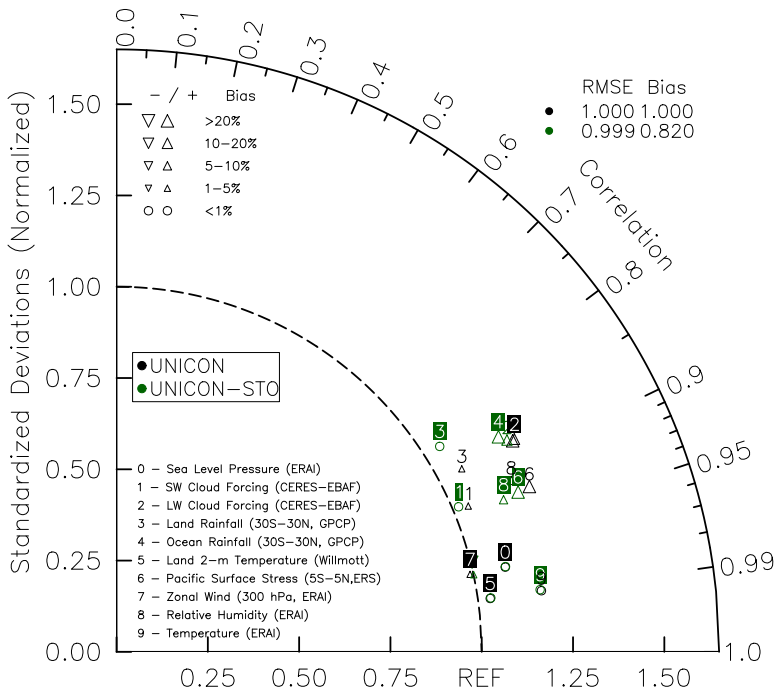

Figure 7.1 A space-time Taylor diagram from the UNICON (black) and UNICON-STO (green) simulations. Using the monthly climatology for all the available grid points, the correlations with the observation and the standardized deviations normalized by observed standard deviation are computed for ten climate variables indicated on the lower-left portion of the figure. The denoted RMSE (bias) is the average of the RMSE (bias) of a simulated individual variable divided by the average RMSE (bias) of UNICON.

ocean and land rainfall, Pacific surface stress, and relative humidity. The correlations with observations are quite similar in UNICON and UNICON-STO and show different trends between variables; for instance, the correlation of land rainfall is reduced ($0.883 \rightarrow 0.844$) and relative humidity is increased ($0.917 \rightarrow 0.931$) from UNICON to UNICON-STO. The result shows that general performances on simulating spatio-temporal patterns are pretty much the same in UNICON and UNICON-STO, but stochastic UNICON slightly improves the model performance in terms of mean bias and variance.

The model performance with stochastic UNICON can be improved with more careful calibration of the model parameters. In Chapter 6, the tunable parameters in stochastic UNICON are calibrated using various single-column model cases over the ocean. Then, the parameters over land are determined from the multiple global simulations with manually adjusted parameters. However, inferred from the reduced correlation of land rainfall in UNICON-STO, there is a possibility that the land parameters are not calibrated properly. In addition, extending the bulk plume to the spectral/stochastic plume model might require adjusting mixing and rain production processes since the characteristics of the bulk plume and individual plumes are different.

Figure 7.2 shows the global climatology of surface precipitation rate from the GPCP observation and the model biases. Both simulations produce higher mean precipitation than the observation, exhibiting distinct positive precipitation biases over the intertropical convergence zone (ITCZ) and South Pacific convergence zone (SPCZ). UNICON-STO reduces the mean bias of precipitation in UNICON by $0.04\,\mathrm{mm\,day^{-1}}$, while the RMSE is increased by $0.02\,\mathrm{mm\,day^{-1}}$. The precipitation biases are weakened over the western Indian Ocean, ITCZ, and western equatorial Atlantic in UNICON-STO. However,

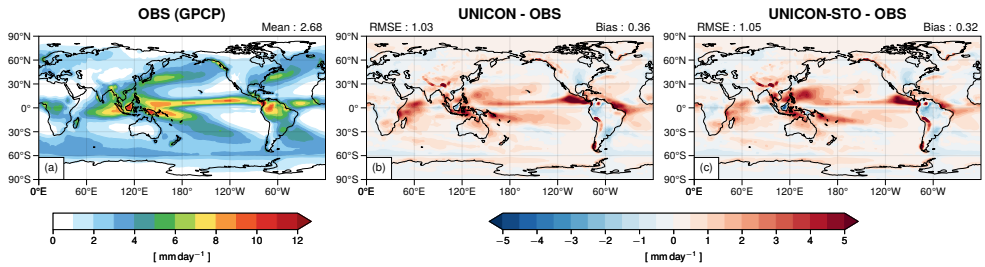

Figure 7.2 Annual surface precipitation rate from (a) the GPCP observation and the biases compared to the observations from (b) UNICON and (c) UNICON-STO. The global mean of the observation or the mean bias of the simulation is shown at the top right of each plot, and the RMSE of the simulation is shown at the top left of each plot.

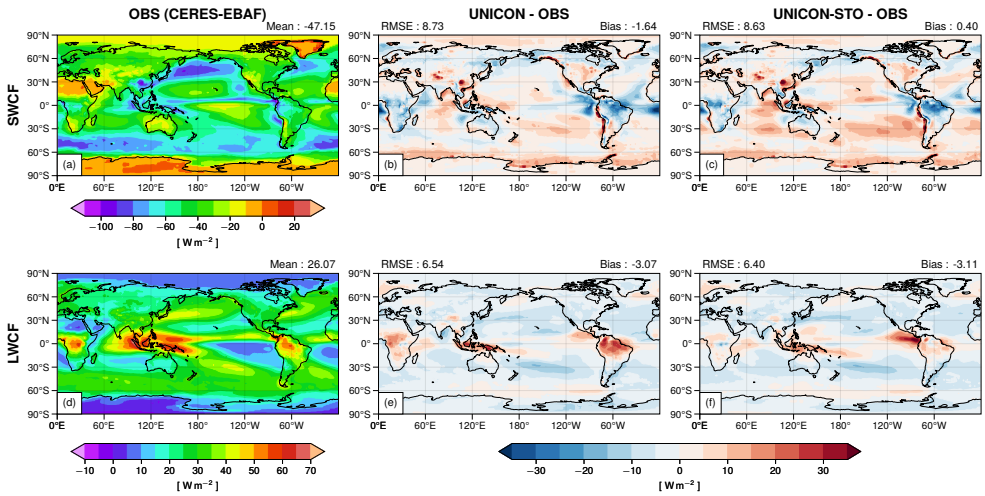

Figure 7.3 Annual shortwave and longwave cloud forcings from (a)(d) the CERES-EBAF observation, and the biases compared to the observation from (b)(e) UNICON and (c)(f) UNICON-STO. The global mean of the observation or the mean bias of the simulation is shown at the top right of each plot, and the RMSE of the simulation is shown at the top left of each plot.

the magnitudes of positive bias over the northwestern Pacific and negative bias over the Maritime Continent are intensified. The precipitation biases over the Maritime Continent and northwestern Pacific appear to be negatively correlated, as indicated in other GCM simulations (e.g., Schiemann et al. 2014). Schiemann et al. (2014) demonstrated that the decrease in precipitation over the Maritime Continent is associated with the weakening of the Walker circulation and the decreased moisture convergence, which lead to an increase in precipitation over the northwestern Pacific. Since the Maritime Continent exerts significant impacts on the modulation of the MJO and other large-scale tropical variabilities (Neale and Slingo 2003; Yang et al. 2019), a detailed investigation of the bias is required.

Figure 7.3 shows the global climatologies of shortwave and longwave cloud forcings from the CERES-EBAF observation and the model biases. The negative mean SWCF bias in UNICON is alleviated in UNICON-STO from $-1.64\,\mathrm{W\,m^{-2}}$ to $0.40\,\mathrm{W\,m^{-2}}$. The increase of SWCF in UNICON-STO is closely related to decreased low cloud fraction, where the global mean low cloud fraction is decreased from 41.73 % to 40.14 %. The pattern of SWCF biases is similar between UNICON and UNICON-STO, while RMSE is slightly decreased from $8.73\,\mathrm{W\,m^{-2}}$ in UNICON to $8.63\,\mathrm{W\,m^{-2}}$ in UNICON-STO. For LWCF, the mean LWCF biases are similar in the two simulations. UNICON-STO alleviates the positive LWCF biases over tropical land presented in UNICON, including the biases over the Amazon, Central Africa, and Maritime Continent. However, positive LWCF bias over the eastern equatorial Pacific is increased in UNICON-STO. The RMSE of LWCF is also slightly reduced from $6.54\,\mathrm{W\,m^{-2}}$ in UNICON to $6.40\,\mathrm{W\,m^{-2}}$ in UNICON-STO.

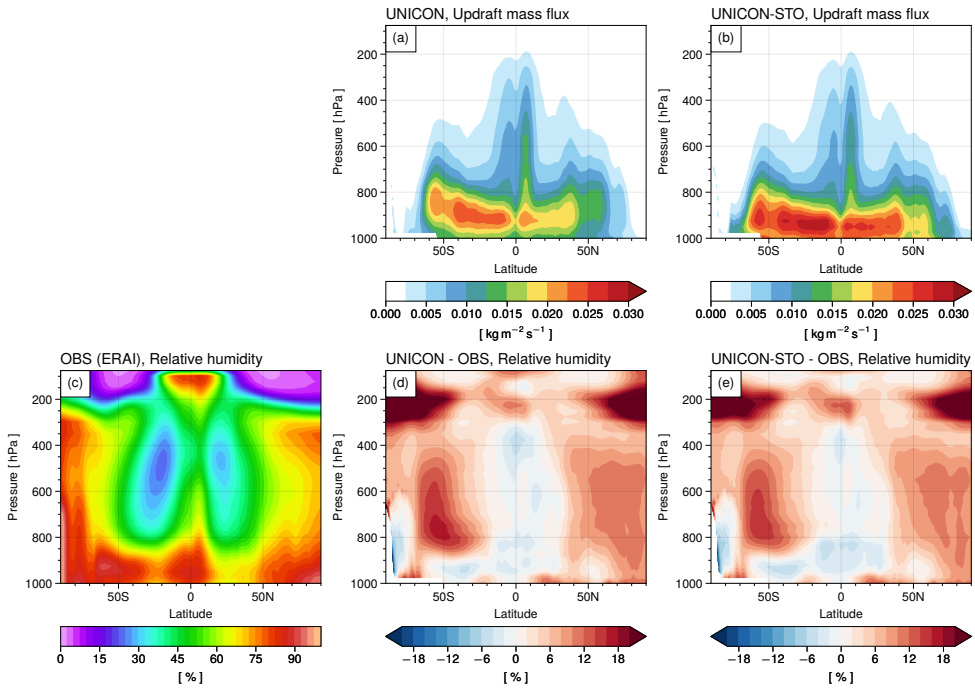

Figure 7.4 Annual zonal-mean vertical cross sections of updraft mass flux from (a) UNICON and (b) UNICON-STO; relative humidity from (c) the ERAI observation and the biases compared to the observation from (d) UNICON and (e) UNICON-STO.

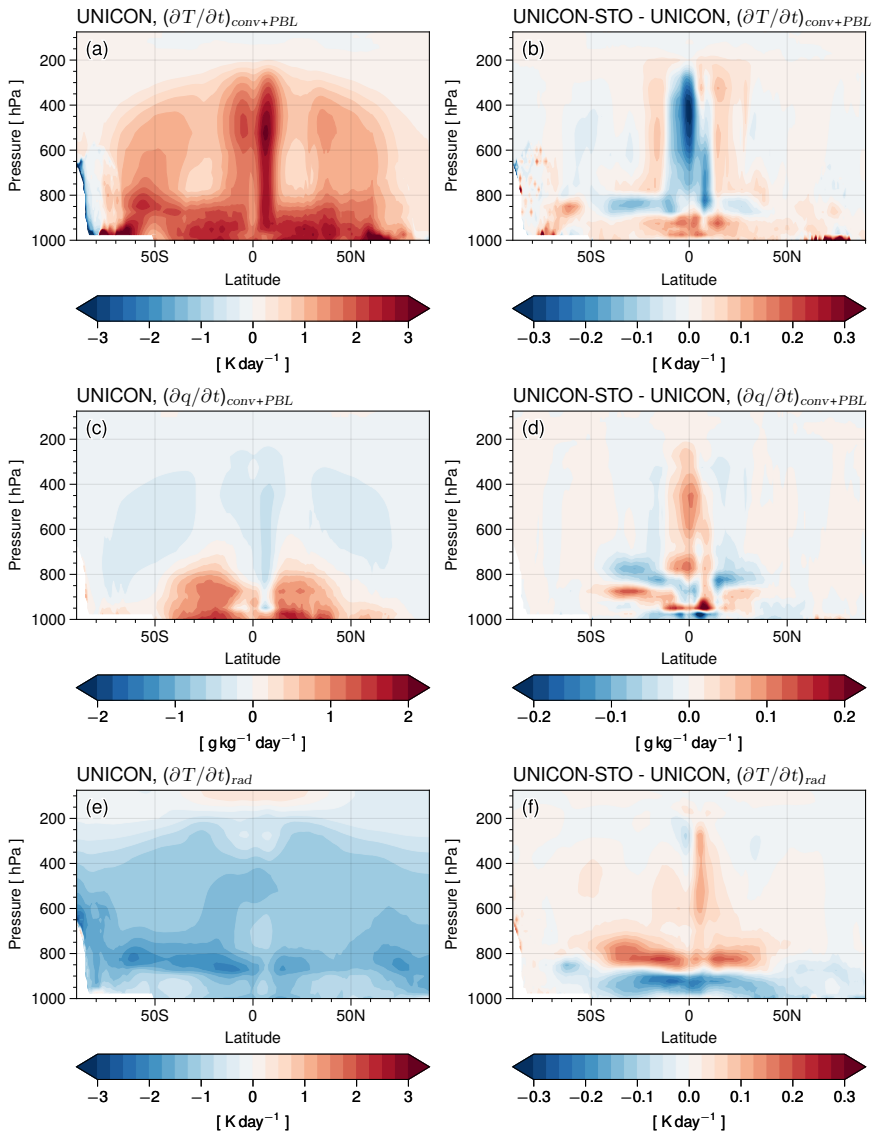

Figure 7.5 Annual zonal-mean vertical cross sections of the (a)(b) temperature tendencies from the convection and PBL schemes, (c)(d) specific humidity tendencies from the convection and PBL schemes, and (e)(f) temperature tendencies from the radiation scheme, obtained from UNICON and UNICON-STO.

The first row of Figure 7.4 shows the annual zonal-mean updraft mass flux of UNICON and UNICON-STO. The two simulations show substantially different updraft mass flux profiles, where UNICON-STO presents a much stronger mass flux below the height of 800 hPa, and the height of mass flux maximum is lowered. This indicates more frequent shallow convection due to the spectral representation of stochastic UNICON, as demonstrated in Section 6.6. The second row of Figure 7.4 shows the annual zonal-mean relative humidity of the ERAI observation and the model biases. Both simulations exhibit strong positive relative humidity biases in the extratropics and relatively smaller negative biases in the tropics. UNICON-STO slightly reduces the positive biases in mid-high latitudes and negative biases in levels above 600 hPa over the tropics. The increase of relative humidity in the upper troposphere over the tropics is due to the anomalous cooling and moistening by convective processes in UNICON-STO relative to UNICON (Figure 7.5b and 7.5d). The relative humidity decrease in mid-high latitudes is associated with complex feedback between radiation and clouds. UNICON-STO produces anomalous heating below 900 hPa and anomalous cooling in 800-900 hPa levels by convective processes relative to UNICON. The anomalous convective tendencies destabilize the lower troposphere and contribute decrease in low cloud fraction. This induces anomalous radiative heating in the levels above 900 hPa and anomalous radiative cooling in the levels below (Figure 7.5f), which compensate for the destabilization of the lower troposphere by convective processes. The anomalous radiative heating majorly contributes to the decrease of relative humidity. While considerable relative humidity errors remain in UNICON-STO, the decrease in relative humidity contributes to reducing the SWCF bias.

7.3.2 MJO Diagnostics

Figure 7.6 shows the wavenumber-frequency spectra of OLR and 850 hPa zonal wind from the observations and simulations. Compared to the observations, the two simulations both produce much stronger power in a wide frequency domain during summer. UNICON and UNICON-STO reproduce the observed MJO peak in 30-80-day periods with zonal wavenumbers 1-2 during summer. However, UNICON produces a power peak stronger than the MJO peak in periods greater than 80 days, while the dominant variability of UNICON-STO is in the 30-80 days range. During winter, UNICON simulates a variability that is too strong in the low-frequency regime and a weaker MJO power (Figure 7.6e). In contrast, UNICON-STO simulates the adequate power of winter MJO (Figure 7.6f). During both summer and winter, UNICON and UNICON-STO overestimate variabilities in low-frequency regimes in westward and eastward directions. UNICON-STO shows substantially larger MJO-related variabilities than the observations for OLR during summer and for 850 hPa zonal wind during both seasons.

Figure 7.7 is the result of a cross-spectrum analysis, showing coherence squared between OLR and 850 hPa zonal wind. The observations display high coherence squared (peaking at greater than 0.6) between OLR and 850 hPa zonal wind in periods of 20-80 days with zonal wavenumbers 1-2, indicating a strong coupling between large-scale circulation and convection in the MJO. UNICON shows a coherence squared peak for the simulated MJO but 15-30 % smaller values relative to the observations. Still, UNICON indicates much larger coherence than that of CAM5 (Park et al. 2019). UNICON-STO shows noticeably larger coherence related to the MJO than UNICON, especially

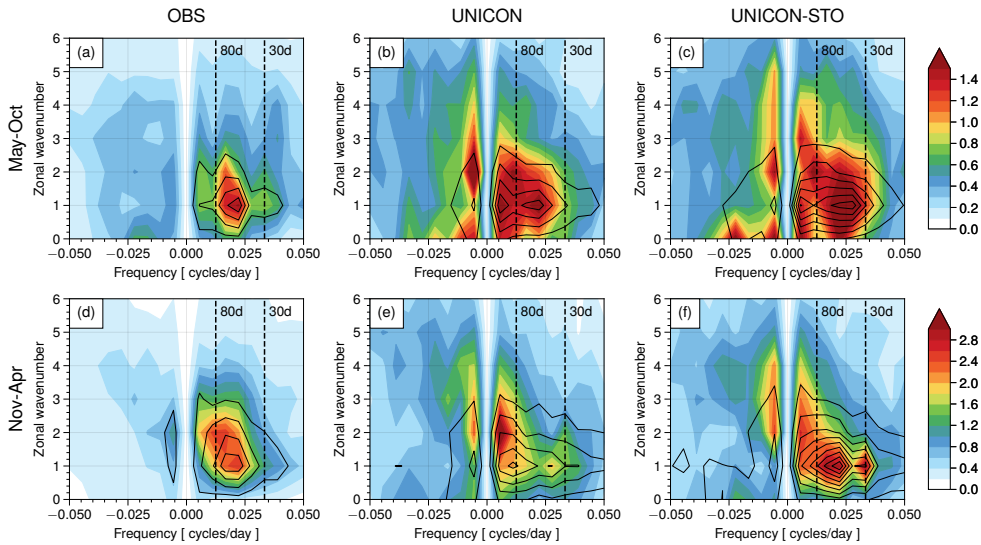

Figure 7.6 Wavenumber-frequency spectra of OLR (shading; $W^2\,m^{-4}$) and 850 hPa zonal wind (contour; $0.02\,m^2\,s^{-2}$ interval) averaged over 10°S-10°N during summer (May-October; first row) and winter (November-April; second row) for (a)(d) the observations, (b)(e) UNICON, and (c)(f) UNICON-STO.

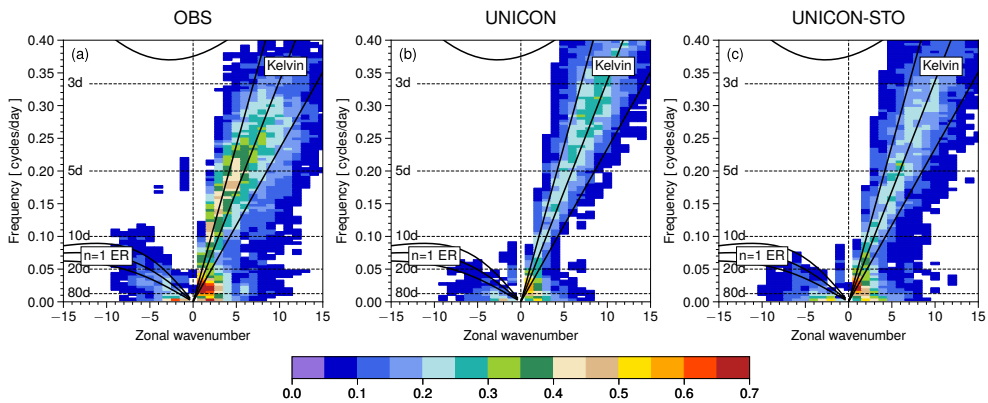

Figure 7.7 Symmetric component of coherence squared between daily anomalies of OLR and 850 hPa zonal wind averaged over 15°S-15°N from (a) the observations, (b) UNICON, and (c) UNICON-STO. The dispersion curves for Kelvin and $n = 1$ equatorial Rossby (ER) waves are shown.

for zonal wavenumber 1. Both UNICON and UNICON-STO show a lack of coherency between OLR and zonal wind in a zonal wavenumber of 2 (2 cycles along the circumference). Stochastic UNICON also improves the simulation of other equatorial waves. UNICON-STO does a better job of reproducing the observed frequency of peak coherency of Kelvin waves (5-10 days) and reproducing coherences of slow Kelvin waves (periods of 8-20 days) with zonal wavenumbers greater than 5. In addition, $n = 1$ equatorial Rossby waves are better represented in UNICON-STO.

The multivariate empirical orthogonal function (EOF) patterns of intraseasonal OLR and 850 and 200 hPa zonal winds (Figure 7.8), which are used to calculate the RMM index, confirm the low coherency between convection and wind for zonal wavenumber 2 in UNICON and UNICON-STO. The sign and order of the EOF1 and EOF2 in the simulations are adjusted to match the observations. In the observations, EOF1 shows a sharp peak of negative OLR and steep changes in zonal winds near 90°E. Note that the observed EOFs are slightly different from Wheeler and Hendon (2004) since different datasets and periods are used. In contrast to the observations, the peaks of OLR and zonal winds EOFs in the simulations are much broader, especially for EOF1. The EOF patterns of the simulations are more like sine waves with zonal wavenumber 1. The EOF structures of UNICON and UNICON-STO are almost identical. However, the total variances of EOF modes in UNICON-STO (EOF1: 17.9 %, EOF2: 21.5 %) are higher than in UNICON (EOF1: 15.1 %, EOF2: 18.4 %), which better matches with the observations (EOF1: 22.2 %, EOF2: 21.9 %).

Figure 7.9 shows lag-longitude diagrams of intraseasonal precipitation (shading) and 850 hPa zonal wind (contour) correlated against precipitation

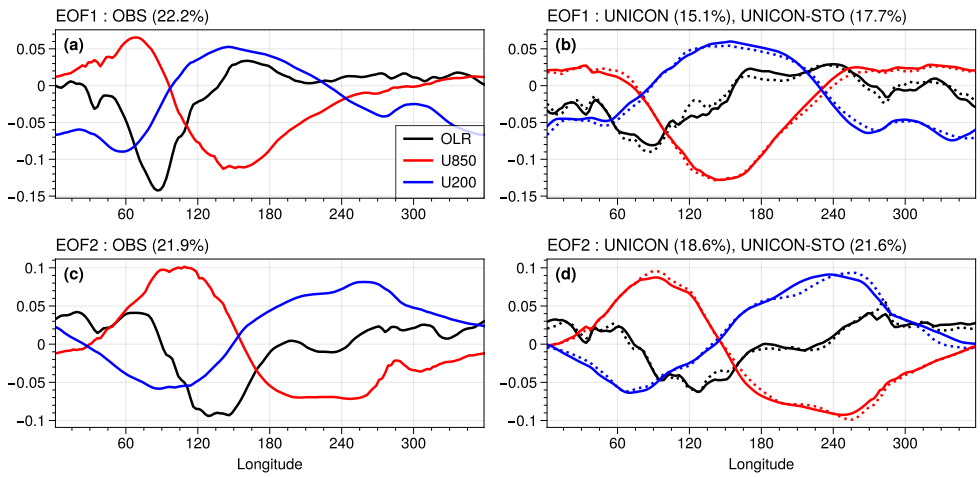

Figure 7.8 All-season multivariate first (first row) and second (second row) combined EOF modes of 20-100-day 15°S-15°N averaged 850 hPa and 200 hPa zonal winds and OLR from the (a)(c) observations, (b)(d) UNICON (dashed), and UNICON-STO (solid). The total variance accounted for each mode is shown in the parentheses at the top of each panel.

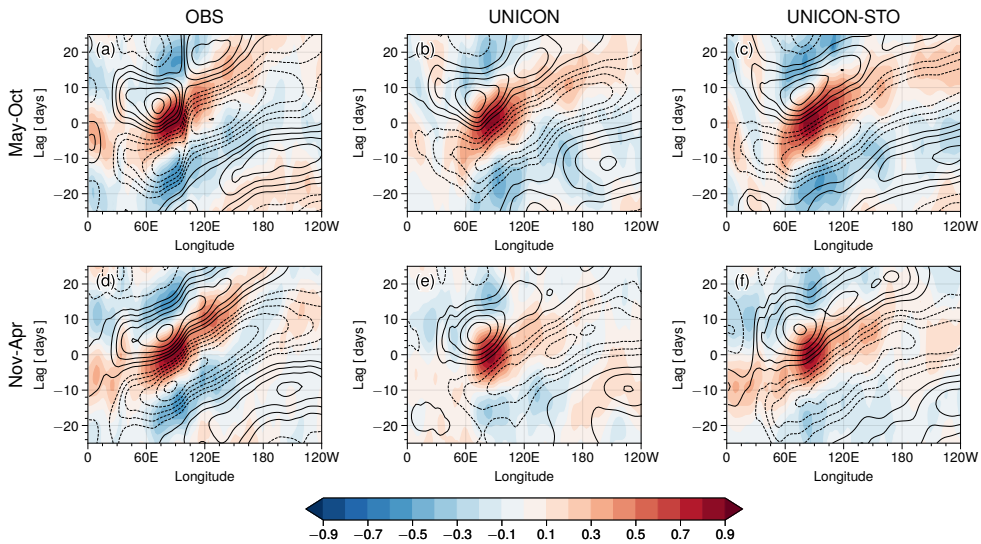

Figure 7.9 Lead-lag correlations of the 20-100-day bandpass-filtered daily precipitation (shading) and 850 hPa zonal wind (contour; 0.1 intervals) correlated to the daily time series of bandpass-filtered precipitation averaged in the area over the Indian Ocean (10°S-10°N, 80°-100°E) as a function of longitude during summer (May-October; first row) and winter (November-April; second row) of 1998-2014, from (a)(d) the observations, (b)(e) UNICON, and (c)(f) UNICON-STO.

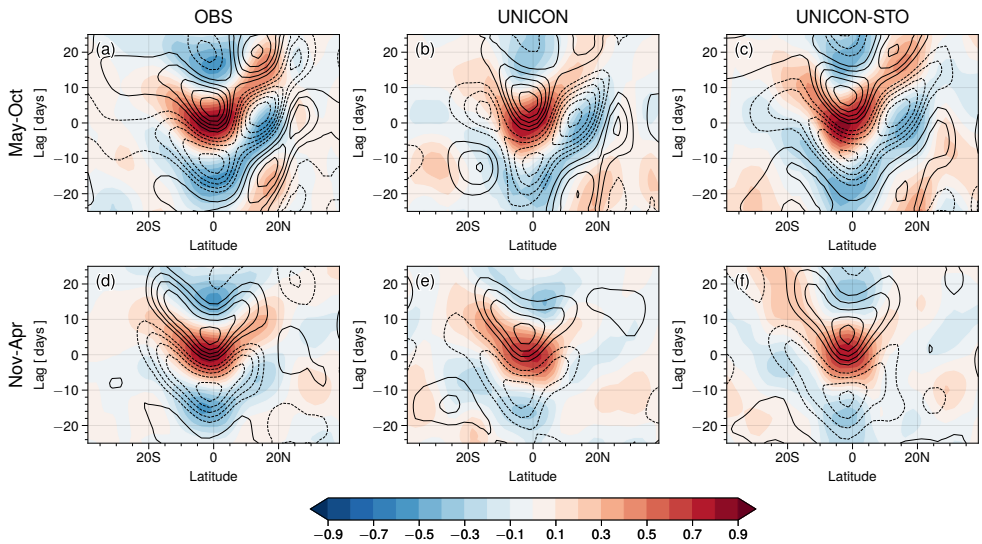

Figure 7.10 Lead-lag correlations of the 20-100-day bandpass-filtered daily precipitation (shading) and 850 hPa zonal wind (contour; 0.1 intervals) correlated to the daily time series of bandpass-filtered precipitation averaged in the area over the Indian Ocean (10°S-10°N, 80°-100°E) as a function of latitude during summer (May-October; first row) and winter (November-April; second row) of 1998-2014, from (a)(d) the observations, (b)(e) UNICON, and (c)(f) UNICON-STO.

at an Indian Ocean reference area. The figure is plotted for the period of 1998-2014 when the TRMM dataset is available. The observations show the eastward propagation of mesoscale precipitation systems and associated wind convergence across the Eastern Hemisphere with a phase speed of about $4\,\mathrm{m\,s^{-1}}$. The lag between zonal wind anomalies and precipitation anomalies is about 5–7 days. During summer, both UNICON and UNICON-STO reproduce the observed eastward propagation of the precipitation and zonal wind anomalies. However, during winter, UNICON substantially underestimates the eastward propagation of precipitation across the Maritime Continent and western equatorial Pacific and associated wind convergence. UNICON-STO simulates more realistic propagation of precipitation and zonal wind anomalies during winter. The observations show an abrupt decrease of correlation (especially 850 hPa zonal wind) at about 110°E due to the barrier effect of the Maritime Continent (Hsu and Lee 2005; Zhang and Ling 2017) during summer. The barrier effect is weaker in winter since the MJO detours the Maritime Continent (Kim et al. 2017). UNICON and UNICON-STO do not show an abrupt correlation decrease during summer, presumably because the wind anomalies over the Maritime Continent and nearby oceans are not realistically simulated. The lag-latitude diagrams (Figure 7.10) indicate that both simulations reproduce the observed northward propagation of the MJO during summer and southward propagation during winter. UNICON-STO better reproduces the observed correlation associated with northward propagation during summer, but during winter, UNICON-STO shows too elongated correlation pattern of precipitation in the southward direction.

Finally, the simulated composite life cycle of intraseasonal anomalies of OLR and 850 hPa wind vectors are examined (Figure 7.11 and 7.12). UNICON

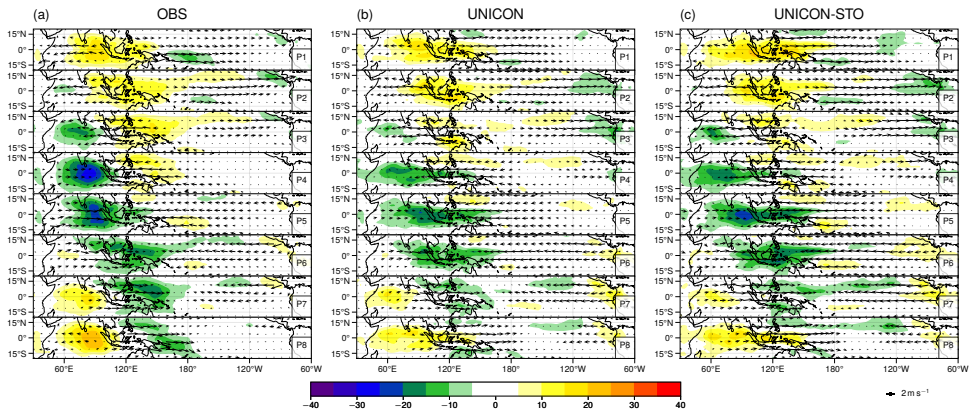

Figure 7.11 Composite of the 20-100-day bandpass-filtered daily anomalies of OLR (shading; $\mathrm{W\,m^{-2}}$) and wind vectors at 850 hPa as a function of RMM phase during November-April from (a) the observations, (b) UNICON, and (c) UNICON-STO.

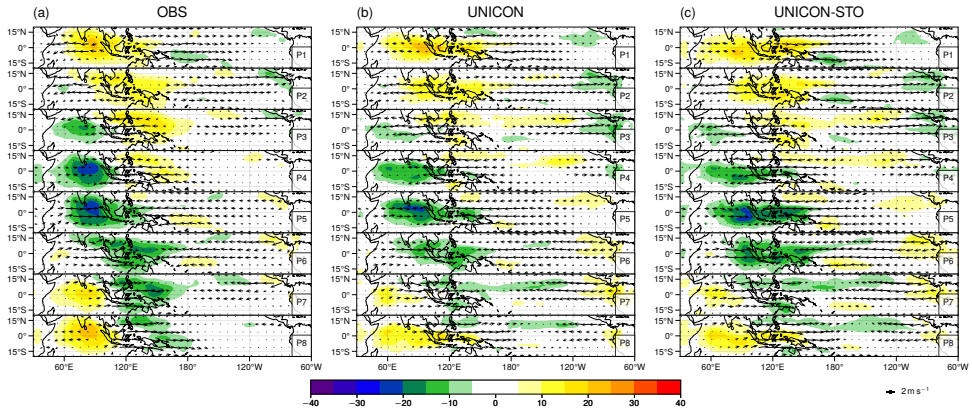

Figure 7.12 Composite of the 20-100-day bandpass-filtered daily anomalies of OLR (shading; $\mathrm{W\,m^{-2}}$) and wind vectors at 850 hPa as a function of RMM phase during May-October from (a) the observations, (b) UNICON, and (c) UNICON-STO.

simulates substantially weaker deep convection over the Indian Ocean and the western equatorial Pacific where the convection passed through the Maritime Continent during winter (Figure 7.11). UNICON-STO noticeably improves the simulation of the life cycle of the winter MJO, simulating stronger MJO-related OLR anomalies. The convection activity after passing through the Maritime Continent is more strongly maintained in UNICON-STO. Nevertheless, the two simulations exhibit too strong wind anomalies over the equatorial Pacific, as indicated by large EOF amplitudes of zonal winds over the Pacific (Figure 7.8).

7.3.3 Precipitation Budget Analysis

Before demonstrating the result of the precipitation budget analysis, we discuss the simulated characteristics of precipitation and their relation to water vapor. Figure 7.13 shows frequency spectra and the fraction of convective precipitation as a function of the daily surface precipitation rate over the tropics. UNICON-STO generally increases the frequency of intense precipitation greater than $25\,\mathrm{mm\,day^{-1}}$ with respect to UNICON. The simulated frequencies in UNICON-STO are more consistent with the TRMM observation than those in UNICON, while UNICON already simulates realistic precipitation frequency spectra. The increased frequency of heavy rainfall is related to the increase in the fraction of convective precipitation in UNICON-STO (Figure 7.13b). Over 95 % of moderate-intensity rainfall is convective precipitation (from the convection schemes) in the simulations, and the ratio of convective precipitation decreases as precipitation intensity increases. UNICON-STO increases up to 10 % of convective precipitation fraction for intense precipitation greater than $25\,\mathrm{mm\,day^{-1}}$.

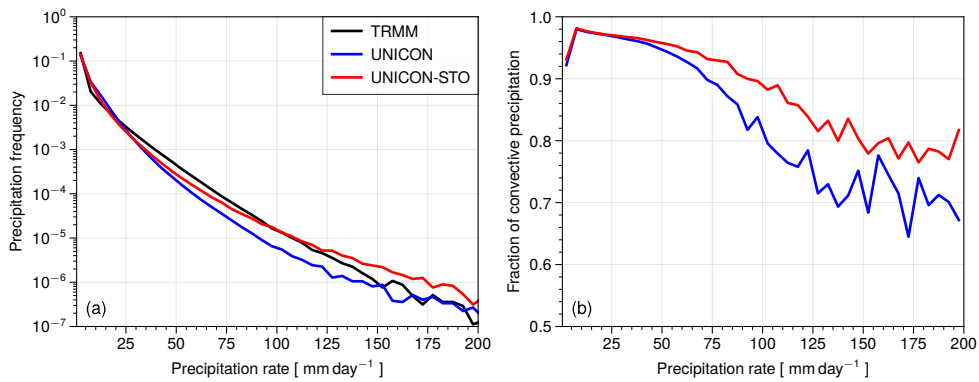

Figure 7.13 (a) Frequency spectra and (b) fraction of convective precipitation as a function of daily surface precipitation rate in the tropical region (15°S-15°N), obtained from UNICON and UNICON-STO. In (a), the frequency spectra of the TRMM 3B42v7 daily precipitation are also shown.

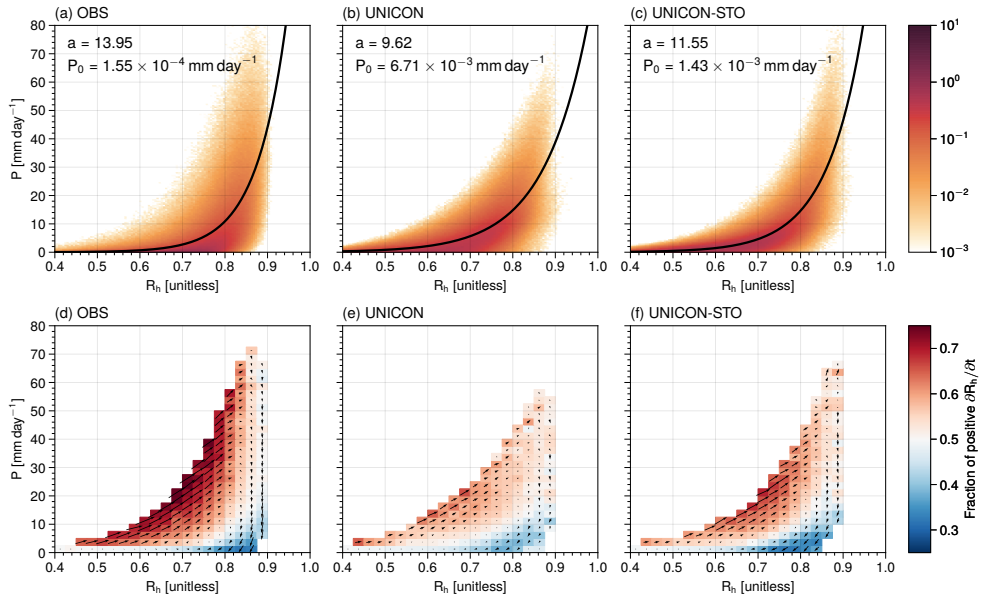

Figure 7.14 Panels in the first-row show the density plots of daily precipitation versus column relative humidity (R_h) from the (a) TRMM and ERA5 observations, (b) UNICON, and (c) UNICON-STO. The black line denotes the nonlinear least squares fit of the data in (7.3). Panels in the second-row show tendencies of R_h and precipitation as vectors and fraction of positive R_h tendency as color shading, where the data are obtained from the (d) TRMM and ERA5 observations, (e) UNICON, and (f) UNICON-STO. The vector indicates the changes of R_h and precipitation per day computed by central differencing averaged in each bin. Bins containing less than 300 data points are discarded. The data are obtained from a horizontal grid of $2.5^\circ \times 2.5^\circ$ in the area of 10°S-10°N and 60°-180°E.

The observed and simulated relationships between column relative humidity (R_h) and precipitation (P) are displayed in Figure 7.14. The data are obtained from the warm pool region where Adames (2017) determined the value of a in (7.3). The first row of the figure shows the density plots of R_h and precipitation and nonlinear least squares fits of data on (7.3). It is clear that the relationship between the two variables is exponential in the observation and simulations, while there are considerable uncertainties. The noticeable deficiency of the model simulations is the overestimation of precipitation intensity at low R_h. For $R_h = 0.7 \sim 0.75$, the simulations tend to produce light-to-moderate rain rates ($P = 5 \sim 20\,\mathrm{mm\,day^{-1}}$) too frequently, and for $R_h > 0.75$, the simulations underestimate the frequency of very light rain rates ($P < 5\,\mathrm{mm\,day^{-1}}$). Rushley et al. (2018) demonstrated that many CMIP5 models have the same issue of early precipitation pickup on a drier regime. This shows the problem of most GCMs where their convection schemes are insensitive to environmental humidity (Derbyshire et al. 2004).

The values of a determined in Figure 7.14 are used to calculate the precipitation budget for the observation and simulations. The fitted value of $a = 13.95$ from the TRMM dataset is in the range of the values obtained from other studies, 15.6 from Bretherton et al. (2004b), 12.1 from Adames (2017), and 14.72 from Rushley et al. (2018). In UNICON, a is measured as a smaller value of 9.67, while a is measured as 11.55 in UNICON-STO, showing a value in between the observation and UNICON. The larger value of a in UNICON-STO is largely contributed by increased intense precipitation in the high R_h regime (Figure 7.14c). The increased density for high R_h and P implies that UNICON-STO simulates stronger organized convection (e.g., Adames 2017). The corresponding mean convective adjustment time scales ($\overline{\tau_c}$)

computed with (7.4) (using the climatological mean of precipitation rate and vertically-integrated saturation specific humidity) over the warm pool region are 17.0 h, 25.1 h, and 22.0 h for the observations, UNICON, and UNICON-STO, respectively. The reduced convective adjustment time scale in UNICON-STO indicates that the fractional entrainment rate in the convection scheme is increased, and convection becomes more sensitive to environmental humidity. This can be explained by the fact that the mean radius of updrafts is decreased due to the increased frequency of shallow cumulus in stochastic UNICON.

The vectors in the second row of Figure 7.14 show changes in R_h and P in a day. The trajectories along the vectors show the life cycles of tropical convective systems, showing clockwise evolution around an attractor (Wolding et al. 2020). Wolding et al. (2020) categorized precipitation types using the TRMM 2A23 data, where shallow convective precipitation occurs in low R_h and P regime, deep convective precipitation occurs in the moderately moist environment ($0.6 < R_h < 0.8$) with high P, and stratiform precipitation occurs in the very moist environment ($R_h > 0.8$). UNICON largely underestimates the magnitudes of daily tendencies of R_h and P, particularly for the positive tendencies in the deep convective precipitation regime (moderate R_h). The weak positive R_h and P tendencies indicate a lack of driving mechanisms (e.g., moisture convergence) for developing organized convection. In the case of moisture convergence, it is known that shallow convection is important since the convective heating in the lower troposphere drives more moisture convergence than is removed by precipitation, resulting in a net moistening (Wolding and Maloney 2015). The positive R_h and P tendencies in the deep convective precipitation regime are considerably stronger in UNICON-STO, while they are still weaker than in the observation. The enhanced tendencies are

also consistent with the increased frequency of intense precipitation. As will be discussed later, UNICON-STO exhibits stronger moistening tendencies in the MJO developing stage, which make a more favorable condition for developing organized convection. The larger contribution of convective precipitation for rain rates greater than $25\,\mathrm{mm\,day^{-1}}$ in UNICON-STO (Figure 7.13b) also indicates increased lower-tropospheric instabilities due to the better representation of shallow convection (also see Figure 7.5b).

Since the multivariate EOF modes of the observation and simulations are substantially different, compositing precipitation budget terms to a specific RMM phase does not provide a fair comparison between the observation and simulations. Therefore, we calculate lead-lag regressions of intraseasonal precipitation budget terms against area-averaged OLR time series in the area over the Indian Ocean (5°S-5°N, 75°–85°E). We flip the sign of the regression coefficients for the figures so that the anomalies correspond to enhanced convection over the equatorial Indian Ocean. The value of the regression coefficient denotes a change in a variable against a decrease in $1\,\mathrm{W\,m^{-2}}$ of OLR. Figure 7.15 shows anomalies of OLR and precipitation tendencies on lag days 0-15 for the observation and simulations. The convection activity matures in the equatorial Indian Ocean on lag day 0, and the convection propagates across the Maritime Continent with increasing lag days. In the observation, positive precipitation tendencies (moisture recharging) precede about 10-15 days on the east of convection peaks, and negative precipitation tendencies follow the convection peaks on the west. The simulations show much weaker precipitation tendencies than the observation, and the simulated distributions of anomalies are somewhat different from the observation. The positive precipitation tendencies in the simulations propagate northeastward

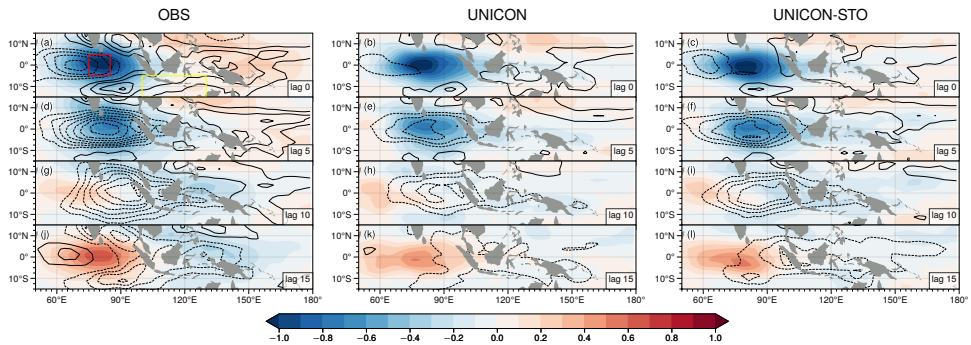

Figure 7.15 20-100-day bandpass-filtered anomalies of OLR (shaded; $\mathrm{W\,m^{-2}}$) and precipitation tendency (contour; $0.005\,\mathrm{mm\,day^{-2}}$ intervals) regressed onto the OLR time series averaged in the area over the Indian Ocean [5°S-5°N, 75°-85°E; the red box in (a)], obtained from (first column) the observations, (second column) UNICON, and (third column) UNICON-STO. The regression coefficients on lag 0, 5, 10, and 15 days are shown.

much faster and leave the Maritime Continent earlier than the observation. However, UNICON-STO simulates stronger precipitation tendencies and also better maintains negative OLR anomalies with longer lags compared to UNICON (note that negative OLR anomalies are stronger in lag day 10 over the Maritime Continent).

Figure 7.16 shows the horizontal distribution of individual precipitation budget terms on lag day 0. The sum of the four terms is approximately equal to the total precipitation tendencies (contour). The equality is not exact because of the numerical errors when computing budget terms. In the observation, the patterns of the horizontal advection terms resemble that of the total precipitation tendency with the same polarity (Figures 7.16a and 7.16d), while the evaporation term shows the opposite polarity (Figure 7.16g). The convective column process enhances moisture tendency in the equatorial Indian Ocean and the Maritime Continent area (Figure 7.16j). The patterns of the precipitation budget terms are similarly reproduced in UNICON and UNICON-STO but with weaker amplitudes. There are some regions where UNICON does not simulate the contribution by the budget terms properly. For example, UNICON simulates drying tendencies by zonal advection ($-u\partial q/\partial x$) over the Maritime Continent area, while the observation shows moistening tendencies. In addition, UNICON simulates too weak moistening by convective column process over the eastern equatorial Indian Ocean and the Maritime Continent region. UNICON-STO alleviates these deficiencies and does a better job of reproducing magnitudes of tendencies by the budget terms. The analysis from Adames (2017) demonstrated that the moistening by the convective column process is associated with bottom-heavy baroclinic vertical motion (which is related to shallow convection), and the drying is associated with

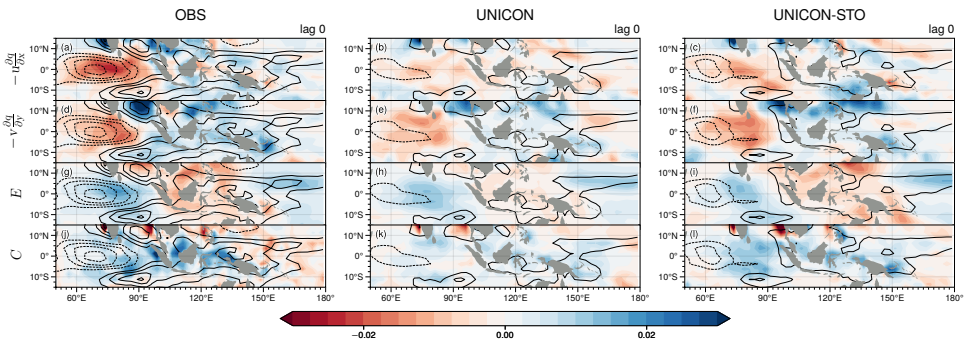

Figure 7.16 As in Figure 7.15, except that each precipitation budget term on lag day 0 is shaded.

elevated stratiform convection. Shallow convection transports moisture from PBL to the lower free troposphere, leading to tropospheric moistening and increasing precipitation. The increased moistening tendencies by the convective column process in UNICON-STO are due to a better representation of shallow convection. However, both UNICON and UNICON-STO do not reproduce drying tendencies by the convective column process over the western equatorial Pacific. This might indicate the deficiency of the convection scheme where stratiform precipitation systems in the MJO decaying stage (anvil clouds) are not realistically simulated, as shown in Section 6.6.

Figure 7.17 shows the regression coefficients of the precipitation budget terms averaged over the reference area over the Indian Ocean where the MJO events initiate. The first row of the figure shows averages during lag -15 to lag 0 days (developing period), and the second row shows averages during lag 0 to lag 15 days (decaying period). During the developing period, mean moistening tendencies exist over the area, and the largest contribution comes from the convective column process, indicating that moistening from shallow convection is a critical factor. UNICON underestimates positive precipitation tendencies in the developing period largely due to the underestimation of the convective column process and zonal advection terms. Particularly, UNICON considerably underestimates the tendencies from the convective column process during winter, indicating that the initiation of winter MJO is suppressed in UNICON (Figure 7.17b). UNICON-STO displays larger total precipitation tendencies and the tendencies from zonal advection and convective column process during the developing period of all seasons, which are more consistent with the observation. Similarly, during the decaying period, UNICON underestimates total precipitation tendencies, and UNICON-STO simulates

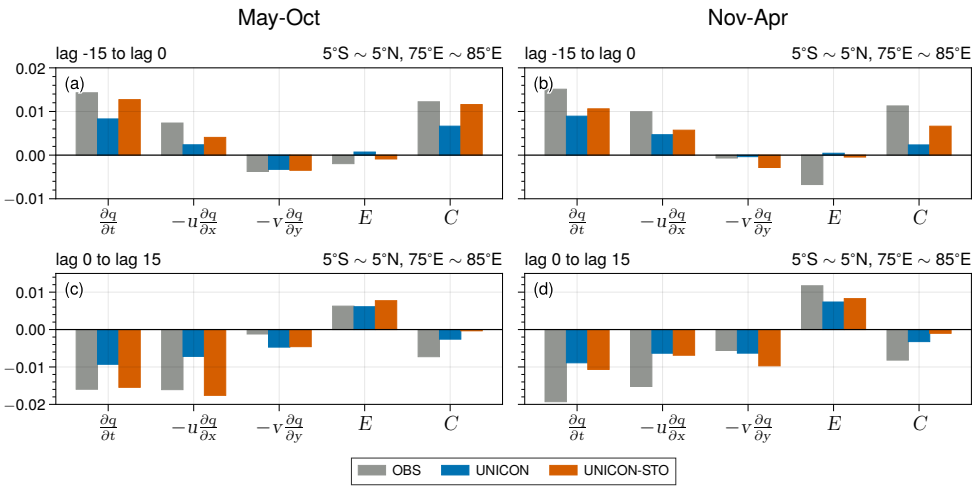

Figure 7.17 Regression coefficients of the precipitation budget terms averaged in the area over the Indian Ocean (5°S-5°N, 75°-85°E; red box in Figure 7.15a). In (a) and (b), the regression coefficients are averaged during lag -15 to lag 0 days for May-October and November-April, respectively. In (c) and (d), the regression coefficients are averaged during lag 0 to lag 15 days for May-October and November-April, respectively.

more realistic precipitation tendencies due to the increased contribution of horizontal advection terms. However, the convective column process terms in both simulations are underestimated in the decaying period, implying the unrealistic representation of stratiform precipitation systems in the simulations discussed above.

To investigate the propagation of the simulated winter MJO, the regression coefficients of budgets are averaged in the area over the southern Maritime Continent (Figure 7.18). Since the MJO detours southward of the Maritime Continent during boreal winter, the magnitudes of precipitation tendencies and budget terms during winter are much larger than those of summer. The largest contribution to the total tendencies comes from the horizontal advection terms, and a similar result is found in Kang et al. (2021). Consistent with the result above, UNICON-STO simulates improved precipitation tendencies and budget terms during early lag days in all seasons. Therefore, the improved winter MJO in UNICON-STO attributes to better simulation of moistening on the initiation of the MJO over the Indian Ocean and propagation over the southern Maritime Continent.

Lastly, the vertical structures of regression coefficients of several atmospheric variables are plotted (Figure 7.19). Jiang et al. (2015) showed that the CMIP5 models with good MJO simulations reproduce vertically tilted structures of anomalous T, q, and ω in observations, so the vertical structure of intraseasonal anomalies can be used as a measure of model performance on convective processes. The convection peak at 75°-85°E is associated with anomalous horizontal wind convergence (Figure 7.19a) and large-scale ascent motion (Figure 7.19b). The top-heavy temperature anomalies come from the strong diabatic heating at the main convection region (Jiang et al. 2015). The

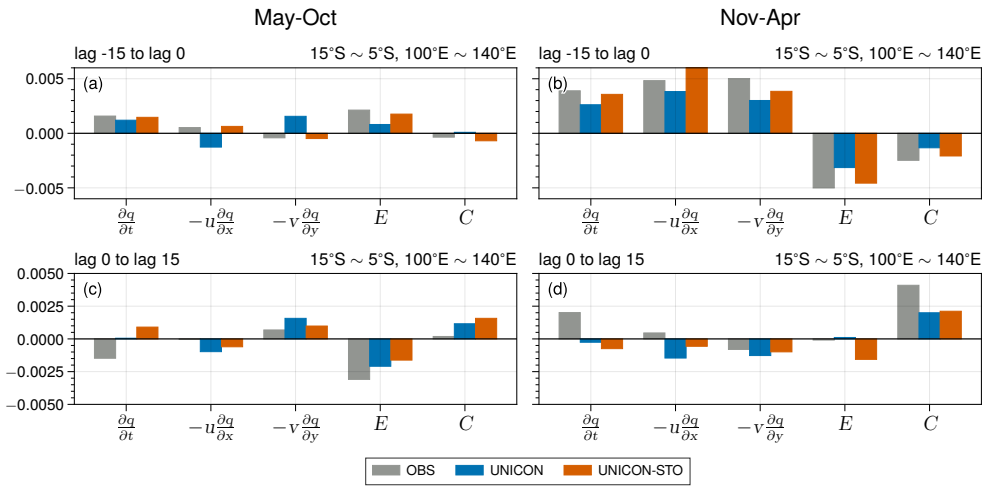

Figure 7.18 Regression coefficients of the precipitation budget terms averaged in the area over the southern Maritime Continent (15°S-5°S, 100°-140°E; the yellow box in Figure 7.15a). In (a) and (b), the regression coefficients are averaged during lag -15 to lag 0 days for May-October and November-April, respectively. In (c) and (d), the regression coefficients are averaged during lag 0 to lag 15 days for May-October and November-April, respectively.

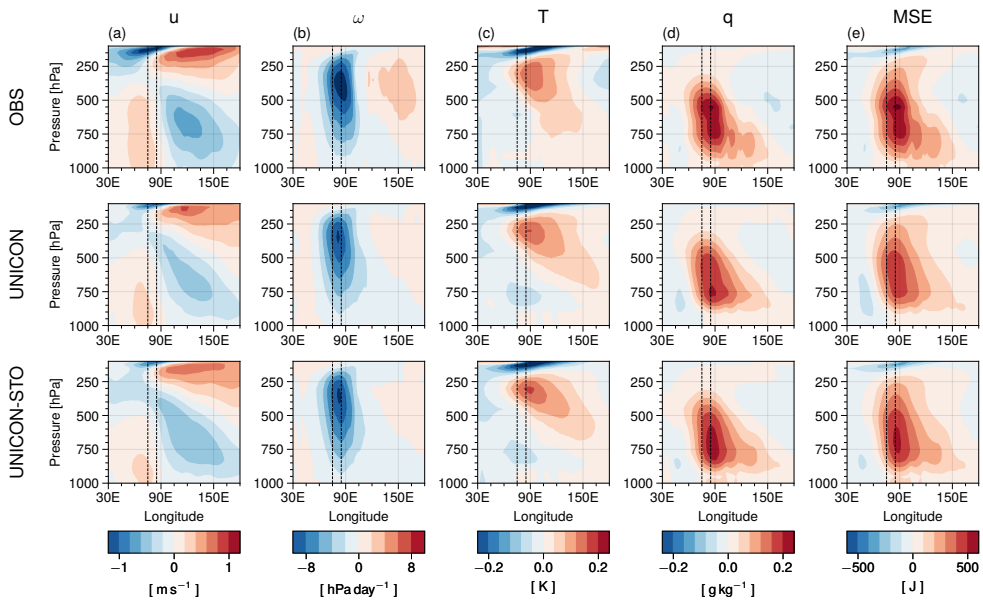

Figure 7.19 Vertical-longitudinal profiles of annual zero lag-regression coefficients of the intraseasonal anomalies of zonal wind (u), vertical pressure velocity (w), temperature (T), specific humidity (q), and moist static energy (MSE) averaged over the latitude band of 10°S-10°N. The vertical dashed lines denote the latitudes of the reference area over the Indian Ocean.

temperature anomalies show westward vertical tilts due to the lowering of convection height in the eastward direction (Figure 7.19c). The simulations reproduce the observed vertical MJO structure reasonably well. However, UNICON-STO simulates more pronounced positive specific humidity and moist static energy anomalies below 700 hPa at the east of the main convection region, signaling a better representation of the preconditioning process for the eastward propagation of the MJO. The anomalies are also enhanced in the main convection region in UNICON-STO, implying that the increased moistening intensified organized convection.

7.4 Discussion

This study emphasizes the importance of spectral representation of convection (the coexistence of shallow and deep convictions in a grid) in a GCM for realistic MJO simulation. Such a model can help understand how convective clouds with different scales interact. We can investigate intraseasonal variabilities of physical tendencies, mass fluxes, and fractional entrainment rates for different types of convection. However, it requires a model to output a large number of four-dimensional variables in high frequency, so we will leave this subject as a future study. In addition, the MJO simulations in a fully-coupled model and with different model resolutions are important issues that need to be investigated.

8 Summary and Conclusions

A convection parameterization in an atmospheric model needs to parameterize subgrid convection, which is characterized by stochastically generated multiple convective updrafts. The primary aim of this study is to develop a stochastic convection parameterization that is capable to physically simulate variability generated by multiple convective updrafts. The new stochastic convection scheme is based on unified convection scheme (UNICON; Park 2014a). Before developing stochastic UNICON, we examined the chracteristics of the global simulation using UNICON and its application. In Chapter 2, we examined the impacts of ENSO and MJO on tropical cyclone genesis based on a set of long-term coupled simulations with UNICON. The general circulation model (GCM) with UNICON, namely SEM0, reproduces the observed impacts of ENSO and MJO on tropical cyclone genesis in various regions around the world more accurately than CESM1. The inter-phase correlations between the observed and SEM0-simulated tropical cyclone genesis over the combined phases of ENSO and MJO are 0.76 and 0.54 over the western North Pacific and North Atlantic oceans, respectively, which are much greater than the corresponding values of CESM1 (0.27 and 0.25).

In Chapter 3, to enhance the forecast skill of tropical SST anomalies including ENSO, we combined a model-analog approach with a linear inverse model (MA-LIM). The model-analogue (MA) is a statistical prediction method

based on the pattern similarity between model and observation, and for this purpose we use the long-term coupled simulation with UNICON. The MA-LIM nudges monthly SST/SSH anomalies forecasted by the LIM to those forecasted by the MA with an appropriate weighting w at each forecast month. In predicting the GCM-simulated and observed Niño3.4 SST anomalies, the LIM performs better than the MA at short leads while the opposite is true at long leads. The MA-LIM with w=0.15 shows the best performance at all leads. The MA-LIM with w=0.15 retains most of the beneficial aspects of the MA and substantially remedies the undesirable aspects of the MA, resulting in the overall best performance in the tropical oceans.

In Chapter 4, we developed a stochastic UNICON which correctly simulates the variability generated by multiple stochastic plumes. The joint area PDF of updraft thermodynamic scalars at the surface is assumed to follow a correlated multivariate Gaussian distribution with its standard deviations and inter-variable correlations derived from the Monin-Obukhov (M-O) similarity theory. The radius of stochastic updraft plumes at the surface is assumed to follow a power-law distribution with a specified scale break radius, $\hat{R}_b$.

A full stochastic method launching multiple stochastic plumes at the surface is able to simulate both the ensemble-mean and variance of grid-mean convective tendency in a realistic way, but it is computationally expensive. Thus, we developed a hybrid method that launches n bin plumes and a single stochastic plume. The key ingredient of the hybrid method is to compute the grid-mean convective tendency as the weighting average of those of a single stochastic plume and n bin plumes.

First, we analyzed the LES simulation to validate the various parametric assumptions. Consistent with the assumption used in stochastic UNICON,

the LES-simulated individual PDFs of $\hat{w}$ and $\hat{\phi}$ at the surface approximately follows the correlated multivariate Gaussian distribution. It was shown that a substantial portion of the variability of convective updraft plumes at the cloud base stems from the variability at the near surface. The vertical profiles of core updraft plumes in the cloud layer are well classified by $\hat{R}_{base}$, implying that $\hat{R}_{base}$ substantially controls the variability of convective plumes. The number PDF of convective updraft plumes at the cloud base follows a well-defined power-law distribution as a function of $\hat{R}$ with a scale break radius of $R_b = 120\,\mathrm{m}$.

Next, we compared the SCM simulations with identically-forced LES. Both the full and hybrid stochastic UNICON adequately reproduce the LES-simulated grid-mean thermodynamic profiles. The properties of convective updraft plumes simulated by the stochastic UNICON are also reasonably similar to those of LES. At the cloud base, the full stochastic SCM sufficiently reproduces the LES-simulated PDFs of $\hat{w}$, $\hat{\theta}_c$, and $\hat{q}_t$ as well as the theoretical exponential distribution of subgrid $\hat{M}$. The composite vertical profiles of $\hat{\phi}$ as a function of $\hat{R}_{base}$ simulated by the full stochastic SCM are quite similar to those from LES. Consistent with the theory, stochastic UNICON adequately reproduces the expected decreases in the spatiotemporal variance of the grid-mean $\hat{M}$ as G increases, enhancing the scale-adaptivity of the original UNICON. It was also shown that all stochastic perturbations in the updraft properties at the surface (e.g., $\hat{R}$, $\hat{w}$, and $\hat{\phi}$) contribute substantially to a correct simulation of the mean thermodynamic state.

In Chapter 5, we propose a stochastic mixing model with a machine learning technique for the mass flux convection schemes. The strategy of the model is to set the stochastic differential equations (SDEs) for the following four mixing

rates presented in the governing equations of mass flux scheme: fractional entrainment rate ϵ, fractional detrainment rate δ, fractional dilution rate ϵ_ϕ, and vertical acceleration $\dot{w}$. The fractional dilution rate is defined in order to calculate the dilution of scalars by mixing process with consideration of the effect of cloud shell. The unknown parameters of the SDEs are modeled using the deep neural network which takes cloud and environment properties as inputs, and the network is trained using the BOMEX and RICO LES datasets. The following input variables for the machine learning model are selected using the permutation importance analysis: $\hat{B}$, $\hat{w}$, $\hat{q}_l$, $\hat{\theta}_c'$, $\hat{q}_t'$, and $\partial\overline{\theta_v}/\partial z$.

The performance of the ML model for predicting the mixing rates is compared with those of previously proposed parameterizations. The ML model predicts ϵ with $R^2 = 0.655$ and δ with $R^2 = 0.665$, outperforming other parameterizations. In addition, the ML model was found to represent the relationship between the input variable and ϵ or δ shown in LES well. However, the ML model predicts vertical acceleration with a relatively low predictive skill of $R^2 = 0.284$, implying that the large stochasticity is associated with the updraft vertical velocity.

The SCM experiment with the new stochastic mixing model showed a reduction of root-mean-square errors of environmental θ_c and q_t profiles by 3% and 34% in the BOMEX case, and 59% and 47% in the RICO case, respectively, compared to the original UNICON. Also, the profiles of simulated mean updraft variables consistently matched with LES profiles. The following configurations of SCM are tested: the default simulation (ML-FullVar), the simulation without the stochastic initialization (ML-MixVar), and the simulation without the stochastic mixing (ML-InitVar). In general, ML-FullVar and ML-MixVar are capable of realistically simulating the variabilities of various updrafts properties,

while the ML-InitVar produced a limited amount of variabilities. The simulation results of ML-FullVar and ML-MixVar are remarkably similar, implying that stochastic mixing is the main source of cloud variabilities.

In Chapter 6, we extended stochastic UNICON, which was originally formulated for shallow convection, to deep convection by parameterizing the impact of mesoscale organized flow on updraft properties. The variances of the joint PDF are the summation of variances from non-organized turbulence and variances from mesoscale organized flow. The variances of mesoscale organized flow are calculated from the UNICON cold pool routine. The scale break radius is parameterized as a linear function of the mesoscale organization parameter. The proposed parameterization is validated using a series of LES simulations of radiative-convective equilibrium. The parameterization is able to predict LES-measured standard deviations of convective updrafts for potential temperature and vertical velocity. The linear relationship between the mesoscale organization parameter and the scale break radius is also verified. Four parameters that are newly introduced are optimized using SCM simulations of the ten intensive observation period (IOP) cases over the ocean.

The GATEIII, TOGAII, DYNAMO-AMIE, DYNAMO-North, and DARWIN cases are time-varying forcing experiments that simulate tropical convection, and they are directly compared with IOP observations. In all five cases, stochastic UNICON reduces the negative temperature biases in the upper troposphere and negative moisture biases in the lower troposphere presented in UNICON simulations. The simulations of precipitation rates are also significantly improved by stochastic UNICON, except for the GATEIII case. In the five cases, stochastic UNICON simulates generally increased updraft

mass fluxes in the lower troposphere and stronger heating and drying tendencies by convective processes compared to UNICON.

The detailed analysis of simulated MJO in the DYNAMO-AMIE case promotes our understanding of the characteristics of simulated convection. Stochastic UNICON realistically simulates the variations of temperature and moisture anomalies associated with three MJO events, while UNICON fails to reproduce the intensity and timing of the anomalies. During the active MJO phases, UNICON and stochastic UNICON produces stronger and deeper convection due to higher relative humidity above 850 hPa level. The simulated mesoscale organization and updraft radius are also greater during the active MJO phases. The stronger heating by convection in stochastic UNICON contributes to reducing negative temperature biases in UNICON. The stronger drying tendencies by convection in stochastic UNICON, particularly during the active MJO phases, increase moistening by vertical advection and consequently reduce negative moisture biases in UNICON.

Finally, the cloud variabilities in the a near-equilibrium deep convection case are examined. Stochastic UNICON exhibits enhanced variabilities of thermodynamic variables, radius, and mass flux of updrafts at the near-surface and cloud-base height. The increased variabilities in the sub-cloud layer lead to increased variabilities in the cloud layer. The non-negligible contribution of shallow convection is found, suggesting that the improvement in the tropical convection cases by stochastic UNICON is contributed to the representation of the coexistence of shallow and deep convection.

In Chapter 7, we evaluate the global climate simulation with stochastic UNICON, focusing on the simulation of the MJO. Two AMIP simulations using the SAM0-UNICON atmospheric GCM with UNICON and stochastic UNICON

are conducted for the period 1979-2014 and compared with observations. The mean RMSEs in UNICON and UNICON-STO are almost identical, while the mean bias is reduced by 18 % from UNICON to UNICON-STO. The reduction of the mean bias largely comes from the alleviation of the mean negative shortwave cloud forcing (SWCF) bias presented in UNICON. UNICON-STO simulates much more frequent shallow convection, and the increased shallow convective heating induce a change in the feedback between radiation and clouds. As a result, positive relative humidity biases over mid-high latitudes presented in UNICON are slightly reduced and mean SWCF is increased in UNICON-STO.

Although SAM0-UNICON is one of the CMIP6 models that have relatively good MJO simulation performance (Le et al. 2021), UNICON-STO further improves various properties of MJO. A spectrum analysis indicates that UNICON-STO better reproduces the wave power maximum in the intraseasonal time scale, while UNICON produces the power maximum at a lower frequency regime. Particularly, UNICON-STO substantially improves the power of winter MJO, while UNICON simulates too weak winter MJO. UNICON-STO also enhances the wave coherency between OLR and 850 hPa zonal wind for the wave components related to the MJO, which UNICON underestimates. The lead-lag correlation analysis indicates that UNICON substantially underestimates the strengths of eastward propagation of convection and associated wind anomalies during winter, and UNICON-STO simulates more realistic propagation patterns. Still, both simulations have a common problem that simulated intraseasonal variabilities are too strong over the central and eastern equatorial Pacific.

The relationship between column relative humidity (R_h) and precipitation (P) is hypothesized as an exponential function of $P = P_0 \exp(aR_h)$. The fitted values of a in the observation, UNICON, and UNICON-STO are 13.95, 9.62, and 11.55, respectively. UNICON-STO has a larger value of a (and smaller convective adjustment time scale) than UNICON because UNICON-STO produces more frequent intense precipitation over the tropics, which better matches with the TRMM observation. These results indicate stronger development of organized convection and increased sensitivity of convection to environmental humidity, in UNICON-STO. UNICON-STO displays stronger positive R_h and P tendencies in the deep convective precipitation regime, implying that stronger moisture convergence is induced by shallow convection.

To decompose the processes that induce moisture tendencies, the precipitation budget analysis is conducted. The magnitudes of intraseasonal moisture tendencies are underestimated in both simulations, but UNICON-STO shows larger total tendencies and budget terms compared to UNICON. UNICON-STO better reproduces moistening tendencies by zonal advection over the Maritime Continent area and by convective column process over the eastern equatorial Indian Ocean. During the MJO development stage over the Indian Ocean, UNICON-STO simulates increased moistening tendencies primarily due to the enhanced convective column process. The vertical structures of MJO-related anomalies confirm that these moistening tendencies are located in the lower troposphere before convection matures.

9 Appendix

9.1 Appendix A: Computation of Convective Tendencies by Stochastic Plumes Sampled from an Area PDF

In our stochastic UNICON, the normalized thermodynamic variable α for convective updraft plumes at the surface is sampled from the area PDF, $P_a(\alpha) \equiv da(\alpha)/d\alpha$. The use of the area PDF is inevitable, because the M-O similarity theory on which the closure of our stochastic UNICON is based is derived from the area average of instantaneous pointwise observations. Once a set of α^i ($\alpha = \alpha_{\hat{w}}, \alpha_{\hat{\theta}_c}, \alpha_{\hat{q}_t}, \alpha_{\hat{u}}, \alpha_{\hat{v}}, \alpha_{\hat{R}}$) is sampled from the multivariate Gaussian area PDF for a specific updraft plume, i ($1 \leq i \leq n_s$), we can compute the plume number density $\hat{N}^i = \hat{a}/\pi\hat{R^i}^2 = (\hat{R}_e^2/\hat{R^i}^2)/G$ using the fractional area $\hat{a}^i = \pi\hat{R}_e^2/G$ and the radius $\hat{R}^i$, where R_e is from (4.16). Our stochastic UNICON computes the convective tendency for a single updraft plume with $\hat{R}^i$ and then multiplies it by its number, $G\hat{N}^i$, which will be referred to as η_s^i. In the case of the full stochastic method ($n_s = G\hat{N}$), the final grid-mean convective tendency is $\eta = \sum_{i=1}^{G\hat{N}} \eta_s^i$, where $\hat{N}$ is the plume number density sampled from the Poisson distribution (4.18). In the case of the single stochastic method ($n_s = 1$), the final grid mean convective tendency is $\eta = G\hat{N}\eta_s^1$. In the case of the hybrid stochastic method ($n_s = 1$), $\eta_s = \eta_s^1$ in (4.20).

9.2 Appendix B: Computation of the Cumulative Density Function (CDF) and the Bin Plume Properties from the Correlated Multivariate Gaussian Distribution

Following the notation of Tallis (1961), the probability density function (PDF) of a correlated multivariate Gaussian distribution of the normalized variables, $\mathbf{x} = (x_1, x_2, ..., x_n)^T$, where n is the number of variables and T is a transpose, can be written as

$$\phi_n(x_1, x_2, ..., x_n) = (2\pi)^{-n/2}|\mathbf{R}|^{-1/2}\exp(-\frac{1}{2}\mathbf{x}^T\mathbf{R}^{-1}\mathbf{x}), \tag{9.1}$$

where $\mathbf{R}$ is a symmetric correlation matrix, $|\mathbf{R}|$ is a determinant of $\mathbf{R}$, and $\mathbf{R}^{-1}$ is an inverse of $\mathbf{R}$. As explained in Section 4.2.2, the transformation of $\alpha_{\hat{R}}$ to $\hat{x} = \hat{R}/R_b$ uses the cumulative density function (CDF) of $P_a(\alpha_{\hat{R}})$ and $P_a(\hat{x})$. The CDF of $P_a(\hat{x})$ is obtained by numerically integrating (4.15). The CDF of $P_a(\alpha_{\hat{R}})$ can be obtained in a similar way by integrating the correlated multivariate Gaussian PDF in the regime of $\alpha_{\hat{w}} > 0$. From (9.1), the joint PDF of $\alpha_{\hat{w}}$ and $\alpha_{\hat{R}}$ is

$$\phi_2(\alpha_{\hat{w}}, \alpha_{\hat{R}}) = \begin{cases} \dfrac{1}{\pi\sqrt{1-r_{wR}^2}}\exp\left(-\dfrac{\alpha_{\hat{R}}^2 + \alpha_{\hat{w}}^2 - 2r_{wR}\alpha_{\hat{R}}\alpha_w}{2(1-r_{wR}^2)}\right), & \alpha_{\hat{w}} > 0, \\ 0, & \alpha_{\hat{w}} \leq 0, \end{cases} \tag{9.2}$$

where r_{wR} is the correlation coefficient between $\alpha_{\hat{w}}$ and $\alpha_{\hat{R}}$. The corresponding CDF as a function of $\alpha_{\hat{R}}$ becomes

$$H(\alpha_{\hat{R}}) = \int_{-\infty}^{\alpha_{\hat{R}}} \int_{0}^{\infty} \frac{1}{\pi\sqrt{1-r_{wR}^2}} \exp\left(-\frac{\alpha_{\hat{R}}^2 + \alpha_{\hat{w}}^2 - 2r_{wR}\alpha_{\hat{R}}\alpha_{\hat{w}}}{2(1-r_{wR}^2)}\right) d\alpha_{\hat{w}} d\alpha_{\hat{R}}$$
$$= \frac{1}{\sqrt{2\,\pi}} \int_{-\infty}^{\alpha_{\hat{R}}} e^{-\alpha_{\hat{R}}^2/2} \left(1 - \text{ erf}\left(-\frac{r_{wR}\,\alpha_{\hat{R}}}{\sqrt{2}\,\sqrt{1-r_{wR}^2}}\right)\right) d\alpha_{\hat{R}} \tag{9.3}$$

which is solved numerically and then used for the transform between $\alpha_{\hat{R}}$ and $\hat{x} = \hat{R}/R_b$ in (4.17).

Stochastic UNICON launches n bin plumes from the surface with a set of mean thermodynamic properties of an individual bin plume. Binning of the multi-variables is performed by defining the bin edges of the variable $\hat{\phi}$ as

$$\alpha_{\hat{\phi}}^{i} = \Phi_{\hat{\phi}}^{-1}(i/n_b(\hat{\phi})), \quad 0 \le i \le n_b(\hat{\phi}), \tag{9.4}$$

where $\Phi_{\hat{\phi}}$ is the CDF of $\hat{\phi}$ and $n(\hat{\phi})$ is the number of bins for $\hat{\phi}$. In the case of HYB12 where $n_b = 12$, $n_b(\hat{R}) = 3$, $n_b(\hat{\theta}_c) = 2$, and $n_b(\hat{q}_t) = 2$. Stochastic UNICON computes the thermodynamic properties of an individual bin using a Monte-Carlo method, i.e., by sampling a large number of random points from the multivariate Gaussian distribution and averaging the points in each bin. With a constant random seed, our Monte-Carlo method does not generate an artificial stochastic variance.

9.3 Appendix C: Computation of Lagrangian Tendencies for the Tracked Updrafts

The fractional dilution rate ϵ_ϕ^t and the vertical acceleration $\dot{w}$ are calculated using Lagrangian tracking of each convective updraft. We calculate these rates as mean tendency during $\Delta t = 60\,\mathrm{s}$ which is the LES output sampling frequency. Let's consider an updraft parcel at height z and time t. The vertical position of the parcel is updated in time with forward differencing with a small sub-step time interval of $\Delta t_{\mathrm{sub}} = 1\,\mathrm{s}$, and then the parcel position at $t + \Delta t$ can be obtained after 60 sub-steps. The updraft vertical velocity between time interval $[t, t + \Delta t]$ is calculated using a linear interpolation between model vertical grid points and sampling times. Similarly, the parcel position at $t - \Delta t$ is calculated using the backward differencing method. Hereinafter, any updraft property x at time $t - \Delta t$, t, and $t + \Delta t$ are denoted as x^{t-1}, x^t, and x^{t+1}, respectively.

The fractional dilution rate is estimated using the decaying passive tracer which is already used to define the plume region in LES. The fractional dilution rates ϵ_ϕ at time t and $t - \Delta t$ are calculated as

$$\epsilon_\phi^t = -\frac{1}{\hat{s}^{\,t+\frac{1}{2}} - \overline{s}^{\,t+\frac{1}{2}}} \left(\frac{\hat{s}^{\,t+1} - \hat{s}^{\,t}}{\Delta t} + \frac{\hat{s}^{\,t+\frac{1}{2}}}{\tau} \right), \tag{9.5}$$

$$\epsilon_\phi^{t-1} = -\frac{1}{\hat{s}^{\,t-\frac{1}{2}} - \overline{s}^{\,t-\frac{1}{2}}} \left(\frac{\hat{s}^{\,t} - \hat{s}^{\,t-1}}{\Delta t} + \frac{\hat{s}^{\,t-\frac{1}{2}}}{\tau} \right), \tag{9.6}$$

where $\hat{s}$ and $\overline{s}$ are the mean concentration of the decaying passive tracer within updraft and environment, respectively, and τ is the decaying time scale of the tracer. The superscript $t + \frac{1}{2}$ denotes the average of values at t and $t + \Delta t$ (e.g. $\hat{s}^{\,t+\frac{1}{2}} = \frac{1}{2}\left(\hat{s}^{\,t+1} + \hat{s}^{\,t}\right)$), and similar for $t - \frac{1}{2}$. The term associated with τ is added to compensate the decaying tendency of the tracer. The vertical

acceleration $\dot{w}$ are calculated as

$$\dot{w}^{\,t} = \frac{\hat{w}^{\,t+1} - \hat{w}^{\,t}}{\Delta t}, \tag{9.7}$$

$$\dot{w}^{\,t-1} = \frac{\hat{w}^{\,t} - \hat{w}^{\,t-1}}{\Delta t}. \tag{9.8}$$

9.4 Appendix D: Computation of mesoscale perturbations in UNICON

UNICON divides the horizontal grid within the PBL into three regions: cold pools ($a_{\rm cp}$), uplift region of mesoscale organized flow (a_Ω), and the remaining portion where perturbations by mesoscale organized flow are zero ($1-a_{\rm cp}-a_\Omega$). The area-weighted sum of perturbations of a conservative scalar ϕ by mesoscale organized flow of these three regions should be zero:

$$a_\Omega \Delta\phi_\Omega + a_{\rm cp}\Delta\phi_{\rm cp} = 0, \tag{9.9}$$

where $\Delta\phi_\Omega = \phi_\Omega - \phi_{\rm PBL}$ is the mean perturbation of ϕ in the uplift region of mesoscale organized flow and $\Delta\phi_{\rm cp} = \phi_{\rm cp} - \phi_{\rm PBL}$ is the mean perturbation of ϕ of cold pools ($\phi_{\rm PBL}$ is the mean ϕ in PBL). a_Ω is parameterized as $a_\Omega = C_\Omega \hat{A}_s$, where $\hat{A}_s = 0.04$ is the net updraft fractional area at the surface and $C_\Omega = 5$ is a constant parameter. Therefore, $\Delta\phi_\Omega$ is computed as

$$\Delta\phi_\Omega = -\frac{a_{\rm cp}\Delta\phi_{\rm cp}}{C_\Omega \hat{A}_s}, \quad \phi = \theta_c, q_t, u, v, \xi. \tag{9.10}$$

For vertical velocity, it is assumed that a certain fraction of available potential energy in PBL is converted into mesoscale kinetic energy through a convective overturning process. Δw_Ω is computed as

$$\Delta w_\Omega = a_{\rm cp}\left[\left(\frac{g}{\theta_{v,\rm ref}}\right)\left(\frac{k_* h \theta_v'}{C_\Omega \hat{A}_s}\right)\right]^{1/2}, \tag{9.11}$$

where g is the gravitational acceleration, $\theta_{v,\mathrm{ref}} = 300\,\mathrm{K}$ is the reference virtual potential temperature, $k_* = 0.08$ is the conversion factor of available potential energy, h is the PBL-top height, and θ'_v is the virtual potential temperature difference between cold pools and other area. UNICON assumes that the properties of convective updrafts at the near-surface are modulated by the subgrid mesoscale organized flow.

9.5 Appendix E: The Relationship between Low-level Cloud Amount and Its Proxies over the Globe by Cloud Type

We extend upon previous work to examine the relationship between low-level cloud amount (LCA) and various proxies for LCA – estimated low-level cloud fraction (ELF), lower tropospheric stability (LTS), and estimated inversion strength (EIS) – by low-level cloud type (CL) over the globe using individual surface and upper-air observations. Individual CL has its own distinct environmental structure, and therefore our extended analysis by CL can provide insights into the strengths and weaknesses of various proxies and help to improve them.

Overall, ELF performs better than LTS and EIS in diagnosing the variations in LCA among various CLs, indicating that a previously identified superior performance of ELF compared to LTS and EIS as a global proxy for LCA comes from its realistic correlations with various CLs rather than with a specific CL. However, ELF, LTS, and EIS have a problem in diagnosing the changes in LCA when noCL (no low-level cloud) is reported and also when Cu (cumulus) is reported over deserts where background stratus does not exist. This incorrect

diagnosis of noCL as a cloudy condition is more clearly seen in the analysis of individual CL frequencies binned by proxy values. If noCL is excluded, ELF, LTS, and EIS have good inter-CL correlations with the amount when present (AWP) of individual CLs. In the future, an advanced ELF needs to be formulated to deal with the decrease in LCA when the inversion base height is lower than the lifting condensation level to diagnose cumulus updraft fraction, as well as the amount of stratiform clouds and detrained cumulus, and to parameterize the scale height as a function of appropriate environmental variables.

Bibliography

Abadi, M. et al., 2015: *TensorFlow: large-scale machine learning on heterogeneous systems*. Software available from tensorflow.org. URL: `https://www.tensorflow.org/`.

Adames, Á. F., 2017: Precipitation budget of the Madden–Julian oscillation. *Journal of the Atmospheric Sciences*, **74**, 1799–1817.

Adler, R. F. et al., 2003: The version-2 global precipitation climatology project (GPCP) monthly precipitation analysis (1979-present). *Journal of Hydrometeorology*, **4**, 1147–1167.

Ahn, M.-S., D. Kim, D. Kang, J. Lee, K. R. Sperber, P. J. Gleckler, X. Jiang, Y.-G. Ham, and H. Kim, 2020: MJO propagation across the Maritime Continent: Are CMIP6 models better than CMIP5 models? *Geophysical Research Letters*, **47**, e2020GL087250.

Ahn, M.-S., D. Kim, S. Park, and Y.-G. Ham, 2019: Do we need to parameterize mesoscale convective organization to mitigate the MJO-mean state trade-off? *Geophysical Research Letters*, **46**, 2293–2301.

Ahn, M.-S., D. Kim, K. R. Sperber, I.-S. Kang, E. Maloney, D. Waliser, and H. Hendon, 2017: MJO simulation in CMIP5 climate models: MJO skill metrics and process-oriented diagnosis. *Climate Dynamics*, **49**, 4023–4045.

Alexander, M. A., I. Bladé, M. Newman, J. R. Lanzante, N.-C. Lau, and J. D. Scott, 2002: The atmospheric bridge: The influence of ENSO teleconnections on air–sea interaction over the global oceans. *Journal of Climate*, **15**, 2205–2231.

Alexander, M. A., N.-C. Lau, and J. D. Scott, 2004: Broadening the atmospheric bridge paradigm: ENSO teleconnections to the tropical west Pacific-Indian Oceans over the seasonal cycle and to the North Pacific in summer. *Earth?s Climate: The Ocean-Atmosphere Interaction, Geophys. Monogr*, **147**, 85–103.

Altmann, A., L. Toloşi, O. Sander, and T. Lengauer, 2010: Permutation importance: A corrected feature importance measure. *Bioinformatics*, **26**, 1340–1347.

An, S.-I., and F.-F. Jin, 2004: Nonlinearity and asymmetry of ENSO. *Journal of Climate*, **17**, 2399–2412.

Andreas, E. L., R. J. Hill, J. R. Gosz, D. I. Moore, W. D. Otto, and A. D. Sarma, 1998: Statistics of surface-layer turbulence over terrain with metre-scale heterogeneity. *Boundary-Layer Meteorology*, **86**, 379–408.

Arakawa, A., and W. Schubert, 1974: Interaction of a cumulus cloud ensemble with the large-scale environment, Part I. *Journal of the Atmospheric Sciences*, **31**, 674–701.

Baba, Y., 2019: Spectral cumulus parameterization based on cloud-resolving model. *Climate Dynamics*, **52**, 309–334.

Baba, Y., 2021: Improved intraseasonal variability in the initialization of SINTEX-F2 using a spectral cumulus parameterization. *International Journal of Climatology*, **41**, 6690–6712.

Baba, Y., and M. A. Giorgetta, 2020: Tropical variability simulated in ICON-A with a spectral cumulus parameterization. *Journal of Advances in Modeling Earth Systems*, **12**, e2019MS001732.

Balmaseda, M. A., K. Mogensen, and A. T. Weaver, 2013: Evaluation of the ECMWF ocean reanalysis system ORAS4. *Quarterly Journal of the Royal Meteorological Society*, **139**, 1132–1161.

Barrett, B. S., and L. M. Leslie, 2009: Links between tropical cyclone activity and Madden–Julian oscillation phase in the North Atlantic and northeast Pacific basins. *Monthly Weather Review*, **137**, 727–744.

Bechtold, P., M. Köhler, T. Jung, F. Doblas-Reyes, M. Leutbecher, M. J. Rodwell, F. Vitart, and G. Balsamo, 2008: Advances in simulating atmospheric variability with the ECMWF model: from synoptic to decadal time-scales. *Quarterly Journal of the Royal Meteorological Society*, **134**, 1337–1351.

Bell, R., K. Hodges, P. L. Vidale, J. Strachan, and M. Roberts, 2014: Simulation of the global ENSO–tropical cyclone teleconnection by a high-resolution coupled general circulation model. *Journal of Climate*, **27**, 6404–6422.

Bellenger, H., É. Guilyardi, J. Leloup, M. Lengaigne, and J. Vialard, 2014: ENSO representation in climate models: from CMIP3 to CMIP5. *Climate Dynamics*, **42**, 1999–2018.

Bentamy, A., P. Queffeulou, Y. Quilfen, and K. Katsaros, 1999: Ocean surface wind fields estimated from satellite active and passive microwave instruments. *IEEE Transactions on Geoscience and Remote Sensing*, **37**, 2469–2486.

Betts, A., and M. Miller, 1986: A new convective adjustment scheme. Part II: Single column tests using GATE wave, BOMEX, ATEX and arctic airmass data sets. *Quarterly Journal of the Royal Meteorological Society*, **112**, 693–709.

Betts, A. K., 1975: Parametric interpretation of trade-wind cumulus budget studies. *Journal of the Atmospheric Sciences*, **32**, 1934–1945.

Beucler, T., M. Pritchard, S. Rasp, J. Ott, P. Baldi, and P. Gentine, 2021: Enforcing analytic constraints in neural networks emulating physical systems. *Physical Review Letters*, **126**, 098302.

Blossey, P. N., C. S. Bretherton, M. Zhang, A. Cheng, S. Endo, T. Heus, Y. Liu, A. P. Lock, S. R. de Roode, and K.-M. Xu, 2013: Marine low cloud sensitivity to an idealized climate change: the CGILS LES intercomparison. *Journal of Advances in Modeling Earth Systems*, **5**, 234–258.

Böing, S. J., H. J. Jonker, A. P. Siebesma, and W. W. Grabowski, 2012: Influence of the subcloud layer on the development of a deep convective ensemble. *Journal of the Atmospheric Sciences*, **69**, 2682–2698.

Bretherton, C. S., J. R. McCaa, and H. Grenier, 2004a: A new parameterization for shallow cumulus convection and its application to marine subtropical cloud-topped boundary layers. Part I: description and 1D results. *Monthly Weather Review*, **132**, 864–882.

Bretherton, C. S., and S. Park, 2009: A new moist turbulence parameterization in the community atmosphere model. *Journal of Climate*, **22**, 3422–3448.

Bretherton, C. S., M. E. Peters, and L. E. Back, 2004b: Relationships between water vapor path and precipitation over the tropical oceans. *Journal of Climate*, **17**, 1517–1528.

Brockwell, P. J., R. J. Hyndman, and G. K. Grunwald, 1991: Continuous time threshold autoregressive models. *Statistica Sinica*, 401–410.

Buizza, R., M Milleer, and T. N. Palmer, 1999: Stochastic representation of model uncertainties in the ecmwf ensemble prediction system. *Quarterly Journal of the Royal Meteorological Society*, **125**, 2887–2908.

Cai, Q., G. J. Zhang, and T. Zhou, 2013: Impacts of shallow convection on MJO simulation: a moist static energy and moisture budget analysis. *Journal of Climate*, **26**, 2417–2431.

Camargo, S. J., K. A. Emanuel, and A. H. Sobel, 2007: Use of a genesis potential index to diagnose ENSO effects on tropical cyclone genesis. *Journal of Climate*, **20**, 4819–4834.

Camargo, S. J., M. C. Wheeler, and A. H. Sobel, 2009: Diagnosis of the MJO modulation of tropical cyclogenesis using an empirical index. *Journal of the Atmospheric Sciences*, **66**, 3061–3074.

Chan, J. C., 1985: Tropical cyclone activity in the northwest Pacific in relation to the El Niño/Southern Oscillation phenomenon. *Monthly Weather Review*, **113**, 599–606.

Chand, S. S., K. J. Tory, H. Ye, and K. J. Walsh, 2017: Projected increase in El Niño-driven tropical cyclone frequency in the Pacific. *Nature Climate Change*, **7**, 123.

Cheinet, S., 2003: A multiple mass-flux parameterization for the surface-generated convection. part i: dry plumes. *Journal of the Atmospheric Sciences*, **60**, 2313–2327.

Chen, B., and B. E. Mapes, 2018: Effects of a simple convective organization scheme in a two-plume GCM. *Journal of Advances in Modeling Earth Systems*, **10**, 867–880.

Chen, C.-C., J. H. Richter, C. Liu, M. W. Moncrieff, Q. Tang, W. Lin, S. Xie, and P. J. Rasch, 2021: Effects of organized convection parameterization on the MJO and precipitation in E3SMv1. Part I: Mesoscale heating. *Journal of Advances in Modeling Earth Systems*, **13**, e2020MS002401.

Chen, G., J. Ling, R. Zhang, Z. Xiao, and C. Li, 2022: The MJO from CMIP5 to CMIP6: Perspectives from tracking MJO precipitation. *Geophysical Research Letters*, **49**, e2021GL095241.

Chen, J.-H., and S.-J. Lin, 2011: The remarkable predictability of inter-annual variability of Atlantic hurricanes during the past decade. *Geophysical Research Letters*, **38**.

Cheng, M., C. Lu, and Y. Liu, 2015: Variation in entrainment rate and relationship with cloud microphysical properties on the scale of 5 m. *Science Bulletin*, **60**, 707–717.

Chu, J.-H., C. R. Sampson, A. S. Levine, and E. Fukada, 2002: The joint typhoon warning center tropical cyclone best-tracks, 1945–2000. *Ref. NRL/MR/7540-02*, **16**.

Chu, P.-S., 2004: ENSO and tropical cyclone activity. *Hurricanes and typhoons: Past, present, and potential*, 297–332.

Chu, P.-S., and J. Wang, 1997: Tropical cyclone occurrences in the vicinity of Hawaii: Are the differences between El Niño and non–El Niño years significant? *Journal of Climate*, **10**, 2683–2689.

Cohen, B. G., and G. C. Craig, 2006: Fluctuations in an equilibrium convective ensemble. Part II: Numerical experiments. *Journal of the Atmospheric Sciences*, **63**, 2005–2015.

Couvreux, F, F Hourdin, and C Rio, 2010: Resolved versus parametrized boundary-layer plumes. Part I: a parametrization-oriented conditional sampling in large-eddy simulations. *Boundary-Layer Meteorology*, **134**, 441–458.

Couvreux, F. et al., 2021: Process-based climate model development harnessing machine learning: I. A calibration tool for parameterization improvement. *Journal of Advances in Modeling Earth Systems*, **13**, e2020MS002217.

Craig, G. C., and B. G. Cohen, 2006: Fluctuations in an equilibrium convective ensemble. Part I: Theoretical formulation. *Journal of the Atmospheric Sciences*, **63**, 1996–2004.

Cybenko, G., 1989: Approximation by superpositions of a sigmoidal function. *Mathematics of Control, Signals and Systems*, **2**, 303–314.

Davini, P., F. D'Andrea, S.-B. Park, and P. Gentine, 2017: Coherent structures in large-eddy simulations of a nonprecipitating stratocumulus-topped boundary layer. *Journal of the Atmospheric Sciences*, **74**, 4117–4137.

Dawe, J. T., and P. H. Austin, 2011a: Interpolation of LES cloud surfaces for use in direct calculations of entrainment and detrainment. *Monthly Weather Review*, **139**, 444–456.

Dawe, J. T., and P. H. Austin, 2011b: The influence of the cloud shell on tracer budget measurements of LES cloud entrainment. *Journal of the Atmospheric Sciences*, **68**, 2909–2920.

Dawe, J. T., and P. H. Austin, 2012: Statistical analysis of an LES shallow cumulus cloud ensemble using a cloud tracking algorithm. *Atmospheric Chemistry and Physics*, **12**, 1101–1119.

Dawe, J. T., and P. H. Austin, 2013: Direct entrainment and detrainment rate distributions of individual shallow cumulus clouds in an LES. *Atmospheric Chemistry and Physics Discussions*, **13**, 5365–5410.

De La Chevrotiere, M., B. Khouider, and A. J. Majda, 2014: Calibration of the stochastic multicloud model using Bayesian inference. *SIAM Journal on Scientific Computing*, **36**, B538–B560.

Deb, K., 2014: Multi-objective optimization. *Search methodologies*. Springer, 403–449.

Derbyshire, S. H., I. Beau, P. Bechtold, J.-Y. Grandpeix, J.-M. Piriou, J.-L. Redelsperger, and P. M. M. Soares, 2004: Sensitivity of moist convection to environmental humidity. *Quarterly Journal of the Royal Meteorological Society*, **130**, 3055–3079.

Dillon, J. V., I. Langmore, D. Tran, E. Brevdo, S. Vasudevan, D. Moore, B. Patton, A. Alemi, M. Hoffman, and R. A. Saurous, 2017: TensorFlow distributions. *arXiv preprint arXiv:1711.10604*.

Ding, H., M. Newman, M. A. Alexander, and A. T. Wittenberg, 2018: Skillful climate forecasts of the tropical Indo-Pacific ocean using model-analogs. *Journal of Climate*, **31**, 5437–5459.

Ding, H., M. Newman, M. A. Alexander, and A. T. Wittenberg, 2019: Diagnosing secular variations in retrospective ENSO seasonal forecast skill using CMIP5 model-analogs. *Geophysical Research Letters*, **46**, 1721–1730.

D'Andrea, F., P. Gentine, A. K. Betts, and B. R. Lintner, 2014: Triggering deep convection with a probabilistic plume model. *Journal of the Atmospheric Sciences*, **71**, 3881–3901.

Esbensen, S., 1978: Bulk thermodynamic effects and properties of small tropical cumuli. *Journal of the Atmospheric Sciences*, **35**, 826–837.

Eyring, V., S. Bony, G. A. Meehl, C. A. Senior, B. Stevens, R. J. Stouffer, and K. E. Taylor, 2016: Overview of the Coupled Model Intercomparison Project Phase 6 (CMIP6) experimental design and organization. *Geoscientific Model Development*, **9**, 1937–1958.

Feng, Z., S. Hagos, A. K. Rowe, C. D. Burleyson, M. N. Martini, and S. P. de Szoeke, 2015: Mechanisms of convective cloud organization by cold pools over tropical warm ocean during the AMIE/DYNAMO field campaign. *Journal of Advances in Modeling Earth Systems*, **7**, 357–381.

Frierson, D. M. W., 2007: The dynamics of idealized convection schemes and their effect on the zonally averaged tropical circulation. *Journal of the Atmospheric Sciences*, **64**, 1959–1976.

Fu, Q., S. K. Krueger, and K. Liou, 1995: Interactions of radiation and convection in simulated tropical cloud clusters. *Journal of the Atmospheric Sciences*, **52**, 1310–1328.

González, J., Z. Dai, P. Hennig, and N. Lawrence, 2016: Batch Bayesian optimization via local penalization. *Artificial intelligence and statistics*. PMLR, 648–657.

Gray, W. M., 1984: Atlantic seasonal hurricane frequency. Part I: El Niño and 30 mb quasi-biennial oscillation influences. *Monthly Weather Review*, **112**, 1649–1668.

Gregory, D., 2001: Estimation of entrainment rate in simple models of convective clouds. *Quarterly Journal of the Royal Meteorological Society*, **127**, 53–72.

Hall, J. D., A. J. Matthews, and D. J. Karoly, 2001: The modulation of tropical cyclone activity in the Australian region by the Madden–Julian oscillation. *Monthly Weather Review*, **129**, 2970–2982.

Hannah, W. M., 2017: Entrainment versus dilution in tropical deep convection. *Journal of the Atmospheric Sciences*, **74**, 3725–3747.

Hannah, W. M., and E. D. Maloney, 2011: The role of moisture–convection feedbacks in simulating the Madden–Julian oscillation. *Journal of Climate*, **24**, 2754–2770.

Hendon, H. H., M. C. Wheeler, and C. Zhang, 2007: Seasonal dependence of the MJO–ENSO relationship. *Journal of Climate*, **20**, 531–543.

Hersbach, H. et al., 2020: The ERA5 global reanalysis. *Quarterly Journal of the Royal Meteorological Society*, **146**, 1999–2049.

Heureux, M. L., A. F. Levine, M. Newman, C. Ganter, J. Luo, M. K. Tippett, and T. N. Stockdale, 2019: El-Nino-Southern Oscillation (ENSO) in a changing climate. Volume 10. AGU Books. Wiley-Blackwell, 489.

Heus, T., G. van Dijk, H. J. Jonker, and H. E. van den Akker, 2008a: Mixing in shallow cumulus clouds studied by Lagrangian particle tracking. *Journal of the Atmospheric Sciences*, **65**, 2581–2597.

Heus, T., F. Pols, H. Jonker, H. van den Akker, and D. Lenschow, 2008b: Analysis of the downward transport in RICO observations. *18th Symposium on Boundary Layers and Turbulence.*

Heus, T., and A. Seifert, 2013: Automated tracking of shallow cumulus clouds in large domain, long duration large eddy simulations. *Geoscientific Model Development*, **6**, 1261–1273.

Ho, C.-H., J.-H. Kim, J.-H. Jeong, H.-S. Kim, and D. Chen, 2006: Variation of tropical cyclone activity in the South Indian Ocean: El Niño–Southern Oscillation and Madden-Julian Oscillation effects. *Journal of Geophysical Research: Atmospheres*, **111**.

Hohenegger, C., and B. Stevens, 2013: Preconditioning deep convection with cumulus congestus. *Journal of the Atmospheric Sciences*, **70**, 448–464.

Holland, J. Z., and E. M. Rasmusson, 1973: Measurements of the atmospheric mass, energy, and momentum budgets over a 500-kilometer square of tropical ocean. *Monthly Weather Review*, **101**, 44–55.

Honnert, R., G. A. Efstathiou, R. J. Beare, J. Ito, A. Lock, R. Neggers, R. S. Plant, H. H. Shin, L. Tomassini, and B. Zhou, 2020: The atmospheric boundary layer and the "gray zone" of turbulence: A critical review. *Journal of Geophysical Research: Atmospheres*, **125**, e2019JD030317.

Honnert, R., V. Masson, and F. Couvreux, 2011: A diagnostic for evaluating the representation of turbulence in atmospheric models at the kilometric scale. *Journal of the Atmospheric Sciences*, **68**, 3112–3131.

Hourdin, F., D. Williamson, C. Rio, F. Couvreux, R. Roehrig, N. Villefranque, I. Musat, L. Fairhead, F. B. Diallo, and V. Volodina, 2021: Process-based climate model development harnessing machine learning: II. Model calibration from single column to global. *Journal of Advances in Modeling Earth Systems*, **13**, e2020MS002225.

Houze, R. A., and A. K. Betts, 1981: Convection in GATE. *Reviews of Geophysics*, **19**, 541–576.

Houze Jr, R. A., 2004: Mesoscale convective systems. *Reviews of Geophysics*, **42**.

Hsu, H.-H., and M.-Y. Lee, 2005: Topographic effects on the eastward propagation and initiation of the Madden–Julian oscillation. *Journal of Climate*, **18**, 795–809.

Huffman, G., D. Bolvin, E. Nelkin, D. Wolff, R. Adler, G. Gu, Y. Hong, K. Bowman, and E. Stocker, 2007: The TRMM Multisatellite Precipitation Analysis (TMPA): Quasi-global, multiyear, combined-sensor precipitation estimates at fine scales. *Journal of Hydrometeorology*, **8**, 38–55. ISSN: 1525-7541.

Hurrell, J. W., M. M. Holland, P. R. Gent, S. Ghan, J. E. Kay, P. J. Kushner, J.-F. Lamarque, W. G. Large, D Lawrence, K. Lindsay, et al., 2013: The community earth system model: a framework for collaborative research. *Bulletin of the American Meteorological Society*, **94**, 1339–1360.

Iacono, M. J., J. S. Delamere, E. J. Mlawer, M. W. Shephard, S. A. Clough, and W. D. Collins, 2008: Radiative forcing by long-lived greenhouse gases: Calculations with the AER radiative transfer models. *Journal of Geophysical Research: Atmospheres*, **113**.

Iizuka, S., and T. Matsuura, 2008: ENSO and western North Pacific tropical cyclone activity simulated in a CGCM. *Climate dynamics*, **30**, 815–830.

Janiga, M. A., and C. Zhang, 2016: MJO moisture budget during DYNAMO in a cloud-resolving model. *Journal of the Atmospheric Sciences*, **73**, 2257–2278.

Jiang, X., M. Zhao, and D. E. Waliser, 2012: Modulation of tropical cyclones over the eastern Pacific by the intraseasonal variability simulated in an AGCM. *Journal of Climate*, **25**, 6524–6538.

Jiang, X. et al., 2015: Vertical structure and physical processes of the Madden-Julian oscillation: Exploring key model physics in climate simulations. *Journal of Geophysical Research: Atmospheres*, **120**, 4718–4748.

Jin, F.-F., J Boucharel, and I.-I. Lin, 2014: Eastern Pacific tropical cyclones intensified by El Niño delivery of subsurface ocean heat. *Nature*, **516**, 82.

Johnson, R. H., P. E. Ciesielski, and T. M. Rickenbach, 2016: A further look at Q1 and Q2 from TOGA COARE. *Meteorological Monographs*, **56**, 1.1 –1.12.

Jones, D. R., M. Schonlau, and W. J. Welch, 1998: Efficient global optimization of expensive black-box functions. *Journal of Global Optimization*, **13**, 455–492.

Kain, J. S., 2004: The Kain–Fritsch convective parameterization: an update. *Journal of Applied Meteorology*, **43**, 170–181.

Kain, J. S., and J. M. Fritsch, 1990: A one-dimensional entraining/detraining plume model and its application in convective parameterization. *Journal of the Atmospheric Sciences*, **47**, 2784–2802.

Kalnay, E., M. Kanamitsu, R. Kistler, W. Collins, D Deaven, L Gandin, M. Iredell, S. Saha, G. White, J. Woollen, et al., 1996: The ncep/ncar 40-year reanalysis project. *Bulletin of the American meteorological Society*, **77**, 437–471.

Kang, D., D. Kim, M.-S. Ahn, and S.-I. An, 2021: The role of the background meridional moisture gradient on the propagation of the MJO over the Maritime Continent. *Journal of Climate*, **34**, 6565–6581.

Keane, R. J., G. C. Craig, C. Keil, and G. Zängl, 2014: The Plant–Craig stochastic convection scheme in ICON and its scale adaptivity. *Journal of the Atmospheric Sciences*, **71**, 3404–3415.

Keane, R. J., and R. S. Plant, 2012: Large-scale length and time-scales for use with stochastic convective parametrization. *Quarterly Journal of the Royal Meteorological Society*, **138**, 1150–1164.

Kessler, E., 1969: On the distribution and continuity of water substance in atmospheric circulations. *On the distribution and continuity of water substance in atmospheric circulations*. Springer, 1–84.

Khairoutdinov, M. F., and Y. Kogan, 2000: A new cloud physics parameterization in a large-eddy simulation model of marine stratocumulus. *Monthly Weather Review*, **128**, 229–243.

Khairoutdinov, M. F., S. K. Krueger, C.-H. Moeng, P. A. Bogenschutz, and D. A. Randall, 2009: Large-eddy simulation of maritime deep tropical convection. *Journal of Advances in Modeling Earth Systems*, **1**, Art. #15.

Kim, D., H. Kim, and M.-I. Lee, 2017: Why does the MJO detour the Maritime Continent during austral summer? *Geophysical Research Letters*, **44**, 2579–2587.

Kim, D., M.-I. Lee, H.-M. Kim, S. D. Schubert, and J. H. Yoo, 2014: The modulation of tropical storm activity in the Western North Pacific by the Madden–Julian Oscillation in GEOS-5 AGCM experiments. *Atmospheric Science Letters*, **15**, 335–341.

Kingma, D. P., and J. Ba, 2015: Adam: A method for stochastic optimization. *arXiv preprint arXiv:1412.6980*.

Klambauer, G., T. Unterthiner, A. Mayr, and S. Hochreiter, 2017: Self-normalizing neural networks. *Proceedings of the 31st international conference on neural information processing systems*, 972–981.

Klocke, D., R. Pincus, and J. Quaas, 2011: On constraining estimates of climate sensitivity with present-day observations through model weighting. *Journal of Climate*, **24**, 6092–6099.

Kogan, Y., 2013: A cumulus cloud microphysics parameterization for cloud-resolving models. *Journal of the Atmospheric Sciences*, **70**, 1423–1436.

Kurowski, M. J., K. Suselj, W. W. Grabowski, and J. Teixeira, 2018: Shallow-to-deep transition of continental moist convection: cold pools, surface fluxes, and mesoscale organization. *Journal of the Atmospheric Sciences*, **75**, 4071–4090.

Lander, M. A., 1994: An exploratory analysis of the relationship between tropical storm formation in the western North Pacific and ENSO. *Monthly Weather Review*, **122**, 636–651.

Langhans, W., J. Mueller, and W. D. Collins, 2019: Optimization of the eddy-diffusivity/mass-flux shallow cumulus and boundary-layer parameterization using surrogate models. *Journal of Advances in Modeling Earth Systems*, **11**, 402–416.

Langhans, W., and D. M. Romps, 2015: The origin of water vapor rings in tropical oceanic cold pools. *Geophysical Research Letters*, **42**, 7825–7834.

Lau, N.-C., and M. J. Nath, 1996: The role of the "atmospheric bridge" in linking tropical Pacific ENSO events to extratropical SST anomalies. *Journal of Climate*, **9**, 2036–2057.

Lavender, S. L., and A. J. Matthews, 2009: Response of the West African monsoon to the Madden–Julian oscillation. *Journal of Climate*, **22**, 4097–4116.

Lawrence, M. G., and P. J. Rasch, 2005: Tracer transport in deep convective updrafts: plume ensemble versus bulk formulations. *Journal of the Atmospheric Sciences*, **62**, 2880–2894.

Le, P. V., C. Guilloteau, A. Mamalakis, and E. Foufoula-Georgiou, 2021: Underestimated MJO variability in CMIP6 models. *Geophysical Research Letters*, **48**, e2020GL092244.

Lee, R. W., S. J. Woolnough, A. J. Charlton-Perez, and F. Vitart, 2019: ENSO modulation of MJO teleconnections to the North Atlantic and Europe. *Geophysical Research Letters*, **46**, 13535–13545.

Letham, B., B. Karrer, G. Ottoni, and E. Bakshy, 2019: Constrained Bayesian optimization with noisy experiments. *Bayesian Analysis*, **14**, 495–519.

Li, C., and C. Wang, 2014: Simulated impacts of two types of ENSO events on tropical cyclone activity in the western North Pacific: large-scale atmospheric response. *Climate dynamics*, **42**, 2727–2743.

Li, G., and S.-P. Xie, 2014: Tropical biases in CMIP5 multimodel ensemble: the excessive equatorial Pacific cold tongue and double ITCZ problems. *Journal of Climate*, **27**, 1765–1780.

Li, R. C., W. Zhou, J. C. Chan, and P. Huang, 2012: Asymmetric modulation of western North Pacific cyclogenesis by the Madden–Julian oscillation under ENSO conditions. *Journal of Climate*, **25**, 5374–5385.

Li, X., T.-K. L. Wong, R. T. Chen, and D. Duvenaud, 2020: Scalable gradients for stochastic differential equations. *International Conference on Artificial Intelligence and Statistics*. PMLR, 3870–3882.

Liebmann, B., H. H. Hendon, and J. D. Glick, 1994: The relationship between tropical cyclones of the western Pacific and Indian Oceans and the Madden-Julian oscillation. *Journal of the Meteorological Society of Japan. Ser. II*, **72**, 401–412.

Liebmann, B., and C. A. Smith, 1996: Description of a complete (interpolated) outgoing longwave radiation dataset. *Bulletin of the American Meteorological Society*, **77**, 1275–1277.

Lin, J.-L., G. N. Kiladis, B. E. Mapes, K. M. Weickmann, K. R. Sperber, W. Lin, M. C. Wheeler, S. D. Schubert, A. Del Genio, L. J. Donner, et al., 2006: Tropical intraseasonal variability in 14 IPCC AR4 climate models. Part I: Convective signals. *Journal of climate*, **19**, 2665–2690.

Lin, J. W.-B., and J. D. Neelin, 2000: Influence of a stochastic moist convective parameterization on tropical climate variability. *Geophysical research letters*, **27**, 3691–3694.

Lin, J. W.-B., and J. D. Neelin, 2002: Considerations for stochastic convective parameterization. *Journal of the Atmospheric Sciences*, **59**, 959–975.

Lin, S.-J., and R. B. Rood, 1996: Multidimensional flux-form semi-Lagrangian transport schemes. *Monthly Weather Review*, **124**, 2046–2070.

Lin, X., and R. H. Johnson, 1996: Kinematic and thermodynamic characteristics of the flow over the western Pacific warm pool during TOGA COARE. *Journal of the Atmospheric Sciences*, **53**, 695–715.

Liu, X. et al., 2012: Toward a minimal representation of aerosols in climate models: Description and evaluation in the Community Atmosphere Model CAM5. *Geoscientific Model Development*, **5**, 709–739.

Liu, X., O. Tsukamot, T. Oikawa, and E. Ohtaki, 1998: A study of correlations of scalar quantities in the atmospheric surface layer. *Boundary-Layer Meteorology*, **87**, 499–508.

Loeb, N. G., B. A. Wielicki, D. R. Doelling, G. L. Smith, D. F. Keyes, S. Kato, N. Manalo-Smith, and T. Wong, 2009: Toward optimal closure of the earth's top-of-atmosphere radiation budget. *Journal of Climate*, **22**, 748–766.

Lorenz, D. J., and D. L. Hartmann, 2006: The effect of the MJO on the North American monsoon. *Journal of Climate*, **19**, 333–343.

Lu, C., Y. Liu, G. J. Zhang, X. Wu, S. Endo, L. Cao, Y. Li, and X. Guo, 2016: Improving parameterization of entrainment rate for shallow convection with aircraft measurements and large-eddy simulation. *Journal of the Atmospheric Sciences*, **73**, 761–773.

Lu, C., C. Sun, Y. Liu, G. J. Zhang, Y. Lin, W. Gao, S. Niu, Y. Yin, Y. Qiu, and L. Jin, 2018: Observational relationship between entrainment rate and environmental relative humidity and implications for convection parameterization. *Geophysical Research Letters*, **45**, 495–504.

Madden, R. A., and P. R. Julian, 1971: Detection of a 40-50 day oscillation in the zonal wind in the tropical Pacific. *Journal of the Atmospheric Sciences*, **28**, 702–708.

Maloney, E. D., and D. L. Hartmann, 2000a: Modulation of eastern North Pacific hurricanes by the Madden–Julian oscillation. *Journal of Climate*, **13**, 1451–1460.

Maloney, E. D., and D. L. Hartmann, 2000b: Modulation of hurricane activity in the Gulf of Mexico by the Madden-Julian oscillation. *Science*, **287**, 2002–2004.

Mapes, B., and R. Neale, 2011: Parameterizing convective organization to escape the entrainment dilemma. *Journal of Advances in Modeling Earth Systems*, **3**, M06004.

Maronga, B., and J. Reuder, 2017: On the formulation and universality of monin–obukhov similarity functions for mean gradients and standard deviations in the unstable surface layer: results from surface-layer-resolving large-eddy simulations. *Journal of the Atmospheric Sciences*, **74**, 989–1010.

May, P. T., J. H. Mather, G. Vaughan, C. Jakob, G. M. McFarquhar, K. N. Bower, and G. G. Mace, 2008: The tropical warm pool international cloud experiment. *Bulletin of the American Meteorological Society*, **89**, 629–646.

Mckay, M., R. Beckman, and W. Conover, 1979: A comparison of three methods for selecting vales of input variables in the analysis of output from a computer code. *Technometrics*, **21**, 239–245.

Mellado, J. P., 2017: Cloud-top entrainment in stratocumulus clouds. *Annual Review of Fluid Mechanics*, **49**, 145–169.

Monin, A., and A. Obukhov, 1954: Basic laws of turbulent mixing in the surface layer of the atmosphere. *Contrib. Geophys. Inst. Acad. Sci. USSR*, **151**, 163–187.

Moon, J.-Y., B. Wang, and K.-J. Ha, 2011: ENSO regulation of MJO teleconnection. *Climate Dynamics*, **37**, 1133–1149.

Morrison, H., and A. Gettelman, 2008: A new two-moment bulk stratiform cloud microphysics scheme in the Community Atmosphere Model, version 3 (CAM3). Part I: Description and numerical tests. *Journal of Climate*, **21**, 3642–3659.

Murakami, H., and M. Sugi, 2010: Effect of model resolution on tropical cyclone climate projections. *Sola*, **6**, 73–76.

Murphy, J. M., D. M. Sexton, D. N. Barnett, G. S. Jones, M. J. Webb, M. Collins, and D. A. Stainforth, 2004: Quantification of modelling uncertainties in a large ensemble of climate change simulations. *Nature*, **430**, 768–772.

Neale, R., and J. Slingo, 2003: The Maritime Continent and its role in the global climate: A GCM study. *Journal of Climate*, **16**, 834–848.

Neale, R. B., C.-C. Chen, A. Gettelman, P. H. Lauritzen, S. Park, D. L. Williamson, A. J. Conley, R. Garcia, D. Kinnison, J.-F. Lamarque, et al., 2010: Description of the NCAR community atmosphere model (CAM 5.0). *NCAR Tech. Note NCAR/TN-486+ STR*, **1**, 1–12.

Neelin, J. D., A. Bracco, H. Luo, J. C. McWilliams, and J. E. Meyerson, 2010: Considerations for parameter optimization and sensitivity in climate models. *Proceedings of the National Academy of Sciences*, **107**, 21349–21354.

Neggers, R., 2015: Exploring bin-macrophysics models for moist convective transport and clouds. *Journal of Advances in Modeling Earth Systems*, **7**, 2079–2104.

Neggers, R., P. Griewank, and T Heus, 2019: Power-law scaling in the internal variability of cumulus cloud size distributions due to subsampling and spatial organization. *Journal of the Atmospheric Sciences*, **76**, 1489–1503.

Neggers, R., H. Jonker, and A. Siebesma, 2003: Size statistics of cumulus cloud populations in large-eddy simulations. *Journal of the Atmospheric Sciences*, **60**, 1060–1074.

Neggers, R., A. Siebesma, and H. Jonker, 2002: A multiparcel model for shallow cumulus convection. *Journal of the Atmospheric Sciences*, **59**, 1655–1668.

Newman, M., and P. D. Sardeshmukh, 2017: Are we near the predictability limit of tropical Indo-Pacific sea surface temperatures? *Geophysical Research Letters*, **44**, 8520–8529.

O'Brien, T. A., F. Li, W. D. Collins, S. A. Rauscher, T. D. Ringler, M. Taylor, S. M. Hagos, and L. R. Leung, 2013: Observed scaling in clouds and precipitation and scale incognizance in regional to global atmospheric models. *Journal of Climate*, **26**, 9313–9333.

O'Malley, T., E. Bursztein, J. Long, F. Chollet, H. Jin, L. Invernizzi, et al., 2019: *Keras Tuner*. `https://github.com/keras-team/keras-tuner`.

Ooyama, K., 1971: A theory on parameterization of cumulus convection. *Journal of the Meteorological Society of Japan. Ser. II*, **49**, 744–756.

Orbe, C., L. V. Roekel, Ángel F. Adames, A. Dezfuli, J. Fasullo, P. J. Gleckler, J. Lee, W. Li, L. Nazarenko, G. A. Schmidt, K. R. Sperber, and M. Zhao, 2020: Representation of modes of variability in six US climate models. *Journal of Climate*, **33**, 7591–7617.

Ott, J., M. Pritchard, N. Best, E. Linstead, M. Curcic, and P. Baldi, 2020: A Fortran-Keras deep learning bridge for scientific computing. *Scientific Programming*, **2020**.

Palmer, T. N., R Buizza, F Doblas-Reyes, T. Jung, M. Leutbecher, G. J. Shutts, M Steinheimer, and A. Weisheimer, 2009: Stochastic parametrization and model uncertainty. *ECMWF Technical Memoranda*, **598**, 1–42.

Pan, D.-M., and D. D. Randall, 1998: A cumulus parameterization with a prognostic closure. *Quarterly Journal of the Royal Meteorological Society*, **124**, 949–981.

Panofsky, H. A., H Tennekes, D. H. Lenschow, and J. Wyngaard, 1977: The characteristics of turbulent velocity components in the surface layer under convective conditions. *Boundary-Layer Meteorology*, **11**, 355–361.

Park, S., 2004: Remote ENSO influence on Mediterranean sky conditions during late summer and autumn: Evidence for a slowly evolving atmospheric bridge. *Quarterly Journal of the Royal Meteorological Society: A journal of the atmospheric sciences, applied meteorology and physical oceanography*, **130**, 2409–2422.

Park, S., 2014a: A unified convection scheme (UNICON). Part I: formulation. *Journal of the Atmospheric Sciences*, **71**, 3902–3930.

Park, S., 2014b: A unified convection scheme (UNICON). Part II: simulation. *Journal of the Atmospheric Sciences*, **71**, 3931–3973.

Park, S., E.-H. Baek, B.-M. Kim, and S.-J. Kim, 2017: Impact of detrained cumulus on climate simulated by the Community Atmosphere Model Version 5 with a unified convection scheme. *Journal of Advances in Modeling Earth Systems*, **9**, 1399–1411.

Park, S., and C. S. Bretherton, 2009: The University of Washington shallow convection and moist turbulence schemes and their impact on climate simulations with the Community Atmosphere Model. *Journal of Climate*, **22**, 3449–3469.

Park, S., C. S. Bretherton, and P. J. Rasch, 2014: Integrating cloud processes in the community atmosphere model, version 5. *Journal of Climate*, **27**, 6821–6856.

Park, S., and C. B. Leovy, 2004: Marine low-cloud anomalies associated with ENSO. *Journal of Climate*, **17**, 3448–3469.

Park, S., J. Shin, S. Kim, E. Oh, and Y. Kim, 2019: Global climate simulated by the Seoul National University atmosphere model version 0 with a unified convection scheme (SAM0-UNICON). *Journal of Climate*, **32**, 2917–2949.

Pathak, R., H. P. Dasari, S. El Mohtar, A. C. Subramanian, S. Sahany, S. K. Mishra, O. Knio, and I. Hoteit, 2021: Uncertainty quantification and Bayesian inference of cloud parameterization in the NCAR single column community atmosphere model (SCAM6). *Frontiers in Climate*, **3**, 1–23.

Penland, C., and P. D. Sardeshmukh, 1995: The optimal growth of tropical sea surface temperature anomalies. *Journal of climate*, **8**, 1999–2024.

Pincus, R., H. W. Barker, and J.-J. Morcrette, 2003: A fast, flexible, approximate technique for computing radiative transfer in inhomogeneous cloud fields. *Journal of Geophysical Research: Atmospheres*, **108**.

Plant, R. S., and G. C. Craig, 2008: A stochastic parameterization for deep convection based on equilibrium statistics. *Journal of the Atmospheric Sciences*, **65**, 87–105.

Powell, S. W., and R. A. Houze Jr., 2013: The cloud population and onset of the Madden-Julian oscillation over the Indian ocean during DYNAMO-AMIE. *Journal of Geophysical Research: Atmospheres*, **118**, 11979–11995.

Rasmussen, C. E., 2003: Gaussian processes in machine learning. *Summer School on Machine Learning*. Springer, 63–71.

Rasmusson, E. M., and T. H. Carpenter, 1982: Variations in tropical sea surface temperature and surface wind fields associated with the Southern Oscillation/El Niño. *Monthly Weather Review*, **110**, 354–384.

Rasp, S., M. S. Pritchard, and P. Gentine, 2018: Deep learning to represent subgrid processes in climate models. *Proceedings of the National Academy of Sciences*, **115**, 9684–9689.

Rauber, R. M. et al., 2007: Rain in shallow cumulus over the ocean: the RICO campaign. *Bulletin of the American Meteorological Society*, **88**, 1912–1928.

Raymond, D. J., and A. M. Blyth, 1986: A stochastic mixing model for non-precipitating cumulus clouds. *Journal of the Atmospheric Sciences*, **43**, 2708–2718.

Rayner, N., D. E. Parker, E. Horton, C. K. Folland, L. V. Alexander, D. Rowell, E. Kent, and A Kaplan, 2003: Global analyses of sea surface temperature, sea ice, and night marine air temperature since the late nineteenth century. *Journal of Geophysical Research: Atmospheres*, **108**.

Rickenbach, T. M., and S. A. Rutledge, 1998: Convection in TOGA COARE: horizontal scale, morphology, and rainfall production. *Journal of the Atmospheric Sciences*, **55**, 2715–2729.

Romps, D. M., 2010: A direct measure of entrainment. *Journal of the Atmospheric Sciences*, **67**, 1908–1927.

Romps, D. M., 2016: The stochastic parcel model: a deterministic parameterization of stochastically entraining convection. *Journal of Advances in Modeling Earth Systems*, **8**, 319–344.

Romps, D. M., and Z. Kuang, 2010: Nature versus nurture in shallow convection. *Journal of the Atmospheric Sciences*, **67**, 1655–1666.

Roode, S. R. de, A. P. Siebesma, H. J. J. Jonker, and Y. de Voogd, 2012: Parameterization of the vertical velocity equation for shallow cumulus clouds. *Monthly Weather Review*, **140**, 2424–2436.

Rooy, W. C. de, P. Bechtold, K. Fröhlich, C. Hohenegger, H. Jonker, D. Mironov, A Pier Siebesma, J. Teixeira, and J.-I. Yano, 2013: Entrainment and detrainment in cumulus convection: an overview. *Quarterly Journal of the Royal Meteorological Society*, **139**, 1–19.

Rooy, W. C. de, and A. P. Siebesma, 2008: A simple parameterization for detrainment in shallow cumulus. *Monthly Weather Review*, **136**, 560–576.

Ropelewski, C. F., and M. S. Halpert, 1987: Global and regional scale precipitation patterns associated with the El Niño/Southern Oscillation. *Monthly weather review*, **115**, 1606–1626.

Rowell, D. P., 2001: Teleconnections between the tropical Pacific and the Sahel. *Quarterly Journal of the Royal Meteorological Society*, **127**, 1683–1706.

Rushley, S. S., D. Kim, C. S. Bretherton, and M.-S. Ahn, 2018: Reexamining the nonlinear moisture-precipitation relationship over the tropical oceans. *Geophysical Research Letters*, **45**, 1133–1140.

Sakradzija, M., A. Seifert, and A. Dipankar, 2016: A stochastic scale-aware parameterization of shallow cumulus convection across the convective gray zone. *Journal of Advances in Modeling Earth Systems*, **8**, 786–812.

Sakradzija, M., A. Seifert, and T. Heus, 2015: Fluctuations in a quasi-stationary shallow cumulus cloud ensemble. *Nonlinear Processes in Geophysics*, **22**, 65–85.

Salzen, K. von, and N. A. McFarlane, 2002: Parameterization of the bulk effects of lateral and cloud-top entrainment in transient shallow cumulus clouds. *Journal of the Atmospheric Sciences*, **59**, 1405–1430.

Satoh, M., K Oouchi, T Nasuno, H Taniguchi, Y Yamada, H Tomita, C Kodama, J Kinter, D Achuthavarier, J Manganello, et al., 2012: The Intra-Seasonal Oscillation and its control of tropical cyclones simulated by high-resolution global atmospheric models. *Climate dynamics*, **39**, 2185–2206.

Schiemann, R., M.-E. Demory, M. S. Mizielinski, M. J. Roberts, L. C. Shaffrey, J. Strachan, and P. L. Vidale, 2014: The sensitivity of the tropical circulation and Maritime Continent precipitation to climate model resolution. *Climate Dynamics*, **42**, 2455–2468.

Seifert, A, and K. D. Beheng, 2006: A two-moment cloud microphysics parameterization for mixed-phase clouds. Part 1: Model description. *Meteorology and Atmospheric Physics*, **92**, 45–66.

Seifert, A., and K. D. Beheng, 2001: A double-moment parameterization for simulating autoconversion, accretion and selfcollection. *Atmospheric Research*, **59**, 265–281.

Seifert, A., and T. Heus, 2013: Large-eddy simulation of organized precipitating trade wind cumulus clouds. *Atmospheric Chemistry and Physics*, **13**, 5631–5645.

Seifert, A., T. Heus, R. Pincus, and B. Stevens, 2015: Large-eddy simulation of the transient and near-equilibrium behavior of precipitating shallow convection. *Journal of Advances in Modeling Earth Systems*, **7**, 1918–1937.

Siebesma, A. P., 1998: Shallow cumulus convection. *Buoyant convection in geophysical flows*. Springer, 441–486.

Siebesma, A. P., P. M. Soares, and J. Teixeira, 2007: A combined eddy-diffusivity mass-flux approach for the convective boundary layer. *Journal of the Atmospheric Sciences*, **64**, 1230–1248.

Siebesma, A. P. et al., 2003: A large eddy simulation intercomparison study of shallow cumulus convection. *Journal of the Atmospheric Sciences*, **60**, 1201–1219.

Simmons, A., S. Uppala, D. Dee, and S. Kobayashi, 2007: ERA-Interim: New ECMWF reanalysis products from 1989 onwards. *ECMWF newsletter*, **110**, 25–35.

Singh, S. V., R. H. Kripalani, and D. R. Sikka, 1992: Interannual variability of the Madden–Julian oscillations in Indian summer monsoon rainfall. *Journal of Climate*, **5**, 973–978.

Slingo, J., K. Sperber, J. Boyle, J.-P. Ceron, M Dix, B Dugas, W Ebisuzaki, J Fyfe, D Gregory, J.-F. Gueremy, et al., 1996: Intraseasonal oscillations in 15 atmospheric general circulation models: results from an AMIP diagnostic subproject. *Climate Dynamics*, **12**, 325–357.

Sorbjan, Z., 1986: On similarity in the atmospheric boundary layer. *Boundary-Layer Meteorology*, **34**, 377–397.

Stevens, B., C.-H. Moeng, and P. P. Sullivan, 1999: Large-eddy simulations of radiatively driven convection: sensitivities to the representation of small scales. *Journal of the Atmospheric Sciences*, **56**, 3963–3984.

Stevens, B., and A. Seifert, 2008: Understanding macrophysical outcomes of microphysical choices in simulations of shallow cumulus convection. *Journal of the Meteorological Society of Japan*, **86**, 143–162.

Stevens, B. et al., 2005: Evaluation of large-eddy simulations via observations of nocturnal marine stratocumulus. *Monthly Weather Review*, **133**, 1443–1462.

Stirling, A., and R. Stratton, 2012: Entrainment processes in the diurnal cycle of deep convection over land. *Quarterly Journal of the Royal Meteorological Society*, **138**, 1135–1149.

Strachan, J., P. L. Vidale, K. Hodges, M. Roberts, and M.-E. Demory, 2013: Investigating global tropical cyclone activity with a hierarchy of AGCMs: The role of model resolution. *Journal of Climate*, **26**, 133–152.

Stramer, O., P. Brockwell, and R. Tweedie, 1996: Continuous-time threshold AR (1) processes. *Advances in Applied Probability*, **28**, 728–746.

Stull, R. B., 1985: A fair-weather cumulus cloud classification scheme for mixed-layer studies. *Journal of Applied Meteorology and Climatology*, **24**, 49–56.

Suselj, K., M. J. Kurowski, and J. Teixeira, 2019: A unified eddy-diffusivity/mass-flux approach for modeling atmospheric convection. *Journal of the Atmospheric Sciences*, **76**, 2505–2537.

Sušelj, K., J. Teixeira, and D. Chung, 2013: A unified model for moist convective boundary layers based on a stochastic eddy-diffusivity/mass-flux parameterization. *Journal of the Atmospheric Sciences*, **70**, 1929–1953.

Tallis, G. M., 1961: The moment generating function of the truncated multinormal distribution. *Journal of the Royal Statistical Society. Series B (Methodological)*, 223–229.

Taraphdar, S., F. Zhang, L. R. Leung, X. Chen, and O. M. Pauluis, 2018: MJO affects the monsoon onset timing over the Indian region. *Geophysical Research Letters*, **45**, 10011–10018.

Taylor, K. E., 2001: Summarizing multiple aspects of model performance in a single diagram. *Journal of Geophysical Research: Atmospheres*, **106**, 7183–7192.

Teixeira, J., and C. A. Reynolds, 2008: Stochastic nature of physical parameterizations in ensemble prediction: a stochastic convection approach. *Monthly Weather Review*, **136**, 483–496.

Tiedtke, M., 1989: A comprehensive mass flux scheme for cumulus parameterization in large-scale models. *Monthly Weather Review*, **117**, 1779–1800.

Tompkins, A. M., 2000: The impact of dimensionality on long-term cloud-resolving model simulations. *Monthly Weather Review*, **128**, 1521–1535.

Tompkins, A. M., 2001: Organization of tropical convection in low vertical wind shears: The role of cold pools. *Journal of the Atmospheric Sciences*, **58**, 1650–1672.

Torri, G., Z. Kuang, and Y. Tian, 2015: Mechanisms for convection triggering by cold pools. *Geophysical Research Letters*, **42**, 1943–1950.

Trenberth, K. E., G. W. Branstator, D. Karoly, A. Kumar, N.-C. Lau, and C. Ropelewski, 1998: Progress during TOGA in understanding and modeling global teleconnections associated with tropical sea surface temperatures. *Journal of Geophysical Research: Oceans*, **103**, 14291–14324.

Turner, J., 1963: The motion of buoyant elements in turbulent surroundings. *Journal of Fluid Mechanics*, **16**, 1–16.

Tzen, B., and M. Raginsky, 2019: Neural stochastic differential equations: deep latent Gaussian models in the diffusion limit. *arXiv preprint arXiv:1905.09883*.

vanZanten, M. C. et al., 2011: Controls on precipitation and cloudiness in simulations of trade-wind cumulus as observed during RICO. *Journal of Advances in Modeling Earth Systems*, **3**, M06001.

Vitart, F, 2009: Impact of the Madden Julian Oscillation on tropical storms and risk of landfall in the ECMWF forecast system. *Geophysical Research Letters*, **36**.

Vitart, F, and J. Anderson, 2001: Sensitivity of Atlantic tropical storm frequency to ENSO and interdecadal variability of SSTs in an ensemble of AGCM integrations. *Journal of Climate*, **14**, 533–545.

Vitart, F., 2006: Seasonal forecasting of tropical storm frequency using a multi-model ensemble. *Quarterly Journal of the Royal Meteorological Society: A journal of the atmospheric sciences, applied meteorology and physical oceanography*, **132**, 647–666.

Waliser, D. et al., 2009: MJO simulation diagnostics. *Journal of Climate*, **22**, 3006–3030.

Wang, B., and J. C. Chan, 2002: How strong ENSO events affect tropical storm activity over the western North Pacific. *Journal of Climate*, **15**, 1643–1658.

Wang, X., and M. Zhang, 2014: Vertical velocity in shallow convection for different plume types. *Journal of Advances in Modeling Earth Systems*, **6**, 478–489.

Wang, Y., G. J. Zhang, and G. C. Craig, 2016: Stochastic convective parameterization improving the simulation of tropical precipitation variability in the NCAR CAM5. *Geophysical Research Letters*, **43**, 6612–6619.

Wang, Z., 2020: A method for a direct measure of entrainment and detrainment. *Monthly Weather Review*, **148**, 3329–3340.

Webster, P. J., and R. Lukas, 1992: TOGA COARE: The coupled ocean–atmosphere response experiment. *Bulletin of the American Meteorological Society*, **73**, 1377–1416.

Wheeler, M. C., and H. H. Hendon, 2004: An all-season real-time multivariate MJO index: development of an index for monitoring and prediction. *Monthly Weather Review*, **132**, 1917–1932.

Willmott, C. J., and K. Matsuura, 1995: Smart interpolation of annually averaged air temperature in the United States. *Journal of Applied Meteorology*, **34**, 2577–2586.

Wilson, J., 2008: Monin-obukhov functions for standard deviations of velocity. *Boundary-Layer Meteorology*, **129**, 353–369.

Winkler, C. R., M. Newman, and P. D. Sardeshmukh, 2001: A linear model of wintertime low-frequency variability. Part I: Formulation and forecast skill. *Journal of Climate*, **14**, 4474–4494.

Wolding, B. O., J. Dias, G. Kiladis, F. Ahmed, S. W. Powell, E. Maloney, and M. Branson, 2020: Interactions between moisture and tropical convection. Part I: The coevolution of moisture and convection. *Journal of the Atmospheric Sciences*, **77**, 1783–1799.

Wolding, B. O., and E. D. Maloney, 2015: Objective diagnostics and the Madden–Julian oscillation. Part II: Application to moist static energy and moisture budgets. *Journal of Climate*, **28**, 7786–7808.

Wood, R., and P. R. Field, 2011: The distribution of cloud horizontal sizes. *Journal of Climate*, **24**, 4800–4816.

Wu, G., and N.-C. Lau, 1992: A GCM simulation of the relationship between tropical-storm formation and ENSO. *Monthly Weather Review*, **120**, 958–977.

Wyngaard, J., O. Coté, and Y Izumi, 1971: Local free convection, similarity, and the budgets of shear stress and heat flux. *Journal of the Atmospheric Sciences*, **28**, 1171–1182.

Xu, K.-M., A. Arakawa, and S. K. Krueger, 1992: The macroscopic behavior of cumulus ensembles simulated by a cumulus ensemble model. *Journal of the Atmospheric Sciences*, **49**, 2402–2420.

Yanai, M., S. Esbensen, and J.-H. Chu, 1973: Determination of bulk properties of tropical cloud clusters from large-scale heat and moisture budgets. *Journal of the Atmospheric Sciences*, **30**, 611–627.

Yang, B., M. Wang, G. J. Zhang, Z. Guo, A. Huang, Y. Zhang, and Y. Qian, 2021: Linking deep and shallow convective mass fluxes via an assumed entrainment distribution in CAM5-CLUBB: parameterization and simulated precipitation variability. *Journal of Advances in Modeling Earth Systems*, **13**, e2020MS002357.

Yang, S., T. Zhang, Z. Li, and S. Dong, 2019: Climate variability over the Maritime Continent and its role in global climate variation: A review. *Journal of Meteorological Research*, **33**, 993–1015.

Yano, J.-I., and R. S. Plant, 2020: Why does Arakawa and Schubert's convective quasi-equilibrium closure not work? Mathematical analysis and implications. *Journal of the Atmospheric Sciences*, **77**, 1371–1385.

Yeo, K., and D. M. Romps, 2013: Measurement of convective entrainment using Lagrangian particles. *Journal of the Atmospheric Sciences*, **70**, 266–277.

Yoneyama, K., C. Zhang, and C. N. Long, 2013: Tracking pulses of the Madden–Julian oscillation. *Bulletin of the American Meteorological Society*, **94**, 1871–1891.

Yoo, C., S. Park, D. Kim, J.-H. Yoon, and H.-M. Kim, 2015: Boreal winter MJO teleconnection in the Community Atmosphere Model version 5 with the unified convection parameterization. *Journal of Climate*, **28**, 8135–8150.

Yoshimura, H., R. Mizuta, and H. Murakami, 2015: A spectral cumulus parameterization scheme interpolating between two convective updrafts with semi-Lagrangian calculation of transport by compensatory subsidence. *Monthly Weather Review*, **143**, 597–621.

Yuan, T., 2011: Cloud macroscopic organization: order emerging from randomness. *Atmospheric Chemistry and Physics*, **11**, 7483–7490.

Yuval, J., and P. A. O'Gorman, 2020: Stable machine-learning parameterization of subgrid processes for climate modeling at a range of resolutions. *Nature Communications*, **11**, 1–10.

Zhang, C., and J. Ling, 2017: Barrier effect of the Indo-Pacific Maritime Continent on the MJO: Perspectives from tracking MJO precipitation. *Journal of Climate*, **30**, 3439–3459.

Zhang, G., and N. McFarlane, 1995a: Sensitivity of climate simulations to the parameterization of cumulus convection in the Canadian Climate Centre general circulation model. *Atmosphere–Ocean*, **33**, 407–446.

Zhang, G. J., and N. A. McFarlane, 1995b: Sensitivity of climate simulations to the parameterization of cumulus convection in the canadian climate centre general circulation model. *Atmosphere-Ocean*, **33**, 407–446.

Zhang, M. et al., 2013: CGILS: results from the first phase of an international project to understand the physical mechanisms of low cloud feedbacks in single column models. *Journal of Advances in Modeling Earth Systems*, **5**, 826–842.

Zhao, H., L. Wu, and W. Zhou, 2010: Assessing the influence of the ENSO on tropical cyclone prevailing tracks in the western North Pacific. *Advances in Atmospheric Sciences*, **27**, 1361–1371.

Zhao, M. et al., 2018: The GFDL global atmosphere and land model AM4.0/LM4.0: 2. Model description, sensitivity studies, and tuning strategies. *Journal of Advances in Modeling Earth Systems*, **10**, 735–769.

Zheng, Y., J.-L. Lin, and T. Shinoda, 2012: The equatorial Pacific cold tongue simulated by IPCC AR4 coupled GCMs: upper ocean heat budget and feedback analysis. *Journal of Geophysical Research: Oceans*, **117**.

Zhu, L., C. Lu, S. Yan, Y. Liu, G. J. Zhang, F. Mei, B. Zhu, J. D. Fast, A. Matthews, and M. S. Pekour, 2021: A new approach for simultaneous estimation of entrainment and detrainment rates in non-precipitating shallow cumulus. *Geophysical Research Letters*, **48**, e2021GL093817.

국 문 초 록

대류 모수화는 역학 모델에서 다루는 규모보다 작은 규모의 대류성 난류를 모형화한다. 대류 모수화를 개발하는 것과 관련하여 여러 도전적인 문제들이 존재하지만 최근 주목을 받고 있는 주요 문제 중 하나는 확률론적 대류 모수화이다. 수치 기상 예측 모델과 기후 모델의 수평 격자 크기가 작아지면 격자 내의 대류 활동은 확률적이며 준평형 가정이 유효하지 않다. 본 연구에서는 대류성 구름 변동성을 생성하는 물리적 과정들을 조사하고 통합 대류 모수화를 기반으로 다양한 격자 크기에 대한 대류 경향의 평균 및 분산을 모의하는 확률론적 모수화를 개발한다.

먼저, 통합 대류 모수화의 전지구 모의 특성을 평가하였다. 통합 대류 모수화를 포함한 Community Earth System Model 버전 1을 사용하여 엘니뇨-남방진동과 매든-줄리안 진동이 열대성 저기압 발생에 미치는 영향을 분석하였다. 전반적으로 통합 대류 모수화를 포함한 모형은 관측된 열대성 저기압 발생에 대한 매든-줄리안 진동의 영향과 엘니뇨-남방진동과 매든-줄리안 진동의 결합한 영향을 CESM1 보다 잘 재현하였다. 이어서 통합 대류 모수화의 장기 결합 전지구 모의를 사용하여 엘니뇨-남방진동 예측을 위한 새로운 방법인 MA-LIM을 개발하였다. MA-LIM은 선형 역 모델에 의해 예측된 해수면 온도 및 해수면 높이 아노말리를 모델 아날로그 예측에 넛징한다. 짧은 예측월에서 선형 역 모형은 모델 아날로그보다 니뇨3.4 해수면 온도 아노말리를 더 잘 예측한다. 반면 MA-LIM은 모든 예측월에 대해 가장 좋은 성능을 보인다. MA-LIM은 모델 아날로그의 성능이 떨어지는 측면들을 해결하는 것으로 나타났다.

통합 대류 모수화를 확장하여 얕은 대류를 위한 확률론적 통합 대류 모수화를 개발하였다. 지표 근처의 대류성 상승기류들은 상승기류 수직속도와 열역학적 스칼라의 다변수 가우시안 분포에서 샘플링되고, 분포의 표준편차와 변수 간 상관계수는 지표층 상사 이론에서 계산된다. 지표의 상승기류 반지름은 특정 규모 제한 반지름을 가진 멱법칙 분포를 따른다. 계산 효율성을 향상하기 위해 n 개의 빈 플룸과 한 개의 확률론적 플룸으로 구성된 하이브리드 샘플링 방법을 고안하였으며, 각 플룸은 각각 그리드 평균 대류 경향의 평균과 분산을 제어한다. BOMEX 얕은 대류 사례의 큰 에디 모사를 사용하여 단일기둥모델에서 확률론적 통합 대류 모수화를 평가하였다. 큰 에디 모사에서 모의된 수직속도와 열역학적 변수들은 확률론적 통합 대류 모수화의 가정과 일관되게 각각 반가우시안과 가우시안 분포를 따른다. 큰 에디 모사 결과는 운저고도에서 열역학적 변수의 변동성의 상당 부분이 표면에서 기인한다는 것을 보여주었으며, 표면에서부터 시작된 건조대류에서부터 다양한 유형의 습윤대류를 모의하는 확률론적 통합 대류 모수화의 개념을 증명한다. 전반적으로 확률론적 통합 대류 모수화는 큰 에디 모사에서 모의된 도메인 크기 및 상승기류 반지름에 대한 종속성을 포함하여 열역학적 변수들의 평균 및 분산뿐만 아니라 격자 평균 열역학적 상태를 재현한다.

표면 근처에서의 확률론적 초기화에 이어서 기계학습 기법을 사용한 확률론적 혼합 모델을 제시하였다. 이 모델은 부분 연행률, 부분 이탈률, 부분 희석률 및 수직 가속도에 대한 확률미분방정식으로 구성된다. 확률미분방정식의 미지수들은 구름 및 환경 속성의 인풋을 가지는 심층 신경망을 사용하여 모수화된다. 심층 신경망은 이전에 제안된 모수화보다 연행률 및 이탈률을 더 잘 예측하는 것으로 나타났다. 새로운 혼합 모델은 확률론적 통합 대류 모수화에 적용되었으며 두 가지 해양 얕은 대류 사례에 대해 단일기둥모델으로 평가하였다. 새로운 혼합 모델을 사용한 시뮬레이션은 다양한 대류 상승기류 특성의 현실적인 평균과 분산을 계산하였고, 적절한 양의 변동성이 생성되었다. 상승기류 질량속과

습윤보존량들이 정확하게 모의 됨으로써 기존 통합 대류 모수화의 모델 에러가 감소하였다.

중규모 조직 흐름의 영향을 모수화하여 얕은 대류에 대해 공식화된 확률론적 통합 대류 모수화를 깊은 대류로 확장하였다. 확장된 확률론적 대류 모수화는 표면 근처에서 상승 기류의 열역학적 특성을 다변수 가우시안 분포로 모수화한다. 분포의 분산은 조직화되지 않은 난류의 분산 및 중규모 조직 흐름의 분산의 합으로 모수화되었다. 규모 제한 반지름은 중규모 조직 흐름 강도의 선형 함수로 모수화하였다. 확률론적 통합 대류 모수화에 도입된 매개변수들은 해양의 단일 기둥모델 모의 10가지 사례를 사용하여 최적화되었다. 최적화된 확률론적 통합 대류 모수화는 열대 대류 사례에 대해서 기존 통합 대류 모수화의 열역학적 프로파일 및 강수율의 모의 에러를 크게 감소시켰다. 매든-줄리안 진동과 관련된 온도 및 습도 아노말리 변동의 모의 또한 개선하였다. 이상화된 깊은 대류 사례를 추가로 모의하였고, 확률론적 통합 대류 모수화가 상승기류 반지름에 따라 증가한 구름 변동성을 생성하며 얕은 대류와 깊은 대류의 공존을 나타내는 능력이 있음을 확인하였다.

매든-줄리안 진동을 중심으로 확률론적 통합 대류 모수화의 전지구 모의 성능을 평가하고 통합 대류 모수화와 비교하였다. 평균 기후의 모의 성능은 통합 대류 모수화와 확률론적 통합 대류 모수화가 거의 유사하나 확률론적 통합 대류 모수화가 평균 편향을 약간 감소시킨다. 계절 내 변동성 모의의 경우 확률론적 통합 대류 모수화가 여러 측면에서 향상된 모습을 보인다. 확률론적 통합 대류 모수화는 통합 대류 모수화에서 약하게 모의된 겨울 매든-줄리안 진동의 강도와 전파 패턴을 개선한다. 많은 기후 모형이 과소모의하는 매든-줄리안 진동과 관련된 대류와 대규모 순환 간의 일관성 또한 향상되었다. 확률론적 통합 대류 모수화에 의한 매든-줄리안 진동 모의의 개선은 모델에서 수분과 대류 사이의 관계가 향상된 것과 관련이 깊다. 확률론적 통합 대류 모수화에 의한 얕은 대류의

빈도 증가는 대류 정점에 앞서서 더 강한 수분 수렴으로 이어지고 조직화된 대류의 더 강력한 발달과 빈번한 강한 강수를 초래한다. 강수버젯 분석은 확률론적 통합 대류 모수화가 매든-줄리안 진동 발달 기간 동안 수평 이류 및 대류 과정으로 인한 수분 경향을 증가시킴을 보였다.

주요어: 박사, 대류 도시 기상 연구실, 학위 논문, 확률론적 모수화, 대류, 모수화, 기후 모형

학 번: 2016-20420

감사의 글

지난 7년간의 학위과정을 인도해주신 주님께 감사드립니다. 부족한 제가 학위과정을 무사히 마칠 수 있었던 것은 학자의 꿈을 응원해주고 가까이서 많은 도움을 주었던 사람들 덕분입니다. 이 글을 통해 그분들께 감사의 말씀을 드립니다.

가장 먼저, 지도교수님이신 백종진 교수님께 깊이 감사드립니다. 백종진 교수님을 지도교수님으로 만나 너무 다행이라고 생각합니다. 다른 연구실에서 온 저를 연구실의 일원으로 받아주시고 제가 기존에 하던 연구를 계속 이어서 할 수 있도록 도와주셨습니다. 분명 쉽지 않은 결정이셨을 테지만 제가 꿈을 이어나갈 수 있도록 배려해주신 은혜에 감사드립니다. 학문적으로 그리고 다른 면에서 부족함이 많은 저를 항상 따뜻한 조언과 격려로 이끌어주셨습니다. 과학적인 사고란 어떠한 것인지, 연구자로서 어떠한 자세로 연구에 임해야 하는지 짧다면 짧은 기간 동안 중요한 배움을 얻었습니다. 그것은 단지 연구에서뿐만 아니라 인생을 살아가는 방식에 있어서도 중요한 가르침이었습니다. 학문과 학생 지도에 열정적이신 교수님을 보며 저 또한 그러한 학자로 성장하고 싶은 꿈을 키우게 되었습니다. 앞으로 교수님께서 주신 가르침들을 잊지 않고 성장하는 연구자가 되겠습니다.

학위논문을 완성할 수 있도록 다방면으로 도움을 주신 학위논문 심사위원 분들께도 감사드립니다. 심사위원장을 맡아주신 손석우 교수님 그리고 위원을 맡아주신 부산대학교 엄준식 교수님, KIAPS 한지영 박사님, 경북대학교 송환진 박사님께 감사드립니다. 바쁘신 와중에도 아낌없는 조언과 코멘트들을 주셔

서 다양한 시선에서 연구를 보완하고 학위논문을 완성할 수 있었습니다. 부족한 연구이지만 모두 격려의 말씀을 주셨고 덕분에 끝까지 힘을 낼 수 있었습니다. 특별히 손석우 교수님께서 학부생 인턴 때 시작된 인연으로 모델링 연구를 시작할 수 있도록 도와주시고 학위를 마칠 수 있도록 도와주신 데에 감사의 말씀을 드립니다. 학부와 대학원 기간 동안 수업을 통해 많은 가르침을 주신 모든 대기전공 교수님들께도 감사드립니다. 수준 높은 수업을 통해서 대기과학의 기초 지식을 쌓을 수 있었고 무엇보다 가까이서 학문에 대한 열정을 목격하였던 것은 큰 영광이었습니다. 또한 대학원 기간 동안 힘써주신 허종윤 선생님, 김종원 선생님, 류현희 선생님, 유정현 선생님, 전문연구요원 담당 조교님 비롯한 대기과 및 지환부 행정실 직원분들께도 감사의 말씀을 드립니다.

대학원 생활을 함께한 연구실 멤버들에게도 고맙다는 인사를 드리고 싶습니다. 다른 연구실에서 온 저를 따뜻하게 맞아주고 늦은 시간까지 함께 고생하며 힘이 되어주어 고맙습니다. 앞으로 동업자이자 친구로서 오랫동안 인연을 유지하며 함께 꿈을 키워갔으면 좋겠습니다. 한결이형, 학위과정 준비가 막막했는데 항상 친절히 도와주어서 고마워요. 연구실 선배로서 후배들을 망설임 없이 돕는 모습을 보고 저도 그런 선배가 되어야겠다는 생각이 들어요. 승주형, 함께 있는 동안 즐거웠고 본인 연구에 아주 열정적인 모습이 제게 자극이 되었어요. 교수가 되신 것 다시 축하드리고 앞으로 캐나다, 미국에서 즐겁게 연구하시길 바라요. 주현씨, 한동안 연구실 일들을 묵묵히 도맡아 하고 또 제게 많은 도움을 주어서 고마워요. 이제 학위 마치기까지 얼마 남지 않았는데 분명 잘 해내실 거라 믿어요. 성호, 호기심 많고 열정적인 모습을 보면서 많이 배워. 내 귀찮은 부탁들도 잘 들어줘서 고마웠어. 종원, 주말까지 연구실에 나오며 티내지 않고 열심히 하는 모습이 기억에 남네. 앞으로 대학원 생활도 분명 잘 해낼 거야. 아베다, 다른 나라에 와서 추운 날씨에 고생이지만 열심히 하니까 곧 좋은 결과 있을 거예요. 탄비르 그리고 잠바, 짧지만 함께 연구하며 생활하는 동안 즐거웠어요. 혹시 제주도 여행

갈 일 있으면 연락하세요. 나머지 연구실 선배님들도 가끔 연구실에 찾아오셔서 조언해주셔서 감사합니다.

특별히, 이전 대학원 지도교수이셨던 박성수 교수님께도 감사의 말씀을 드립니다. 저의 부족함으로 인해 교수님과 학위과정을 마치지 못했지만, 제가 모델 연구를 계속하겠다고 마음먹은 것은 교수님의 영향이 큽니다. 교수님께서 주신 가르침들 잊지 않고 부끄럽지 않은 연구자가 되는 것이 유일하게 제가 교수님의 은혜에 보답하는 방법일 것입니다. 함께 연구했었던 찬우와 시윤이 그리고 은실 누나도 정말 고마웠고 꼭 나중에 어딘가에서 다시 함께 연구할 수 있었으면 좋겠어. 항상 응원할게, 파이팅.

2011년 서울대학교 입학 이후 벌써 10년 넘게 한 학교에서 여러 인연을 만나며 함께 성장해왔습니다. 11학번 학부 친구 중 결혼한 사람도 있고 해외에 나가서 공부하는 친구들도 있고 서로 다른 모습으로 살고 있지만, 여정을 함께하는 사람들이 있다는 것이 얼마나 든든한지 모릅니다. 돌이켜보면 너무나 즐거운 추억들이 많았습니다. 그리고 대학원 16학번 동기들도 도움을 주고받고 서로 응원하며 어느덧 박사과정을 마쳤거나 곧 마치게 되었습니다. 처음에는 대학원 생활이 끝이 없는 것처럼 막막했지만 함께하는 사람들이 있어서 벌써 이렇게 되었습니다. 그리고 먼저 길을 갔던 선배님들과 미래를 열어갈 후배들이 있기에 가능하지 않았나 싶습니다. 이 모든 분께 감사드리고 앞으로의 길을 응원합니다. 고향 친구들, 고등학교 동기들, 그리고 저를 위해서 기도해주시는 제주도와 서울의 교회 식구들에게도 감사드립니다.

이 학위논문은 하늘의 별이 되신 아버지께 바칩니다. 생전에 제가 외국에 공부하러 나가면 따라가시겠다던 아버지, 분명 하늘에서 자랑스러워하고 계실 것을 믿습니다. 밤낮으로 기도하시고 저를 너무나 사랑하시는 어머니, 제가 부끄러움이 많아 자주 표현하지 못하지만 저도 너무 사랑합니다. 가정의 버팀목이 되어주는 할머니, 동생들에게도 고맙고 사랑한다는 말을 전합니다.